

**A Thesis Submitted for the Degree of PhD at the University of Warwick**

**Permanent WRAP URL:**

<http://wrap.warwick.ac.uk/81826>

**Copyright and reuse:**

This thesis is made available online and is protected by original copyright.

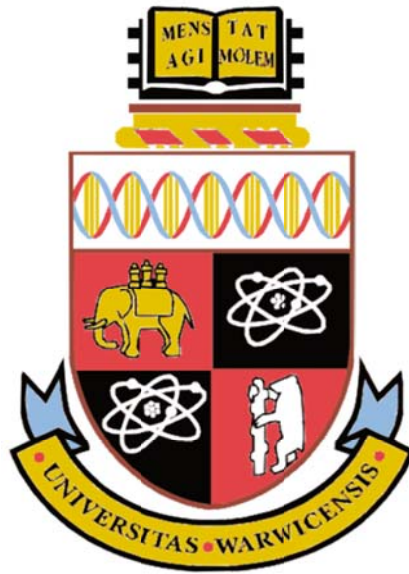
Please scroll down to view the document itself.

Please refer to the repository record for this item for information to help you to cite it.

Our policy information is available from the repository home page.

For more information, please contact the WRAP Team at: [wrap@warwick.ac.uk](mailto:wrap@warwick.ac.uk)

# **A Semi-analytical Approach Utilising Limit Analysis for Slope Stability Assessment and Optimal Design**



Weigao Wu

A thesis submitted for the degree of Doctor  
of Philosophy at the University of Warwick

May 2016

## **Abstract**

### **A Semi-analytical Approach Utilising Limit Analysis for Slope Stability Assessment and Optimal Design**

A thesis submitted for the degree of Doctor of Philosophy  
at the University of Warwick

Weigao Wu

An analytical upper bound method of limit analysis is adopted to derive generalized formulations for assessing the stability of slopes made of geomaterials obeying both the linear Mohr-Coulomb failure criterion and the non-linear Hoek-Brown failure criterion. The thesis is aimed at seeking slope profiles of optimal stability and facilitating the optimal design of pile reinforcement. The effect of the presence of cracks, water pressure, seismic actions, non-homogeneous anisotropic ground and blast-induced damage is investigated. An extensive parametrical study was carried out. A large number of stability and design charts were provided for the benefit of practitioners. A software package to evaluate the safety of slope was created to overcome the limitations of chart-based design using analytical methods.

The main findings of this study can be summarized as follows. Firstly, to avoid potential local failure (sliding of the soil/rock mass behind cracks), the most critical failure mechanism should be determined under the constraint of maximum stable crack depth. Secondly, the application of the tangential technique to tackle the non-

linear Hoek-Brown failure criterion is an acceptable and convenient tool compared with the equivalent  $c - \phi$  method and the variational approach. The minimization of the least upper bound solution corresponding to the Hoek-Brown failure criterion has to be implemented under certain stress constraints to avoid any unrealistic selection of tangent lines. Thirdly, contrary to the previous literature assuming entirely concave shapes, the optimal profiles exhibit both a concave and a convex part. In comparison with the traditional planar profiles, the percentage of increase in the stability factor can reach (up to) 49%. In addition, for engineered slope excavation, given the same stability factor, the average slope inclination of an optimal slope is always higher than that of a planar slope. The amount of ground excavated for the optimal profile can be as little as 50% of that for a planar profile. Lastly, above-pile failure mechanisms must be taken into account when determining the optimal pile position otherwise the installation of piles may be completely ineffective.



## Acknowledgements

Many people have offered me help during my doctoral research period, including my supervisor, my colleagues, my friends and my parents.

Firstly, I would like to give my sincere gratitude to Professor Stefano Utili, my sole supervisor, for his extraordinary patience and consistent encouragement. He has walked me through all the stages during the last four years from the initial proposal of the research topic to thesis writing. Without his enlightening and illuminating instructions, the thesis could not have reached its present form. I have benefited enormously from his critical and rigorous attitude towards academic studies.

I am also greatly indebted to my colleagues, Chrysoula Voulgari, Akram Hasan Abd and Bowen Yang for their invaluable discussions throughout my PhD life and proofreading before the submission of the manuscript. They graciously made considerable comments and sound suggestions for the content and writing of the thesis. Moreover, I am very lucky to have Giulia Carbonari and Aurore Naina as my roommates. I will never forget the taste of the birthday cake they made for me.

Finally, in particular, I am grateful to my parents for their support. They are such good listeners that I always feel reassured after chatting with them. Last but not least, I really appreciate the support by the China Scholarship Council - University of Warwick Scholarships, which covered my tuition fees and living allowance.

# Contents

Abstract.....	i
Acknowledgements.....	iii
Notation .....	vii
Chapter 1 Introduction .....	1
1.1 Background and motivation .....	1
1.2 Thesis outline.....	5
Chapter 2 Literature Review .....	8
2.1 Brief review of methodologies in slope stability assessment.....	8
2.1.1 Limit equilibrium method (LEM) .....	8
2.1.2 Displacement-based finite element method (FEM).....	12
2.1.3 Limit analysis (LA).....	15
2.1.4 Finite element limit analysis (FELA) .....	17
2.1.5 Choice of the method .....	18
2.2 Optimal profile of a slope .....	20
2.3 Optimal position of pile reinforcement.....	24
2.4 Challenges in slope stability assessment .....	26
2.4.1 The presence of cracks.....	27
2.4.2 Seismic loading.....	28
2.4.3 Non-linear strength envelope .....	30
Chapter 3 Stability Assessment of Slopes Made of Geomaterials Obeying the Mohr-Coulomb Failure Criterion.....	33
3.1 Presence of cracks .....	33
3.1.1 Upper bound formulation considering the presence of pre-existing cracks	34
3.1.2 The maximum stable crack depth for pre-existing cracks .....	41
3.1.3 Stability charts in the presence of the most adverse pre-existing cracks..	42
3.1.4 Crack forming as part of the slope failure mechanism .....	45
3.2 Water pressure .....	48
3.2.1 Water appearing in the crack only.....	49
3.2.2 Seepage induced pore water pressure distribution.....	52
3.3 Seismic loading .....	57
3.4 Non-homogenous slopes with anisotropic strength .....	61
3.5 Conclusions .....	67

Chapter 4 Stability Assessment of Slopes Made of Rocks Obeying the Hoek-Brown Failure Criterion .....	69
4.1 Introduction of rock slope failure mode.....	70
4.2 The Hoek-Brown failure criterion .....	72
4.3 Tangential technique .....	75
4.3.1 Cracks of known depth.....	79
4.3.2 Cracks of known location .....	81
4.3.3 Cracks of unspecified depth and location.....	83
4.4 Equivalent $c - \phi$ method.....	90
4.5 Variational approach, the combined method .....	93
4.6 Comparisons of results .....	99
4.6 Blast-induced non-homogeneity in rock slopes .....	105
4.7 Conclusions .....	113
Chapter 5 Optimal Profiles of Slopes .....	115
5.1 Introduction .....	115
5.2 Upper bound formulation for a slope of an arbitrary profile .....	119
5.3 Optimization algorithms to determine the optimal profile.....	125
5.4 Results and comparisons .....	134
5.5 Validation by numerical analyses .....	140
5.6 Study of the geometrical and physical properties of the optimal profile ..	147
5.7 Applications of the optimal slope.....	153
5.7.1. Safety monitoring during excavation .....	153
5.7.2. Re-profiling/profiling a slope to maximize the factor of safety .....	157
5.8 The effect of the presence of pre-existing cracks on soil slopes.....	160
5.9 The effect of non-homogeneity and anisotropy of the ground on optimal slopes	165
5.10 The optimal profiles of slopes made of rock obeying the Hoek-Brown failure criterion.....	169
5.11 The effect of blast-induced damage on rock slopes.....	174
5.12 Conclusions .....	179
Chapter 6 Optimal Design of Pile Reinforcement .....	182
6.1 The most effective pile location .....	184
6.2 Location of the pile ensuring maximum stability factor for the slope .....	196
6.3 The effect of cracks on optimal pile position .....	205
6.4 The effect of pore water pressure on optimal pile position.....	212

6.5	The effect of seismic action on optimal pile position.....	218
6.6	Performance-based optimal design of piles during earthquakes.....	225
6.7	Conclusions .....	231
Chapter 7 Development of a Software Package for Slope Stability Assessment..		233
7.1	Theoretical basis .....	233
7.1.1	Generalized formulation for homogeneous slopes .....	233
7.1.2	Generalized formulation for non-homogeneous slopes.....	237
7.1.3	Sensitivity analysis.....	239
7.2	Framework of the software package.....	239
7.3	Examples and validations .....	244
Chapter 8 Conclusions and Recommendations for Future Work .....		248
8.1	Summary.....	248
8.2	Recommendations for future work .....	254
Appendix A Layered slopes analysis .....		255
Appendix B Program Scripts (MATLAB R2014b) .....		259
Bibliography .....		288

## Notation

$A_{cc}$	$A_{cc} = A_{concave} + A_{convex}$
$A_{concave}$	area of concave part of an optimal slope
$A_{convex}$	area of convex part of an optimal slope
$A_{ex}$	excavated area
$A_i, i=1,2,3\dots7$	areas of several fictitious areas to divide a slope
$b_s$	width of a slice
$c$	generic cohesion
$c_e$	equivalent cohesion
$c_f$	cohesion at failure
$c_h$	horizontal principal cohesion
$c_i$	cohesion at the point where its major principal stress is inclined at angle $i$ to the vertical direction
$c_g$	cohesion of the geomaterial away from failure
$c_t$	intercept of a tangent to a non-linear failure envelope
$c_v$	vertical principal cohesion
$D$	disturbance coefficient
$D_1$	centre-to-centre piles spacing
$D_2$	opening between piles
$D_d$	disturbance coefficient along excavation face
$D_i$	disturbance coefficient of undamaged rock
$D_L$	energy dissipation between layers
$D_S$	energy dissipation along the slip surface
$d_c$	energy dissipation along the crack during crack formation
$E, E_L, E_R$	inter-slice normal force
$F$	factor of safety
$F_{double}$	two-parameter factor of safety
$F_p$	resultant force brought from the piles
$F_{single}$	single-parameter factor of safety
$F_w$	resultant force of water pressure
$f_d$	$f_d = f_{d-c} + f_{d-log}$
$f_{d-c}$	function used to calculate the rate of energy dissipation along the crack

$f_{d-log}, f_{d-log}''$	function used to calculate the rate of energy dissipation due to cohesion
$f'_{d-log}$	function used to calculate the rate of energy dissipation for materials obeying a non-linear failure criterion
$f_H, f_h$	function used to calculate the stability factor
$f_i, i=1,2,3...7$	functions used to calculate the rates of external work $\dot{W}_i$
$f_{ih}, i=1,2,3...7$	functions used to calculate the rates of external work $\dot{W}_{ih}$
$f_{iv}, i=1,2,3...7$	$f_{iv} = (1 + k_v)f_i$
$f_p, f_{p,1}, f_{p,2}$	function used to calculate the rate of resistance work $\dot{W}_p$
$GSI$	geological strength index
$g$	trend line function in Figure 5.24
$H$	generic slope height
$H_{critical}$	critical height of a slope
$H_{eq}$	critical height of a slope using the equivalent $c - \phi$ method
$H_i$	current excavation depth
$H_{tan}$	critical height of a slope using the tangential technique
$H_{total}$	total designed excavation height
$H_{VA}$	critical height of a slope using the variational approach
$h_b$	buried depth of piles
$h_{cr}$	height of tension crack zone
$h_f$	depth of the failure surface measured from slope surface
$h_s$	height of a slice
$K_W$	$K_W = \delta_w/\delta$ , coefficient indicating the amount of water in the crack
$K_{pl}$	coefficient indicating the magnitude of the stabilizing force brought from piles
$k_c$	yield acceleration coefficient
$k_h$	horizontal seismic acceleration coefficient
$k_i$	relative position of a nodal point $i$ on slope face
$k_v$	vertical seismic acceleration coefficient
$L$	horizontal distance from slope toe to crest
$L_0$	horizontal distance from slope crest to the point of failure line daylighting on upper slope
$L_c$	horizontal distance from slope crest to opening of the crack daylighting on upper slope

$l_s$	length of slice base
$M_f$	anti-sliding moment
$M_p$	resultant moment brought from piles
$m$	a parameter used in the Hoek-Brown failure criterion related to rock type
$m_F$	coefficient for the type of lateral pressure distribution along the pile
$m_i$	value of $m$ for intact rock
$N$	stability factor
$N_{concave}$	stability factor of the optimal concave slope
$N_{FELB}$	stability factor obtained by using finite element lower bound method
$N_{FEUB}$	stability factor obtained by using finite element upper bound method
$N_{H-B}$	stability factor for slopes made of rocks obeying the Hoek-Brown failure criterion
$N_{log-spiral}$	stability factor of the optimal logarithmic spiral slope
$N_{M-C}$	stability factor for slopes made of geomaterials obeying the Mohr-Coulomb failure criterion
$N_{M-C,\beta}$	stability factor of an intact slope of inclination $\beta$
$N_{M-C,90}$	stability factor of an intact vertical slope
$N_{min}$	the minimum value of the stability factor with the change of crack depth and location
$N_{optimal}$	stability factor of the optimal slope
$N_{planar}$	stability factor of the planar slope
$N_{UB}$	stability factor obtained by using analytical upper bound method
$N_{VA}$	stability factor obtained by using the combined method
$N^*$	stability number
$n$	a parameter used in the Hoek-Brown failure criterion related to the degree of imperfection of the rock mass
$n_0, n_1, n_2, n_i$	ratios of relative cohesions at various depth
$P_b$	base normal force of a slice
$p_{w-c}, p_{w-log}$	functions used to calculate the rates of external work done by water pressure
$Q$	total virtual work of the sliding mass

$q_1, q_2, q_3$	functions used to calculate the rate of external work $\dot{W}_d$
$r_u$	pore water pressure coefficient
$s$	a parameter used in the Hoek-Brown failure criterion related to the degree of fracturing
$T_s$	base shear force of a slice
$T^*$	external loads
$u$	water pressure
$u_x$	maximum horizontal displacement
$W$	weight of the sliding mass
$\dot{W}_{d-c}$	rate of energy dissipation along the crack
$\dot{W}_{d-log}, \dot{W}_{d-log}''$	rate of energy dissipation due to cohesion
$\dot{W}_{d-log}'$	rate of energy dissipation for geomaterials obeying a non-linear failure criterion
$\dot{W}_{external}$	rate of external work
$\dot{W}_{internal}$	rate of internal energy dissipation
$\dot{W}_i, i=1,2,3 \dots 7$	rates of external work done by the gravity of several fictitious areas
$\dot{W}_{ih}, i=1,2,3 \dots 7$	rates of external work done by the horizontal seismic actions on several fictitious areas
$\dot{W}_p, \dot{W}_{p,1}, \dot{W}_{p,2}$	rate of resistance work done by pile reinforcement
$\dot{W}_s, \dot{W}_{s,h}, \dot{W}_{s,v}$	rate of external work done by seismic actions
$\dot{W}_w$	rate of external work done by pore water pressure
$\dot{W}_{w-c}$	rate of external work done by water in a crack
$\dot{W}_\gamma$	rate of external work done by gravity
$X, X_L, X_R$	inter-slice shear force
$x$	crack position measured from slope crest
$x_1, x_2$	variables identifying the zone in a slope whose stability is affected by the presence of cracks
$x_p$	pile location
$\alpha$	upper slope inclination
$\beta$	slope inclination
$\beta_c$	critical slope inclination
$\beta'$	angle used to identify a below failure mechanism
$\gamma$	unit weight of the ground
$\gamma_w$	unit weight of water



$\delta$	crack depth
$\delta_c$	most adverse crack depth
$\delta_{max}$	maximum allowable crack depth
$\delta_w$	normalized length of the water-filled part of a crack
$\eta$	$\eta = \delta/H$ , normalized crack depth
$\eta_{max}$	maximum normalized crack depth
$\theta_c, \theta_0, \theta_h$	angles to define a logarithmic spiral failure mechanism
$\ddot{\theta}$	angular acceleration
$\kappa$	$\kappa = c_h/c_v$ , anisotropy factor
$\xi$	angle between the velocity discontinuity vector and the failure surface
$\sigma_1, \sigma_3$	major and minor principle stresses
$\sigma_{3max}$	Maximum bound of $\sigma_3$ to determine equivalent $c_e$ and $\phi_e$
$\sigma_c$	compressive strength of the ground
$\sigma_{ci}$	uniaxial compression strength
$\sigma_{cm}$	rock mass strength
$\sigma_n$	normal stress
$\sigma_t$	tensile strength
$\tau$	shear stress
$\tau_g$	shear strength of the ground
$\phi$	generic friction angle
$\phi_e$	equivalent friction angle
$\phi_f$	friction angle at failure
$\phi_m$	mobilized friction angle
$\phi_g$	internal friction angle of the geomaterial away from failure
$\phi_t$	inclination of a tangent to a non-linear failure envelope
$\chi$	crack inclination
$\psi$	dilatancy angle
$\omega$	angular velocity of the sliding mass

# Chapter 1 Introduction

## 1.1 Background and motivation

Landsides are a major threat to human life and property. They can be triggered by weathering, earthquakes, rainfall and improper man-made excavations, etc. Major landslides occurred around the globe in the past century are listed in Table 1-1. According to British Geological Survey (GeoSure 2011), almost 1/3 of the UK territory is prone to landslide accidents, as shown in Figure 1-1. Thus, slope stability assessment and reinforcement design are among the most important research topics in the world of geotechnical engineering. Early investigation of the stability of slopes dates back to Terzaghi (1943). However, despite years of study, people's knowledge of the mechanism behind slope failure is still limited, and current stability assessment methods are unsatisfactory in certain cases.

Table 1-1. Major landslides occurred worldwide in the past century (USGS 2015).

Year	Country (State/Province)	Name & type(s)	Triggering process	Impact
1911	Tadzhik Rep. (Formerly USSR)	Usoy rock slide	Usoy earthquake M = 7.4	Usoy village destroyed; 54 killed; Murgab River dammed, impounding 65-km long still existing Lake Sarez
1919	Indonesia (Java)	Kalut lahars (Volcanic mudflows)	Eruption of Kalut volcano	5,110 killed; 104 villages destroyed or damaged
1920	China (Ningxia)	Haiyuan landslides	Haiyuan earthquake	100,000 killed; many villages destroyed
1921	Kazakh Rep. (formerly USSR)	Alma-Ata debris flow	Snowmelt	500 killed
1933	China (Sichuan)	Deixi landslides	Deixi earthquake M = 7.5	6,800 killed by landslides; 2,500 drowned when landslide dam failed
1939	Japan (Hyogo)	Mount Rokko slides and mud flows	Heavy rain	505 dead/missing; 130,000 homes destroyed or badly damaged by mass movements and/or floods
1949	Tadzhik Rep. (formerly USSR)	Khait rock slide	Khait earthquake M = 7.5	12,000 - 20,000 killed or missing; 33 villages destroyed
1953	Japan (Wakayama)	Arita River slides and debris/mud flows	Heavy rain	460 dead/missing; 4,772 homes destroyed by mass movements/floods
1953	Japan (Kyoto)	Minamiy- amashiro slides & debris/mud flows	Heavy rain	336 dead/missing; 5,122 homes destroyed or badly damaged by mass movements/floods

1958	Japan (Shizuoka)	Kanogawa slides and mud/debris flows	Heavy rain	1,094 dead/missing; 19,754 homes destroyed or badly damaged by mass movements/floods
1962	Peru (Ancash)	Nevados Huascaran debris avalanche	Not known	4,000-5,000 killed; much of village of Ranrahirca destroyed
1963	Italy (Friuli-venezia-Griulia)	Vaiont Reservoir Rockslide	Not known	2,000 killed; city of Longarone badly damaged; total damages: US\$200 million (1963 \$)
1964	United States (Alaska)	1964 Alaska landslides	Prince William Sound Earthquake M = 9.4	Estimated US\$280 million (1964 \$) damages
1965	China (Yunnan)	Rock slide	Not known	Four villages destroyed; 444 dead
1966	Brazil (Rio de Janeiro)	Rio de Janeiro slides, avalanches, debris/mud flows	Heavy rain	1,000 dead from landslides and floods
1967	Brazil (Serra das Araras)	Serra das Araras slides, avalanches, debris/mud flows	Heavy rain	1,700 dead from landslides and floods
1970	Peru (Ancash)	Nevados Huascaran debris avalanche	Earthquake M = 7.7	18,000 dead; town of Yungay destroyed; Ranrahirca partially destroyed
1974	Peru (Huancavelica)	Mayunmarca rock slide-debris avalanche	Not known	Mayunmarca village destroyed, 450 killed; failure of 150-m-high landslide dam caused major downstream flooding
1980	United States (Washington)	Mount St. Helens rock slide-debris avalanche	Eruption of Mount St. Helens	Only 5-10 killed, but major destruction of homes, highways, etc.; major debris flow; deaths low because of evacuation
1983	United States (Utah)	Thistle debris slide	Snowmelt & heavy rain	Major railroad and highways destroyed; Spanish Fork flooding town of Thistle dammed; no deaths
1983	China (Gansu)	Saleshan landslide	Not known	237 dead; four villages buried; two reservoirs filled
1985	Colombia (Tolima)	Nevado del Ruiz debris flows	Eruption of Nevado del Ruiz	Four towns and villages destroyed; flow in valley of Lagunillas River killed more than 20,000 in city of Armero.
1986	Papua, New Guinea (East New Britain)	Bairaman Rock slide-debris avalanche	Bairaman earthquake M = 7.1	Village of Bairaman destroyed by debris flow from breached landslide dam; evacuation prevented casualties; huge effect on local landscape
1987	Ecuador (Napo)	Reventador landslides	Reventador earthquakes M = 6.1 and 6.9	1,000 killed; many kms of trans-Ecuadorian oil pipeline and highway destroyed; total losses: US\$ 1 billion (1987 \$)
1994	Colombia (Cauca)	Paez landslides	Paez earthquake, M = 6.4	Several villages partially destroyed by landslides; 271 dead; 1,700 missing; 158 injured; 12,000 displaced.
1998	Honduras, Guatemala, Nicaragua, El Salvador	Hurricane Mitch flooding Landslides debris-flows	Hurricane Mitch	Approximately 10,000 people killed in the flooding and landslides, which occurred throughout the region. Casitas volcano in Nicaragua experienced large debris flows. Impossible to differentiate deaths from landslides from deaths due to flooding.
1999	Venezuela (Vargas)	Vargas tragedy	Heavy rain	Caused by a heavy storm that deposited 30000 people killed.

2004	Indonesia (South Sulawesi)	Mt. Bawakaraeng landslide	Collapse of caldera wall	32 casualties.
2005	United States (California)	La Conchita Landslide	Remobilization of a previous landslide deposit	13 houses were destroyed and 23 others severely damaged, 10 confirmed fatalities.
2006	Philippines (Southern Leyte)	Southern Leyte mudslide	Heavy rain	The landslide overwhelmed the village of Guinsaugon resulting in the loss of over 1100 people, including 250 schoolchildren who were attending morning classes at the Guinsaugon School.
2007	Bangladesh (Chittagong)	Chittagong mudslides	Illegal hillside cutting and monsoon rains	Landslides in two days killed at least 123 people in the port city.
2008	Egypt (Cairo)	Cairo landslide	Not known	Rockfall from cliffs, individual boulders up to 70 tonnes, 119 people died in the rockslide.
2009	China (Taiwan)	Shiaolin landslide	Typhoon	439-600 casualties.
2010	Uganda (Bududa District)	2010 Uganda Landslide	Heavy rain	The slides buried three villages, leaving 83 dead and more than 300 missing.
2013	India (Uttarakhand)	2013 Uttarakhand floods	Floods	More than 5,700 people were "presumed dead".
2014	Afghanistan (Badakhshan Province)	Badakhshan mudslides	A pair of mudslides	The number of deaths varying from 350 to 2,700. Around 300 houses were buried and over 14,000 were affected.
2015	Colombia (Antioquia Department)	2015 Colombian landslide	Heavy rain	At least 78 people were killed by the landslide. An addition 37 people were injured.

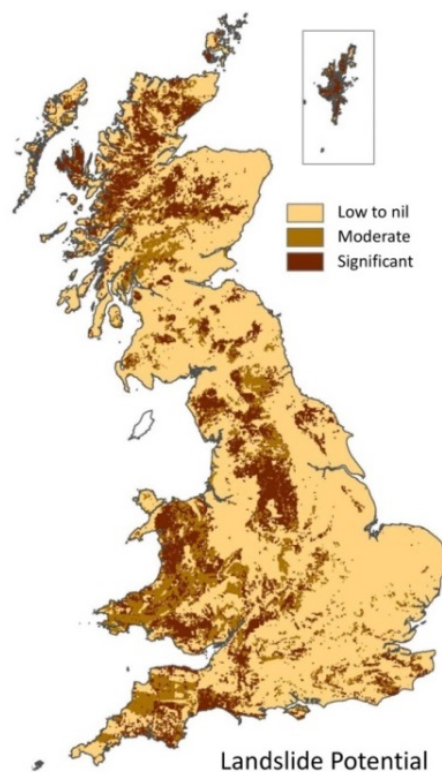


Figure 1-1. Landslide potential in the United Kingdom (GeoSure 2011).

Although numerical simulations such as the displacement-based finite element method with strength reduction technique (Zienkiewicz et al. 1975), finite element limit analysis (Sloan 2013) and distinct element method (Cundall and Strack 1979) are widely applied in evaluating slope stability, they continue to struggle with issues such as mesh dependency, computational efficiency, numerical convergence.

Analytical limit analysis was established by Drucker et al. (1950, 1952) and has been employed in various fields in geotechnical engineering extensively since Chen (1975). Compared with the widely-acknowledged limit equilibrium methods, limit analysis is a more rigorous approach which is ensured by the bound theorems.

In this thesis, an analytical upper bound method of limit analysis is adopted to derive generalized formulations for assessing the stability of slopes made of geomaterials obeying both the linear Mohr-Coulomb failure criterion and the non-linear Hoek-Brown failure criterion. When the factor of safety of a slope is considered to be insufficient, reinforcement measures will take place. The thesis seeks slope profiles of optimal stability when the slope crest and toe are fixed points in space. In addition, the optimal position of pile reinforcement is reappraised with special emphasis placed on both pass-through-pile and above-pile failure mechanisms, which are critical in the optimal pile design.

The effect of the presence of cracks, water pressure, seismic actions, non-homogeneous anisotropic ground and blast-induced damage is investigated. An extensive parametrical study was carried out, and a large number of stability and design charts were provided. Moreover, a software package to evaluate slope stability was created to overcome the limitation of chart-based design using traditional analytical methods and to become a powerful competitor against existing commercial software based on limit equilibrium and finite element method such as Slide (Rocscience 2006), Phase2 (Rocscience 2015) and OptumG2 (OptumCE 2013)

## 1.2 Thesis outline

To begin with, in Chapter 2, the methodologies available for slope stability assessment are reviewed. The pros and cons of different methods are summarized and compared. The reason why the analytical kinematic approach of limit analysis is adopted as the main research tool is explained. In addition, the current findings on the slope profiles of optimal stability and the optimal position of pile reinforcement are reviewed. Moreover, the challenges encountered in the slope stability assessment and the optimal design are evaluated.

Chapter 3 lays out the analytical formulation of the stability assessment of slopes made of geomaterials obeying the Mohr-Coulomb failure criterion. This chapter provides a unitary theoretical framework upon which the following chapters are built. Upper bound solutions are derived for slopes in the presence of both vertical and inclined cracks, various hydraulic conditions and seismic actions. With regard to hydraulic conditions, two scenarios are considered, i.e., water only presents in cracks and seepage induced pore water pressure distribution. The pseudo-static approach is adopted to account for seismic actions. Moreover, the effect of ground strength anisotropy and spatial non-homogeneity in the vertical direction is considered. Stability charts corresponding to different types of loadings and ground conditions are provided.

Chapter 4 evaluates the stability of rock slopes assuming the Hoek-Brown failure criterion including for the first time the presence of pre-existing cracks and blast-induced damage on rocks. Three different techniques are employed and compared: the tangential line technique, the equivalent cohesion-friction angle method and the variational approach.

Chapter 5 aims to seek the optimal profile of a slope whose crest and toe points are fixed. The optimal profile is here defined as the shape corresponding to maximum stability, i.e., the stability factor of the optimal shape is the highest among any shape satisfying a given set of geometrical constraints. With the discretization of slope profile, the stability factors of slopes of any arbitrary shapes are derived. Two different optimization algorithms, i.e., pattern search and genetic algorithm are employed to locate the optimal profile. The results obtained from the proposed kinematic formulation are compared with previous analytical solutions and validated with displacement-based finite element method and finite element limit analyses. In addition, since the new upper bound formulation is capable of computing the stability factors of slopes of any arbitrary shape, the stability of a slope whose shape is varying during the excavation process can be assessed. Moreover, the influence of the presence of pre-existing cracks, non-homogeneity and anisotropy of the ground strength on the optimal profiles is studied. Finally, the optimal profiles corresponding to slopes made of rocks obeying the Hoek-Brown failure criterion are investigated. The effect of blast-induced damage on the stability of the optimal slope is studied.

Chapter 6 discusses the optimal design of pile reinforcement, which can be divided into three categories: the most effective pile location, the location of the pile ensuring maximum stability factor and the location with the minimum accumulative displacement during an earthquake. Above-pile failure mechanism is taken into account for the first time when deriving the analytical solution based upon the upper bound limit analysis. Design charts illustrating all three cases are provided. Also the effect of the presence of cracks, water pressure and seismic actions is evaluated.

Previous research findings employing limit analysis are chart-based. But no stability chart can cover a wide range of ground strength parameters, slope geometries and loading conditions, therefore practitioners at times find it difficult

to use charts for a specific slope project. In Chapter 7, the development of a software package for slope stability assessment based on the analytical upper bound method is introduced. Demonstrations of the software features and validations with other existing software are provided.

Chapter 8 summarizes the findings of previous chapters and provides recommendations for future work.



## Chapter 2 Literature Review

Slope stability analysis is performed to assess the safety of natural slopes and ensure the sound design of man-made slopes (e.g. embankment, open-pit mining, excavation etc.). Slope stability assessment methods may be divided into two major groups: analytical/semi-analytical solutions (e.g., single wedge analysis, limit equilibrium methods, limit analysis) and numerical simulations (e.g., displacement-based finite element method with strength reduction technique, finite element limit analysis). Engineers must fully understand the limitations of each technique to make the right choice in practice.

In this chapter, different slope stability analysis methodologies are reviewed. The pros and cons of each technique are summarized. The reason for employing the upper bound method of limit analysis as the main research tool in the thesis is illustrated.

Then, the topic of the optimal profile of man-made slopes is introduced. In addition, current findings on the optimal position of pile reinforcement are reviewed. These are two important ways to stabilize slopes. Moreover, the challenges encountered in slope stability assessment are discussed.

### 2.1 Brief review of methodologies in slope stability assessment

#### 2.1.1 Limit equilibrium method (LEM)

The limit equilibrium method (LEM) is the earliest technique for assessing slope stability, and is still the most routinely employed approach in engineering practice. As shown in Figure 2-1, soil/rock mass *ABC* above an assumed failure surface is

treated as a rigid body at limit equilibrium. The normal and shear stresses along the failure mechanism  $\widehat{AC}$  follow the Mohr-Coulomb failure criterion. The factor of safety  $F$  of the slope is defined as the ratio of shear strength  $\tau_s$  of the material over the actual shear stress  $\tau$  along  $\widehat{AC}$ :

$$F = \frac{\tau_s}{\tau} \quad (2-1)$$

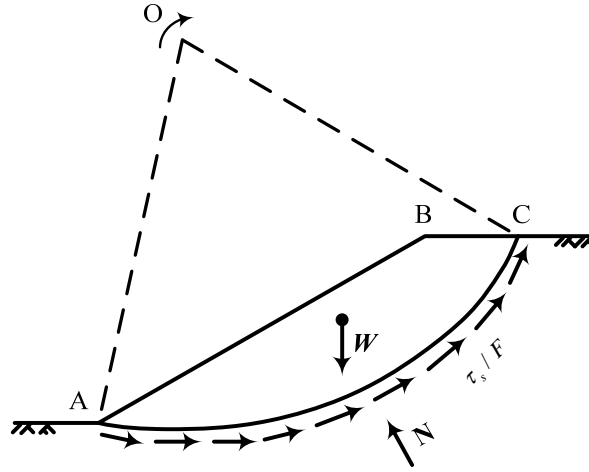


Figure 2-1. A slope at limit equilibrium.

The factor of safety is obtained by finding the least  $F$  corresponding to all tentative failure mechanisms, mainly through trial and error. However, since  $\tau_f$  in Eq. (2-1) is not constant along the failure surface, Eq. (2-1) cannot be applied directly to search for the minimum of  $F$ . Hence, the slice method is proposed as a solution.

Limit equilibrium methods (LEM), sometimes just known as slice methods, divide the slope into several vertical, horizontal or inclined slices (see Figure 2-2). Each slice and the entire sliding mass must meet both static and moment equilibrium equations. The block  $ABC$  reaches a limit state on an assumed failure

mechanism. The factor of safety  $F$  remains constant along the failure mechanism for each slice.

In Figure 2-2, for illustrative purposes, the failure surface  $\widehat{AC}$  is assumed to be circular, with  $O$  as its centre and  $R$  its radius. The block  $ABC$  is divided into  $n$  vertical slices, each with a width of  $b_s$ . The base for each slice is assumed to be a straight line, which has an inclination of  $\alpha$  to the horizontal. The height of the slice is  $h_s$ .

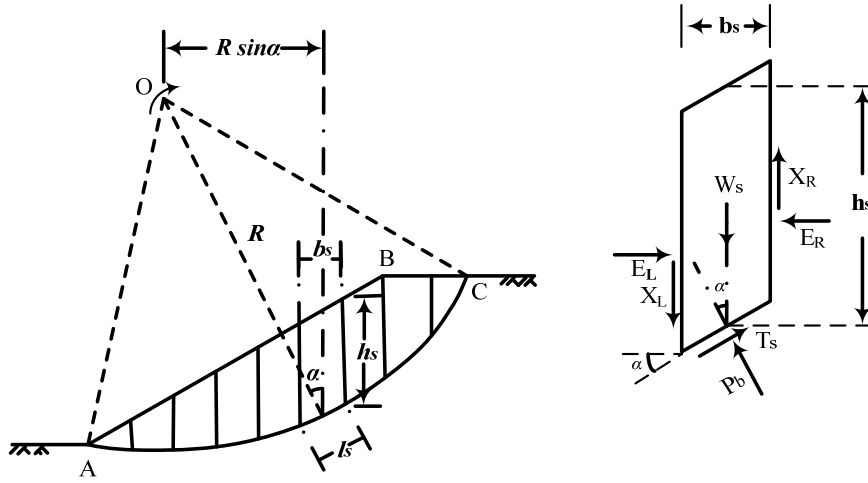


Figure 2-2. Schema of slice method.

The forces acting on each slice are:

- 1) Self-weight of each slice  $W = \gamma b_s h_s$ , with  $\gamma$  the unit weight of the material.
- 2) Base normal force  $P_b = \sigma_n l_s$ , with  $\sigma_n$  the normal stress along the base,  $l_s$  the length of the base.
- 3) Base shear force  $T = \tau l_s$ , with  $\tau$  the shear stress along the base.
- 4) Inter-slice normal force  $E_L$  and  $E_R$ .
- 5) Inter-slice shear force  $X_L$  and  $X_R$ .

Different slice methods have different assumptions to eliminate unknowns. For instance, Fellenius (1936) neglected the inter-slice forces  $E_L$ ,  $E_R$ ,  $X_L$  and  $X_R$ .

and obtained conservative estimation of  $F$ . Later on, Bishop (1955) proposed a slice method that is capable of taking into account the inter-slice forces. The inter-slice normal forces  $E_L$  and  $E_R$  are assumed to act horizontally and the inter-slice shear force  $X_L = X_R = 0$ .

The failure surfaces in the Fellenius method and the Bishop method are assumed to be circular, which are not always valid. Janbu (1954, 1972) developed a more general slice method considering non-circular failure surfaces. The line of action points (thrust line) of inter-slice normal forces  $E_L$  and  $E_R$  are postulated. The height of action point is generally be  $1/3$  of slice height  $h_s$ . Moreover, Morgenstern and Price (1965) put forward a more generalized slice method that can satisfy all force and moment equilibrium equations. There is no assumption about the shape of the failure surface. The force diagrams for different slice methods are illustrated in Figure 2-3.

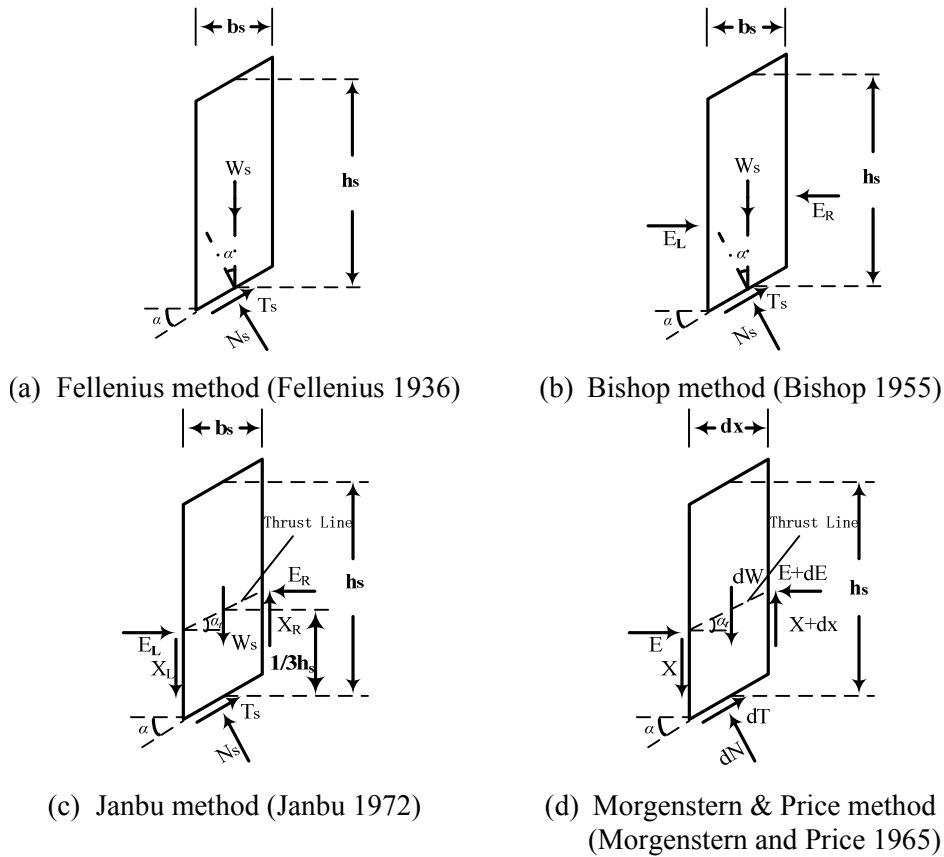


Figure 2-3. Force diagrams for different slice methods.

Although the limit equilibrium method (LEM) neglects the plastic flow rule for the material and make arbitrary assumptions on the inter-slice forces and the shapes of slip surface in some cases, however LEM is still a very popular slope stability assessment method in practice. The issues of accuracy, difficulties and limitations in the calculations are carefully addressed and widely discussed in substantive review papers such as Wright et al. (1973), Fredlund and Krahn (1977), Ching and Fredlund (1983) and Krahn (2003). Thanks to work done by Leshchinsky and Huang (1992), Lam and Fredlund (1993), Espinoza et al. (1994), Zhu et al. (2003), Deng et al. (2014), etc., modern limit equilibrium methods are capable of tackling sophisticated geometry, irregular water conditions, various linear and non-linear shear strength models, etc. In addition, the results obtained from LEM are compared with numerical simulations such as the displacement-based finite element method and finite element limit analysis (e.g., Ugai and Leshchinsky 1995, Duncan 1996, Yu et al. 1998, Hammah 2005, Cheng et al. 2007a) to ensure credible slope stability assessment and design.

### **2.1.2 Displacement-based finite element method (FEM)**

The displacement-based finite element method (FEM) is widely applied in geotechnical engineering since Clough and Duncan (1971) based on the concept of a discrete formulation. It is a powerful tool to assess slope stability, because finite element analyses can provide estimates of displacement patterns and mobilized stresses within the slopes, which has the following advantages over the limit equilibrium method:

- 1) Even if the force and moment equilibrium equations are satisfied in certain “rigorous” slice methods, only the global equilibrium of the slices is imposed. The

finite element method ensures the imposition of local equilibrium at the level of each element within the slope.

2) Limit equilibrium methods calculate the overall factor of safety of a given slope, but no information on the displacements of the slope. The finite element method is capable of obtaining both stress and displacement fields, which is very important for performance-based design.

3) Limit equilibrium methods investigate slopes made of materials obeying the linear Mohr-Coulomb failure criterion. However, some geomaterials may be better described by non-linear criteria. Sophisticated constitutive models can be incorporated in finite element slope stability analyses.

4) Finite element method is better to model various loading conditions and a complex geology such as layered slopes, the presence of a weak layer, soil-structure interaction, rain infiltration, blast-induced vibration, etc.

5) No assumptions need to be made in advance about the shape or location of the potential failure surface, inter-slice forces and their directions. The most critical failure mechanism obtained can be extremely general, and does not have to be limited to circular or logarithmic spiral curves as required by most limit equilibrium methods.

Generally speaking, there are two approaches to evaluating slope stability using the displacement-based finite element method. One approach is to increase the gravity/external load (Li et al. 2009b) until failure happens, while the second approach is to reduce the shear strength of the material. The latter one, first proposed by Zienkiewicz et al. (1975), is also known as the strength reduction technique, and is by far more popular in the research community.

To find the factor of safety of a given slope, it is important to define the limit state when the slope is about to fail. There are three typical indicators of slope instability:

- (a) Non-convergence within a user-specified number of iterations in the finite element program. (Ugai 1989)
- (b) The onset of a sudden big jump of the maximum nodal displacement in certain area of the slope compared to that before failure. (Zienkiewicz et al. 1975)
- (c) A plastic zone developing from slope toe to the top. (Luan et al. 2003)

The slope is regarded as being on the verge of failure when one or several indicators are satisfied. Among them, indicator (b) is the most accepted criterion. Zienkiewicz et al. (1975) divided both cohesion and internal friction angle of the material in a homogenous slope by  $F$  to bring the slope to a limit state.  $F$  is then determined as the factor of safety of the slope. Later, Matsui and San (1992) took up the work done by Zienkiewicz et al. (1975) and named the method as “strength reduction technique”. They found that the factors of safety obtained from the traditional limit equilibrium method and finite element method are very close to each other.

Duncan (1996) summarized the experience of using FEM in various aspects, including the choice of stress-strain relationship of the material and the discrepancy in results compared with field measurements. Griffiths and Lane (1999) and Griffiths and Marquez (2007) conducted a comprehensive 2D and 3D elastoplastic FEM analysis, using the strength reduction technique. The cases of homogeneous slopes, slopes with weak layers, slopes sitting on weak foundation and dams under water drawdown are investigated. A large amount of results are compared with those obtained from limit equilibrium method.

The main drawback of the application of FEM in slope stability analyses is that results can be different depending on which indicator of slope failure is selected. Without a universally accepted indicator, the interpretation of FEM results still causes a problem, and users should rely on their experience and intuition. On the other hand, the internal stress state within the slope after strength reduction is different from the initial condition. Moreover, the mesh density,

number of load steps, the numerical integration scheme, the tolerances used to check convergence of the global equilibrium iterations and the type of element employed in the model (Sloan 2013) may affect the obtained results. Thus, the results obtained from FEM should be deemed as a reference, together with some other techniques.

### 2.1.3 Limit analysis (LA)

Stress equilibrium equations, stress-strain relations and compatibility equations must be satisfied in order to work out a unique solution in finite element analyses. However, a descriptive stress-strain relation is not always accessible especially for geotechnical materials. The main advantage of the application of limit analysis is that the limit or ultimate collapse load can be obtained directly without a step-by-step elastoplastic analysis.

Limit analysis is based on the limit theorems formulated by Drucker et al. (1950, 1952), and assume that the geotechnical structures under investigation undergo small deformations that they are made of rigid-perfectly plastic materials and follow an associated flow rule (normality rule). Two key theorems are (the so-called) upper bound and lower bound theorems: (Chen 1975, 1990)

Theorem I (lower bound, LB) - The loads, determined from a distribution of stress alone, that satisfies: (a) the equilibrium equations; (b) the stress boundary conditions; and (c) the yield criterion, are not greater than the actual collapse loads.

Theorem II (upper bound, UB) - The loads, determined by equating the external rate of work to the internal rate of dissipation in an assumed kinematically admissible velocity field, that satisfies: (a) the velocity boundary conditions; and (b) the strain and velocity compatibility conditions, are not less than the actual collapse load.



Thus, the actual collapse load can be bracketed when upper bound and lower bound values are known. Sometimes a lower and upper bound identical to each other are found so that a precise collapse load can be ascertained on this basis. However, most of the time it is not possible to construct statically admissible stress fields needed by the lower bound theorem. Thus, the kinematic approach of limit analysis (upper bound method) is more popular, and widely employed.

The extensive application of limit analysis in soil mechanics began with Chen (1969), and has been extended to various aspects of geotechnical engineering such as the bearing capacity of footings (Michalowski 1997a, Soubra 1999), determination of the coefficients of active/passive earth pressures (Soubra 2000, Yang 2007) and face stability of tunnels (Leca and Dormieux 1990, Lee and Nam 2001 and Huang and Yang 2011). Upper bound solutions concerning the stability of slopes were proposed to assess the influence of pore water pressure (Michalowski 1995, Viratjandr and Michalowski 2006 and Yang and Zou 2006), seismic actions (You and Michalowski 1999, Michalowski 2002), geosynthetic reinforcement (Michalowski 1997b, Michalowski 1998 and Michalowski 2008) and the presence of cracks (Utili 2013, Michalowski 2013).

As described in Chen (1975, 1990) and Donald and Chen (1997), within the framework of the upper bound limit analysis, slopes are assumed to be made of geomaterials that obey a convex yield condition such as the Mohr-Coulomb failure criterion, with the plastic deformations being governed by the associative flow rule. The application of the kinematic approach is based on equating the rate of work done by external loads (e.g., water pressure, seismic forces and surface loads) and body forces to the internal energy dissipation rate for an assumed kinematically admissible failure mechanism at limit state. This is illustrated in the following equation:

$$\int_{\Omega} \sigma'_{ij} \dot{\epsilon}^*_{ij} d\Omega + \int_{\Gamma} \sigma'_{\Gamma} \dot{\epsilon}^*_{\Gamma} d\Gamma = WV^* + TV^* \quad (2-2)$$

where the first term on the left-hand side of Eq. (2-2) is the rate of work done by the effective stress  $\sigma'_{ij}$  over the virtual strain rates  $\dot{\epsilon}^*_{ij}$ , dissipated within  $\Omega$ , the volume of the sliding soil/rock mass. The second left-hand side term is the internal energy dissipation along the slip surface  $\Gamma$ . The two terms on the right-hand side refer to the rates of work done by the weight of soil  $W$  and external loads  $T^*$  respectively.  $V^*$  is the velocity at the points where  $W$  and  $T^*$  apply. A so-called stability factor  $\frac{\gamma H}{c}$  (according to the terminology of Taylor 1948) can be derived from Eq. (2-2) and will be treated as a measurement of slope stability in the following chapters.

#### 2.1.4 Finite element limit analysis (FELA)

It is extremely difficult to construct statically admissible stress fields according to the lower bound theorem. Moreover, kinematically admissible failure mechanisms for upper bound solutions have to be defined beforehand, which is not available in case of slopes with complex geometry and loading conditions. The theory of finite element limit analysis (FELA) provides a solution, and it combines the bounding theorems with the power of the finite element discretization technique and has become a powerful approach to assess slope stability.

Lysmer (1970) is one of the early pioneers in the development of finite element lower bound analysis. The theory has been significantly improved by Sloan (1988), Yu et al. (1998), Lyamin and Sloan (2002a) and Makrodimopoulos and Martin (2006) to tackle non-linear yield surfaces and incorporate more efficient optimization processes (e.g., non-linear and order cone programming). On the other hand, based on the success of implementing the finite element lower

bound limit analysis, Sloan (1989) proposed an upper bound counterpart by using linear programming. Lyamin and Sloan (2002b) continued to develop the first rigorous upper bound method that comprises both continuum and discontinuity deformation, using non-linear programming. Krabbenhoft et al. (2005) went on to modify the theory by adopting a new stress-based method using an assembly of continuum elements to account for velocity discontinuities, which is capable of accommodating non-linear yield surfaces. Moreover, second order cone programming is employed by Makrodimopoulos and Martin (2007) to increase the efficiency of the optimization process in FELA.

Finite element limit analysis is capable of solving the factor of safety of a slope by applying a strength reduction technique without any information about the complicated stress-strain relationship of the material. The error of the calculation can be estimated by the bound theorems. With the rise of computational power, the heterogeneity and anisotropy of the geomaterial, complex boundary and loading conditions, the effect of water pressure and seismic actions, etc. can be modelled. In addition, FELA is suitable to simulate jointed material and soil/structure interfaces for its intrinsic advantage of incorporating discontinuities in the stress and velocity fields. However, FELA still has the same drawbacks (mesh dependency, element types, numerical convergence, etc.) as those in traditional FEM.

#### **2.1.5 Choice of the method**

The four methods (LEM, FEM, LA, FELA) introduced in the previous sections are widely adopted in slope stability assessment. As summarized in Sloan (2013), the properties of each technique are compared in Table 2-1. Since no single method

can outperform the others, the choice of method to be used has to be determined on a case by case basis.

Considering the two analytical solutions of limit equilibrium and limit analysis, although practitioners are more familiar with the limit equilibrium method, its reliability has suffered a lot from some arbitrary assumptions of the inter-slice forces and failure surfaces in certain limit equilibrium methods (Fredlund and Krahn 1977, Yu et al. 1998). In addition, LEM becomes less efficient or even struggles to converge when sophisticated geometry and loading conditions are encountered (Fredlund 1984, Krahn 2003). Analytical limit analysis is a more rigorous approach, which is ensured by the lower and upper bound theorems (Chen 1975). More importantly, the theory of limit analysis is consistently enhanced by the recent development of solutions (e.g., Utili and Nova 2007, Utili 2013) to tackle new challenges in slope stability assessment and design.

In this thesis, slope profiles of optimal stability are systematically explored through global optimization techniques. Hundreds of thousands of slope stability analyses have to be executed, which makes the numerical methods less favourable. In addition, extensive parametrical assessment and comprehensive stability charts production require an extremely efficient method. The kinematic approach of limit analysis is a suitable candidate for its theoretical rigor, simplicity and the ability to cope with some issues, such as the presence of cracks, water pressure and seismic actions.

However, the limitations of the upper bound approach such as the overestimation of slope stability and the assumption of associated flow rule should also be borne in mind (Tschuchnigg et al. 2015). Thus, in the thesis, the displacement-based finite element method with strength reduction technique and finite element limit analysis are adopted as a reference to validate the results obtained by the analytical upper bound solutions.

Table 2-1. Comparisons among different slope stability assessment methods (Sloan 2013).

Property	LEM	FEM	UB LA	LB LA
Assumed failure mechanism?	Yes	No	Yes	-
Equilibrium satisfied?	Yes In slices	Yes At nodes	-	Yes
Flow rule satisfied?	No	Yes At integration points	Yes	-
Complex loading and boundary conditions possible?	No	Yes	Yes	Yes
Complex material models possible?	No	Yes	No	No
Coupled analysis possible?	No	Yes	No	No
Error estimate?	No	No	Yes With lower bound	Yes With upper bound
Note: UB LA represents upper bound limit analysis LB LA represents lower bound limit analysis				

## 2.2 Optimal profile of a slope

In conventional slope stability assessment, it is generally assumed that the slope is planar from crest to toe. However, natural slopes are invariably curved. Very few systematic studies have been carried out on the stability of non-planar slopes.

Jenike and Yen (1962) presented the results of slope stability analyses in axial symmetry using the slip-line theory formulated by Sokolovskiĭ (1960). They found that S-shaped critical profiles are able to describe the theoretical failure shape. However, as the radius of the slope increases, the profile of the stable slope in axial symmetry approaches the profile of the slope in plane strain, which has an entirely concave shape.

Piteau and Jennings (1970) investigated the impact of curvature in plain-strain conditions on the stability of slopes in four diamond mines in South Africa. Slopes were all at incipient failure (i.e. factor of safety of 1). The average slope height was

100m. They found that that average slope angle for slopes with radii of curvature of 60m was  $39.5^\circ$  as compared to  $27.3^\circ$  for slopes with radii of curvature of 300m.

Hoek and Bray (1981) summarized the influence of slope curvature on slope stability as follows. The stability of slopes can be measured by the steepest allowable slope inclinations under a given factor of safety. When the radius of curvature of a concave slope (see Figure 2-4) is less than the height of the slope, the critical slope inclination can be  $10^\circ$  steeper than that of a planar slope recommended by a routine limit equilibrium stability analysis. In the case of a convex slope with a radius of curvature smaller than the slope height, the slope could be  $10^\circ$  flatter than the inclination of a planar slope. With the increase of the radius of curvature in excess of a value greater than the slope height, these corrections should be brought down for either concave or convex slopes. For radii of curvature beyond twice the slope height, the slope inclination is obtained according to a conventional slope stability analysis. The factor of safety is plotted against different values of  $d/L$  (see Figure 2-4) in Figure 2-5.

In order to validate the findings in Hoek and Bray (1981) and quantify the impact of slope curvature on stability, a series of analyses using finite difference strength reduction technique were performed by Lorig and Varona (2001). A 500m high dry slope made of an isotropic homogenous material with  $35^\circ$  friction, 0.66 MPa cohesion, and  $2600 \text{ kg/m}^3$  density is modelled and two series of analysis were implemented. In the first series, the factor of safety was calculated for axisymmetric conditions with different radii of curvature. The results are shown in Table 2-2. In the second series, the critical slope angle  $\beta_c$  was increased until a factor of safety of 1.3 had been achieved. The results of second series of analyses are illustrated in Table 2-3, which are consistent with the findings in Hoek and Bray (1981).

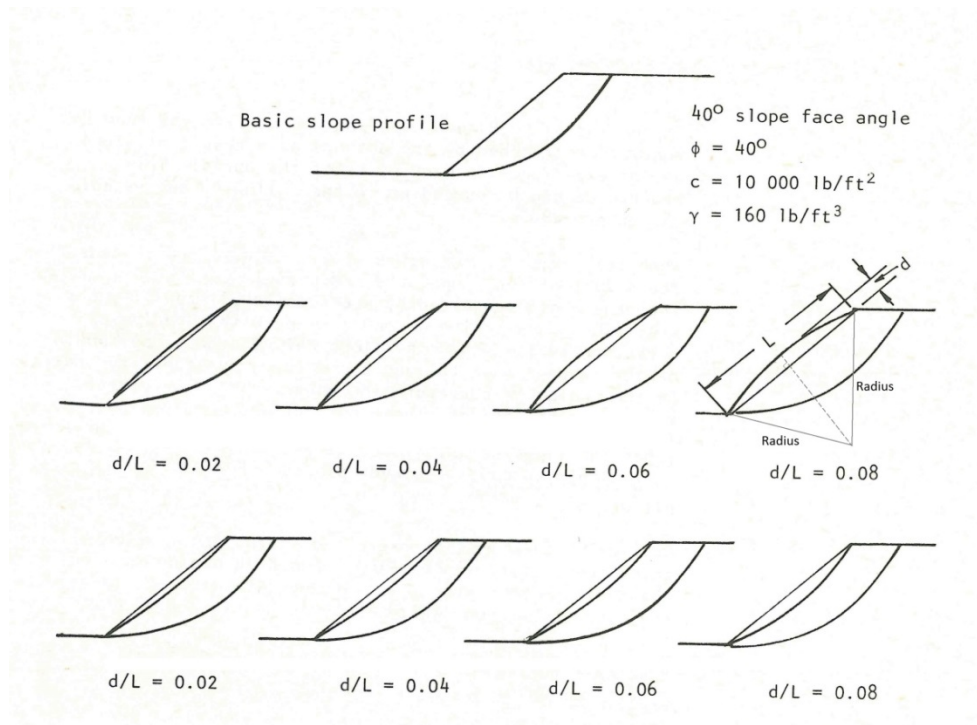


Figure 2-4. Circular slopes with different radii. (Hoek and Bray 1981)

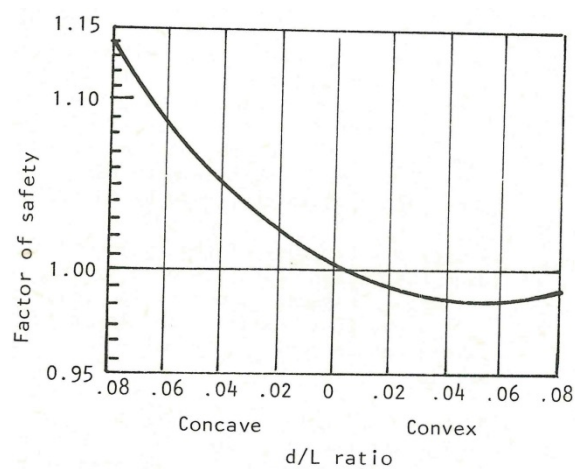


Figure 2-5. Factor of safety against the curvature of circular slope profile. Analysis is carried out using Janbu method (Hoek and Bray 1981).

Table 2-2. Effect of radius of curvature on factor of safety  $F$  for 45° slope.

$\beta_c = 45^\circ$	R=100 m	R=250 m	R=500 m	$R \rightarrow \infty$
	$F=1.75$	$F=1.65$	$F=1.55$	$F=1.3$

Table 2-3. Effect of radius of curvature on slope angle for factor of safety  $F = 1.3$ .

$F = 1.3$	R=100 m	R=250 m	R=500 m	$R \rightarrow \infty$
	$\beta_c = 75^\circ$	$\beta_c = 65^\circ$	$\beta_c = 55^\circ$	$\beta_c = 45^\circ$

The following investigation concentrates on the effect of geometries on three-dimensional slope stability using limit equilibrium method (Xing 1988) and displacement-based finite element method with strength reduction (Rassam and Williams 1999, Cała 2007, Nian et al. 2012, Zhang et al. 2013, Zhang et al. 2015). None of them attempted to find the best slope profile providing the highest stability. In addition, the analyses of previous authors are limited to some pre-determined classes of shape and restricted slope features.

Although the stability of slopes of non-planar profile is evaluated in the aforementioned literature, the shape of the slope profile is imposed, and treated as an input data. The optimal profile of a slope under given geometry constraints has never been attempted before. Planar profiles are taken for granted and routinely adopted when constructing man-made slopes.

Utili and Nova (2007) looked for the most stable profile in the class of slopes profiles with logarithmic spiral shape. To do so, they derived a new formulation in limit analysis to compute the external work made by a double logarithmic spiral shaped soil region sliding away based on the kinematic approach of limit analysis. The optimal log-spiral profiles are determined by maximizing the stability factor. In comparison with slopes with planar profile, the percentage of increase provided by the best spiral in terms of the stability factor can reach as high as 30.5% (depending on the ground properties). If the amount of soil mass to be excavated is fixed, the improvement is even larger.

Theoretical and experimental findings (such as Stefano et al. 2000, Rieke-Zapp and Nearing 2005) seem to indicate that slopes of concave profiles are more capable of resisting erosion. Therefore, based on the optimal profile found for a



weightless or frictionless slope, solved by Sokolovskiĭ (1960) and Sokolovskii (1965), Jeldes et al. (2013) and Jeldes et al. (2014) derived an approximate solution for slopes with  $\phi > 0$  and  $\gamma > 0$  to determine the geometry of optimal concave slopes. This type of profiles belongs to a specific shape of concave slope which is determined by the slip-line method of characteristics.

Although the above studies attempted to seek the best concave profile, none of them considered the arbitrariness of the potential optimal profile and its contribution to enhance slope stability. Hence it was decided to systematically investigate the most stable slope shape for various geometrical constraints and ground properties.

### **2.3 Optimal position of pile reinforcement**

When the factor of safety of a slope is considered to be insufficient, reinforcement measures will take place, one of which is re-profiling the slope with the new found optimal profile and another is to install piles. Anti-sliding piles are widely implemented to stabilize slopes in practice. The investigation of the optimal position of piles is very important because it can maximize pile capacity and bring enormous economic benefit.

The slope-pile system brings new challenges to the existing slope stability assessment procedures by considering the complexity of soil-pile interaction, which has enjoyed an extensive investigation over recent decades. Ito and Matsui (1975) appeared to be the first to develop a theoretical framework to analyze the distribution mode of lateral force around the piles. The impact of pile diameters, spacing between piles and material strength were studied. Soon afterwards, Ito et al. (1979, 1981, 1982) continued to improve the theory by considering the cases of single/multiple row of piles, different locations of piles, constraints of pile heads,

etc. Matsui et al. (1982) carried out small-scale experiments to model soil-pile interaction to verify the theory. The following studies can be categorized into four groups using different methods: limit equilibrium method (Poulos 1995, Lee et al. 1995, Hassiotis et al. 1997, Zeng and Liang 2002), finite element/finite difference analyses (Chen and Poulos 1993, Cai and Ugai 2000, Jeong et al. 2003, Won et al. 2005, Firat 2009, Wei and Cheng 2009, Kourkoulis et al. 2010, Kourkoulis et al. 2011), limit analysis (Ausilio et al. 2001, Nian et al. 2008, Li et al. 2009c), field and physical model tests (Tika et al. 1996, Mezazigh and Levacher 1998, Leung et al. 2000, Pan et al. 2002, Abdoun et al. 2003, Brandenberg et al. 2005, de Sousa Coutinho 2006, Smethurst and Powrie 2007, Frank and Pouget 2008, Guo and Qin 2010, Hayward et al. 2000, Knappett and Madabhushi 2011).

As summarized in Li et al. (2012), the obtained results in predicting the optimal position of pile reinforcement are rather different, or even contradict each other. Poulos (1995) pointed out that the row of piles should be placed in the vicinity of the center of the critical failure surface, to refrain from merely relocating the failure surface behind or in front of the piles. Hassiotis et al. (1997) concluded that the piles should be installed close to the top of the slope, to achieve the maximum safety factor, when the slope is steep in particular. Cai and Ugai (2000) proposed that piles should be located in the center of the slope to realize maximum safety. Ausilio et al. (2001) deduced that the optimal location of the piles within the slope is near the toe of the slope, where the stabilizing force required to increase the safety factor to the desired value takes a minimum value. The conclusion is ascribed to the assumed logarithmic-spiral failure mechanism in limit analysis having a radius that increases as the surface develops from the top to the toe of the slope. Nian et al. (2008) and Li et al. (2009c) observed similar results by extending the kinematic approach of Ausilio et al. (2001). Both Won et al. (2005) and Wei and Cheng (2009) used FLAC3D and drew the conclusion that the optimal pile position falls between the middle of slope and the middle of the

critical slip surface. Lee et al. (1995) found out that the most effective pile positions are at the toe and crest of the slope for homogeneous cohesive soil slopes, and between the middle and the crest of the slope for a two-layered soil slope.

The results of all numerical analyses disclose that the optimal position of a row of piles is close to the middle of the slope. However, by using the combined limit equilibrium analysis and Ito-Matsui's formula (Ito and Matsui 1975), the optimal position approaches the top of the slope. Moreover, according to the results obtained by analytical limit analysis method, the optimal position is near the toe of the slope. There are discrepancies in terms of how the resistance force provided by the anti-sliding piles is considered and what type of the failure mechanism is assumed to be in the formulations. The presence of piles is treated as an equivalent force and a moment in the analytical solutions such as Hassiotis et al. (1997), Ausilio et al. (2001) and Li et al. (2012) but the influence of the soil-pile interaction is neglected. As pointed out by Wei and Cheng (2009), the critical failure surface is divided into two sections when the pile spacing is small, and these two sections will gradually get connect with the increase of pile spacing until a clear single critical failure surface is formed. However, in the all analytical solutions (limit equilibrium method and limit analysis), the failure surfaces are assumed a prior as a continuous circular or logarithmic spiral line.

In this thesis, the optimal pile position is reappraised by using the analytical upper bound limit analysis.

## **2.4 Challenges in slope stability assessment**

Besides the shear strength parameters, slope geometry and reinforcement measures, other factors that would affect the stability of a slope include the presence of cracks, seismic actions and the non-linearity of failure criteria of the ground materials.

These factors pose significant challenges to the traditional slope stability assessment assuming only continuous, static ground obeying the linear Mohr-Coulomb failure criterion. The following sections discuss the influence of these factors.

#### **2.4.1 The presence of cracks**

Cracks are often found in both soil and rock slopes. The presence of cracks can substantially reduce the resistance to failure (Utili 2013, Michalowski 2013). Therefore, it is important to consider cracks in slope stability analysis. The limit equilibrium method, variational approach and limit analysis are three main analytical techniques adopted to investigate the effect of cracks on slope stability.

The issue of the presence of cracks appeared as early as 1943 in one of the most classic publication in geotechnical engineering, by Terzaghi (1943). It is addressed by the limit equilibrium method. Spencer (1967, 1968, 1973) developed a new slice method, taking into account the effect of tension in the soil at the top of an embankment. An expression is proposed for determining the critical depth of tension cracks. Later on, in the book of Hoek and Bray (1981), the stability of cracked rock slopes is tackled. In addition, water present in tension cracks and on sliding surface is considered. Afterwards, Chowdhury and Zhang (1991) studied the effect of tension cracks on the maximum reinforcement force in embankments. Zhu et al. (2003) is one of the recent studies to include the presence of cracks in the generalised framework of limit equilibrium.

Based on the variational approach, Baker (1981) evaluated the influence of tensile strength on the stability of slopes. The depth of tension cracks and their effect on slope stability is estimated. To answer the criticism of the variational approach raised by De Josselin De Jong (1981) and Castillo and Luceno (1982),

Baker (2003) consolidated the previous theory by imposing sufficient conditions for the existence of the minimum in the limit equilibrium analysis.

Recently, Utili (2013) investigated the stability of slopes made of cohesive frictional material subjected to cracks based on the kinematic approach of limit analysis. In the study, detailed derivations of the upper bound solutions are provided, and the case of water appearing in the cracks is discussed. Meanwhile, Michalowski (2013) also evaluated both slopes with pre-existing cracks and the formation of cracks as part of the failure mechanism using limit analysis. In addition, the pore water pressure effect is considered by imposing  $r_u$  in Michalowski (2013).

In this thesis, the stability analysis of slopes subjected to the presence of cracks is present in a unified and consistent framework based on the kinematic approach of limit analysis.

#### **2.4.2 Seismic loading**

As summarized in Gazetas (1987) and Jibson (2011), there are three general categories to assess the stability or performance of slopes during earthquakes: (1) pseudo-static analysis (2) dynamic stress- deformation analysis and (3) permanent-displacement analysis.

Terzaghi (1950) appeared to be the first to apply permanent static body forces onto the conventional static limit equilibrium to represent the seismic actions, as shown in Figure 2-6. Although the so-called pseudo-static analysis makes some unrealistic assumptions such as the fact that the body force applied is permanent and constant in direction, it is still widely adopted for its simplicity, especially in deriving analytical solutions using limit equilibrium method (e.g., Seed and Idriss 1969, Koppula 1984, San and Leshchinsky 1994, Zhou and Cheng 2014) and limit



In this thesis, the pseudo-static method is employed to investigate the stability of slopes subject to seismic actions. Moreover, seismic displacement calculation procedures proposed by Newmark (1965) are adopted to evaluate the optimal pile position corresponds to that yielding the minimum cumulative displacement during an earthquake

### 2.4.3 Non-linear strength envelope

Experiments (e.g. Hoek and Brown 1980; Agar et al. 1987; Baker 2004; Descamps et al. 2012; Meng et al. 2015; Rathnaweera et al. 2015) show a large amount of evidence that the shear strength for both soil and rock can be better represented by using nonlinear failure envelopes. Therefore, it is important to assess the stability of slopes made of geomaterials obeying a nonlinear failure criterion. This issue has been investigated by limit equilibrium methods, limit analysis and finite element methods.

Among all limit equilibrium slice methods, the normal and shear stress on the slip surface can be obtained more easily using the Fellenius method (Fellenius 1936) since it ignores inter-slice forces. The adoption of non-linear failure criteria in Bishop (Bishop 1955) and Janbu (Janbu 1972) stability analysis is provided in Wyllie et al. (2004). Deng et al. (2014) proposed a generalized limit equilibrium method to incorporate both non-circular failure surfaces and non-linear failure criteria. For rocks obeying the Hoek-Brown failure criterion (Hoek et al. 2002), an equivalent set of cohesion  $c$  and friction angle  $\phi$  is derived to linearize the non-linear failure envelope. Hoek et al. (2002) provided an equation to determine the equivalent  $c - \phi$  values. Li et al. (2008) went on to give new equations considering the impact of slope inclinations.

Baker and Frydman (1983), Zhang and Chen (1987) and Chen and Liu (1990) presented a variational approach to assess the stability of slopes made of material obeying a general non-linear failure criterion. Variational calculus is capable of solving the equation of the most critical failure mechanism, together with the stress distribution along it.

In addition, the tangential technique is widely applied to incorporate a non-linear failure envelope in limit analysis. There are numerous tangents to the non-linear failure envelope (see Figure 2-7). For each of them, stability analysis corresponding to a linear Mohr-Coulomb failure envelope can be implemented by replacing  $c$  with  $c_t$ ,  $\phi$  with  $\phi_t$ . Strength parameters  $c_{t,c}$  and  $\phi_{t,c}$ , which correspond to the tangent yielding the most critical upper bound solution, will be selected as the parameters to linearize the non-linear failure criterion. Collins et al. (1988) and Drescher and Christopoulos (1988) were the first to employ the so-called tangential technique to evaluate the stability of slopes for non-linear failure criteria. Later on, Yang et al. (2004) and Yang and Zou (2006) adopted the same method to account for more complex conditions such as an inclined upper slope surface and the presence of pore water pressure for rocks obeying the generalized Hoek-Brown failure criterion.

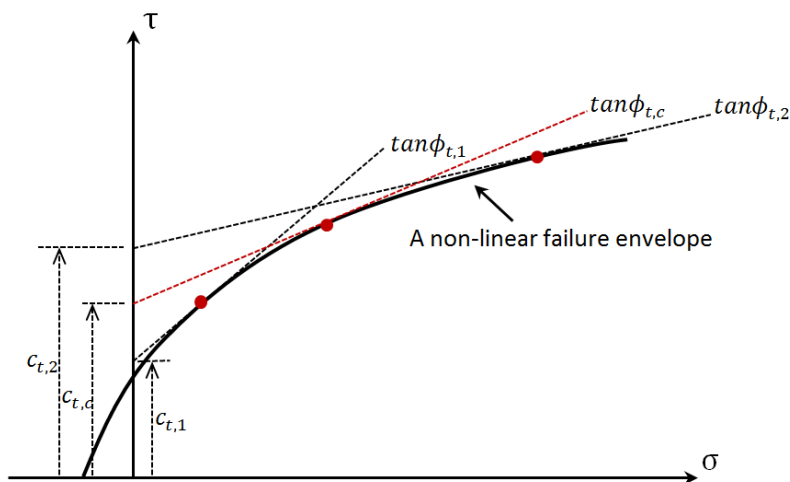


Figure 2-7. Tangential technique for a non-linear failure criterion.



The strength reduction technique in finite element and finite difference numerical modelling is a very powerful approach to evaluate the stability of slopes. However, it is based on the linear Mohr-Coulomb failure criterion. Fu and Liao (2010) derived the instantaneous shear strength of the Hoek-Brown materials at a micro-unit level, and described in detail the implementation of the non-linear shear strength reduction using finite element method. Shen and Karakus (2013) carried on to investigate the three-dimensional effect using FLAC 3D.

Based on the theory of finite element limit analysis (Lyamin and Sloan 2002a, Lyamin and Sloan 2002b, Krabbenhoft et al. 2005, Merifield et al. 2006), Li et al. (2008) provided stability charts for slopes made of rock obeying the Hoek-Brown failure criterion. Comparisons are made with those obtained from limit equilibrium analysis. More complex cases such as the presence of seismic actions and the effect of non-uniform rock mass disturbance are discussed in the following papers (Li et al. 2009a, Li et al. 2011).

This thesis evaluates the stability of rock slopes assuming the non-linear Hoek-Brown failure criterion. Three different techniques are employed and compared: the tangential line technique, the equivalent cohesion-friction angle method and the variational approach.

## **Chapter 3 Stability Assessment of Slopes Made of Geomaterials Obeying the Mohr-Coulomb Failure Criterion**

In this chapter, based on the existing formulations of Chen (1975), Utili (2013) and Michalowski (2013), generalized formulations for assessing the stability of slopes made of geomaterials obeying the linear Mohr-Coulomb failure criterion subjected to the presence of cracks, water pressure and seismic actions are illustrated, using the kinematic approach of limit analysis.

The presence of cracks alters the geometry of the sliding mass. Upper bound formulations are derived for slopes subjected to both vertical and inclined cracks. As for the influence of water pressure, two scenarios, i.e., only water present in the cracks and saturated slopes are discussed. The pseudo-static approach is adopted to account for the seismic actions. In this approach, constant accelerations are assumed to act on the slope.

In addition, the effect of ground strength anisotropy and spatial non-homogeneity in the vertical direction is considered. Stability charts corresponding to different types of loadings and ground conditions are provided.

### **3.1 Presence of cracks**

The majority of analytical solutions for slope stability analyses are based on the assumption that slopes are made of isotropic, homogeneous and continuous material (e.g., Morgenstern and Price 1965, Chen and Giger 1971, Sarma 1979, Michalowski 1995, Yu et al. 1998, etc.). However, the presence of cracks can substantially reduce slope stability (Utili 2013, Michalowski 2013) because of the

length of failure surface is reduced and the additional force due to water pressure filling cracks increases the tendency of slope failure.

Previous literature concerning the influence of the presence of cracks involve mainly the application of limit equilibrium approaches (e.g. Spencer 1967, 1968; Hoek and Bray 1981; Chowdhury and Zhang 1991; Kaniraj and Abdullah 1994), or employing variational calculus (e.g. Baker 1981; Baker 2003). Recently, Uti (2013) investigated the stability of slopes made of cohesive frictional material subjected to cracks based on the kinematic approach of limit analysis. In the study, detailed derivations of the upper bound solutions are provided. Meanwhile, Michalowski (2013) independently evaluated both slopes with pre-existing cracks and the formation of cracks as part of the failure mechanism using the same methodology. In addition, the effect of pore water pressure is assessed by imposing  $r_u$  in Michalowski (2013). In this chapter, the kinematic approach of limit analysis is employed to assess the stability of cracked slopes made of geomaterials obeying the Mohr-Coulomb failure criterion. The upper bound formulations following the work done by Chen (1975), Uti (2013) and Michalowski (2013) are modified to treat a cracked slope as an intact slope having additional surcharge. Both vertical and inclined cracks are included. The advantage of employing this formulation is that cracked slopes made of geomaterials obeying a non-linear failure criterion can be analysed by using the same conceptual framework (see Chapter 4). It also should be noted that the procedures for slope stability assessment in this chapter establish the basis for determining the optimal slope profiles and optimal pile positions in Chapter 5 and Chapter 6.

### **3.1.1 Upper bound formulation considering the presence of pre-existing cracks**

In the following section, the upper bound limit analysis formulation for a slope subjected to pre-existing cracks is illustrated. There are multiple cracks daylighting on the slope under investigation. The failure mechanism passes through one of them. It is assumed that the validity of the normality rule holds true and the shape of the failure mechanism is a logarithmic spiral curve. Within the framework of the upper bound limit analysis, and assuming a rigid-rotational type of failure mechanism and ground materials obeying the Mohr-Coulomb failure criterion, it has been proven by the variational analysis of Chen (1975), Baker and Garber (1978), Baker (1981) and Baker and Frydman (1983) that the logarithmic spiral failure surface is the most critical one for both intact slopes and slopes with pre-existing cracks (regardless of slope geometry).

In Figure 3-1, a block of soil/rock mass **ABCDE** rigidly rotates away about a centre of rotation **O**. The remaining part is bounded by a crack **DE** and a logarithmic spiral **CD**. The angle between the displacement rate  $\dot{u}$  of the soil/rock mass sliding away and the failure line **CD** must be always equal to  $\phi$  according to the normality rule, with  $\phi$  the friction angle at failure. However, it is not the case for the angle  $\xi$  between  $\dot{u}$  and the crack **DE**, which can be different from  $\phi$ . The expression for **CD** written in polar coordinates with reference to the spiral centre **O** is:

$$r = r_0 e^{\tan \phi (\theta - \theta_0)} \quad (3-1)$$

with  $r$  the distance of a generic point of the spiral to its centre **O**,  $\theta$  the angle formed by  $r$  with the horizontal axis, and  $\theta_0$  and  $r_0$  identifying the angle and distance of point **D** to the centre **O**. In Figure 3-1,  $\delta$  is the depth of a crack and  $H$  is the slope height. The failure mechanism is completely defined by angles  $\theta_0, \theta_h, \beta'$  and normalized crack depth  $\eta = \delta/H$ . A slope with cracks daylighting on its upper

surface can be treated as an intact slope with the additional surcharge due to the self-weight of **AEDF**.

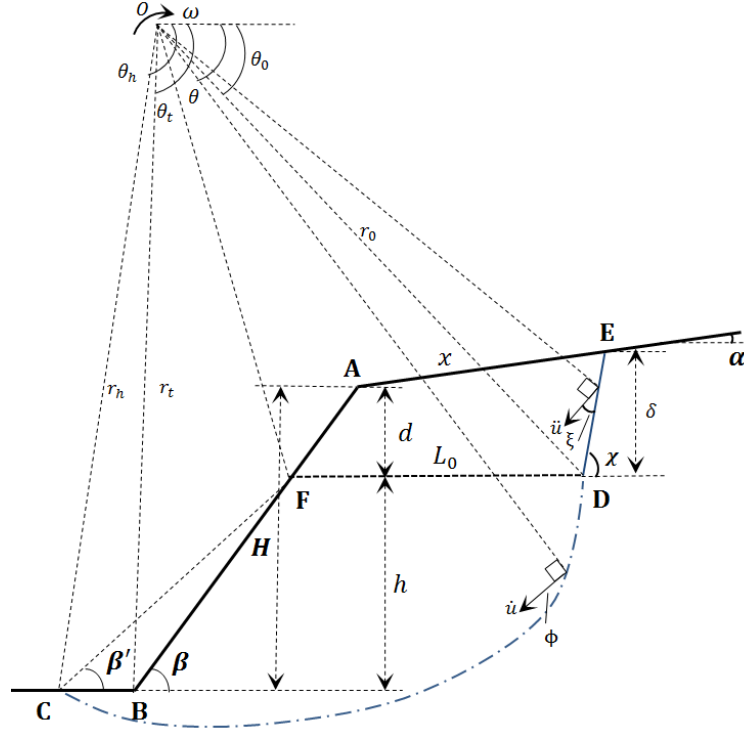


Figure 3-1. Slope geometry and failure mechanism.

The rate of external work due to the weight of region **ABCDE** is computed by the rate of work done by region **FBCD** plus that of region **AFDE** ( $\dot{W}_U$ ). Meanwhile, the rate of external work done by region **FBCD** is the result of work done by **ODC** ( $\dot{W}_1$ ) subtracts **ODF** ( $\dot{W}_2$ ), **OFB** ( $\dot{W}_3$ ) and **OBC** ( $\dot{W}_4$ ). Therefore, the total rate of external work is expressed as:

$$\begin{aligned}\dot{W}_\gamma &= \dot{W}_1 - \dot{W}_2 - \dot{W}_3 - \dot{W}_4 + \dot{W}_U = \dot{W}_1 - \dot{W}_2 - \dot{W}_3 - \dot{W}_4 + \dot{W}_U \\ &= \omega \gamma r_0^3 (f_1 - f_2 - f_3 - f_4 + f_U)\end{aligned}\quad (3-2)$$

The expressions of  $\dot{W}_1 \sim \dot{W}_3$  are found in Chen (1975) and Utili (2013) and here only the final expressions are provided:

$$\begin{aligned}\dot{W}_1 &= \omega \gamma r_0^3 \frac{e^{3 \tan \phi (\theta_h - \theta_0)} (3 \tan \phi \cos \theta_h + \sin \theta_h) - 3 \tan \phi \cos \theta_0 - \sin \theta_0}{3(1 + 9 \tan^2 \phi)} \\ &= \omega \gamma r_0^3 f_1(\theta_0, \theta_h)\end{aligned}\quad (3-3)$$

$$\dot{W}_2 = \omega \gamma r_0^3 \left[ \frac{1}{6} \sin \theta_0 \frac{L_0}{r_0} \left( 2 \cos \theta_0 - \frac{L_0}{r_0} \right) \right] = \omega \gamma r_0^3 f_2(\theta_0, \theta_h, \beta') \quad (3-4)$$

$$\begin{aligned}\dot{W}_3 &= \omega \gamma r_0^3 \frac{h}{6 r_0 \tan \beta} \left( \sin \theta_0 + \cos \theta_0 \tan \beta - \frac{L_0}{r_0} \right) \left( 2 \cos \theta_0 - 2 \frac{L_0}{r_0} - \frac{h}{r_0 \tan \beta} \right) \\ &= \omega \gamma r_0^3 f_3(\theta_0, \theta_h, \beta')\end{aligned}\quad (3-5)$$

with  $\gamma$  being the material unit weight and  $\omega$  being the angular velocity of the sliding mass. The height of the fictitious intact slope is:

$$h = r_0 \left[ e^{\tan \phi (\theta_h - \theta_0)} \sin \theta_h - \sin \theta_0 \right] \quad (3-6)$$

The length of **FD** is:

$$L_0 = r_0 \left\{ \frac{\sin(\theta_h - \theta_0)}{\sin \theta_h} - \left[ e^{\tan \phi (\theta_h - \theta_0)} \sin \theta_h - \sin \theta_0 \right] \cdot \frac{\sin(\theta_h + \beta')}{\sin \theta_h \sin \beta'} \right\} \quad (3-7)$$

Considering the region of **OBC**, the rate of external work is calculated by:

$$\begin{aligned}
\dot{W}_4 &= \omega |x_{G4} - x_0| \gamma A_4 \\
&= \omega \gamma r_0^3 \frac{h}{6r_0} \left( \frac{1}{\tan \beta'} - \frac{1}{\tan \beta} \right) \left( \frac{h}{r_0} + \sin \theta_0 \right) \\
&\times \left( 2 \cos \theta_0 - 2 \frac{L_0}{r_0} - \frac{h}{r_0 \tan \beta'} - \frac{h}{r_0 \tan \beta} \right) \\
&= \omega \gamma r_0^3 f_4(\theta_0, \theta_h, \beta')
\end{aligned} \tag{3-8}$$

where  $x_{G4}$  and  $x_0$  are the horizontal coordinates of the gravity center of **OBC** and the center of rotation **O** respectively.  $A_4$  is the area of **OBC**.

Crack **DE** has an inclination of  $\chi$ . The calculation of  $\dot{W}_U$  is divided into the rate of work done by two triangular regions **AFD** and **AED**, which are written as:

$$\begin{aligned}
\dot{W}_U &= \omega |x_{GU,1} - x_0| \gamma A_{U,1} + \omega |x_{GU,2} - x_0| \gamma A_{U,2} \\
&= \omega \gamma r_0^3 \frac{1}{6} \left[ \frac{L_0 d}{r_0^2} \left( 3 \cos \theta_0 - 2 \frac{L_0}{r_0} + \frac{d}{r_0 \tan \beta} \right) \right. \\
&\quad \left. + \eta H \left( \frac{L_0}{r_0} - \frac{d}{r_0 \tan \beta} + \frac{d}{r_0 \tan \chi} \right) \left( 3 \cos \theta_0 - \frac{L_0}{r_0} + \frac{d}{r_0 \tan \beta} + \frac{\eta H}{r_0 \tan \chi} \right) \right] \\
&= \omega \gamma r_0^3 f_U(\theta_0, \theta_h, \beta', \eta)
\end{aligned} \tag{3-9}$$

where  $x_{GU,1}$  and  $x_{GU,2}$  are the horizontal coordinates of the gravity center of **AFD** and **AED**.  $A_{U,1}$  and  $A_{U,2}$  are the areas of **AFD** and **AED** respectively. The vertical distance from point **A** to **FD** is:

$$d = \frac{\left( 1 - \frac{\tan \alpha}{\tan \chi} \right) \eta H - L_0 \tan \alpha}{1 - \frac{\tan \alpha}{\tan \beta}} \tag{3-10}$$

The total height of the slope (vertical distance measured from slope crest to the toe) is:

$$\begin{aligned}
H &= h + d = \\
&e^{\tan \phi (\theta_h - \theta_0)} \sin \theta_h - \sin \theta_0 - \\
&\frac{\tan \alpha \tan \beta}{\tan \beta - \tan \alpha} \cdot \left\{ \frac{\sin (\theta_h - \theta_0)}{\sin \theta_h} - \left[ e^{\tan \phi (\theta_h - \theta_0)} \sin \theta_h - \sin \theta_0 \right] \cdot \frac{\sin (\theta_h + \beta')}{\sin \theta_h \sin \beta'} \right\} \\
&\frac{1 - \frac{\tan \chi \tan \beta - \tan \alpha \tan \beta}{\tan \chi \tan \beta - \tan \alpha \tan \chi} \eta}{r_0} \quad (3-11) \\
&= f_h (\theta_0, \theta_h, \beta', \eta)
\end{aligned}$$

Because of the presence of pre-existing cracks, internal energy is dissipated only along the spiral  $\widehat{CD}$ . There is no energy dissipation along the crack  $ED$  since the soil/rock mass sliding away has already detached from the soil/rock at rest. The rate of the energy dissipation is calculated by Chen (1975):

$$\begin{aligned}
\dot{W}_{d-\log} &= \int_{\widehat{CD}} c \dot{u} \cos \phi \frac{rd\theta}{\cos \phi} = c\omega \int_{\widehat{CD}} r^2 d\theta = c\omega r_0^2 \int_{\theta_0}^{\theta_h} e^{2 \tan \phi (\theta - \theta_0)} d\theta \\
&= \frac{c\omega r_0^2}{2 \tan \phi} \left[ e^{2 \tan \phi (\theta - \theta_0)} - 1 \right] = c\omega r_0^2 f_{d-\log} (\theta_0, \theta_h, \beta') \quad (3-12)
\end{aligned}$$

with  $c$  the cohesion at failure.

According to the upper bound theorem of limit analysis, the rate of external work is no greater than the rate of internal energy dissipation. Equating the rate of external work to the rate of energy dissipation, leads to:

$$\begin{aligned}
\dot{W}_\gamma &= \dot{W}_1 - \dot{W}_2 - \dot{W}_3 - \dot{W}_4 + \dot{W}_U = \\
&\omega \gamma r_0^3 (f_1 - f_2 - f_3 - f_4 + f_U) = \dot{W}_{d-\log} = c\omega r_0^2 f_{d-\log} \quad (3-13)
\end{aligned}$$

Dividing by  $\omega$  and  $r_0^2$  and rearranging, the stability factor  $\frac{\gamma^H}{c}$  (the terminology of Taylor 1948) for cracked slopes made of geomaterials obeying the Mohr-Coulomb failure criterion is obtained:



$$N_{M-C} = \frac{\gamma H}{c} = \frac{f_{d-\log} \times f_h}{f_1 - f_2 - f_3 - f_4 + f_U} = \frac{g(\phi)}{q(\phi)} \quad (3-14)$$

with

$$g(\phi) = f_{d-\log} \cdot f_h \quad (3-15)$$

and

$$q(\phi) = f_1 - f_2 - f_3 - f_4 + f_U \quad (3-16)$$

The stability factor defined in Eq. (3-14) is a function of four variables  $\theta_0, \theta_h, \beta'$  and  $\eta$  denoting the failure mechanism. Among all the potential failure mechanisms, the most critical one is obtained by a minimization process. The minimum value of the stability factor (corresponding to the most adverse crack) is found by repeated evaluation of Eq. (3-14) over a fine grid of physically meaningful  $\theta_0, \theta_h, \beta'$  and  $\eta$  values. The physical ranges of  $\theta_0$  and  $\theta_h$  are provided by Chen and Liu (1990):

$$0 < \theta_0 < \frac{\pi}{2} + \phi - \alpha \quad (3-17)$$

$$\frac{\pi}{2} + \phi - \beta < \theta_h < \pi - \alpha \quad (3-18)$$

For purely cohesive soil ( $\phi = 0$ ), according to the de L'Hopital rule, the stability factor in Eq. (3-14) becomes:

$$\begin{aligned}
N_{M-C}(\phi=0) &= \lim_{\phi \rightarrow 0} \frac{g(\phi)}{q(\phi)} = \frac{g'(0)}{q'(0)} \\
&= \frac{(\theta_h - \theta_0)(\sin \theta_h - \sin \theta_0)}{[f_1(\phi=0) - f_2(\phi=0) - f_3(\phi=0) - f_4(\phi=0) + f_U(\phi=0)]}
\end{aligned} \tag{3-19}$$

### 3.1.2 The maximum stable crack depth for pre-existing cracks

For illustrative purposes, slopes having horizontal upper slope face ( $\alpha = 0^\circ$ ) and vertical crack ( $\chi = 90^\circ$ ) are considered in the following sections. For slopes subjected to pre-existing cracks, crack depth is limited by the stability of the sub-slope **ED** in Figure 3-1. In fact, if the crack depth is larger than the critical height of slope **ED**, a failure mechanism involving **ED** must take place (see Figure 3-2), which will cause local deformation or failure on the left part of **ED** as well. This type of local failure can be handled by different types of analysis (e.g. FEM or DEM). However, in order to be consistent with the overall method adopted in the thesis, the upper bound limit analysis has been used to determine the maximum stable crack depth.

In the case of a dry slope, Michalowski (2013) calculated the maximum stable crack depth by the lower bound and upper bound solutions to the stability of a vertical crack boundary (analogous to a vertical slope) as:

$$\delta_{\max} = \begin{cases} \frac{2c}{\gamma} \tan\left(\frac{\pi}{4} + \frac{\phi}{2}\right) & \text{lower bound} \\ \frac{3.83c}{\gamma} \tan\left(\frac{\pi}{4} + \frac{\phi}{2}\right) & \text{upper bound} \end{cases} \tag{3-20}$$

In this chapter, to be on the safe side, the upper bound value on the maximum crack depth is taken. In addition, since the lower bound solutions are not available in

many cases, it is convenient to select the upper bound as the maximum crack depth for all cases including both the presence of water pressure and seismic action.

Hence, the maximum normalized crack depth is determined as:

$$\eta_{\max} = \frac{\delta_{\max}}{H} = \frac{N_{M-C,90^\circ}}{N_{M-C,\beta}} \quad (3-21)$$

where  $N_{M-C,\beta}$  is the stability factor of an intact ( $\delta = 0$ ) slope of inclination  $\beta$  and  $N_{M-C,90^\circ}$  is the stability factor of an intact vertical slope. The minimum value of the stability factor defined in Eq. (3-14) should be obtained within the range of  $0 < \eta < \eta_{\max}$ .

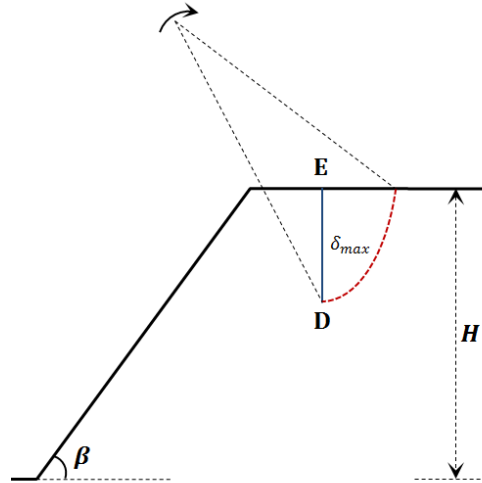


Figure 3-2. Maximum stable crack depth.

### 3.1.3 Stability charts in the presence of the most adverse pre-existing cracks

For the most common circumstances, when there is no information about the depth and the location of cracks, in order to search for the least upper bound solution, the

stability factor  $N_{M-C}$  (defined in Eq. (3-14)) is minimized over all possible  $\theta_0, \theta_h, \beta'$  and  $\eta$  under the constraint of  $\eta < \eta_{max}$ . The most adverse crack is defined as the one yielding the minimum value of the stability factor.

Slope stability assessment involves measuring the margin of safety of a given slope. A common definition of the factor of safety ( $F$ ) is the ratio of the shear strength of the material to the actual shear stress within the slope. For geomaterials obeying the Mohr-Coulomb failure criterion,

$$F = \frac{c_g}{c_f} = \frac{\tan \phi_g}{\tan \phi_f} \quad (3-22)$$

with  $c_g$  and  $\phi_g$  the cohesion and internal angle of shearing resistance of the geomaterial;  $c_f$  and  $\phi_f$  the strength parameters at failure. By replacing  $c, \phi$  with  $\frac{c_g}{F}, \frac{\phi_g}{F}$  in Eq. (3-14), the factor of safety ( $F$ ) appears in both sides of Eq. (3-14) and has to be determined in an iterative manner.

According to Bell (1966) and Michalowski (2002),  $N^*$  is defined as the stability number which is independent of the factor of safety  $F$ :

$$N^* = \frac{1}{N_{M-C} \tan \phi_f} = \frac{c_f}{\gamma H \tan \phi_f} = \frac{c_g / F}{\gamma H (\tan \phi_g / F)} \quad (3-23)$$

$\frac{F}{\tan \phi_g}$  is plotted against  $\frac{c_g}{\gamma H \tan \phi_g}$  corresponding to the case of cracks of unspecified depth and location in Figure 3-3. The most adverse cracks are considered. Figure 3-3 is regarded as a stability chart. Charts-based design is very important for slope stability assessment. There are a wide variety of stability charts available such as Taylor's charts (Taylor 1948), Spencer's charts (Spencer 1967), Hunter and Schuster charts (Hunter and Schuster 1968) and the charts used in

Wyllie et al. (2004) and Tang et al. (2015). The advantage of employing the chart in Figure 3-3 is mainly that it is widely adopted in recent publications when deriving analytical solutions of slope stability (e.g., Michalowski 2013 and Gao et al. 2014). Moreover, practitioners can obtain the factor of safety of a cracked slope directly from the chart without any iteration. For example, let a 10m tall slope with a  $60^\circ$  inclination be comprised of soil whose  $\phi_g = 20^\circ$ ,  $c_g = 20 \text{ kN/m}^2$ , and  $\gamma = 19 \text{ kN/m}^3$ . Using the chart in Figure 3-3, the value of  $c_g/\gamma H \tan \phi_g = 0.289$ . For  $\beta = 60^\circ$  in Figure 3-3,  $F/\tan \phi_g \approx 3.1$ , hence  $F = 3.1 \cdot \tan 20^\circ \approx 1.13$ . It should be pointed out that the factor of safety obtained in Figure 3-3 is a conservative estimate of slope stability, since the crack with the most adverse depth and location is considered. In reality, other pre-existing cracks with depths and locations other than the most adverse one may happen. The factor of safety of the corresponding failure mechanisms may be higher than the value provided in Figure 3-3. Stability charts that correspond to intact slopes can be found in Michalowski (2002).

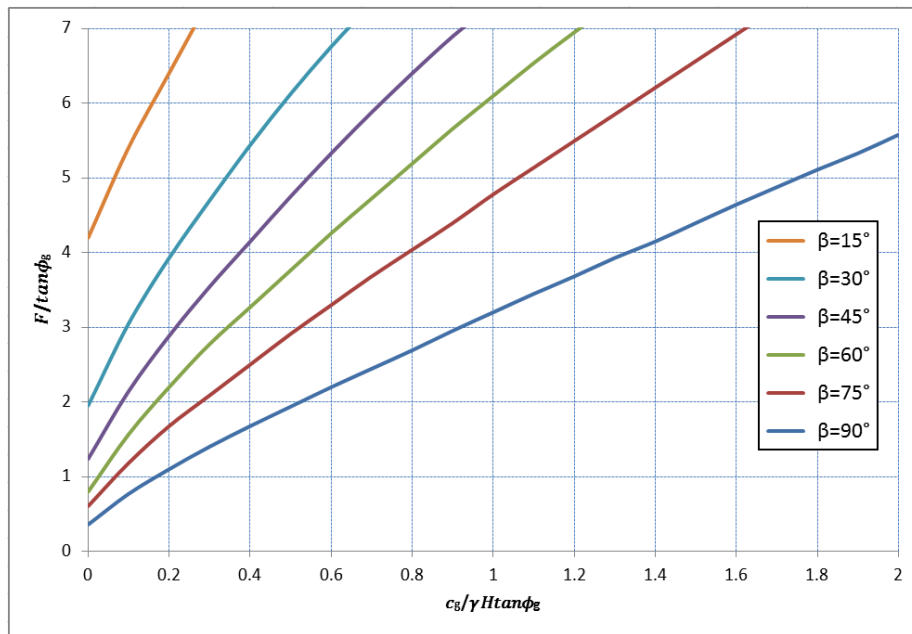


Figure 3-3. Stability chart for slopes subjected to the presence of the most adverse pre-existing cracks.

### 3.1.4 Crack forming as part of the slope failure mechanism

In the previous section, it is assumed that there is no energy dissipation along the crack, since the mass sliding away has already detached from the slope at rest. If crack formation is considered, the stability of slope is evaluated in a different manner. A slope is postulated to be intact at the outset, and the failure mechanism is comprised of two parts: a vertical section (crack) and a logarithmic spiral line (see Figure 3-4). In order to calculate the energy dissipated by the formation of the crack, the envelope of the yield stress where cracks are expected to form should be known beforehand. According to Chen and Drucker (1969) and Michalowski (2013), the classic linear Mohr-Coulomb failure envelope is modified with a circular termination, as shown in Figure 3-5, which is regarded as a more precise description of the material shear and tensile strengths. According to the normality flow rule, the direction of deformation is represented by the velocity discontinuity vector  $[v]$  being perpendicular to the yield envelope, which varies along the circular portion of the failure envelope. This geometric relation leads to a closed-form expression for the rate of energy dissipation along the crack (Michalowski 2013):

$$d_c = [v] \left( \sigma_c \frac{1 - \sin \xi}{2} + \sigma_t \frac{\sin \xi - \sin \phi}{1 - \sin \phi} \right) \quad (3-24)$$

where  $\sigma_c$  and  $\sigma_t$  are the compressive and tensile strengths respectively:

$$\sigma_c = \frac{2c \cos \phi}{1 - \sin \phi} \quad (3-25)$$

$$\sigma_t = \frac{2c \cos \phi}{1 + \sin \phi} \quad (3-26)$$

$\xi$  is the angle velocity discontinuity vector  $[v]$  makes with the direction of an opening crack. The integration of the rate of energy dissipation along the crack is calculated by:

$$\begin{aligned} \dot{W}_{d-c} &= \int_{ED} [v] \left( \sigma_c \frac{1 - \sin \xi}{2} + \sigma_t \frac{\sin \xi - \sin \phi}{1 - \sin \phi} \right) dy \\ &= c\omega r_0^2 \int_0^{f_h} \left( \frac{\sigma_c \sqrt{(\sin \theta_0 - \eta f_h - y)^2 + \cos^2 \theta_0} - (\sin \theta_0 - \eta f_h - y)}{2} \right. \\ &\quad \left. + \frac{\sigma_t \sin \theta_0 - \eta f_h - y - \sin \phi \sqrt{(\sin \theta_0 - \eta f_h - y)^2 + \cos^2 \theta_0}}{1 - \sin \phi} \right) dy \quad (3-27) \\ &= c\omega r_0^2 f_{d-c}(\theta_0, \theta_h, \eta) \end{aligned}$$

Equating the rate of external work to the rate of energy dissipation on both the crack and logarithmic spiral slip line leads to:

$$\begin{aligned} \dot{W}_\gamma &= \omega \gamma r_0^3 (f_1 - f_2 - f_3 - f_4 + f_U) = \dot{W}_{d-\log} + \dot{W}_{d-c} \\ &= c\omega r_0^2 f_{d-\log} + c\omega r_0^2 f_{d-c} = c\omega r_0^2 f_d(\theta_0, \theta_h, \beta', \eta) \end{aligned} \quad (3-28)$$

After rearranging, the stability factor defined in Eq. (3-14) becomes:

$$\frac{\gamma H}{c} = \frac{f_d \times f_h}{f_1 - f_2 - f_3 - f_4 + f_U} \quad (3-29)$$

The least upper bound is determined by the minimization of Eq. (3-29) with four variables  $\theta_0, \theta_h, \beta'$  and  $\eta$  denoting the most critical failure mechanism. Stability charts for both limit tensile strength ( $\sigma_t' = \frac{\sigma_t}{2}$ ) and tension cut-off ( $\sigma_t = 0$ ) cases are provided in Figure 3-6 and Figure 3-7.

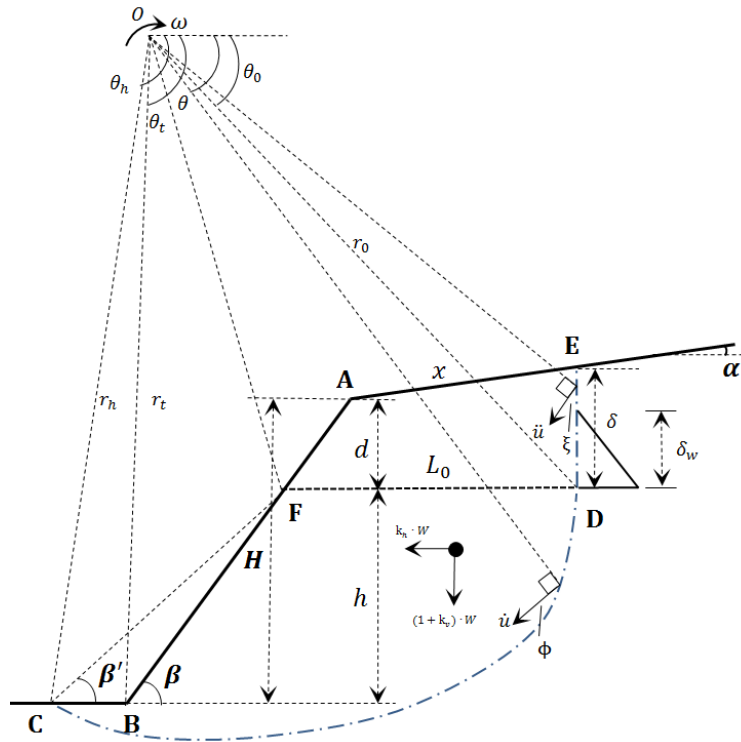


Figure 3-4. Failure mechanism for a slope with a vertical crack daylighting on the upper part.

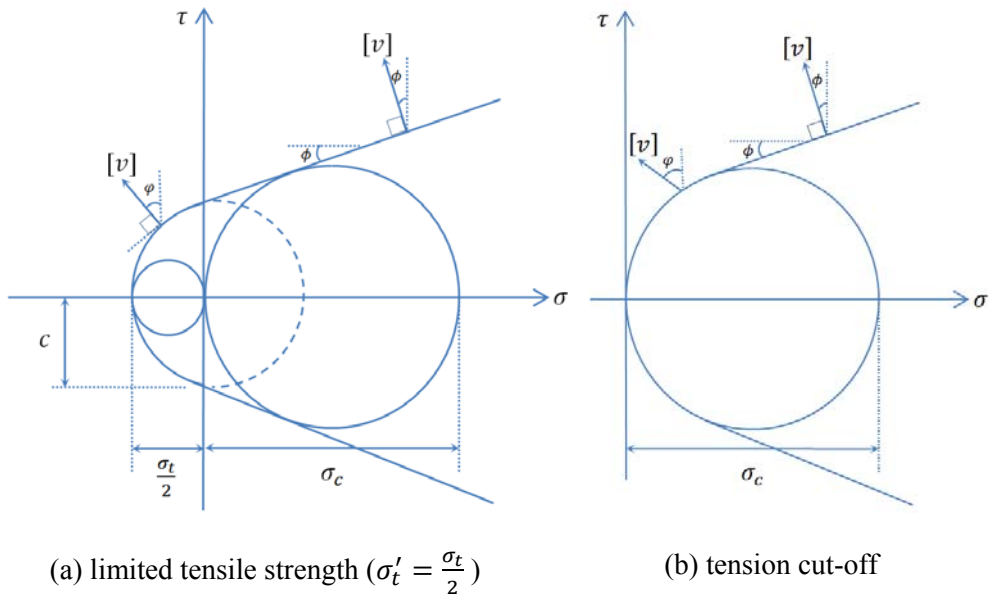


Figure 3-5. Modified failure envelope to account for limited tensile strength and tension cut-off (Michalowski 2013).



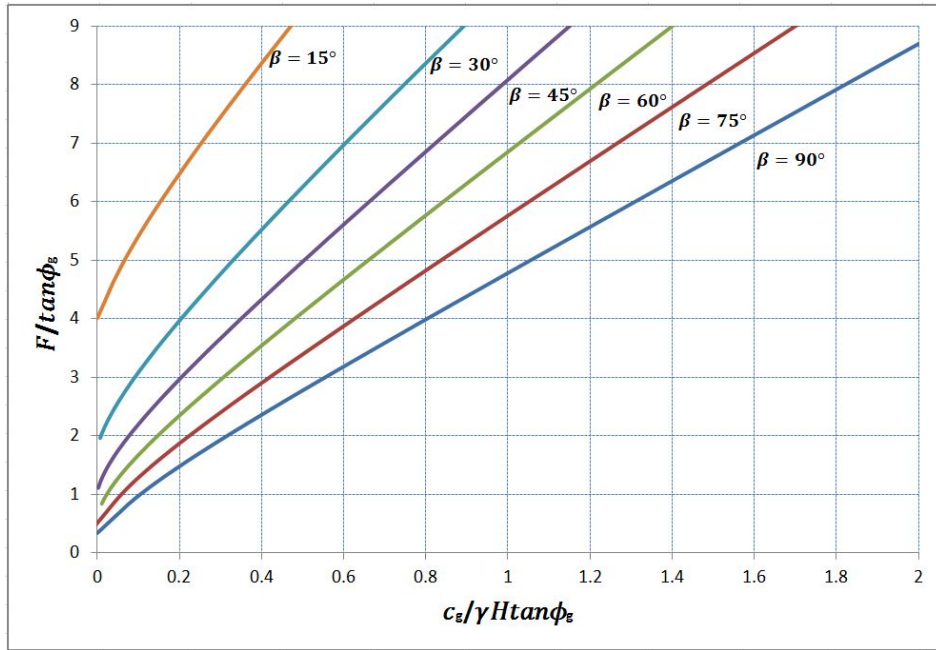


Figure 3-6. Stability chart considering crack formation (limited tensile strength,  $\sigma'_t = \frac{\sigma_t}{2}$ ).

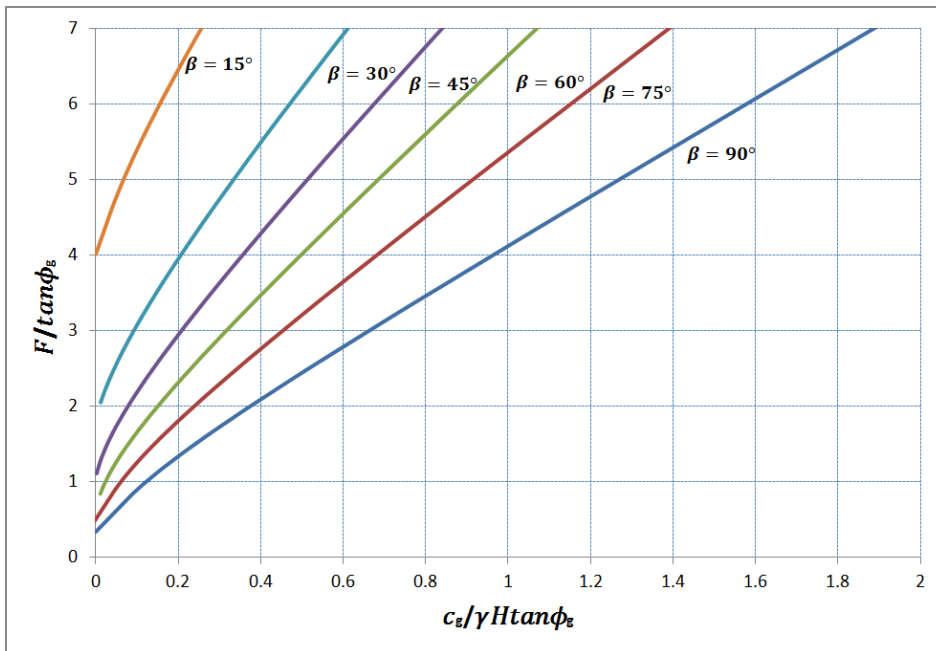


Figure 3-7. Stability chart considering crack formation (tension cut-off).

## 3.2 Water pressure

In this section, the effect of water pressure on destabilizing slopes is investigated. Stability assessment of slopes subjected to two possible groundwater conditions will be illustrated. First, water may be present in the cracks only, for example when a heavy rainstorm results in surface water seeping into the crack and the remainder of the soil/rock mass is relatively impermeable in the short term. Second, for slopes with high permeability, a pore water pressure distribution may develop inside the slope depending on the hydraulic boundary conditions. The derived formulation will also be used in Chapter 6.

### 3.2.1 Water appearing in the crack only

The presence of water in the pre-existing cracks is a major contributor of slope instability, as shown in Figure 3-4. The external work done by water pressure filling the crack  $\dot{W}_{w-c}$  can be expressed as:

$$\begin{aligned}\dot{W}_{w-c} &= \dot{u}_w \cdot F_w \\ &= \omega \left( r_0 \sin \theta_0 - \frac{1}{3} \delta_w \right) \frac{1}{2} \gamma_w \delta_w^2 \\ &= \omega \gamma r_0^3 \left[ \frac{1}{2} \frac{\gamma_w}{\gamma} \left( \frac{\delta_w}{r_0} \right)^2 \left( \sin \theta_0 - \frac{1}{3} \frac{\delta_w}{r_0} \right) \right]\end{aligned}\tag{3-30}$$

where  $F_w$  is the resultant force of water pressure filling the crack, and  $\dot{u}_w$  is the displacement rate of  $F_w$ .  $\gamma_w$  is the unit weight of water and  $\delta_w$  is the length of the water-filled part of crack. A dimensionless coefficient  $K_w$  is introduced to express the amount of water in the crack, e.g.  $K_w = 0$  indicates a dry crack and  $K_w = 1$  means that the crack is full of water (Utili 2013).  $K_w$  ( $0 \leq K_w \leq 1$ ) is defined as  $K_w = \delta_w / \delta$ . Thus, Eq. (3-30) can be rewritten as:

$$\begin{aligned}
\dot{W}_{w-c} &= \omega \gamma r_0^3 \left[ \frac{1}{2} \frac{\gamma_w}{\gamma} \left( \frac{\delta_w}{r_0} \right)^2 \left( \sin \theta_0 - \frac{1}{3} \frac{\delta_w}{r_0} \right) \right] \\
&= \omega \gamma r_0^3 \left[ \frac{1}{2} \frac{\gamma_w}{\gamma} \left( \frac{K_w \delta}{r_0} \right)^2 \left( \sin \theta_0 - \frac{1}{3} \frac{K_w \delta}{r_0} \right) \right] \\
&= \omega \gamma r_0^3 p_{w-c} (\theta_0, \theta_h, \beta', \eta)
\end{aligned} \tag{3-31}$$

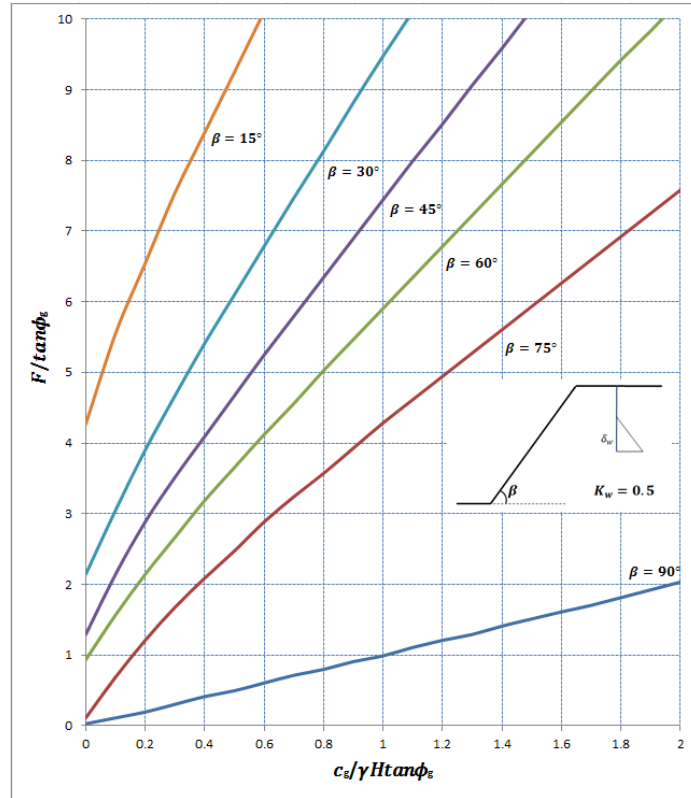
The external work here consists of both the work done by the weight of the sliding mass and that due to water pressure in the crack. Equating the rate of external work to the rate of energy dissipation, leads to:

$$\begin{aligned}
\dot{W}_\gamma + \dot{W}_{w-c} &= \omega \gamma r_0^3 (f_1 - f_2 - f_3 - f_4 + f_U) + \omega \gamma r_0^3 p_{w-c} \\
= \dot{W}_{d-\log} &= c \omega r_0^2 f_{d-\log}
\end{aligned} \tag{3-32}$$

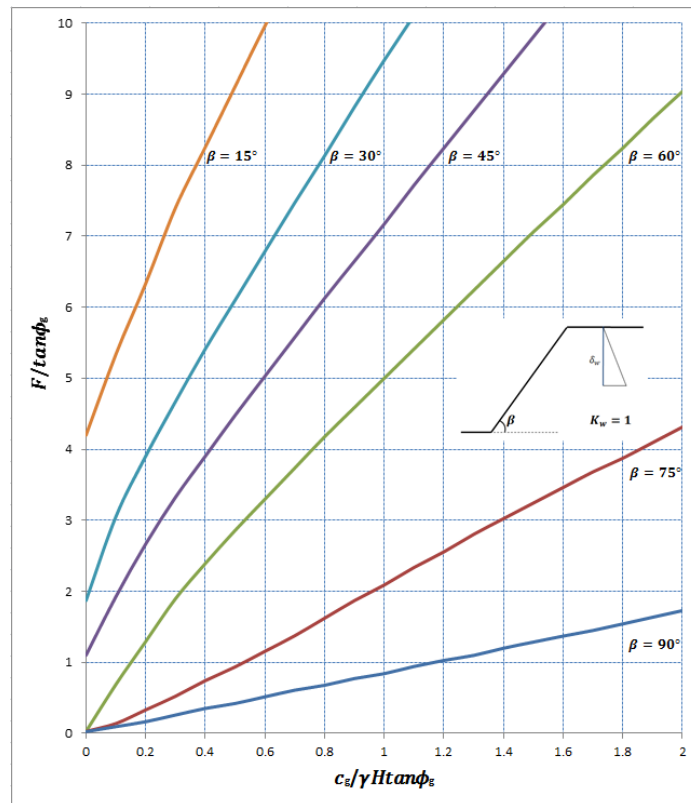
After rearranging, the new stability factor considering the effect of water pressure appearing only in the crack is obtained:

$$\frac{\gamma H}{c} = \frac{f_{d-\log} \times f_h}{f_1 - f_2 - f_3 - f_4 + f_U + p_{w-c}} \tag{3-33}$$

The stability factor defined in Eq. (3-33) is minimized to search for the most critical failure mechanism under the constraint of the maximum stable crack depth defined in Eq. (3-21). Note that Eq. (3-21) is still valid since the soil/rock mass behind the crack is assumed to be dry. Stability charts for water-filled cracks cases (both  $K_w = 0.5$  and  $K_w = 1$ ) are plotted in Figure 3-8. The most adverse pre-existing cracks for the stability of the slope are assumed to be present.



(a)  $K_w = 0.5$



(b)  $K_w = 1$

Figure 3-8. Stability charts considering water pressure appearing only in the crack.

### 3.2.2 Seepage induced pore water pressure distribution

The influence of seepage flow within the slope contains the work done by pore water pressure on the volumetric deformation of the soil/rock mass along the failure surface and water pressure present in the crack.

The overall pore water pressure conditions in slopes were described first by Bishop and Morgenstern (1960) using a coefficient  $r_u = \frac{u}{h_f \gamma}$ , where  $u$  is the pore water pressure and  $h_f$  is the depth of the failure surface measured from the slope surface. This method has been widely adopted as a rapid way to assess the stability of partly saturated slopes using a nominal single value  $r_u$ . Compared with other approaches such as water table and flow net methods (Abramson 2002), the  $r_u$  method is laborious and inaccurate in some cases (Barnes 1999). However, it is still very popular when deriving analytical solutions using either limit equilibrium method (e.g., Low et al. 1998; Jiang and Yamagami 2006) or limit analysis. By imposing  $r_u$ , Michalowski (1995, 2002, 2013) studied the stability of slopes made of geomaterials obeying the Mohr-Coulomb failure criterion subjected to pore water pressure based on the kinematic approach of limit analysis. Yang and Zou (2006) derived the upper bound solutions for slopes made of rock obeying the Hoek-Brown failure criterion by introducing  $r_u$  as well. In this section, it is assumed that the pore water pressure coefficient  $r_u$  is constant throughout the slope.  $r_u = 0.5$  represents approximately a fully submerged slope. When  $r_u < 0.5$ , an average value for a partially submerged slope is assumed.

In Figure 3-4, according to the definition of  $r_u$ , pore water pressure at the bottom of the crack is found by:

$$u = r_u \delta \gamma \quad (3-34)$$

Eq. (3-34) can be rewritten as:

$$u = \delta_w \gamma_w \quad (3-35)$$

Combing Eqs. (3-34) and (3-35), the following expression is obtained:

$$K_w = \frac{\delta_w}{\delta} = r_u \frac{\gamma}{\gamma_w} \quad (3-36)$$

The external work done by water filling the crack and pore water pressure along the failure line may be obtained:

$$\dot{W}_w = \omega \gamma r_0^3 p_{w-c}(\theta_0, \theta_h, \beta', \eta) + \omega \gamma r_0^3 p_{w-\log}(\theta_0, \theta_h, \beta', \eta). \quad (3-37)$$

where  $p_{w-c}$  is defined in Eq. (3-31) and  $p_{w-\log}$  is calculated by Michalowski (1995):

$$p_{w-\log}(\theta_0, \theta_h, \beta', \eta) = r_u \tan \phi \left[ \int_{\theta_0}^{\theta_1} \frac{z_1}{r_0} e^{2 \tan \phi (\theta - \theta_0)} d\theta + \int_{\theta_1}^{\theta_2} \frac{z_2}{r_0} e^{2 \tan \phi (\theta - \theta_0)} d\theta + \int_{\theta_2}^{\theta_h} \frac{z_3}{r_0} e^{2 \tan \phi (\theta - \theta_0)} d\theta \right] \quad (3-38)$$

with  $\theta_1, \theta_2$  (see Figure 3-9) determined by the following constraints:

$$e^{\tan \phi (\theta_1 - \theta_0)} \cos \theta_1 = \cos \theta_0 - \frac{L_0}{r_0} + \frac{d}{r_0} \cot \beta \quad (3-39)$$

$$e^{\tan \phi (\theta_2 - \theta_0)} \cos \theta_2 = \cos \theta_0 - \frac{L_0}{r_0} - \frac{h}{r_0} \cot \beta + \frac{d}{r_0} \cot \beta \quad (3-40)$$

$z_1, z_2$  and  $z_3$  are provided below:

$$\frac{z_2}{r_0} = e^{\tan \phi(\theta - \theta_0)} \sin \theta - \sin \theta_h e^{\tan \phi(\theta_h - \theta_0)} + \left[ e^{\tan \phi(\theta - \theta_0)} \cos \theta - \cos \theta_2 e^{\tan \phi(\theta_2 - \theta_0)} \right] \tan \beta \quad (3-42)$$

The diagram illustrates a rotating mechanism. At the top, a pivot point  $O$  is shown with a curved arrow indicating angular velocity  $\omega$ . Several curved lines represent the path of a point, with angles  $\theta_h$ ,  $\theta_2$ ,  $\theta_1$ , and  $\theta_0$  marked relative to a vertical dashed line. Below this, a horizontal line segment  $CH$  is shown, with point  $B$  on it. A vertical line segment  $BH$  is drawn. A dashed red arc represents a curved path passing through points  $C$ ,  $B$ ,  $H$ ,  $G$ ,  $D$ , and  $E$ . A solid black line segment  $AB$  is drawn, with point  $F$  on it. A vertical line segment  $AG$  is drawn. A horizontal dashed line  $FE$  is drawn. A vertical line segment  $ED$  is drawn. The angle  $\beta$  is marked at point  $B$  between the horizontal line  $CH$  and the line segment  $AB$ . The angle  $\beta'$  is marked at point  $C$  between the horizontal line  $CH$  and the line segment  $CB$ . The angle  $\alpha$  is marked at point  $E$  between the horizontal line  $FE$  and the line segment  $AE$ . The angle  $\delta$  is marked at point  $D$  between the vertical line  $ED$  and the line segment  $DE$ . The vertical distances  $z_1$ ,  $z_2$ , and  $z_3$  are indicated by double-headed arrows.  $z_1$  is the vertical distance from the horizontal line  $FE$  to the point  $D$ .  $z_2$  is the vertical distance from the horizontal line  $CH$  to the point  $B$ .  $z_3$  is the vertical distance from the horizontal line  $CH$  to the point  $H$ .

54

Finally, by equating the rate of external work due to the material weight and water pressure to the rate of energy dissipation and rearranging, the stability factor is obtained:

$$\frac{\gamma H}{c} = \frac{f_{d-\log} \times f_h}{f_1 - f_2 - f_3 - f_4 + f_U + p_{w-c} + p_{w-\log}} \quad (3-44)$$

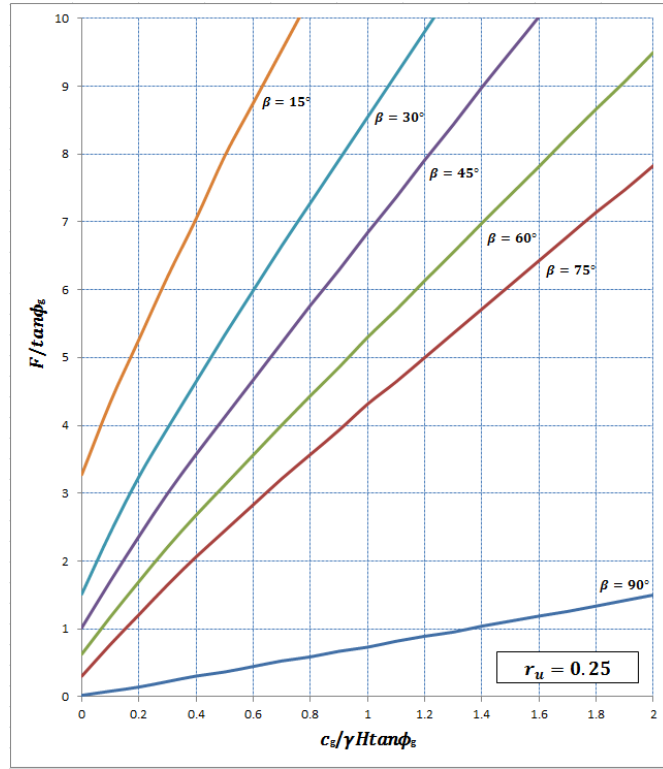
The stability factor defined in Eq. (3-44) is minimized under the constraint of the maximum allowable crack depth. Because of the presence of water pressure, now the maximum allowable crack depth needs to be defined differently compared with Eq. (3-21) :

$$\frac{\delta_{\max}}{H} = \frac{N_{M-c,90^\circ}(r_u)}{N_{M-c,\beta}(r_u)} \quad (3-45)$$

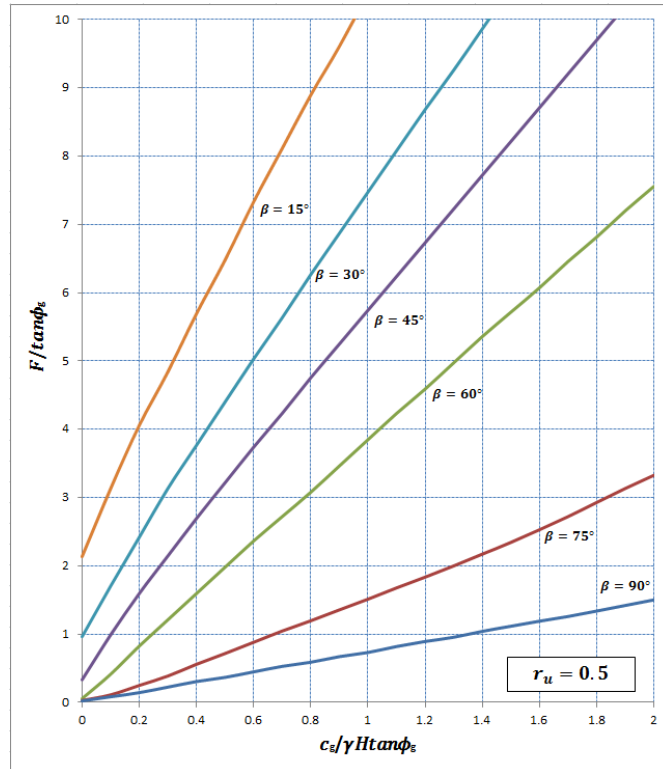
where  $N_{M-c,90^\circ}(r_u)$  is the stability factor of an intact vertical slope when a given  $r_u$  is imposed.  $N_{M-c,\beta}(r_u)$  is the stability factor of an intact slope of inclination  $\beta$  with the same  $r_u$ .

Stability charts for  $r_u = 0.25$  and  $r_u = 0.5$  are provided in Figure 3-10. Pre-existing cracks with the most adverse location and depth are considered.





(a)  $r_u = 0.25$



(b)  $r_u = 0.5$

Figure 3-10. Stability charts considering general pore water pressure distribution.

### 3.3 Seismic loading

Seismic loading is one of the major threats to slope stability. Seismic effect on slopes is routinely considered by imposing pseudo-static forces on the centre of gravity of the slope (see Figure 3-4). The so-called pseudo-static approach has been widely adopted for its simplicity and practical applicability since Terzaghi (1950). Coefficients  $k_h$  and  $k_v$  represent the intensity of horizontal and vertical acceleration as a fraction of the gravity acceleration. In this section, the seismic effect is included in limit analysis as additional work terms in the energy balance Eq. (3-14). The derived formulation will also be used in Chapter 6.

In order to distinguish the work done by the seismic actions from the work due to the material weight, letting  $f_{1v} = (1 + k_v) \cdot f_1, f_{2v} = (1 + k_v) \cdot f_2, f_{3v} = (1 + k_v) \cdot f_3, \dots, f_{Uv} = (1 + k_v) \cdot f_U$  in Eqs. (3-3)-(3-9) includes the vertical seismic acceleration. The calculation of the rate of external work done by horizontal seismic loading is also the summation of the rate of work done by seismic actions on the region of **ODC** ( $\dot{W}_{1h}$ ), **ODF** ( $\dot{W}_{2h}$ ), **OFB** ( $\dot{W}_{3h}$ ), **OBC** ( $\dot{W}_{4h}$ ) and **AFDE** ( $\dot{W}_{Uh}$ ), respectively. For each term, it can be written as:

$$\dot{W}_h = \omega |y_{Gi} - y_0| \gamma A_i \quad (3-46)$$

where  $y_{Gi}$  and  $y_0$  are the vertical coordinates of the gravity center of the region and the center of rotation **O** respectively.  $A_i$  is the area of each region. The expressions for  $\dot{W}_{1h} \sim \dot{W}_{3h}$  are found in Chen and Liu (1990) and Utili and Abd (2016):

$$\begin{aligned} \dot{W}_{1h} &= \omega \gamma r_0^3 \frac{e^{3 \tan \phi (\theta_h - \theta_0)} (3 \tan \phi \sin \theta_h - \cos \theta_h) - 3 \tan \phi \sin \theta_0 + \cos \theta_0}{3(1 + 9 \tan^2 \phi)} \\ &= \omega \gamma r_0^3 f_{1h}(\theta_0, \theta_h) \end{aligned} \quad (3-47)$$

$$\dot{W}_{2h} = \omega \gamma r_0^3 \left( \frac{1}{3} \sin^2 \theta_0 \frac{L_0}{r_0} \right) = \omega \gamma r_0^3 f_{2h}(\theta_0, \theta_h, \beta') \quad (3-48)$$

$$\begin{aligned} \dot{W}_{3h} &= \omega \gamma r_0^3 \frac{h}{6r_0 \tan \beta} \left( \sin \theta_0 + \cos \theta_0 \tan \beta - \frac{L_0}{r_0} \right) \left( 2 \cos \theta_0 - 2 \frac{L_0}{r_0} - \frac{h}{r_0 \tan \beta} \right) \\ &= \omega \gamma r_0^3 f_{3h}(\theta_0, \theta_h, \beta') \end{aligned} \quad (3-49)$$

Considering the region **OBC**,

$$\begin{aligned} \dot{W}_{4h} &= \omega |y_{G4} - y_0| \gamma A_4 \\ &= \omega \gamma r_0^3 \frac{h}{3r_0} \left( \frac{1}{\tan \beta'} - \frac{1}{\tan \beta} \right) \left( \frac{h}{r_0} + \sin \theta_0 \right)^2 \\ &= \omega \gamma r_0^3 f_{4h}(\theta_0, \theta_h, \beta') \end{aligned} \quad (3-50)$$

where  $y_{G4}$  is the vertical coordinates of gravity center of the region **OBC**.

The calculation of  $\dot{W}_{Uh}$  is divided into the rate work done by two triangular regions **AFD** and **AED**, which are written as:

$$\begin{aligned} \dot{W}_{Uh} &= \omega |y_{G5,1} - y_0| \gamma A_{U,1} + \omega |y_{G5,2} - y_0| \gamma A_{U,2} \\ &= \omega \gamma r_0^3 \frac{d}{6r_0} \left[ \left( 3 \sin \theta_0 - 2 \frac{d}{r_0} \right) \left( \frac{L_0}{r_0} - \frac{d}{r_0 \tan \beta} \right) + \frac{L_0}{r_0} \left( 3 \sin \theta_0 - \frac{d}{r_0} \right) \right] \\ &= \omega \gamma r_0^3 f_{Uh}(\theta_0, \theta_h, \beta', \delta) \end{aligned} \quad (3-51)$$

where  $y_{G5,1}$  and  $y_{G5,2}$  are the vertical coordinates of the gravity center of **AFD** and **AED**.

Equating the rate of external work done by the material weight and seismic actions to the rate of energy dissipation, leads to:

$$\begin{aligned}
\dot{W}_\gamma + \dot{W}_s &= \omega \gamma r_0^3 (f_{1v} - f_{2v} - f_{3v} - f_{4v} + f_{Uv}) + \\
&\omega \gamma r_0^3 (f_{1h} - f_{2h} - f_{3h} - f_{4h} + f_{Uh}) \\
&= \dot{W}_{d-\log} = c \omega r_0^2 f_{d-\log}
\end{aligned} \tag{3-52}$$

After rearranging, the stability factor of cracked slopes subject to seismic actions is the modification of Eq. (3-14) by adding extra dynamic terms:

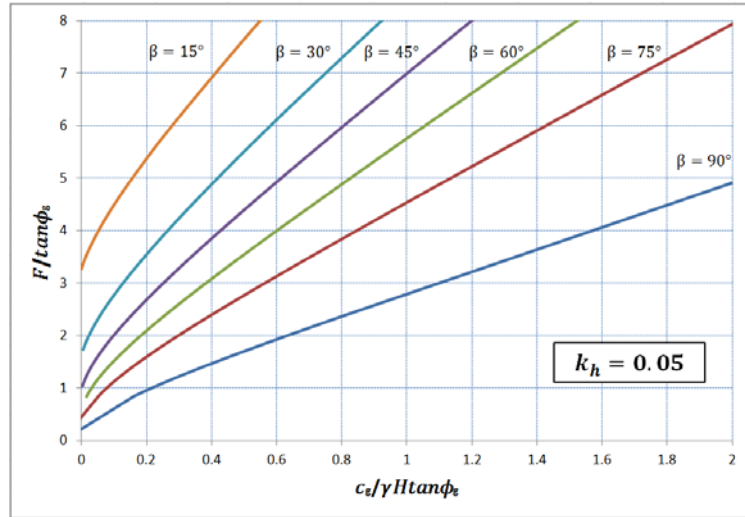
$$\frac{\gamma H}{c} = \frac{f_{d-\log} \times f_h}{(1 + k_v) \times (f_1 - f_2 - f_3 - f_4 + f_U) + f_{1h} - f_{2h} - f_{3h} - f_{4h} + f_{5h}} \tag{3-53}$$

The stability factor is minimized under the constraint of maximum allowable crack depth, which is defined as:

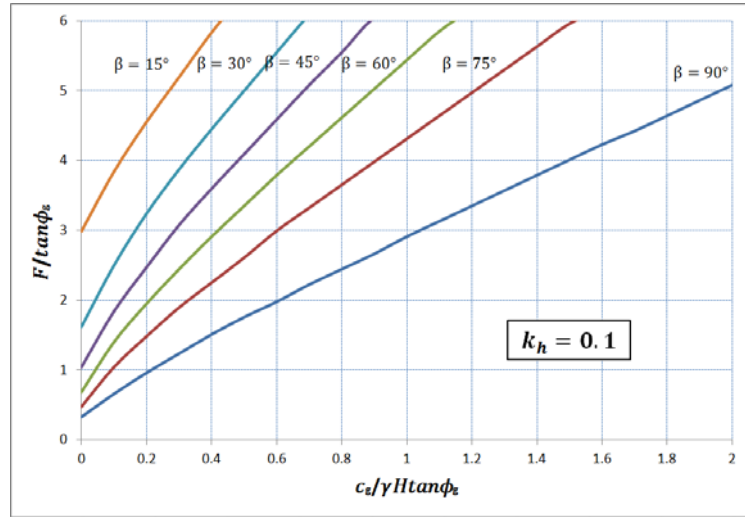
$$\frac{\delta_{\max}}{H} = \frac{N_{M-C,90^\circ}(k_h, k_v)}{N_{M-C,\beta}(k_h, k_v)} \tag{3-54}$$

where  $N_{M-C,90^\circ}(k_h, k_v)$  is the stability factor of an intact vertical slope when a set of  $(k_h, k_v)$  is imposed.  $N_{M-C,\beta}(k_h, k_v)$  is the stability factor of an intact slope of inclination  $\beta$  with the same  $k_h, k_v$ .

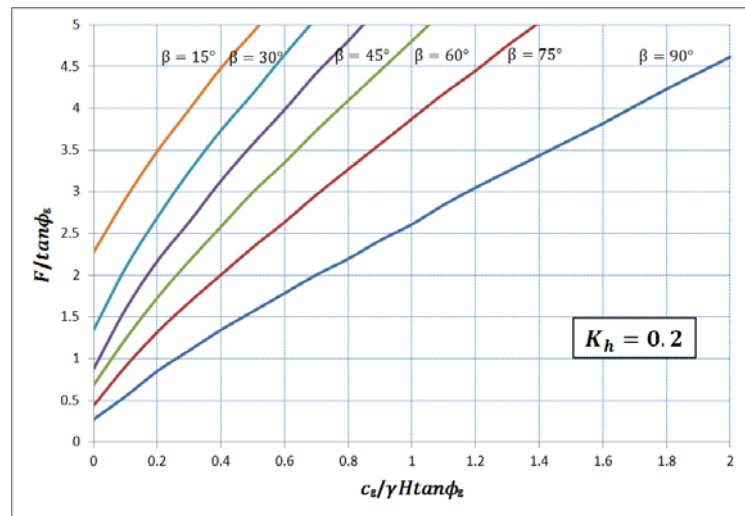
Stability charts for slopes under seismic actions of four typical values of horizontal acceleration, i.e.,  $k_h = 0.05$ ,  $k_h = 0.1$ ,  $k_h = 0.2$  and  $k_h = 0.3$  are provided in Figure 3-11. For illustrative purposes, the vertical acceleration of the earthquake is assumed to be nil. The most adverse pre-existing crack depth and location are considered.



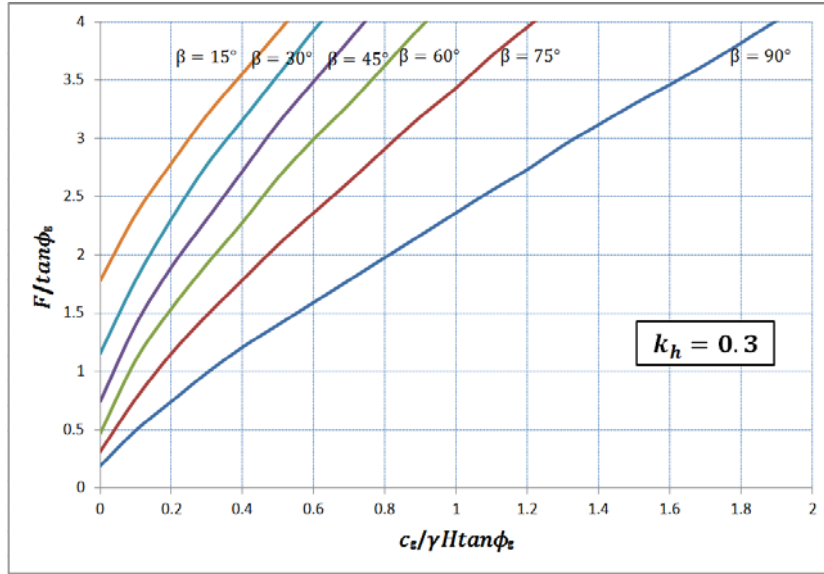
(a)  $k_h = 0.05$



(b)  $k_h = 0.1$



(c)  $k_h = 0.2$



(d)  $k_h = 0.3$

Figure 3-11. Stability charts considering horizontal seismic actions,  $k_v = 0$ .

### 3.4 Non-homogenous slopes with anisotropic strength

By treating the presence of cracks as additional weight on intact slopes, the current research findings on intact slopes may be extended to tackle cracked ones. As an example, in this section, the upper bound solutions for intact slopes considering the effect of ground strength anisotropy and spatial non-homogeneity in the vertical direction proposed by Chen (1975) are extended to include the presence of pre-existing cracks. The derived formulation will also be used in Chapter 5.

Natural soils always show a certain degree of non-homogeneity and anisotropy under natural sedimentation process (Lo 1965; Chen 1975; Nian et al. 2008).  $\phi$  shows little anisotropy and dependence on loading direction (Duncan and Seed 1966; Mayne 1985; Al-Karni and Al-Shamrani 2000), thus it is here assumed to remain a constant in the whole slope. Let us consider five general patterns of cohesion varying with depth within the slope as shown in Figure 3-12 (Chen 1975). The fourth distribution of cohesion is the most general case and will be discussed

in the following, see Figure 3-13 (c).  $n_0c$ ,  $n_1c$ ,  $n_2c$  and  $n_ic$  indicate the magnitudes of cohesion at various depth as shown in Figure 3-13 (c), with  $c$  the cohesion at the depth of  $H$ .

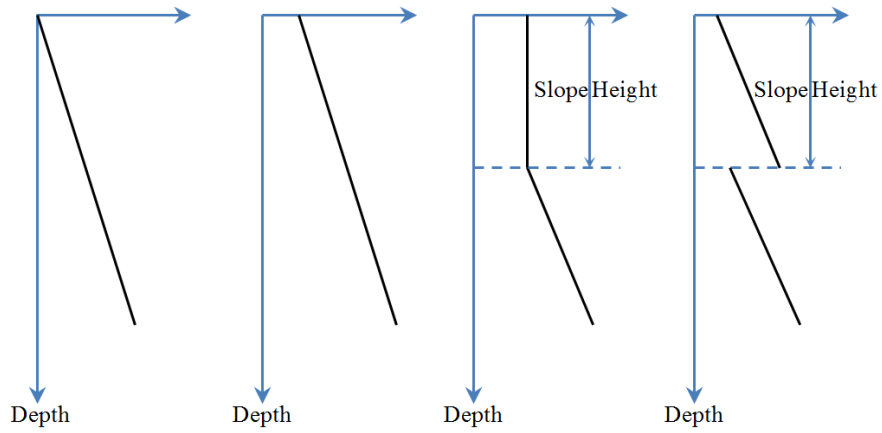


Figure 3-12. Several types of cohesion varying with depth (Chen 1975).

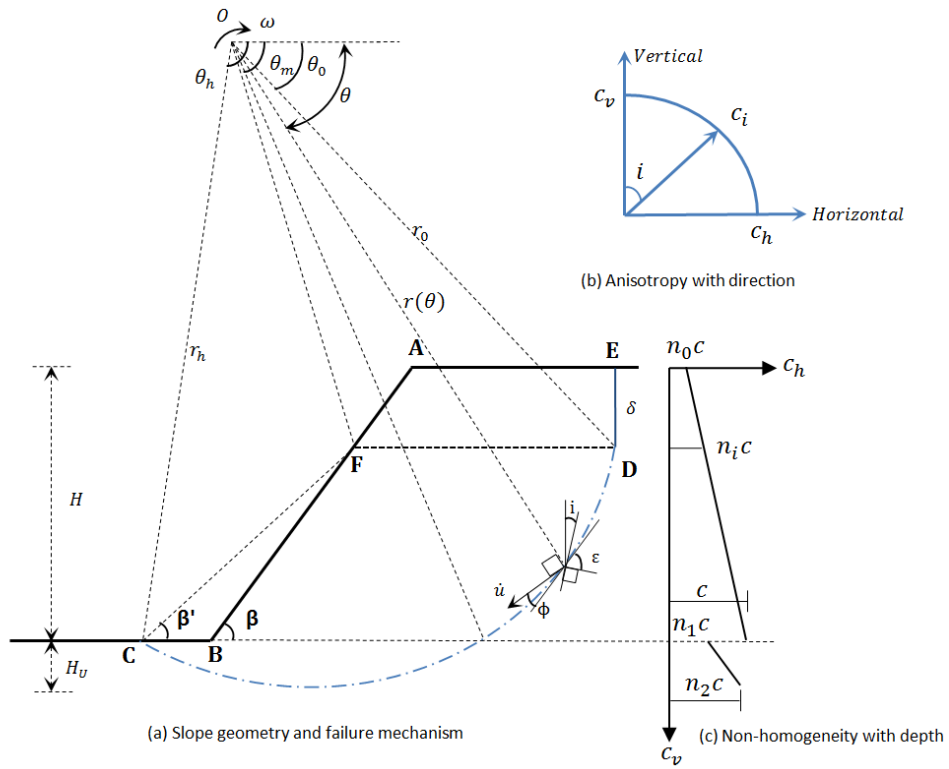


Figure 3-13. Slope geometry, failure mechanism and ground condition.

For anisotropic geomaterials, the exhibited cohesion also depends on the loading direction. According to Figure 3-13 (b), the cohesion  $c_i$  at the point where its major principal stress is inclined at angle  $i$  to the vertical direction is given by Lo (1965) and Chen (1975):

$$c_i = c_h + (c_v - c_h) \cos^2 i \quad (3-55)$$

where  $c_h$  and  $c_v$  are the horizontal and vertical principal cohesions. The ratio of the principal cohesions  $c_h/c_v$ , denoted by  $\kappa$ , is assumed to be the same at all points within the slope. For an isotropic material,  $c_i = c_h = c_v$  and  $\kappa = 1$ .

As shown in Figure 3-13(c), there is an abrupt change of cohesion below the slope toe. Cohesion exhibited along the direction tangent to the failure line can be calculated by using Eq. (3-55). The total rate of internal energy dissipation along the failure line  $\widehat{CD}$  is divided into two parts (Chen 1975):

$$\begin{aligned} \dot{W}_{d-\log} &= \int_{\widehat{CD}} c_i (V \cos \phi) \frac{rd\theta}{\cos \phi} \\ &= \int_{\theta_0}^{\theta_m} (c_i)_1 (V \cos \phi) \frac{rd\theta}{\cos \phi} + \int_{\theta_m}^{\theta_h} (c_i)_2 (V \cos \phi) \frac{rd\theta}{\cos \phi} \end{aligned} \quad (3-56)$$

where angles  $\theta_m$  and  $i$  are obtained by the following geometric relationships:

$$e^{\tan \phi \theta_m} \sin \theta_m = e^{\tan \phi \theta_h} \sin \theta_h \quad (3-57)$$

$$i = \theta - \frac{\pi}{2} - \phi + \varepsilon = \theta + \Phi \quad (3-58)$$

with



$$\Phi = -\left(\frac{\pi}{2} + \varphi - \varepsilon\right) \quad (3-59)$$

Due to the presence of pre-existing cracks, the internal energy dissipates from point  $D$ , as shown in Figure 3-13. The cohesion at the depth of  $\delta$  is  $n_i c$ , with

$$n_i = n_0 + \eta - \eta n_0 \quad (3-60)$$

Referring to Eq. (3-55),  $(c_i)_1$  and  $(c_i)_2$  in Eq. (3-56) are found by:

$$(c_i)_1 = c \left\{ n_i + \frac{(1-n_i)}{(H-\delta)/r_0} \left[ e^{\tan \phi(\theta-\theta_0)} \sin \theta - \sin \theta_0 \right] \right\} \left[ 1 + \frac{1-\kappa}{\kappa} \cos^2 i \right] \quad (3-61)$$

$$(c_i)_2 = c \left\{ n_1 + \frac{(n_2-n_1)}{(H_U/r_0)} \left[ e^{\tan \phi(\theta-\theta_0)} \sin \theta - \sin \theta_m e^{\tan \phi(\theta_m-\theta_0)} \right] \right\} \left[ 1 + \frac{1-\kappa}{\kappa} \cos^2 i \right] \quad (3-62)$$

Substituting Eqs. (3-61) and (3-62) into Eq. (3-56), after rearranging, Eq. (3-56)

becomes:

$$\dot{W}_{d-\log} = c \omega r_0^2 (q_1 + q_2 + q_3) \quad (3-63)$$

with  $q_1, q_2$  and  $q_3$  given by:

$$q_1 = \left\{ \frac{n_i}{e^{2 \tan \phi \theta_0}} \left[ \psi(\theta) + \frac{1-\kappa}{\kappa} \lambda(\theta) \right] \right\}_{\theta_0}^{\theta_m} + \left\{ \frac{n_1}{e^{2 \tan \phi \theta_0}} \left[ \psi(\theta) + \frac{1-\kappa}{\kappa} \lambda(\theta) \right] \right\}_{\theta_m}^{\theta_h} \quad (3-64)$$

$$q_2 = \frac{(1-n_i)}{(H-\delta) e^{3 \tan \phi \theta_0} / r_0} \left\{ \xi(\theta) - \psi(\theta) \sin \theta_0 e^{\tan \phi \theta_0} + \frac{1-\kappa}{\kappa} [\rho(\theta) - \lambda(\theta) \sin \theta_0 e^{\tan \phi \theta_0}] \right\}_{\theta_0}^{\theta_m} \quad (3-65)$$

$$q_3 = \frac{(n_2 - n_1)}{(H_U / r_0) e^{3 \tan \phi \theta_0}} \left\{ \xi(\theta) - \psi(\theta) \sin \theta_m e^{\tan \phi \theta_m} + \frac{1 - \kappa}{\kappa} [\rho(\theta) - \lambda(\theta) \sin \theta_m e^{\tan \phi \theta_m}] \right\}_{\theta_m}^{\theta_h} \quad (3-66)$$

where

$$\xi(\theta) = \frac{(3 \tan \phi \sin \theta - \cos \theta) e^{3 \theta \tan \phi}}{1 + 9 \tan^2 \phi} \quad (3-67)$$

$$\psi(\theta) = \frac{e^{2 \theta \tan \phi}}{2 \tan \phi} \quad (3-68)$$

$$\rho(\theta) = \frac{e^{3 \theta \tan \phi}}{2} \left\{ \begin{aligned} &\cos 2\Phi \left[ \frac{\cos \theta - 3 \tan \phi \sin \theta}{2(1 + 9 \tan^2 \phi)} + \frac{\tan \phi \sin 3\theta - \cos 3\theta}{6(1 + \tan^2 \phi)} \right] \\ &- \sin 2\Phi \left[ \frac{\sin \theta + 3 \tan \phi \cos \theta}{2(1 + 9 \tan^2 \phi)} + \frac{\tan \phi \cos 3\theta + \sin 3\theta}{6(1 + \tan^2 \phi)} \right] \\ &+ \frac{3 \tan \phi \sin \theta - \cos \theta}{1 + 9 \tan^2 \phi} \end{aligned} \right\} \quad (3-69)$$

$$\lambda(\theta) = \frac{e^{2 \theta \tan \phi}}{2} \left\{ \begin{aligned} &\cos 2\Phi \left[ \frac{\tan \phi \cos 2\theta + \sin 2\theta}{2(1 + \tan^2 \phi)} \right] \\ &- \sin 2\Phi \left[ \frac{\tan \phi \sin 2\theta - \cos 2\theta}{2(1 + \tan^2 \phi)} \right] \end{aligned} \right\} + \frac{e^{2 \theta \tan \phi}}{4 \tan \phi} \quad (3-70)$$

$$H_U = e^{\tan \phi \left( \frac{\pi}{2} + \phi - \theta_0 \right)} \cos \phi - \sin \theta_0 - H + \delta \quad (3-71)$$

Equating the rate of external work to the rate of energy dissipation, leads to:

$$\begin{aligned}\dot{W}_\gamma &= \omega \gamma r_0^3 (f_1 - f_2 - f_3 - f_4 + f_U) \\ &= \dot{W}_{d-\log} = c \omega r_0^2 (q_1 + q_2 + q_3)\end{aligned}\quad (3-72)$$

After rearranging, the stability factor of slopes made of anisotropic and nonhomogeneous  $c - \phi$  material is expressed as:

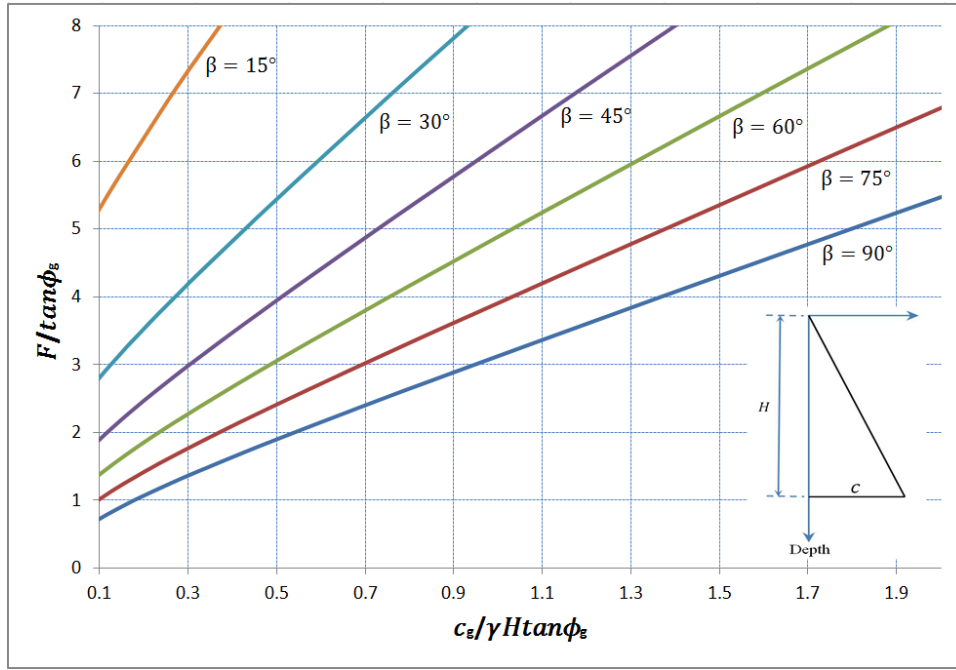
$$\frac{\gamma H}{c} = \frac{(q_1 + q_2 + q_3) \times f_h}{f_1 - f_2 - f_3 - f_4 + f_U} \quad (3-73)$$

The stability factor still needs to be minimized under the constraint of maximum allowable crack depth, which is defined as:

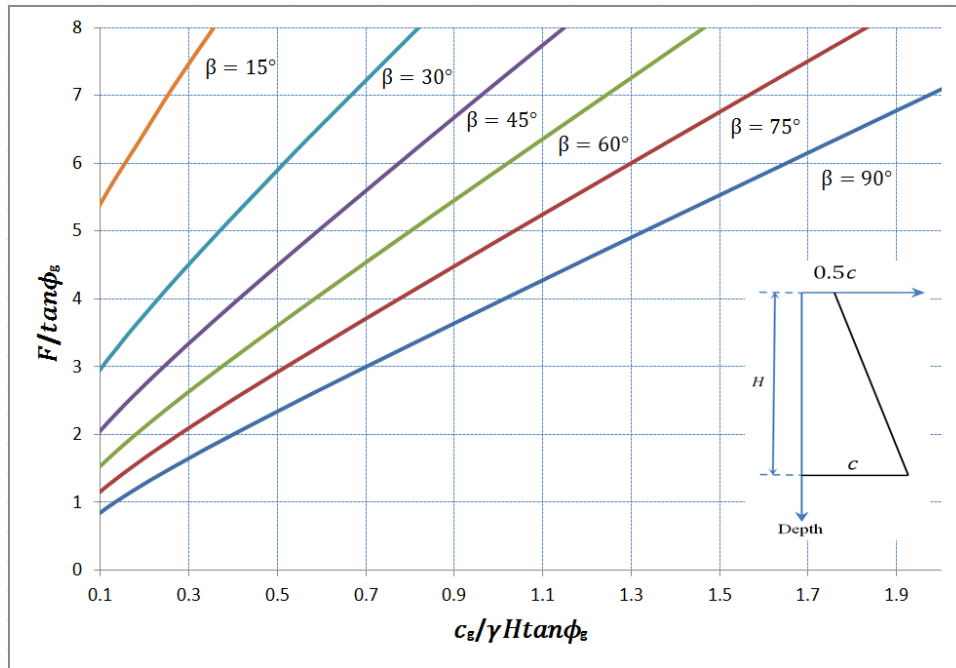
$$\frac{\delta_{\max}}{H} = \frac{N_{M-C,90^\circ}(c_i)}{N_{M-C,\beta}(c_i)} \quad (3-74)$$

where  $N_{M-C,90^\circ}(c_i)$  is the stability factor of an intact vertical slope in the same ground conditions.  $N_{M-C,\beta}(c_i)$  is the stability factor of an intact slope of inclination  $\beta$ .

Stability charts for two typical cases of cohesion linearly varying along depth (i.e.,  $n_0 = 0$  and  $n_0 = 0.5$ ) are presented in Figure 3-14. Again, the most adverse pre-existing cracks are considered.



(a)  $n_0 = 0, \kappa = 1$



(b)  $n_0 = 0.5, \kappa = 1$

Figure 3-14. Stability charts for non-homogenous slopes with anisotropic strength.

### 3.5 Conclusions

In this chapter, upper bound formulations for slopes made of geomaterials obeying the Mohr-Coulomb failure criterion subjected to the presence of cracks, water pressure and seismic actions were present in a unified and consistent framework. A large number of stability charts were provided for the benefit of practitioners. The following conclusions can be drawn:

(a) The upper bound formulations illustrated in this chapter can be regarded as extension and clarification of the work done by Utili (2013) and Michalowski (2013), and are the basis of stability assessment of slopes made of geomaterials obeying the non-linear failure criterion in the following chapters. The issues regarding slopes made of frictionless soil, maximum stable crack depth, different ground and water conditions and the influence of seismic loading are tackled. Stability charts ( $\frac{F}{\tan\phi_g}$  against  $\frac{c_g}{\gamma H \tan\phi_g}$ ) for uniform slopes with water only present in the crack, uniform slopes subjected to different seismic actions and non-homogenous slopes with anisotropic strength are provided for the first time considering the most adverse pre-existing cracks being present in the slope.

(b) It is import to note that in order to seek the most adverse crack depth and location, the stability factor  $\frac{\gamma H}{c}$  is minimized over the angles denoting the failure mechanism and the normalized crack depth. To avoid the potential local failure (sliding of the soil/rock mass behind the crack), the minimization process should be done under the constraint of maximum stable crack depth defined in Eqs. (3-21), (3-45), (3-54) and (3-74).

## **Chapter 4 Stability Assessment of Slopes Made of Rocks Obeying the Hoek-Brown Failure Criterion**

According to experimental evidence (e.g. Hoek and Brown 1980; Agar et al. 1987; Baker 2004; Descamps et al. 2012; Meng et al. 2015; Rathnaweera et al. 2015), the shear strength for both soil and rock is better represented by using nonlinear failure criteria. However, with regard to the strength of soil, even though all soils show a certain degree of nonlinearity, the linear Mohr-Coulomb failure criterion is by far the most applied by researchers and practitioners, due to the advantage in simplicity of using a linear criterion. But rocks present significantly more pronounced nonlinearity than soils, and thus, the Mohr-Coulomb failure criterion is considered unsuitable to describe rock mass behaviour, especially for slope stability problems where rocks are subjected to low confining pressure making the nonlinearity more prominent.

Based on the result of a series of field investigations and triaxial tests on rocks, the non-linear Hoek-Brown failure criterion was first proposed by Hoek and Brown (1980). Three decades after its introduction, there is a stronger consensus in the scientific community that Hoek-Brown failure criterion is a very good criterion for the characterization of rock strength (Hoek 1983, Martin et al. 1999, Fraldi and Guarracino 2009, Rojat et al. 2015). In this chapter, the stability of slopes made of rock obeying the Hoek-Brown failure criterion is investigated for the first time including the presence of pre-existing cracks and blast-induced rock damage. The results have been obtained by employing three different techniques: the tangential line technique, the equivalent cohesion-friction angle method and the variational approach.

## 4.1 Introduction of rock slope failure mode

As reported in Hudson and Harrison (2000), there are two types of failure mechanisms occurring in rock slopes, i.e., a curvilinear one when the rock slope can be considered as an equivalent continuum and a linear one when it is governed by the behaviour of single discontinuities (see Figure 4-1). This chapter is devoted to the first type of mechanism. A rock mass behaves as a continuum either when it is intact or when the scale of discontinuities is small in comparison to the scale of the slope, for instance, in the case of closely fractured or highly weathered rocks, a strongly defined structural pattern (in the geological sense) no longer exists and the slide surface is free to find the line of least resistance through the slope (Wyllie et al. 2004). Hoek (1983) and Li et al. (2008) classified rock masses into three structural groups, namely Group I, Group II and Group III. In Figure 4-1, the transition from an isotropic intact rock (Group I), through a highly anisotropic rock mass (Group II), to a heavily jointed rock mass (Group III) is illustrated. In this chapter, the rock masses of Group I and III are considered. Concerning Group III, the presence of the many discontinuities in the rock mass is accounted for by determining strength parameters for the equivalent continuum via the use of rock mass classification systems (e.g. *RMR*, *GSI*). For the cases of Group I and III, based on site investigation and experience, Hudson and Harrison (2000) state that the slip surface for a slope is curvilinear, and usually terminates at a tension crack at the upper slope surface. This highlights the importance of considering the presence of cracks in the stability analyses of rock slopes.

Previous literature (e.g., Hoek and Bray 1981; Wyllie et al. 2004) investigating the effect of the presence of cracks on rock slopes mainly concentrates on geomaterials obeying the linear Mohr-Coulomb strength criterion. In this chapter, the influence of the presence of pre-existing cracks on the upper

face of slopes made of weak rocks (e.g. highly altered and weathered rocks) and/or rock slopes with closely spaced randomly oriented discontinuities. So rocks of Group I and III are investigated via limit analysis. The rock mass will be treated as a continuum obeying the non-linear Hoek-Brown failure criterion.

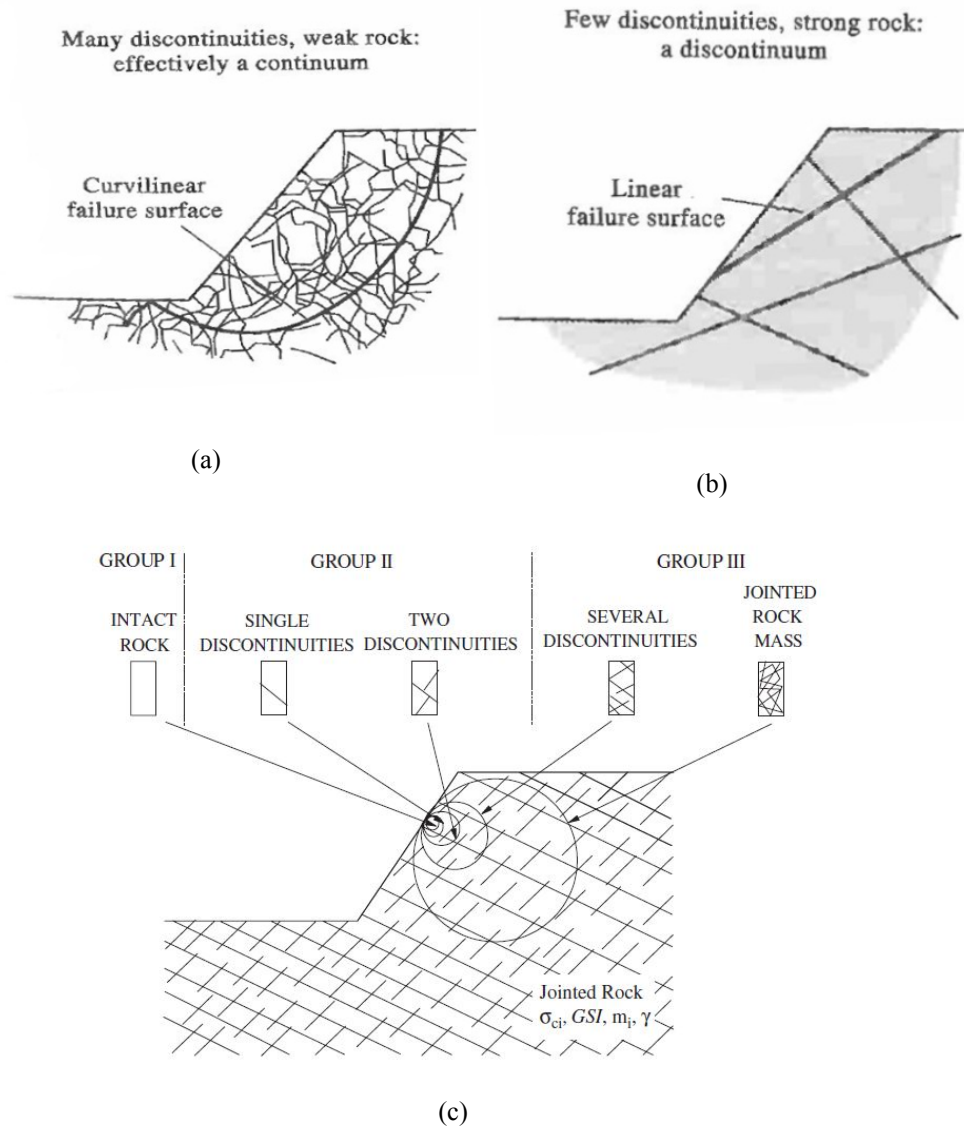


Figure 4-1. Applicability of the continuum approach and the Hoek-Brown failure criterion for rock slope stability problems. (a) A continuum failure mechanism (Hudson and Harrison 2000). (b) A discontinuum failure mechanism (Hudson and Harrison 2000). (c) Three groups to be considered depending on the joint size relative to the domain dimension (Li et al. 2008).



## 4.2 The Hoek-Brown failure criterion

According to the latest version of the Hoek-Brown failure criterion (Hoek et al. 2002), the generalized Hoek-Brown failure criterion is expressed as:

$$\sigma_1 = \sigma_3 + \sigma_{ci} \left( m \frac{\sigma_3}{\sigma_{ci}} + s \right)^n \quad (4-1)$$

with  $\sigma_1, \sigma_3$  the major and minor principle stresses respectively,  $\sigma_{ci}$  the uniaxial compression strength of the intact rock mass,  $m$  a parameter related to the rock type considered,  $s$  a parameter expressing the degree of fracturing of the rock mass and  $n$  a parameter accounting for degree of imperfection of the rock mass. For a given rock type,  $m, s, n$  can be determined from the geological strength index  $GSI$  as follows:

$$m = m_i \exp \left( \frac{GSI - 100}{28 - 14D} \right) \quad (4-2)$$

$$s = \exp \left( \frac{GSI - 100}{9 - 3D} \right) \quad (4-3)$$

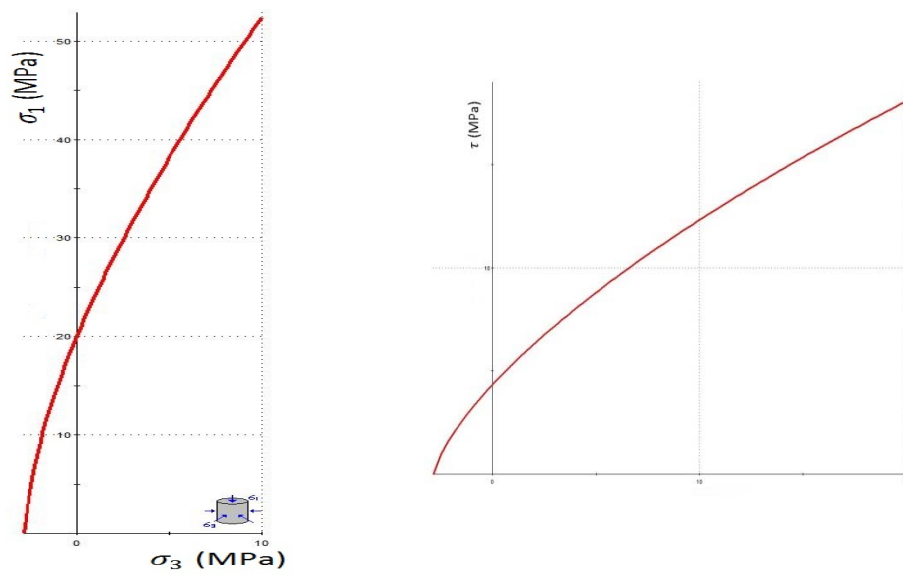
$$n = \frac{1}{2} + \frac{1}{6} (e^{-GSI/15} - e^{-20/3}) \quad (4-4)$$

where  $m_i$  is the value of  $m$  for intact rock and  $D$  is defined as a disturbance coefficient ranging from 0 for undisturbed in situ rock masses to 1 for very disturbed rock masses. The  $GSI$  index, introduced by Hoek et al. (1995), provides a

number which, when combined with the intact rock properties, can be used for estimating the reduction in rock mass strength for different geological conditions. It combines the two fundamental parameters of a rock mass, i.e., the blockiness of the mass and the conditions of the discontinuities in the rock mass (Marinos et al. 2005). The Hoek-Brown failure envelope is a non-linear curve in  $(\sigma_1 - \sigma_3)$  space. In Figure 4-2, the criterion is plotted in the  $(\tau - \sigma)$  space as well. Some typical values of  $m_i$ ,  $s$ ,  $D$  and their physical meaning are listed in Table 4-1 and Table 4-2.

The theory of limit analysis was initially developed for geomaterials obeying the linear Mohr-Coulomb failure criterion (Drucker et al. 1952; Chen 1975). Hence, it is not directly applicable to geomaterials obeying the Hoek-Brown criterion. However, in principle, limit analysis can still be employed as long as the material considered satisfies the normality rule. There are two ways to apply limit analysis to a non-linear failure envelope. One method consists of linearizing the Hoek-Brown failure criterion, so that a single Mohr-Coulomb failure envelope to represent the non-linear curve is found. In this case, only a partial modification of the existing limit analysis formulations based on the Mohr-Coulomb failure criterion is needed. A second method consists of implementing a step-by-step evaluation of the energy dissipated along the yet-to-be-determined failure surface.

Three methods were adopted in this chapter: the so-called tangential technique, the equivalent  $c - \phi$  method and the variational approach. The first two methods belong to the first category while the variational approach falls into the second one.



(a)  $\sigma_1 - \sigma_3$  space


(b)  $\tau - \sigma$  space





Figure 4-2. Hoek-Brown failure envelope for a block of limestone whose  $m_i = 7.3$ ,  $GSI = 100$ ,  $D = 1$ ,  $\sigma_{ci} = 20\text{MPa}$ .

Table 4-1. Typical values of  $m_i$  and  $s$  (Collins et al. 1988)

$m_i$	7.3	10.5	15.7	17.8	26.2	
Rock type	limestone	mudstone	sandstone	andesite	granite	
$s$	1.0	$10^{-1}$	$4 \times 10^{-3}$	$10^{-4}$	$10^{-5}$	$7 \times 10^{-7}$
Degree of fracturing	Intact	Very good	Good	Fair	Poor	Very poor

Table 4-2. Guidelines for estimating disturbance factor  $D$  (Hoek et al. 2002).

Appearance of rock mass	Description of rock mass	Suggested value of $D$
	Excellent quality controlled blasting or excavation by Tunnel Boring Machine results in minimal disturbance to the confined rock mass surrounding a tunnel.	$D = 0$

	<p>Mechanical or hand excavation in poor quality rock masses (no blasting) results in minimal disturbance to the surrounding rock mass.</p> <p>Where squeezing problems result in significant floor heave, disturbance can be severe unless a temporary invert, as shown in the photograph, is placed.</p>	$D = 0$ $D = 0.5$ No invert
	<p>Very poor quality blasting in a hard rock tunnel results in severe local damage, extending 2 or 3 m, in the surrounding rock mass.</p>	$D = 0.8$
	<p>Small scale blasting in civil engineering slopes results in modest rock mass damage, particularly if controlled blasting is used as shown on the left hand side of the photograph. However, stress relief results in some disturbance.</p>	$D = 0.7$ Good blasting $D = 1.0$ Poor blasting
	<p>Very large open pit mine slopes suffer significant disturbance due to heavy production blasting and also due to stress relief from overburden removal.</p> <p>In some softer rocks excavation can be carried out by ripping and dozing and the degree of damage to the slopes is less.</p>	$D = 1.0$ Production blasting $D = 0.7$ Mechanical excavation

### 4.3 Tangential technique

In Chapter 3, the stability assessment of slopes made of geomaterials obeying the Mohr-Coulomb failure criterion was detailed. In this section, the tangential technique will be applied to linearize the non-linear Hoek-Brown failure criterion.

Collins et al. (1988) and Drescher and Christopoulos (1988) were the first to employ the so-called tangential technique to evaluate the stability of slopes for

non-linear failure criteria. Later, Yang et al. (2004) and Yang and Zou (2006) adopted the same method to account for more complex conditions such as an inclined upper slope surface and the presence of pore water pressure for rocks obeying the generalized Hoek-Brown failure criterion.

The Hoek-Brown failure criterion is originally defined in the  $(\sigma_1, \sigma_3)$  space (see Eq. (4-1)) and can be rewritten in terms of shear and normal stresses  $\tau$  and  $\sigma$ . A tangent to the Hoek-Brown failure criterion in  $(\tau, \sigma)$  stress space is expressed as:

$$\tau = \sigma \tan \phi_t + c_t \quad (4-5)$$

where  $c_t$  is the intercept of the tangential line with the  $\tau$  axis, and  $\phi_t$  is the dip angle of the tangent to the Hoek-Brown failure envelope at a generic point considered (See Figure 4-3).

According to Yang et al. (2004), the Hoek-Brown failure criterion in the  $(\tau, \sigma)$  space is a parameter equation in terms of  $\phi_t$ :

$$\frac{\tau}{\sigma_{ci}} = \frac{\cos \phi_t}{2} \left[ \frac{mn(1 - \sin \phi_t)}{2 \sin \phi_t} \right]^{n/(1-n)} \quad (4-6)$$

$$\frac{\sigma}{\sigma_{ci}} = \left( \frac{1}{m} + \frac{\sin \phi_t}{mn} \right) \left[ \frac{mn(1 - \sin \phi_t)}{2 \sin \phi_t} \right]^{1/(1-n)} - \frac{s}{m} \quad (4-7)$$

From Eqs. (4-5), (4-6), (4-7),  $c_t$  is derived as:

$$\begin{aligned} \frac{c_t}{\sigma_{ci}} &= \frac{\cos \phi_t}{2} \left[ \frac{mn(1 - \sin \phi_t)}{2 \sin \phi_t} \right]^{n/(1-n)} \\ &\quad - \frac{\tan \phi_t}{m} \left( 1 + \frac{\sin \phi_t}{n} \right) \left[ \frac{mn(1 - \sin \phi_t)}{2 \sin \phi_t} \right]^{1/(1-n)} + \frac{s}{m} \tan \phi_t \end{aligned} \quad (4-8)$$

There are numerous tangents to the Hoek-Brown failure envelope (see Figure 4-3). For each of these, the stability factor corresponding to a Mohr-Coulomb failure envelope can be calculated by replacing  $c$  with  $c_t$ ,  $\phi$  with  $\phi_t$  in the expressions such as Eq. (3-14) in Chapter 3. Here  $\phi_t$  is treated as a variable to determine the least possible stability factor. Strength parameters  $c_{t,c}$  and  $\phi_{t,c}$ , which correspond to the tangent yielding the least stability factor, will be selected as the parameters to linearize Hoek-Brown failure criterion. Therefore, the upper bound solution for geomaterials satisfying the linear Mohr-Coulomb failure criterion can be extended to account for the non-linear Hoek-Brown failure criterion with an additional variable  $\phi_t$ .

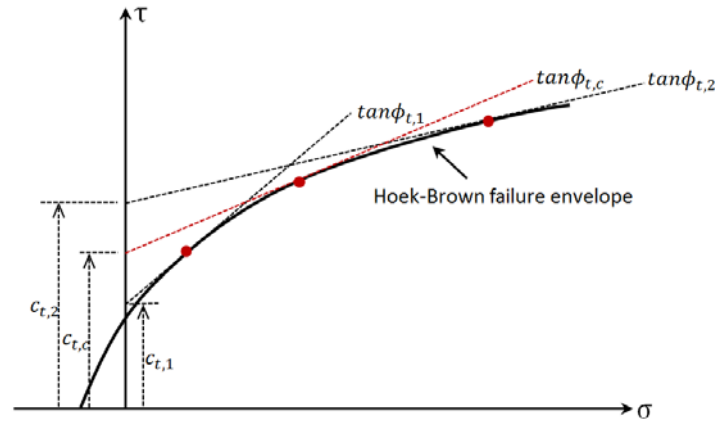


Figure 4-3. Tangential technique for Hoek-Brown failure criterion.

There is some arbitrariness in the choice of reference stress used to define the dimensionless stability factor for a non-linear material (Collins et al. 1988). In this chapter, the stability factor for slopes made of rock obeying the Hoek-Brown failure criterion is defined as  $N_{H-B} = \frac{\gamma H}{\sigma_{ci}}$  according to Li et al. (2008) and Shen et al. (2013), because other rock strength parameters such as tensile strength can be obtained from  $\sigma_{ci}$ . And  $\sigma_{ci}$  is the most accessible parameter in measuring rock strength (Wyllie et al. 2004).  $\frac{\gamma H}{\sigma_{ci}}$  is derived by the modification of Eq. (3-14) corresponding to the Mohr-Coulomb failure criterion:

$$\begin{aligned}
N_{H-B} &= \frac{\gamma H}{\sigma_{ci}} = \frac{\gamma H}{c_t} \cdot \frac{c_t}{\sigma_{ci}} = N_{M-C}|_{\phi=\phi_t} \cdot \frac{c_t}{\sigma_{ci}} \\
&= \frac{f_{d-\log} \times f_h}{f_1 - f_2 - f_3 - f_4 + f_U} \times \\
&\quad \left\{ \frac{\cos \phi_t}{2} \left[ \frac{mn(1 - \sin \phi_t)}{2 \sin \phi_t} \right]^{n/(1-n)} \right. \\
&\quad \left. - \frac{\tan \phi_t}{m} \left( 1 + \frac{\sin \phi_t}{n} \right) \left[ \frac{mn(1 - \sin \phi_t)}{2 \sin \phi_t} \right]^{1/(1-n)} + \frac{s}{m} \tan \phi_t \right\}
\end{aligned} \tag{4-9}$$

$\phi$  is replaced by  $\phi_t$  in the expressions of  $f_1 \sim f_4$ ,  $f_U$  and  $f_h$ . According to the upper bound theorem, the least upper bound is associated with the minimum value of  $N_{H-B}$  which is to be found by evaluating repeatedly Eq. (4-9) over the five variables  $\theta_0, \theta_h, \beta', \eta$  and  $\phi_t$  in the range of values of engineering interest. It should be noted that  $\frac{\sigma}{\sigma_{ci}}$  defined in Eq. (4-7) must be within the range of  $-\frac{s}{m} < \frac{\sigma}{\sigma_{ci}} < 1$  to avoid any unrealistic selection of  $\phi_t$ .  $-\frac{s}{m}\sigma_{ci}$  is the tensile strength of the rock. However, Collins et al. (1988) and Yang et al. (2004) overlooked the constraint and arrived at some unrealistic results, e.g., Table II in Collins et al. (1988) and Table II in Yang et al. (2004).

If the ground condition and the height of a slope are known, in addition, the factor of safety  $F$  is assumed to apply to  $\sigma_{ci}$  only,  $F$  can be obtained from Eq. (4-9) directly:

$$F = N_{H-B} \frac{\sigma_{ci}}{\gamma H} \tag{4-10}$$

Three different types of problems concerning the depth and location of the cracks are to be studied:

- (a) Slopes with cracks of known depth but unspecified location (for instance the depth of tension crack zone can be estimated).
- (b) Slopes with cracks of known location but unspecified depth (a typical scenario for rock slopes).
- (c) Slopes with cracks of unspecified depth and location (the most adverse crack is to be sought to yield the minimum stability).

#### 4.3.1 Cracks of known depth

To start with, the problem of cracks of known depth but unspecified location is handled. Since the normalized crack depth  $\eta$  is known, the variables in Eq. (4-9) to determine the most critical failure mechanism reduce to four. For illustrative purposes, rock slopes having horizontal upper slope face ( $\alpha = 0^\circ$ ) and vertical crack ( $\chi = 90^\circ$ ) are considered in the following sections. The constraint of maximum stable crack depth can be expressed as:

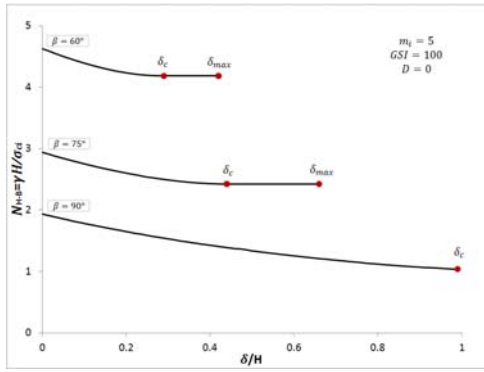
$$\eta_{\max} = \frac{\delta_{\max}}{H} = \frac{N_{H-B,90^\circ}}{N_{H-B,\beta}} \quad (4-11)$$

defining  $N_{H-B,\beta}$  as the stability factor of an intact ( $\delta = 0$ ) slope of inclination  $\beta$  and  $N_{H-B,90^\circ}$  as the stability factor of an intact vertical slope. The minimum value of the stability factor defined in Eq. (4-9) subject to cracks with known depth is determined within the range of  $0 < \eta < \eta_{\max}$ .

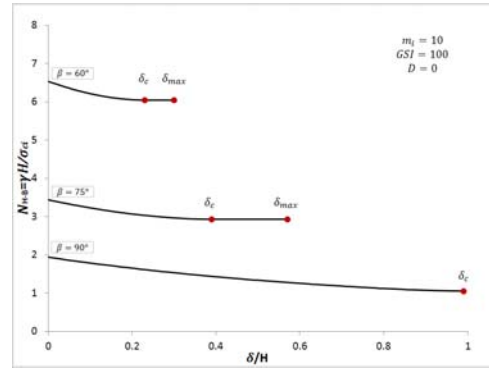
In Figure 4-4, for slopes made of different rock types (i.e.,  $m_i = 5, 10, 20, 30$  and  $GSI = 20, 40, 60, 80, 100$ ), the stability factors  $N_{H-B}$  defined in Eq. (4-9) are plotted against the normalized crack depth  $\delta/H$  corresponding to different inclinations (i.e.,  $\beta = 60^\circ, 75^\circ$  and  $90^\circ$ ). For non-vertical slopes ( $\beta \neq 90^\circ$ ), there is



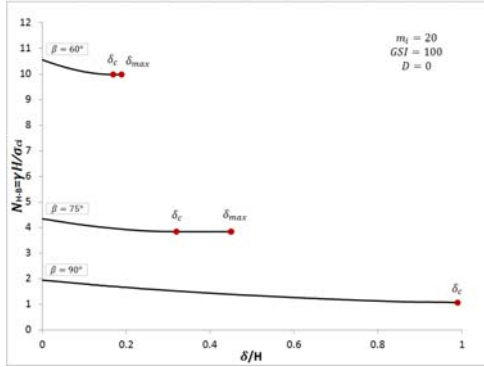
a minimum value of the stability factor for each inclination and its corresponding crack depth is  $\delta_c$ , beyond which the crack depth no longer affects the stability of the slope, so that the value of the stability factor  $N_{H-B}$  is constant for  $\delta > \delta_c$  until  $\delta = \delta_{max}$ . For a given rock type, the length of  $\delta_c$  increases with progressively steeper inclination. In addition,  $\delta_c$  increases with higher values of  $m_i$  and  $GSI$ . For vertical slope, the curve shows a monotonic decreasing trend with a minimum value of  $N_{H-B}$  at  $\delta/H = 1$ .



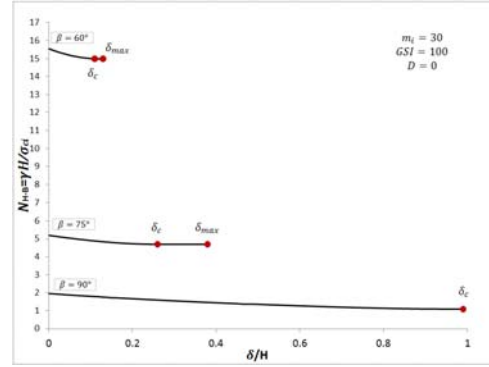
(a)  $m_i = 5, GSI = 100, D = 0$



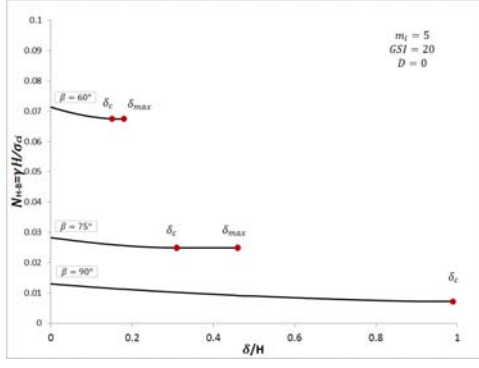
(b)  $m_i = 10, GSI = 100, D = 0$



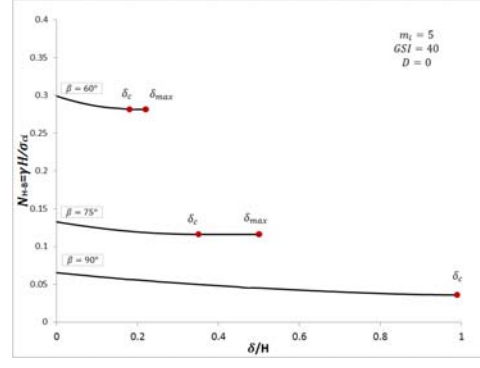
(c)  $m_i = 20, GSI = 100, D = 0$



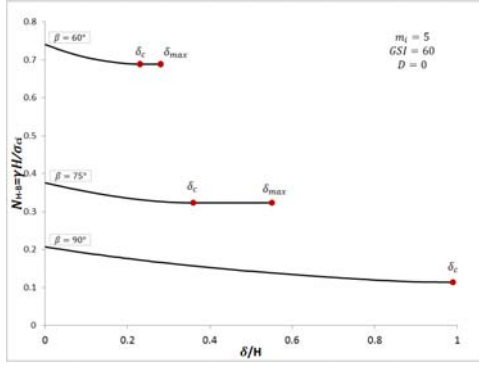
(d)  $m_i = 30, GSI = 100, D = 0$



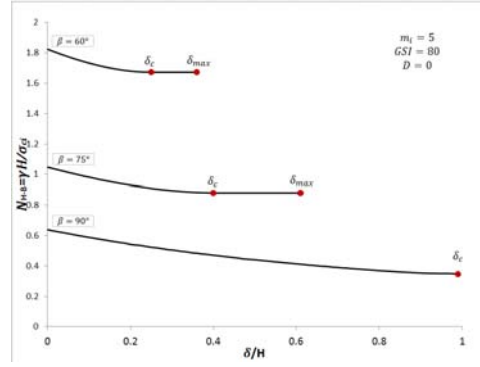
(e)  $m_i = 5, GSI = 20, D = 0$



(f)  $m_i = 5, GSI = 40, D = 0$



(g)  $m_i = 5, GSI = 60, D = 0$



(h)  $m_i = 5, GSI = 80, D = 0$

Figure 4-4. Stability factor  $N_{H-B}$  against crack depth for various slope inclinations and rock strength parameters.

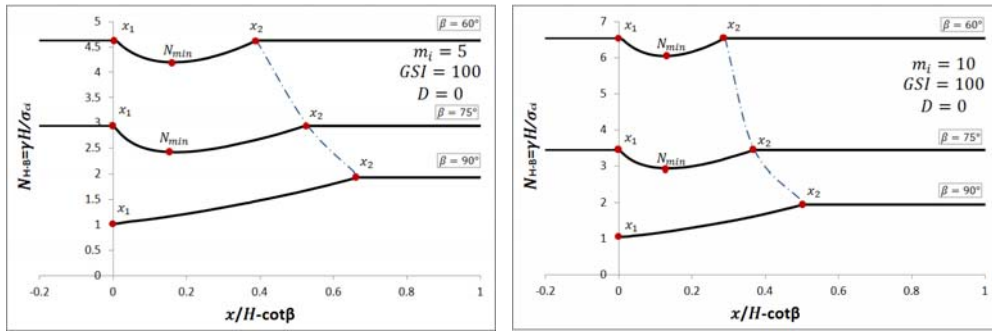
### 4.3.2 Cracks of known location

The case of cracks of known location, measured as the horizontal distance  $\frac{x}{H}$  (the length of  $AE$  over the total height of slope, shown in Figure 3-1) from the slope crest, but with unspecified depth is addressed in this section. Both the region where the presence of cracks makes the slope less stable and the region where slope stability is not affected by cracks are of great interest.

Since the location of the crack is known, the variables to determine the failure mechanism reduce to four, and the following constraint of these variables is found:

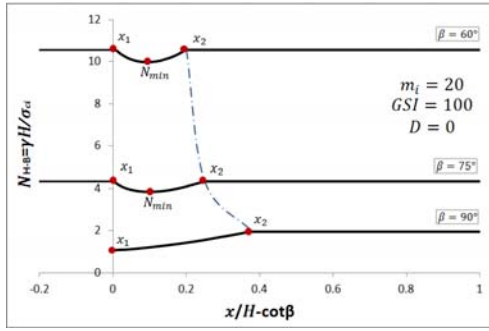
$$\begin{aligned}
& \frac{x}{H} \cos \alpha \\
& + \frac{\eta - \left\{ \frac{\sin(\theta_h - \theta_0)}{\sin \theta_h} - \left[ e^{\tan \phi(\theta_h - \theta_0)} \sin \theta_h - \sin \theta_0 \right] \frac{\sin(\theta_h + \beta')}{\sin \theta_h \sin \beta'} \right\} \tan \alpha}{\tan \beta - \tan \alpha} \\
& = \frac{\sin(\theta_h - \theta_0)}{\sin(\theta_h + \alpha)} \\
& - \left[ e^{\tan \phi(\theta_h - \theta_0)} \sin(\theta_h + \alpha) - \sin(\theta_0 + \alpha) \right] \frac{\sin(\theta_h + \beta')}{\sin(\theta_h + \alpha) \sin(\beta' - \alpha)}
\end{aligned} \tag{4-12}$$

The stability factors defined in Eq. (4-9) are minimized under the constraint of Eqs. (4-11) and (4-12). In Figure 4-5, the stability factors  $N_{H-B}$  are plotted against different values of  $\frac{x}{H} - \cot \beta$  for slopes in various rock types with  $\beta = 60^\circ, 75^\circ$  and  $90^\circ$ . There are regions bounded by  $x_1$  and  $x_2$  where the stability factors are lower than those of intact slopes. These regions are defined as the affected zones. Within the affected zone,  $\frac{x}{H}$  corresponding to the minimum value of the stability factor  $N_{min}$  yields the most adverse location of the crack. If  $GSI$  is fixed (in Figure 4-5 (a)~(d)), rocks with higher value of  $m$  tend to have a narrower affected zone. However, when  $m_i$  is fixed (in Figure 4-5 (e)~(h)), the rock slopes with lower  $GSI$  have wider affected zones. Practitioners can have an instant evaluation that if the cracks fall outside of  $x_1 - x_2$ , the stability of the slope will not be affected by the presence of cracks.

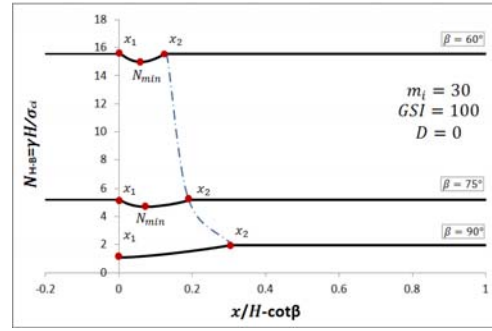


(a)  $m_i = 5, GSI = 100, D = 0$

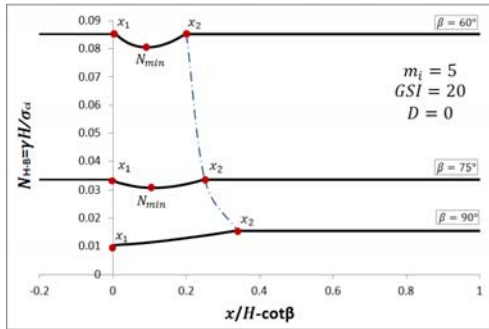
(b)  $m_i = 10, GSI = 100, D = 0$



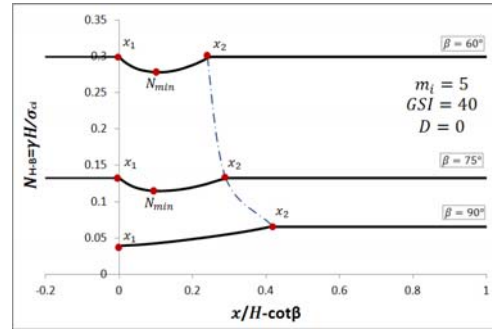
(c)  $m_i = 20, GSI = 100, D = 0$



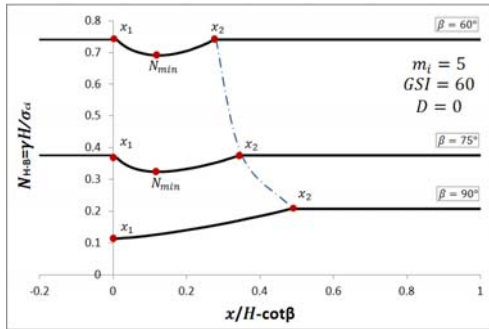
(d)  $m_i = 30, GSI = 100, D = 0$



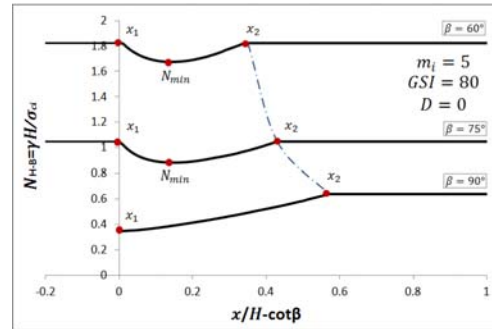
(e)  $m_i = 5, GSI = 20, D = 0$



(f)  $m_i = 5, GSI = 40, D = 0$



(g)  $m_i = 5, GSI = 60, D = 0$



(h)  $m_i = 5, GSI = 80, D = 0$

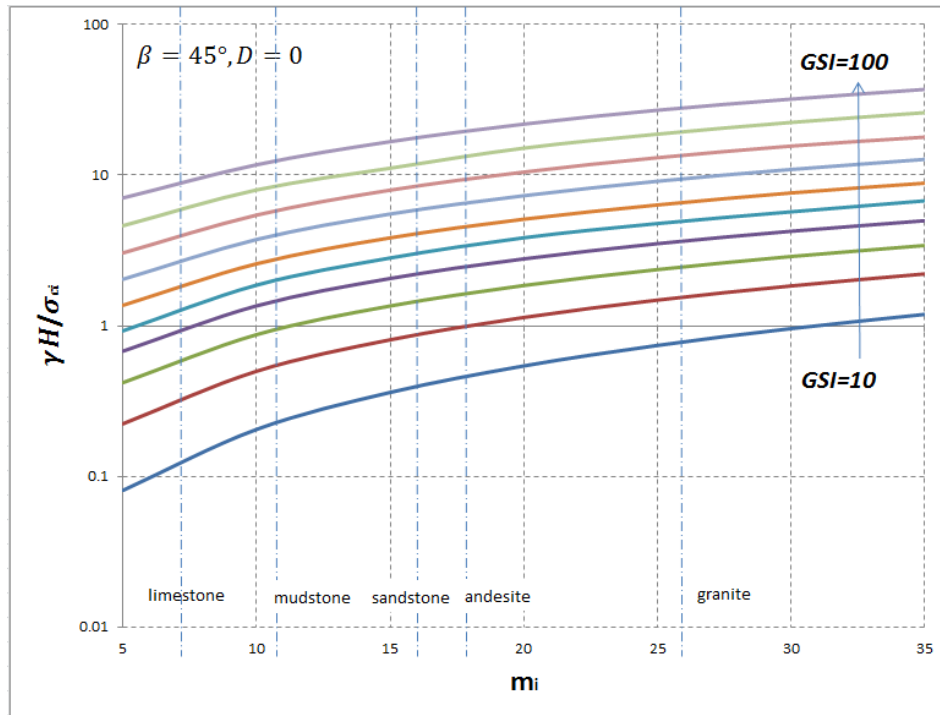
Figure 4-5. Stability factor  $N_{H-B}$  against crack location for various slope inclinations and rock strength parameters.

### 4.3.3 Cracks of unspecified depth and location

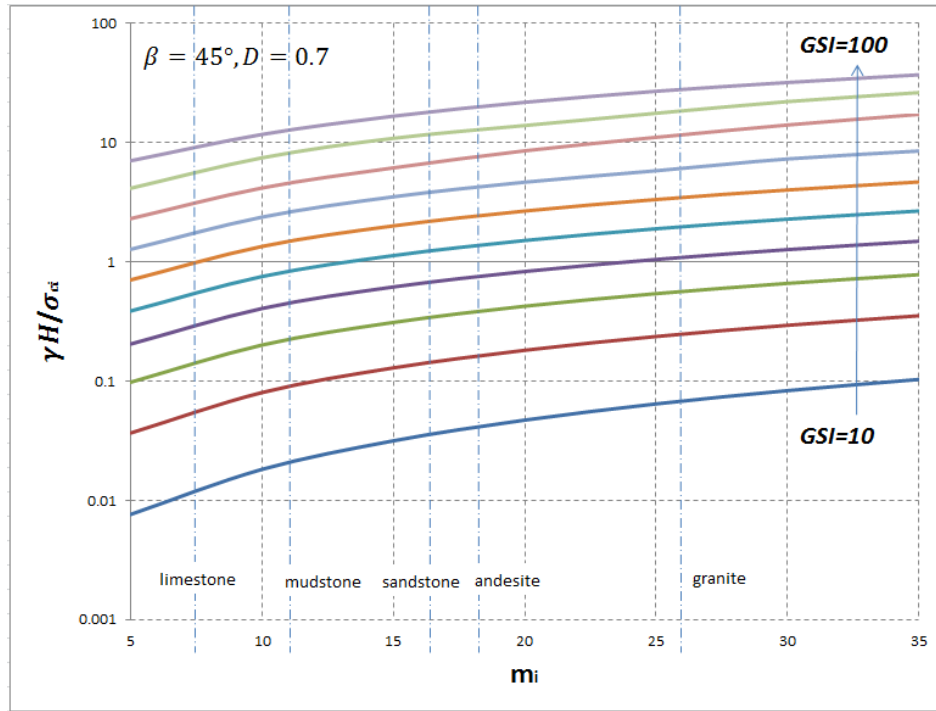
For the most common circumstances, when there is no information about the depth and the location of cracks, in order to search for the least upper bound solution, the stability factor  $N_{H-B}$  is minimized over all possible  $\theta_0, \theta_h, \beta', \eta$  and  $\phi_t$  under the constraint of  $\eta < \eta_{max}$ , maximum stable crack depth defined in Eq. (4-11). The

most adverse crack is defined as the one yielding the minimum value of the stability factor.

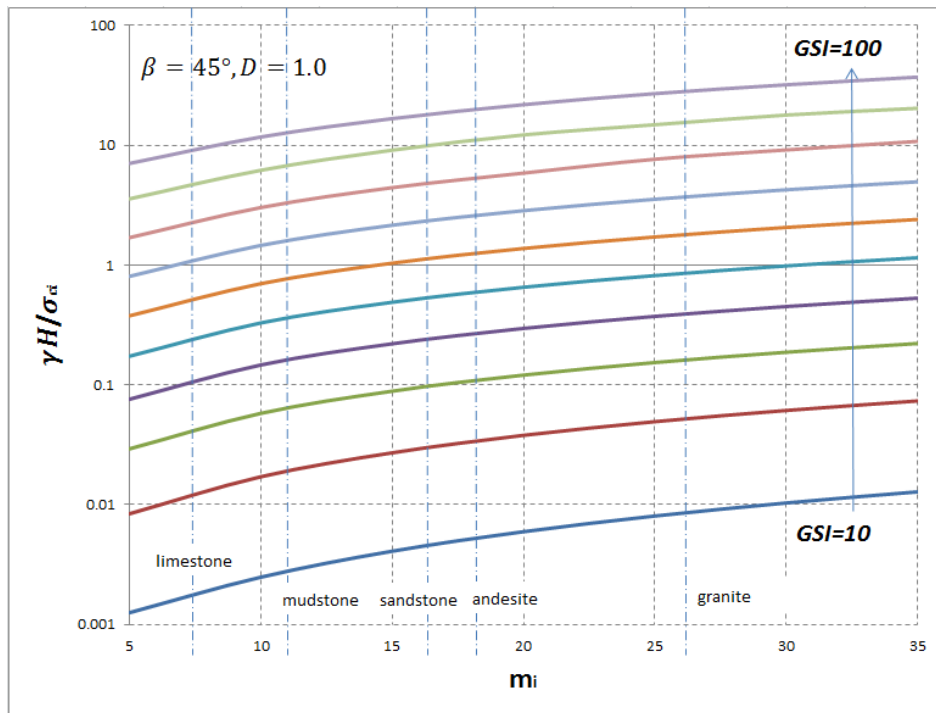
Stability charts corresponding to different inclinations ( $\beta = 45^\circ, 60^\circ, 75^\circ, 90^\circ$ ), different rock types,  $GSI$  and degree of fracture  $D$  are presented in Figure 4-6. The stability factors are found to increase when  $m_i$  or  $GSI$  increases. As expected, the stability factors decrease with a larger number of  $D$  (a higher level of disturbance).



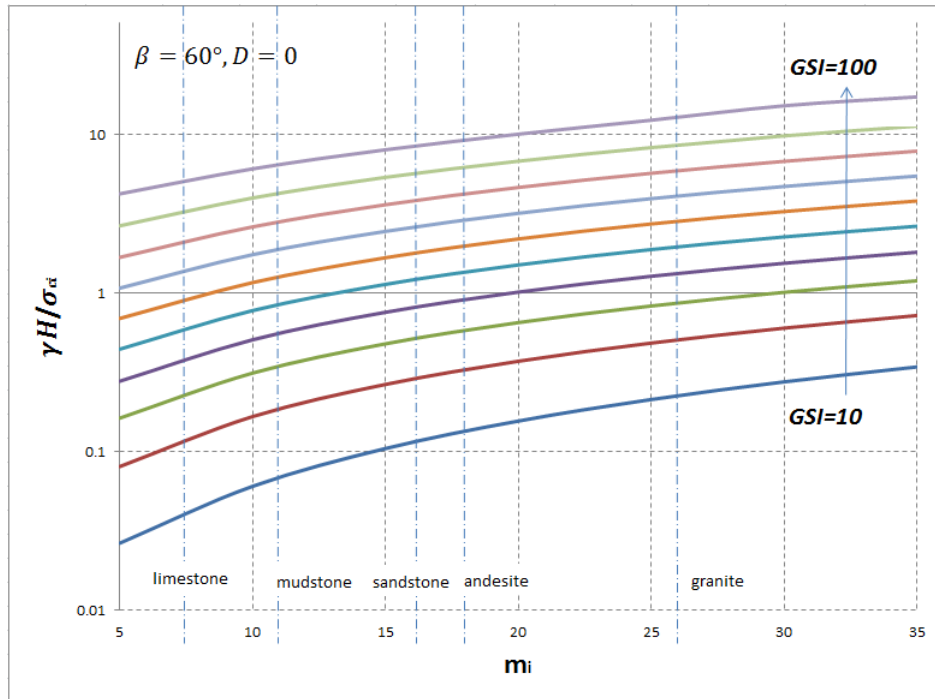
(a)  $\beta = 45^\circ, D = 0$



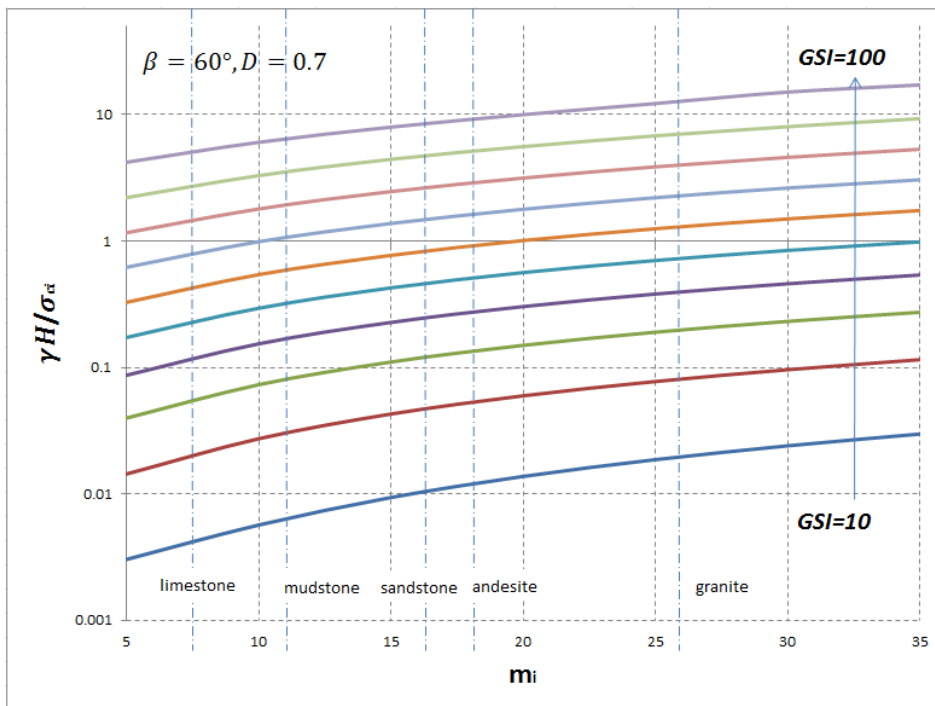
(b)  $\beta = 45^\circ, D = 0.7$



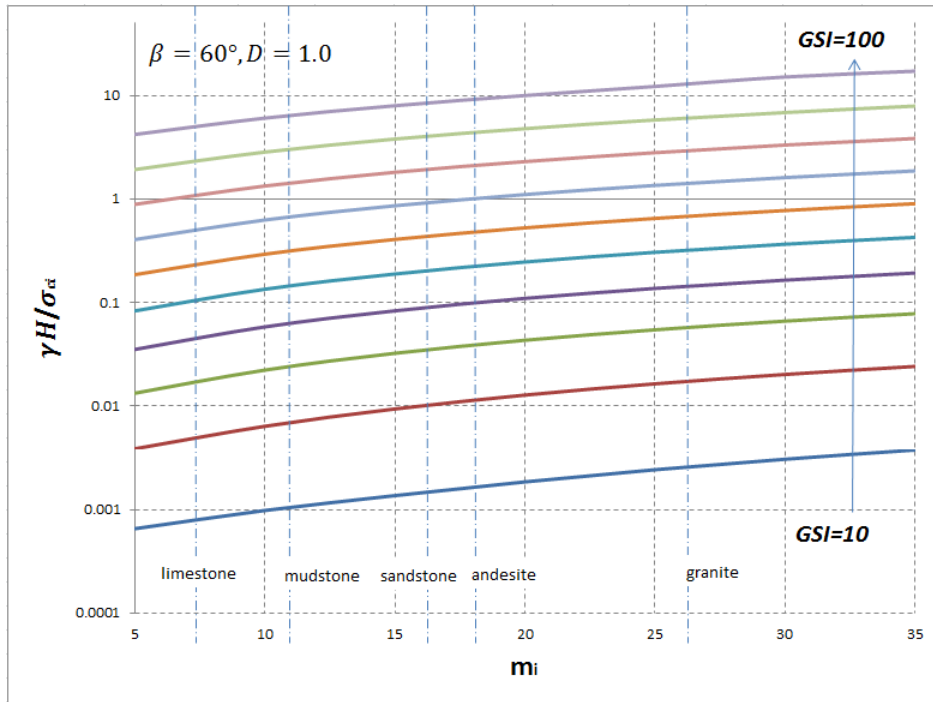
(c)  $\beta = 45^\circ, D = 1$



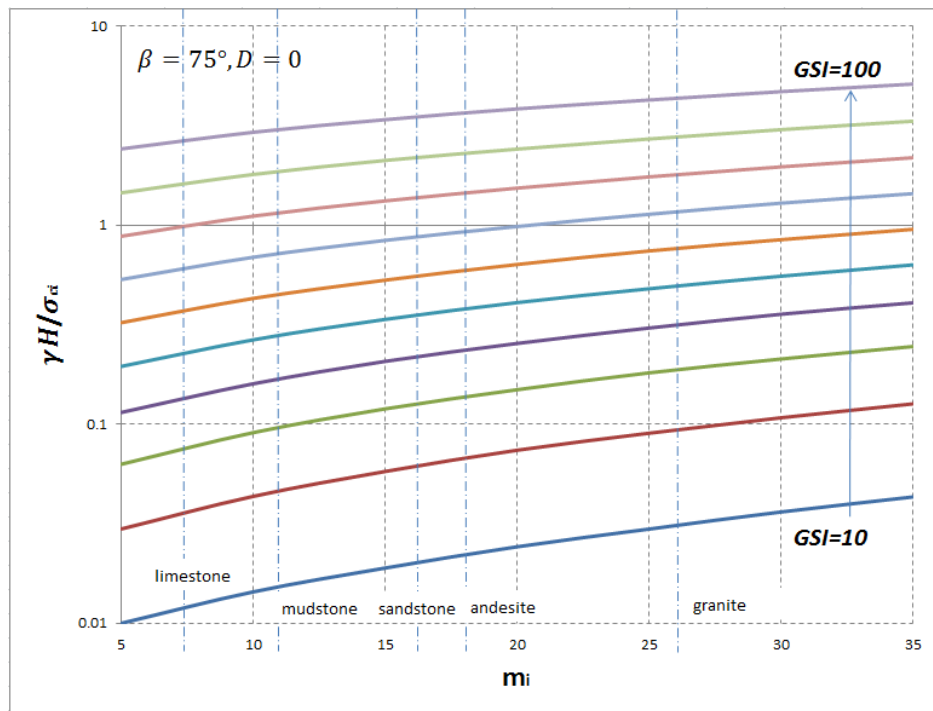
(d)  $\beta = 60^\circ, D = 0$



(e)  $\beta = 60^\circ, D = 0.7$

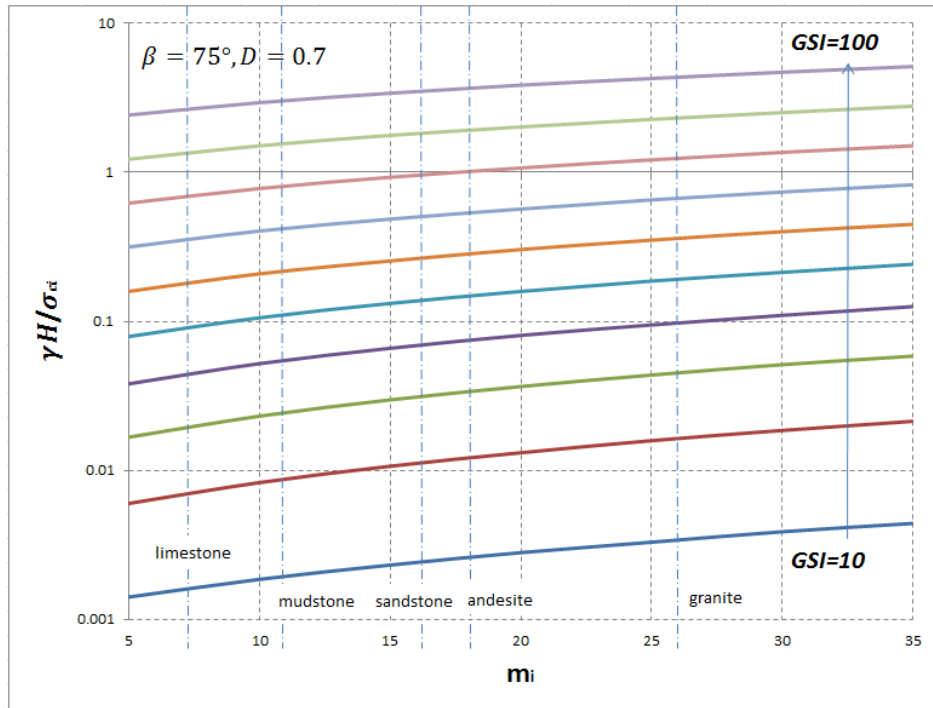


(f)  $\beta = 60^\circ, D = 1$

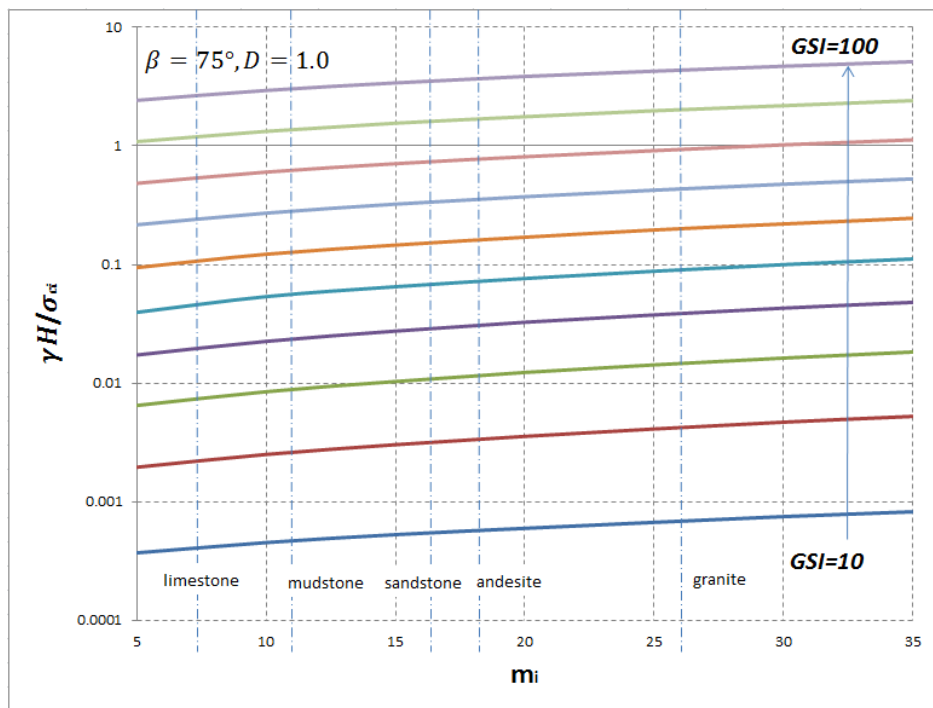


(g)  $\beta = 75^\circ, D = 0$

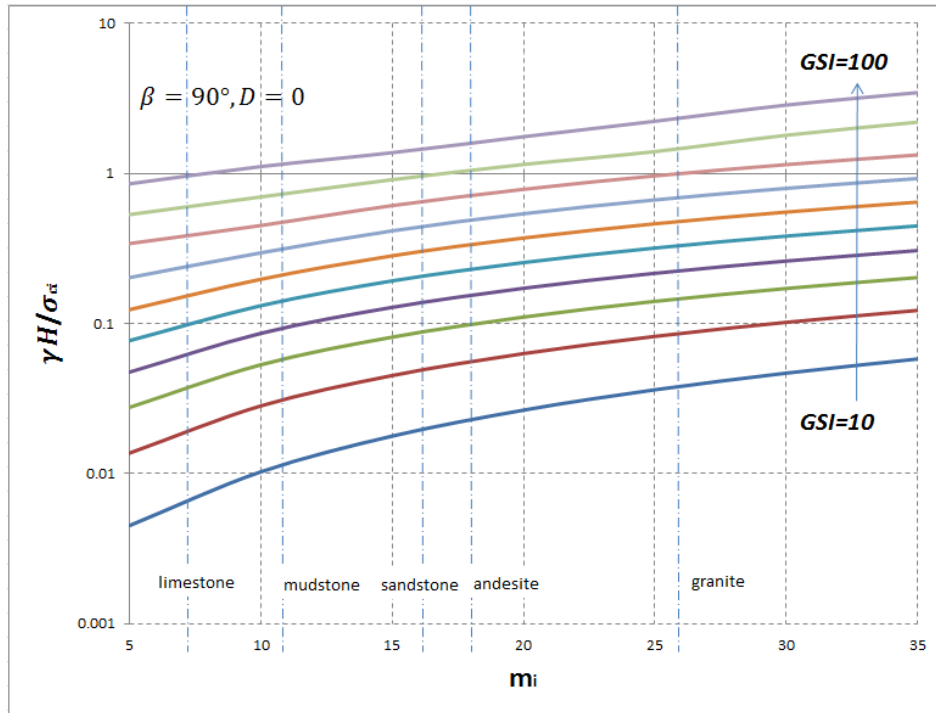




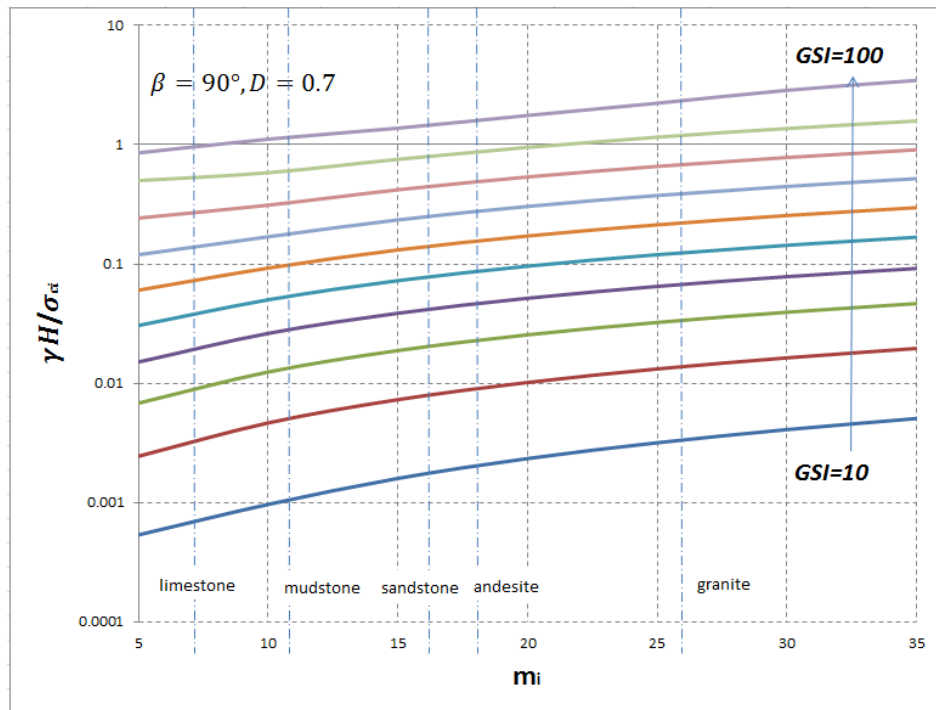
(h)  $\beta = 75^\circ, D = 0.7$



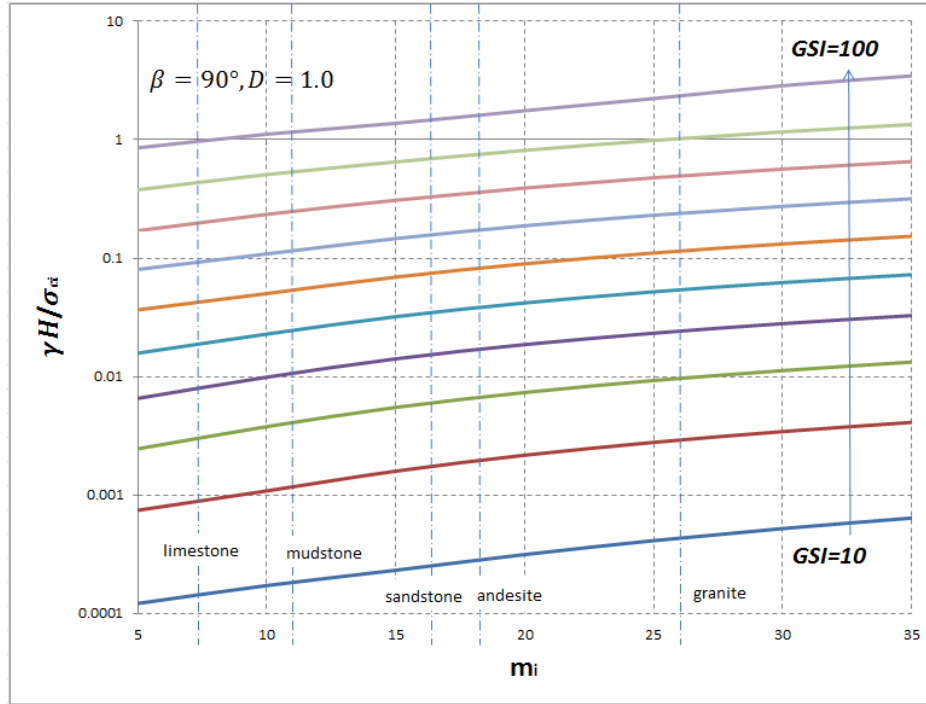
(i)  $\beta = 75^\circ, D = 1$



(j)  $\beta = 90^\circ, D = 0$



(k)  $\beta = 90^\circ, D = 0.7$



(I)  $\beta = 90^\circ, D = 1$

Figure 4-6. Stability charts for different slope inclination and various rock types.

#### 4.4 Equivalent $c - \phi$ method

The tangential method described in 4.1 is an ingenious way to tackle the non-linear failure criterion based on the classic limit analysis. However, since most geotechnical software is still written in terms of the Mohr-Coulomb failure criterion, it is necessary to determine equivalent cohesion  $c_e$  and friction angle  $\phi_e$  for rock mass obeying the Hoek-Brown failure criterion. This is done by fitting an average linear relationship to the curve generated by solving Eq. (4-1) for a range of minor principal stress values defined by  $\sigma_t < \sigma_3 < \sigma_{3max}$ , as illustrated in Figure 4-7.  $\sigma_{3max}$  is the upper limit of confining stress over which the relationship between the Hoek-Brown and the Mohr-Coulomb criteria is considered. As suggested by Hoek et al. (2002), the equivalent  $c_e$  and  $\phi_e$  ready to use as the Mohr-

Coulomb parameters are obtained by balancing the areas above and below the Mohr-Coulomb plot (see Figure 4-7):

$$\phi_e = \sin^{-1} \left[ \frac{3nm(s + m\sigma_{3n})^{n-1}}{(1+n)(2+n) + 3nm(s + m\sigma_{3n})^{n-1}} \right] \quad (4-13)$$

$$c_e = \frac{\sigma_{ci} \left[ (1+2n)s + (1-n)m\sigma_{3n} \right] (s + m\sigma_{3n})^{n-1}}{(1+n)(2+n) \sqrt{1 + \left[ 6nm(s + m\sigma_{3n})^{n-1} \right] / \left[ (1+n)(2+n) \right]}} \quad (4-14)$$

where  $\sigma_{3n} = \sigma_{3\max} / \sigma_{ci}$ .

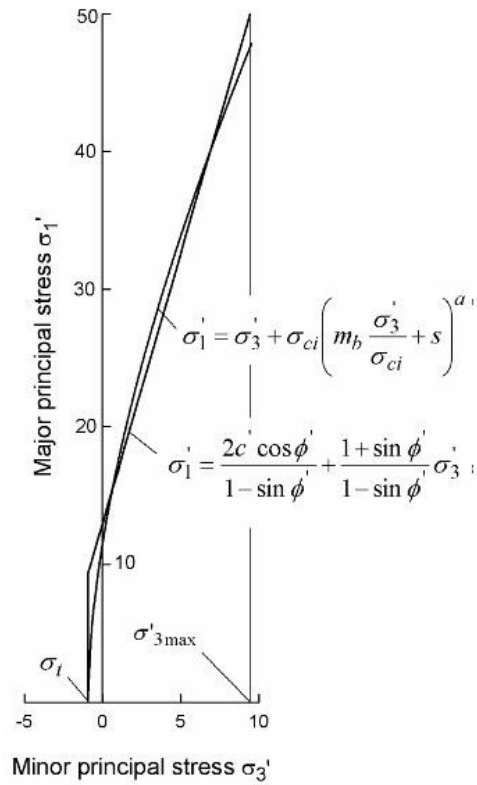


Figure 4-7. Relationships between major and minor principal stresses for the Hoek-Brown and the equivalent Mohr-Coulomb criteria (Hoek et al. 2002).

It should be noted that the value of  $\sigma_{3max}$  has to be determined for each particular case. For slope stability analyses,  $\sigma_{3max}$  is suggested by Hoek et al. (2002):

$$\frac{\sigma_{3max}}{\sigma_{cm}} = 0.72 \left( \frac{\sigma_{cm}}{\gamma H} \right)^{-0.91} \quad (4-15)$$

where  $H$  is the height of the slope,  $\sigma_{cm}$  is called the ‘global rock mass strength’ (see Hoek and Brown 1997) and is expressed as:

$$\sigma_{cm} = \frac{2c \cos \phi}{1 - \sin \phi} = \sigma_{ci} \frac{(m + 4s - n(m - 8s))(m / 4 + s)^{n-1}}{2(1 + n)(2 + n)} \quad (4-16)$$

However, the determination of  $\sigma_{3max}$  remains questionable. Slope inclination should affect  $\sigma_{3max}$  since the state of stress within the slope is a function of  $\beta$ . Li et al. (2008) conducted both numerical limit analysis and Bishop’s simplified method using the software *SLIDE* (Rocscience 2006) to propose two new expressions of  $\sigma_{3max}$ , where dependency on slope inclination is included:

$$\frac{\sigma_{3max}}{\sigma_{cm}} = 0.2 \left( \frac{\sigma_{cm}}{\gamma H} \right)^{-1.07} \quad (\text{steep slope } \beta \geq 45^\circ) \quad (4-17)$$

$$\frac{\sigma_{3max}}{\sigma_{cm}} = 0.41 \left( \frac{\sigma_{cm}}{\gamma H} \right)^{-1.23} \quad (\text{gentle slope } \beta \leq 45^\circ) \quad (4-18)$$

Once the equivalent  $c_e$  and  $\phi_e$  are obtained, the stability of slopes made of rock obeying the non-linear Hoek-Brown failure criterion can be assessed by the findings in Chapter 3.

#### 4.5 Variational approach, the combined method

Baker and Garber (1978) presented a variational approach to assess the stability of slopes made of geomaterials obeying the Mohr-Coulomb failure criterion. Soon afterwards, Baker (1981) extended the formulations to account for presence of tension cracks. Baker and Frydman (1983), Zhang and Chen (1987) and Chen and Liu (1990) went on to extend the approach by investigating the stability of slopes made of geomaterials obeying a general non-linear failure criteria. In this section, the combined method proposed by Chen and Liu (1990) is modified and developed to consider cracked slopes made of rock obeying the non-linear Hoek-Brown failure criterion.

It has been proven by variational calculus that the logarithmic spiral failure mechanism used in Chapter 3 and section 4.3 is the most critical failure surface for a rigid-body rotational sliding mechanism (Baker and Garber 1978; Chen 1975). However, this holds true only for geomaterials obeying the Mohr-Coulomb failure criterion. Fortunately, variational calculus is capable of solving the expression of most critical failure surface together with the stress distribution along it for a general non-linear failure criterion. For a slope with pre-existing cracks on its upper face, the geometry of the slope can be treated as an intact slope with extra weight of **AEDF** on the top (see Figure 4-8). Thus, the formulations given by Chen and Liu (1990) for intact slopes can be modified to evaluate the stability of cracked rock slopes for the Hoek-Brown failure criterion.

For an isotropic and homogeneous slope, a single rigid-body rotation along a surface of velocity discontinuity is considered. The generalized Hoek-Brown failure criterion (Hoek et al. 2002) can be written in terms of shear and normal stresses (see Eqs. (4-6) and (4-7)). By combining Eq. (4-6) and Eq. (4-7), yields:

$$\tau = \frac{\sigma_{ci} \cos \phi_t}{2} \left( \frac{m \cdot \frac{\sigma}{\sigma_{ci}} + s}{\frac{\sin \phi_t}{n} + 1} \right)^n = f(\sigma) \quad (4-19)$$

Considering the equilibrium of the rock mass *ABCDE* shown in Figure 4-8, the total virtual work of the sliding mass is:

$$Q = \dot{u}F_H + \dot{v}F_V + \dot{\Omega}F_M \quad (4-20)$$

where  $F_M$  is the resultant moment about the centre of rotation  $O$ ,  $F_H$ ,  $F_V$  are the resultant horizontal and vertical forces acting on the rigid body respectively.  $\dot{\Omega}$  is the rate of virtual rotation of the rigid body.  $\dot{u}$  and  $\dot{v}$  are the rates of horizontal and vertical virtual displacement to the reference point  $O$ . The expressions for  $F_H$ ,  $F_V$ ,  $F_M$  can be found in Chen and Liu (1990):

$$F_H = \int_{x_0}^{x_n} \left( \sigma \frac{dy}{dx} - \tau \right) dx \quad (4-21)$$

$$F_V = \int_{x_0}^{x_n} \left[ \gamma(y - \bar{y}) \sin \theta - \left( \sigma + \tau \frac{dy}{dx} \right) \right] dx \quad (4-22)$$

$$F_M = \int_{x_0}^{x_n} \left[ \left( \sigma + \tau \frac{dy}{dx} \right) x - (y - \bar{y}) \gamma x + \left( \sigma \frac{dy}{dx} - \tau \right) y \right] dx \quad (4-23)$$

with  $y(x)$  expressing the slip surface where  $\tau = f(\sigma)$  is satisfied.  $\sigma(x)$  and  $\tau(x)$  are normal and shear stress distribution along  $y(x)$ .  $x_0$  and  $x_n$  are start and end coordinates of  $y(x)$ .  $\bar{y}(x)$  describes the slope surface.

After rearranging, the total virtual work may be also written as:

$$Q = \dot{\Omega} \int_{x_0}^{x_n} F dx \quad (4-24)$$

where

$$F = \sigma \left[ \left( \frac{\dot{v}}{\dot{\Omega}} - x \right) - \left( \frac{\dot{u}}{\dot{\Omega}} + y \right) \frac{dy}{dx} \right] + \tau \left[ \left( \frac{\dot{v}}{\dot{\Omega}} - x \right) \frac{dy}{dx} + \left( \frac{\dot{u}}{\dot{\Omega}} + y \right) \right] - \gamma (y - \bar{y}) \left( \frac{\dot{v}}{\dot{\Omega}} - x \right) \quad (4-25)$$

According to the virtual work principle (Dym and Shames 1973), if a static equilibrium system is subjected to an arbitrary, kinematically admissible virtual displacement, the total virtual work done by both the external and internal force must be equal to zero. Then, the problem becomes a typical variational calculus issue: integral  $Q$  is stationary when its first variation vanishes. The Euler differential equations are used to obtain the necessary conditions expressing the requirement of stationary:

$$\frac{d}{dx} \left[ \frac{\partial F}{\partial \sigma'} \right] - \frac{\partial F}{\partial \sigma} + \lambda \frac{\partial G}{\partial \sigma} = 0 \quad (4-26)$$

$$\frac{d}{dx} \left[ \frac{\partial F}{\partial y'} \right] - \frac{\partial F}{\partial y} + \lambda \frac{\partial G}{\partial y} = 0 \quad (4-27)$$



where

$$y' = \frac{dy}{dx} = \frac{(r' \sin \theta + r \cos \theta)}{(r \sin \theta - r' \cos \theta)} \quad (4-28)$$

$$G(\sigma, \tau) = \tau - f(\sigma) = 0 \quad (4-29)$$

Two necessary conditions for finding the most critical solution are given by Baker and Frydman (1983) and Chen and Liu (1990), which provide both the expressions for the failure mechanism and the stress distribution along it:

$$\frac{dr}{d\theta} = r \frac{d\tau}{d\sigma} \quad (4-30)$$

$$\frac{d\sigma}{d\theta} + 2\tau - \gamma r \cos \theta = 0 \quad (4-31)$$

Eq. (4-31) can be rewritten as:

$$\frac{d\sigma}{d\phi_i} \frac{d\phi_i}{d\theta} + 2\tau - \gamma r \cos \theta = 0 \quad (4-32)$$

Eqs. (4-30) and (4-32) constitute a pair of differential equations for determining the most critical slip surface and its associated stress distribution. Using Eq. (4-19) and after solving the integral of Eq. (4-30), we obtain:

$$r = r_0 e^{\frac{n \sin 2\phi_i}{2(1 - \sin \phi_i)(n + \sin \phi_i)}(\theta - \theta_0)} \quad (4-33)$$

Referring to Eq. (4-7) and after rearranging (4-32), gives:

$$\frac{d\phi_t}{d\theta} = \frac{mn(n-1)(\sin \phi_t - 1) \left( \frac{2 \sin \phi_t}{mn - mn \sin \phi_t} \right)^{\frac{1}{1-n}} \times \left( \gamma r_0 e^{\frac{n \sin 2\phi_t}{2(1-\sin \phi_t)(n+\sin \phi_t)}(\theta-\theta_0)} \cos \theta - \sigma_{ci} \cos \phi_t \left( \frac{2 \sin \phi_t}{mn - mn \sin \phi_t} \right)^{\frac{n}{n-1}} \right) \tan \phi_t}{\sigma_{ci} (n + n \sin \phi_t + (n-1) \sin^2 \phi_t)} \quad (4-34)$$

The position of the entry point of the failure surface  $D(\theta_0)$  is a variable. According to Zhang and Chen (1987), the transversality condition of point  $D$  can be expressed as:

$$\sigma \cos \theta_0 + \tau \left( \sin \theta_0 + \cos \theta_0 \frac{\tan \phi_t \sin \theta_0 + \cos \theta_0}{\sin \theta_0 - \tan \phi_t \cos \theta_0} \right) = 0 \quad (4-35)$$

The combined method proposed by Chen and Liu (1990) adopts both the characteristics of the failure mechanism and stress distribution derived from variational calculus and kinematic approach in limit analysis. The expressions for the failure mechanism and the stress distribution are given in Eqs. (4-33) and (4-34). The least upper bound is achieved by a minimization procedure. In the following, the expression for the stability factor using the combined method is derived.



with  $f_1, f_2, f_4, f_U$  found in Eqs. (3-3)-(3-9). Dividing by  $\omega$  and  $r_0^2$  and rearranging, the stability factor  $\frac{\gamma H}{\sigma_{ci}}$  is obtained:

$$N_{VA} = \frac{\gamma H}{\sigma_{ci}} = \frac{f'_{d-\log} \times f_h}{f_1 - f_2 - f_3 - f_4 + f_U} \quad (4-38)$$

The most critical failure mechanism is still determined by minimizing Eq. (4-38) over four variables:  $\theta_0, \theta_h, \beta'$  and  $\eta$ .  $\phi_t$  at the entry point of the failure mechanism depends on the transversality condition in Eq. (4-35). However, since  $f'_{d-\log}$  is written in the form of an integral, it has to be solved by using numerical integration. According to Chen and Liu (1990), it is worth noting that the proposed combined method combines both the upper-bound and lower-bound methods together. Kinematic constraints, yield criterion and equilibrium equations are all satisfied.

## 4.6 Comparisons of results

In order to make comparisons among the results obtained from the tangential technique, equivalent  $c - \phi$  method and the variation approach, the critical heights of slopes in a same ground condition derived from all three methods are compared. The expressions of the critical heights are solved according to Eqs. (4-9), (3-14) and (4-38) in the following:

$$H_{\tan} = \frac{\sigma_{ci} N_{H-B}}{\gamma} \quad (4-39)$$

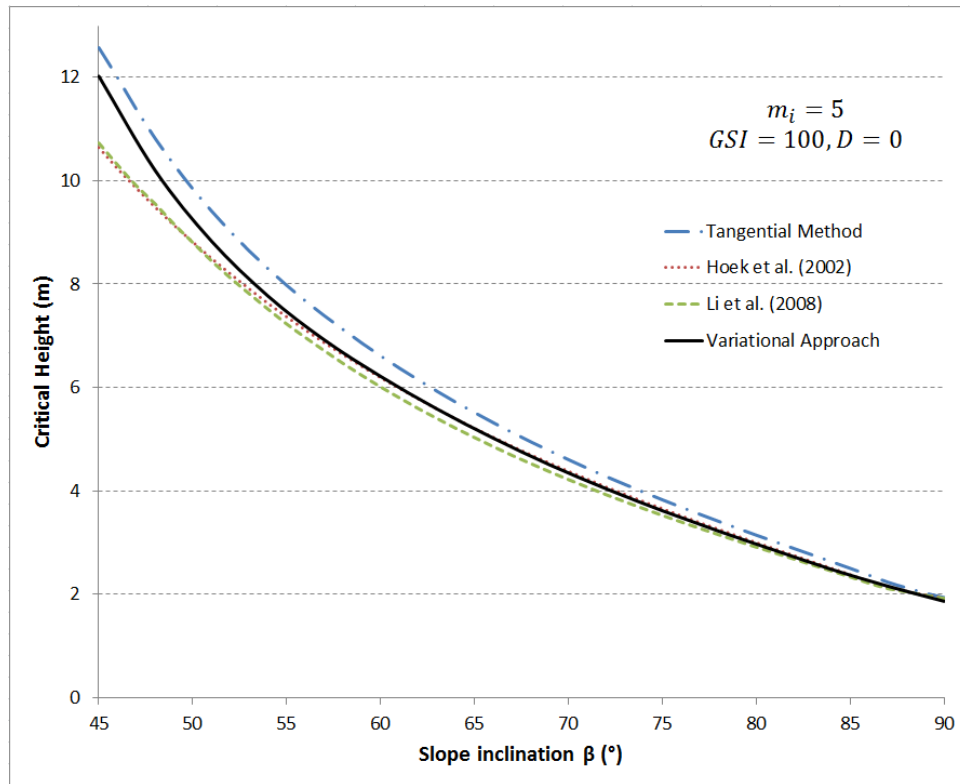
$$H_{eq} = \frac{c_e N_{M-C}}{\gamma} \quad (4-40)$$

$$H_{VA} = \frac{\sigma_{ci} N_{VA}}{\gamma} \quad (4-41)$$

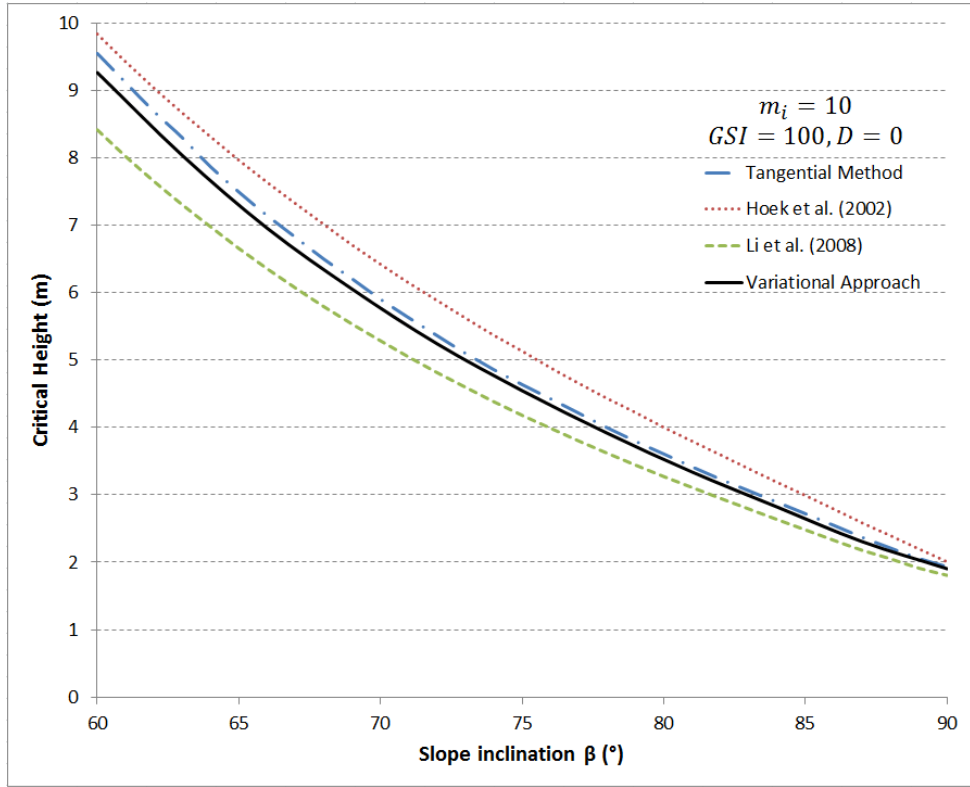
The equivalent cohesion  $c_e$  corresponding to a given set of  $m_i, GSI, D$  and  $\sigma_{ci}$  is used to replace  $c$  in Eq. (3-14). In addition,  $\gamma$  in Eqs. (4-40), (4-39) and (4-41) is assumed to be the same. Since  $c_e$  is dependent on the choice of slope height (in Eqs. (4-15), (4-17) and (4-18)), the critical height of  $H_{eq}$  has to be solved by an iterative procedure.

In Figure 4-9, slopes made of different rock type ( $m_i = 5, 10, 20, 30$ ;  $GSI = 20, 40, 60, 80, 100$ ) are investigated. The corresponding equivalent  $c_e$  and  $\phi_e$  are determined according to Hoek et al. (2002) (Eq. (4-15)) and Li et al. (2008) (Eqs. (4-17) and (4-18)) respectively. The most adverse pre-existing cracks are considered. The results of the critical heights ( $H_{tan}, H_{eq}, H_{VA}$ ) against slope inclinations are plotted and compared. Although the difference among all three methods evolves with different rock parameters, it can be observed that the critical heights obtained by the variational approach  $H_{VA}$  are always lower than those obtained by the tangential technique  $H_{tan}$  since the tangent method leads to overestimate the strength of rock mass. The biggest difference between  $H_{tan}$  and  $H_{VA}$  is 9.66% when  $m_i = 5, GSI = 20$ . With the increase of rock strength, the difference becomes less. On the other hand, the largest gap between  $H_{eq}$  (Li et al. 2008) and  $H_{VA}$  is 12.04%. The values of  $H_{eq}$  obtained according to Hoek et al. (2002) tend to overestimate the critical heights. The overestimation compared with  $H_{VA}$  can reach as high as 94.95% when  $m_i = 30, GSI = 100$ . The difference among all three methods becomes less obvious when slope inclination increases. Thus, both the tangential technique and the equivalent  $c - \phi$  method (Li et al. 2008) are good approximation to linearize Hoek-Brown failure envelope of the material, especially when slope inclination is high. These two methods are popular for their simplicity of use, while the applicability of the variational approach depends on the

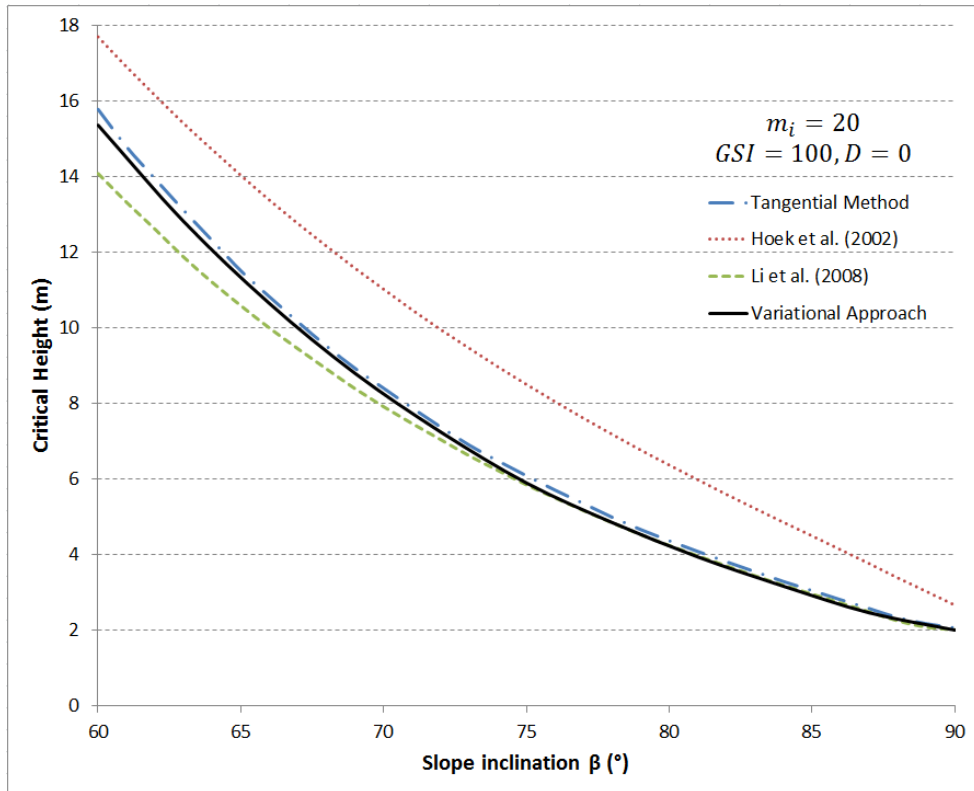
types of the slope geometry and external loadings. The equivalent  $c_e$  and  $\phi_e$  obtained from Hoek et al. (2002) are an overestimation of the strength of rock mass obeying the Hoek-Brown failure criterion for its independence on slope inclination and the adoption of the less rigorous Bishop circular slice method.



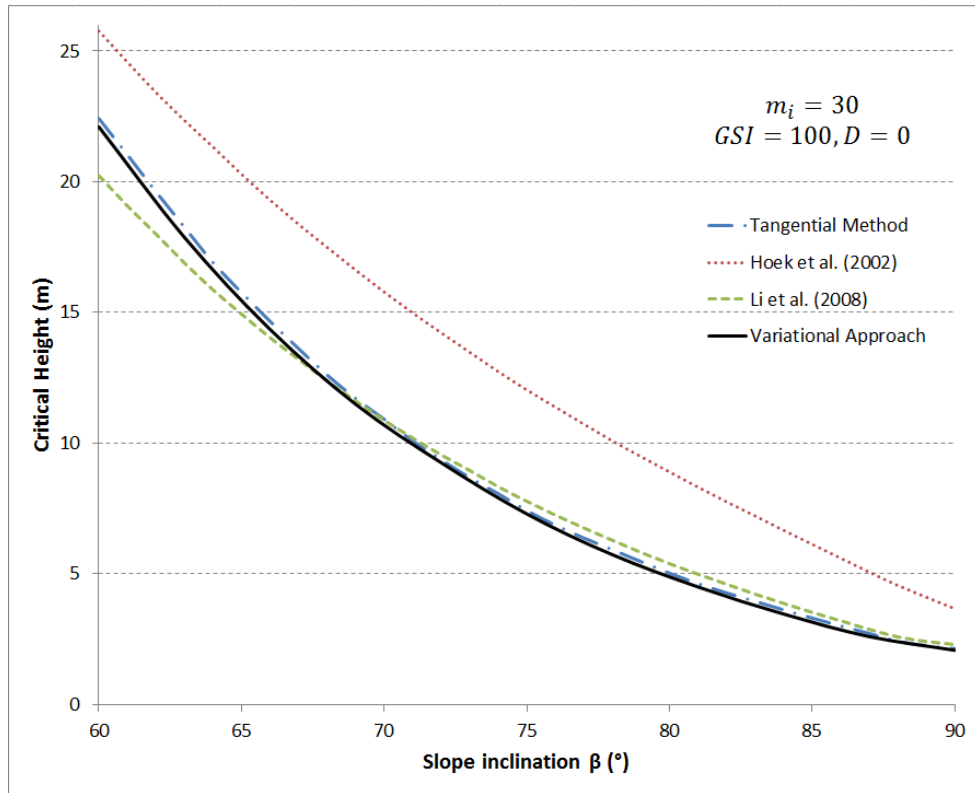
(a)  $m_i = 5, GSI = 100, D = 0$



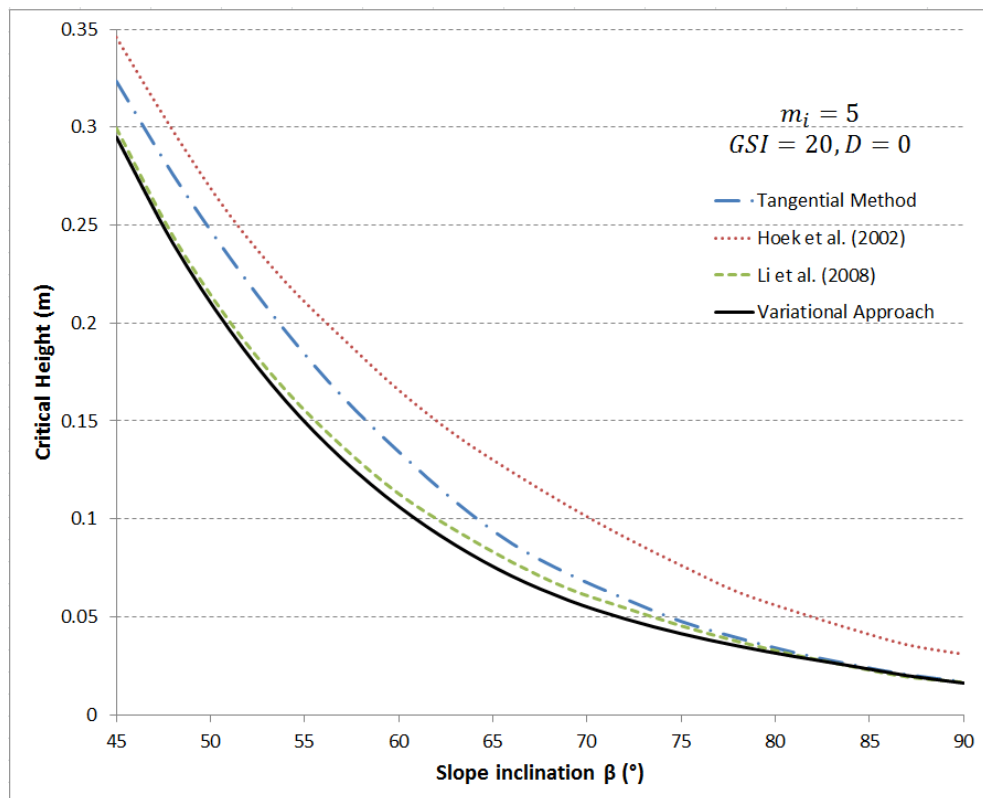
(b)  $m_i = 10, GSI = 100, D = 0$



(c)  $m_i = 20, GSI = 100, D = 0$

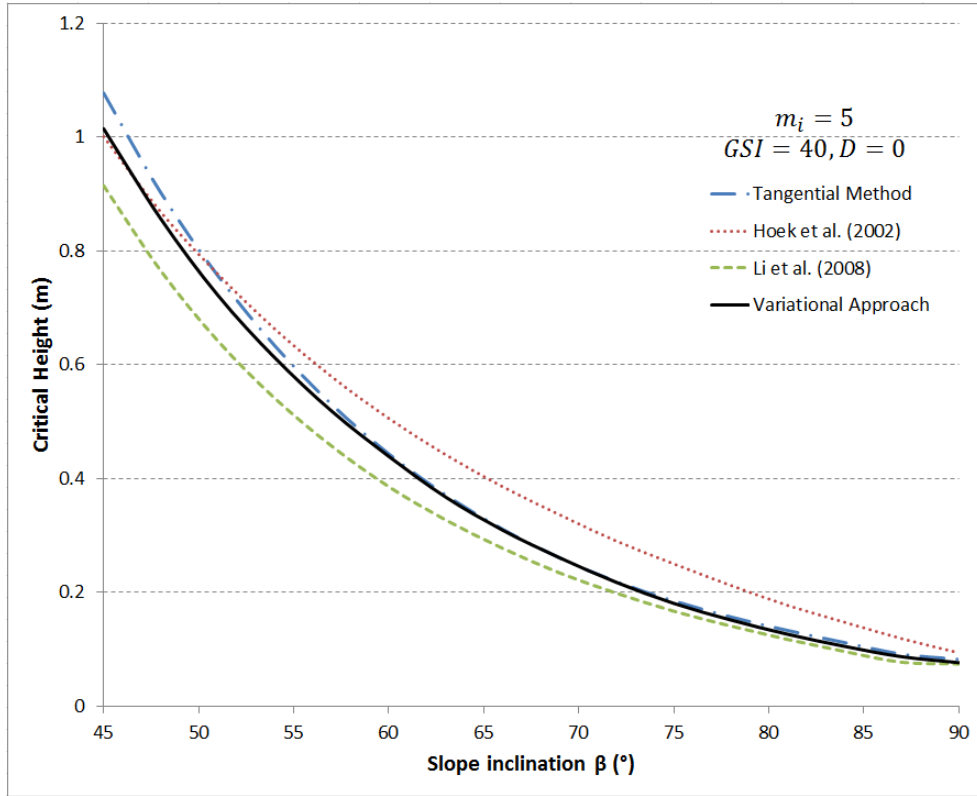


(d)  $m_i = 30, GSI = 100, D = 0$

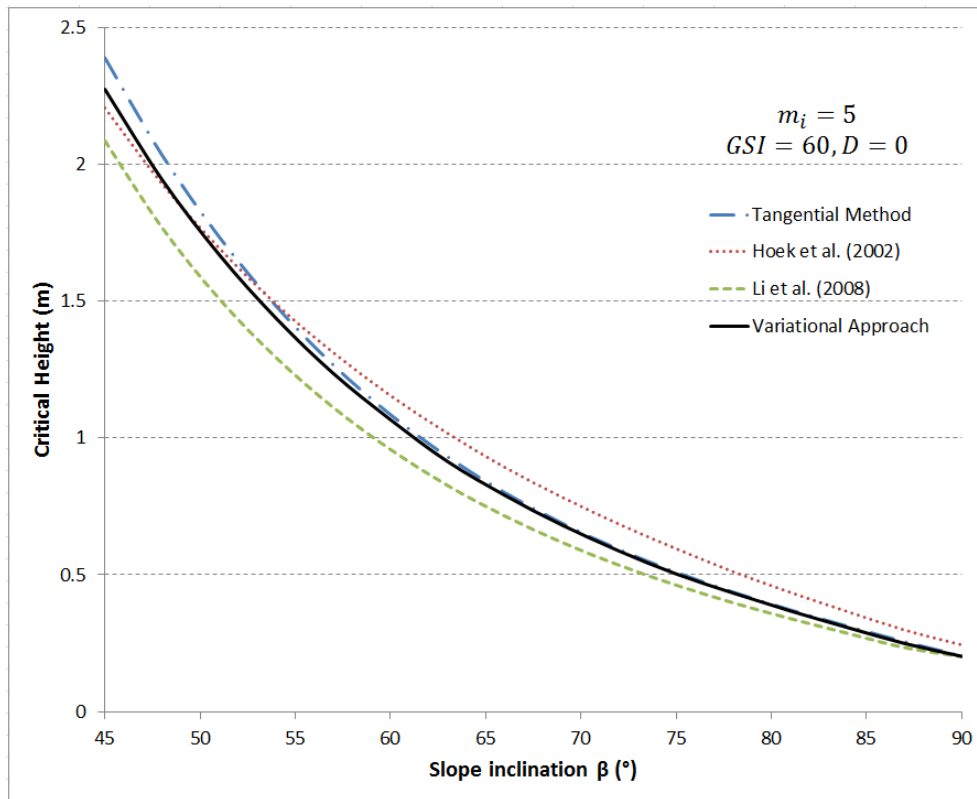


(e)  $m_i = 5, GSI = 20, D = 0$

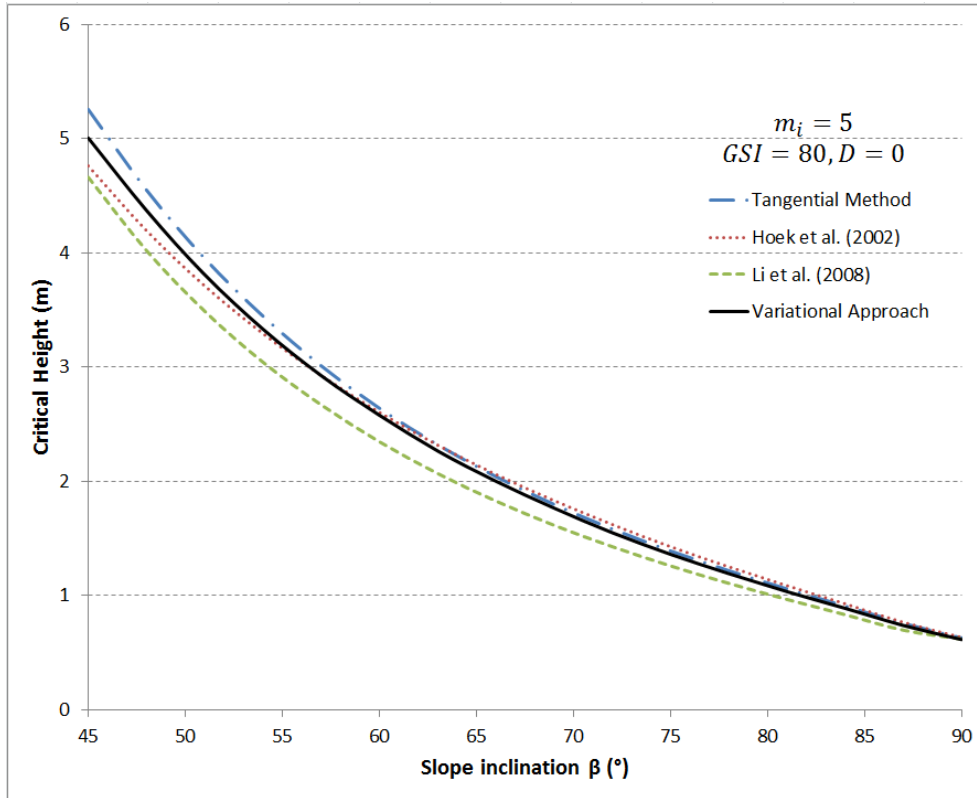




(f)  $m_i = 5, GSI = 40, D = 0$



(g)  $m_i = 5, GSI = 60, D = 0$



(h)  $m_i = 5, GSI = 80, D = 0$

Figure 4-9. Comparison among different methods.

## 4.6 Blast-induced non-homogeneity in rock slopes

Construction work (e.g., excavation and blasting) to create man-made slopes inevitably brings damage to the strength of geomaterials. In order to account for rock strength loss during construction, a disturbance factor  $D$  is defined in the Hoek-Brown failure criterion (see Eqs. (4-2) and (4-3)). It ranges from 0 for undisturbed in situ rock masses to 1 for very disturbed rock mass properties. In the previous section 4.1, a rock slope with a uniform  $D$  is considered. Stability charts considering different disturbance level ( $D = 0$ ,  $D = 0.7$  and  $D = 1.0$ ) are provided in Figure 4-6. In this section, the case of disturbance factor  $D$  varying linearly according to the distance to the excavation face is investigated.

To the best of the author's knowledge, due to the impact of different construction techniques, the quality of controlled blasting, the scale of overburden removal and the strength of the material, few studies have been able to unveil the distribution of the damage during a blasting excavation with general acceptance. It is suggested by Marinos et al. (2005) and Li et al. (2011) that disturbance factor  $D$  decreases as a linear function of the distance from the exposed slope, which is adopted in this section.

The disturbance coefficient  $D_d$  along the excavation face is assumed to be constant. The rock strength within the slope is somehow affected by blasting, but the damage is less compared with that on the excavation surface. The affected area due to blasting can be divided into three zones. In Zone 1, the disturbance factor  $D$  varies linearly along the horizontal direction, from  $D_d$  at the crest to  $D_i$  (the value for undamaged rock, in most cases  $D_i = 0$ ) at a distance of  $H$ . In Zone 2, the disturbance factor  $D$  varies linearly along a direction  $(\frac{\pi}{2} - \beta$  to the horizontal), from  $D_d$  on the slope face to  $D_i$  at a distance of  $H$  from the slope profile. In Zone 3, the disturbance factor  $D$  varies linearly with depth, from  $D_d$  on the surface to  $D_i$  at the depth of  $H \times \cos \beta$ .



where

$$y(\theta) = e^{\tan \phi(\theta_h - \theta_0)} \cdot \sin \theta_h - e^{\tan \phi(\theta - \theta_0)} \cdot \sin \theta \quad (4-43)$$

$$x(\theta) = e^{\tan \phi(\theta - \theta_0)} \cdot \cos \theta - e^{\tan \phi(\theta_h - \theta_0)} \cdot \cos \theta_h - \frac{H}{r_0} \left( \frac{1}{\tan \beta'} - \frac{1}{\tan \beta} \right) \quad (4-44)$$

The parameters for the Hoek-Brown failure criterion are no longer constant throughout the slope, but are functions of  $\theta$ . They can be written as:

$$m(\theta) = m_i \exp \left( \frac{GSI - 100}{28 - 14D(\theta)} \right) \quad (4-45)$$

$$s(\theta) = \exp \left( \frac{GSI - 100}{9 - 3D(\theta)} \right) \quad (4-46)$$

$$\begin{aligned} \frac{c_t(\theta)}{\sigma_{ci}} &= \frac{\cos \phi_t}{2} \left[ \frac{m(\theta)n(1 - \sin \phi_t)}{2 \sin \phi_t} \right]^{n/(1-n)} \\ &- \frac{\tan \phi_t}{m(\theta)} \left( 1 + \frac{\sin \phi_t}{n} \right) \left[ \frac{m(\theta)n(1 - \sin \phi_t)}{2 \sin \phi_t} \right]^{1/(1-n)} + \frac{s(\theta)}{m(\theta)} \tan \phi_t \end{aligned} \quad (4-47)$$

where  $n$  is defined in Eq. (4-4).

The tangential technique is employed to calculate the stability factor for non-homogenous rock slopes under blasting. The rate of the energy dissipation along the failure line  $\widehat{CD}$  is:

$$\int_{CD} c_t(\theta) \dot{u} \cos \phi_t \frac{rd\theta}{\cos \phi_t} = \omega r_0^2 \int_{\theta_0}^{\theta_h} c_t(\theta) e^{2 \tan \phi_t (\theta - \theta_0)} d\theta \quad (4-48)$$

Equating the rate of external work (defined in Eq. (3-2)) to the rate of energy dissipation, leads to:

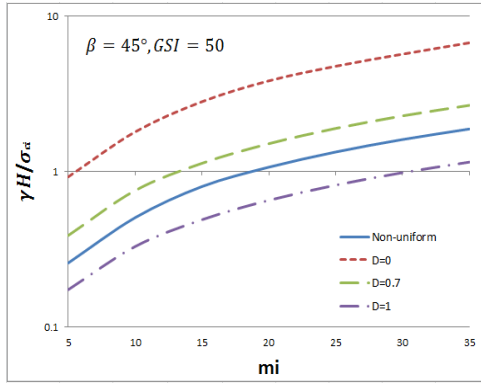
$$\omega \gamma r_0^3 (f_1 - f_2 - f_3 - f_4 + f_U) = \omega r_0^2 \int_{\theta_0}^{\theta_h} c_t(\theta) e^{2 \tan \phi_t (\theta - \theta_0)} d\theta \quad (4-49)$$

Dividing by  $\omega$  and  $r_0^2$  and rearranging, the stability factor considering the effect of blast-induced damage is obtained:

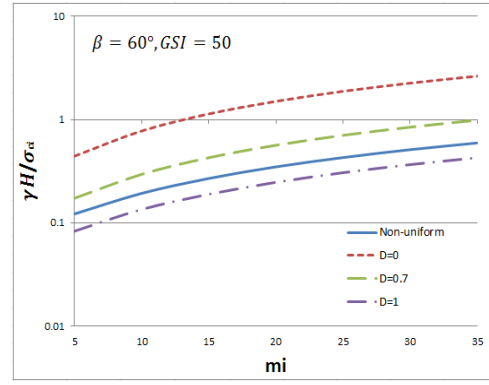
$$\frac{\gamma H}{\sigma_{ci}} = \frac{f_h}{f_1 - f_2 - f_3 - f_4 + f_U} \cdot \int_{\theta_0}^{\theta_h} \frac{c_t(\theta)}{\sigma_{ci}} \cdot e^{2 \tan \phi_t (\theta - \theta_0)} d\theta \quad (4-50)$$

The least upper bound solution is obtained by minimizing Eq. (4-50). The most critical failure mechanism is still determined by four variables:  $\theta_0$ ,  $\theta_h$ ,  $\beta'$  and  $\eta$ . Numerical integration is required to solve the integral in Eq. (4-50).

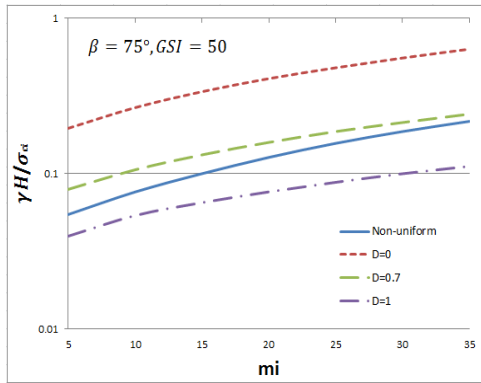
In Figure 4-11, the stability factors corresponding to both uniform rock slopes ( $D = 0, D = 0.7, D = 1$ ) and non-homogeneous rock slopes under blasting ( $D_i = 0, D_d = 1$ ) are plotted against different  $m_i$  for slope inclinations  $\beta = 45^\circ, 60^\circ, 75^\circ$  and  $90^\circ$ . The stability factors of non-uniform slopes are bracketed between those of uniform slopes with  $D = 0.7$  and  $D = 1$ .



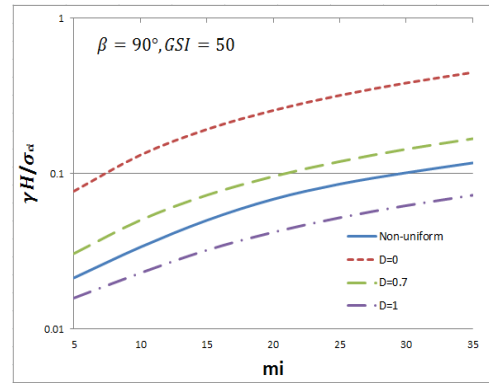
(a)  $\beta = 45^\circ, GSI = 50$



(b)  $\beta = 60^\circ, GSI = 50$



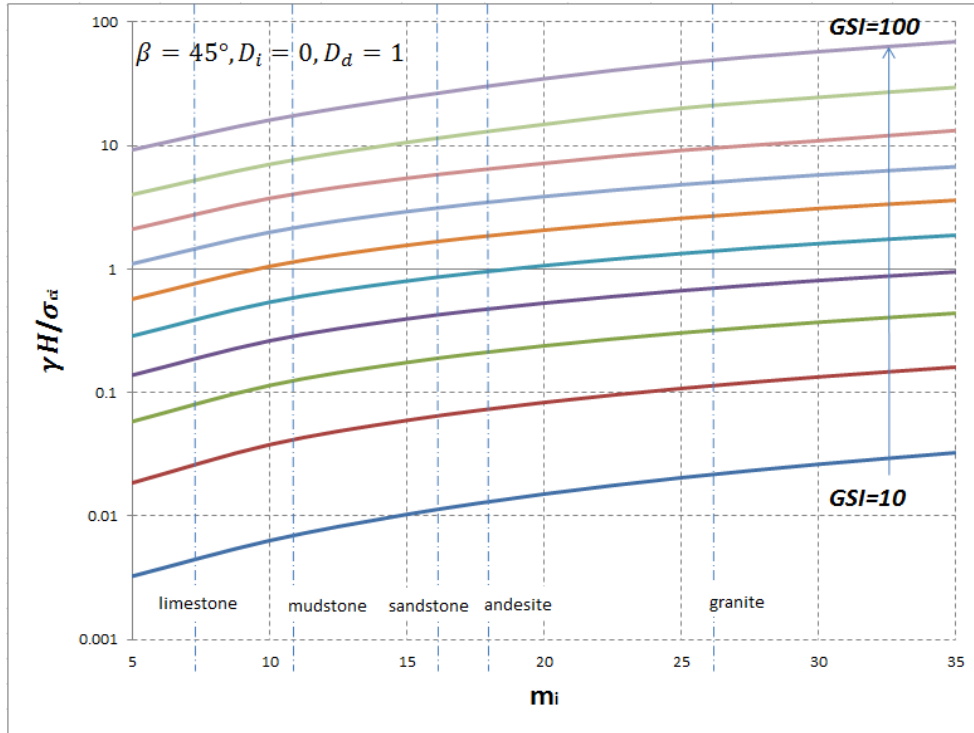
(c)  $\beta = 75^\circ, GSI = 50$



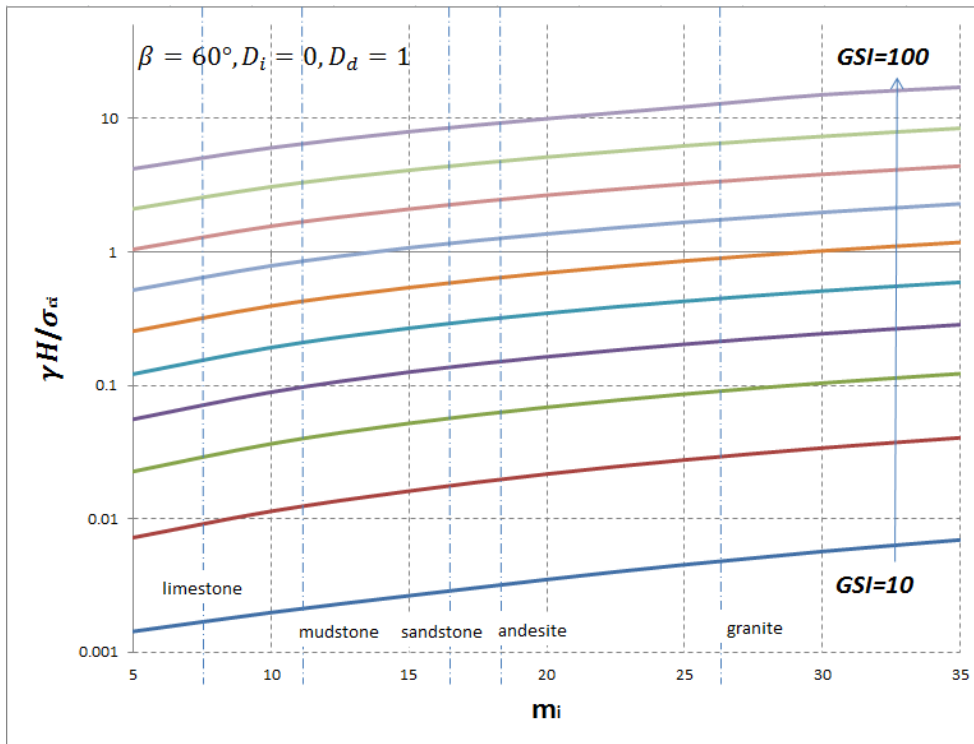
(d)  $\beta = 90^\circ, GSI = 50$

Figure 4-11. Stability factors against  $m_i$  for uniform and non-uniform ( $D_i = 0, D_d = 1$ ) slopes.

Stability charts corresponding to different  $m_i$  and various values of  $GSI$  considering linearly varying disturbance factor ( $D_i = 0, D_d = 1$ ) are also provided in Figure 4-12.

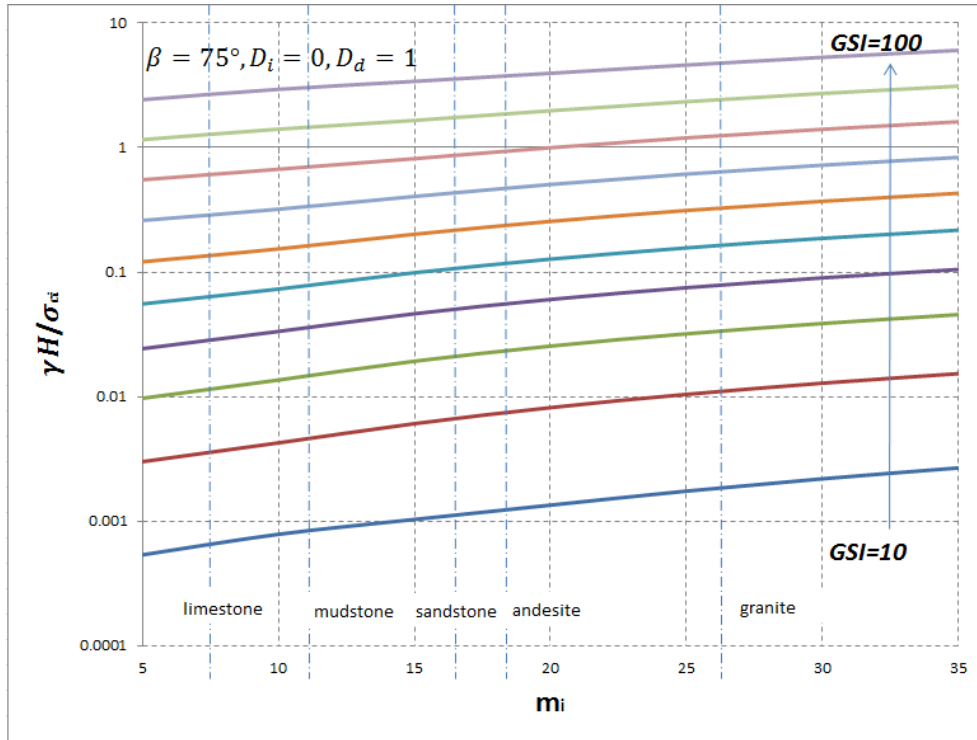


(a)  $\beta = 45^\circ, D_i = 0, D_d = 1$

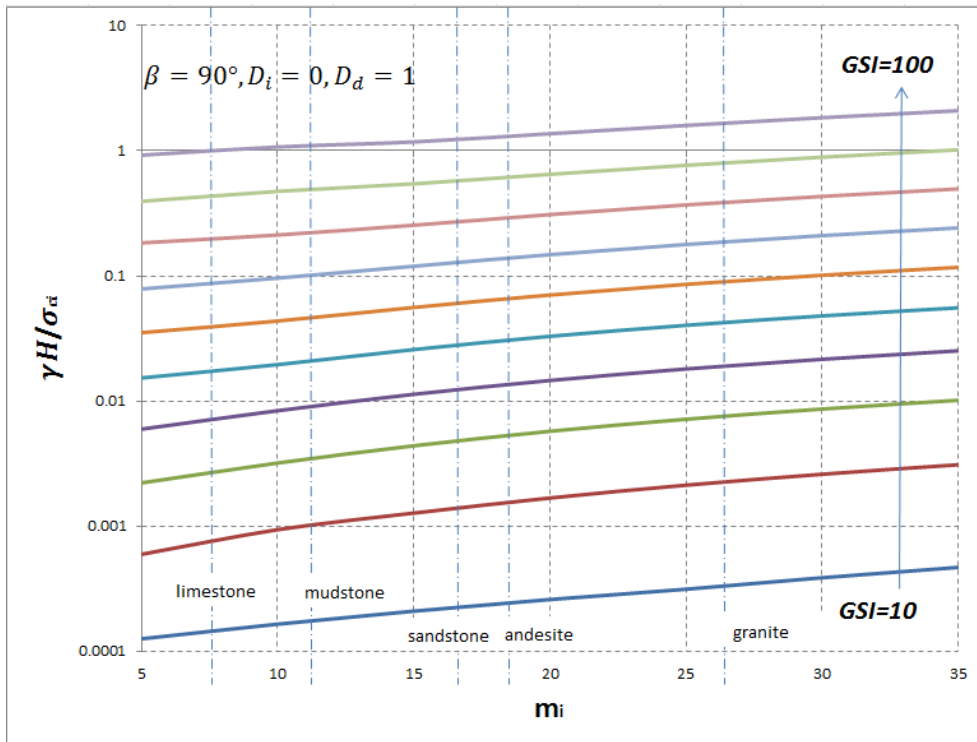


(b)  $\beta = 60^\circ, D_i = 0, D_d = 1$





(c)  $\beta = 75^\circ, D_i = 0, D_d = 1$



(d)  $\beta = 90^\circ, D_i = 0, D_d = 1$

Figure 4-12. Stability charts for various rock types considering linearly varying disturbance factor.

## 4.7 Conclusions

In this chapter, the stability of cracked slopes made of rock obeying the non-linear Hoek-Brown failure criterion was investigated using three methods (i.e., tangential technique, equivalent  $c - \phi$  method and variational approach). In addition, the safety analyses of non-homogeneous slopes under blasting are studied. The following conclusions can be drawn:

(a) The results obtained by the tangential technique are still upper bound solutions, which is an overestimation of the material strength and the safety of slopes. Compared with the more rigorous (both equilibrium equations and kinematic constraints are satisfied, see Chen and Liu 1990) variational approach, it is important to learn the difference of results between these two methods. It was reported by Drescher and Christopoulos (1988) that the adoption of the tangential technique only overestimates the stability factor of slopes made of geomaterials obeying the power-law failure criterion by less than 1%. However, it is illustrated in section 4.6 that the disparity between the tangential technique and the variational approach for the Hoek-Brown failure criterion can be as high as 9.66% when the rock mass is weak. Nevertheless, the application of the tangential technique is still an acceptable and convenient tool for evaluating the stability of slopes for the Hoek-Brown failure criterion. It is worth noting that the use of the equivalent  $c - \phi$  method according to Li et al. (2008) yields satisfactory results, with the biggest difference being 12.04% for low  $GSI$  values.

(b) The minimization process in finding the least upper bound for the stability factor defined in Eqs. (4-9) and (4-50) has to be conducted under the constraint of  $-\frac{s}{m} < \frac{\sigma}{\sigma_{ci}} < 1$  to avoid unrealistic selection of  $\phi_t$ . However, Collins et al. (1988) and Yang et al. (2004) overlooked the constraint and arrived at some unrealistic results, e.g., Table II in Collins et al. (1988) and Table II in Yang et al. (2004). The

critical heights obtained from these two papers can be more than 50% less than those from Hoek et al. (2002) and Li et al. (2008).

(c) The analytical upper bound formulation for rock slopes subject to blast-induced damage (disturbance factor  $D$  varying linearly according to the distance to the excavation face) was derived for the first time.

## Chapter 5 Optimal Profiles of Slopes

The optimal profile of a slope whose crest and toe are fixed points in space is investigated by means of the kinematic approach of limit analysis. The optimal profile is here defined as the shape corresponding to maximum stability, i.e., the stability factor of the optimal shape is the highest among any shape satisfying the set geometrical constraint imposed (the position of the toe and crest). With the discretization of slope profile, the stability factors of slopes of any arbitrary shapes are derived. Two different optimization algorithms, i.e., genetic algorithm and pattern search are employed for locating the optimal profile. The results obtained from the proposed kinematic formulation are compared with previous analytical solutions and validated through the displacement-based finite element method and finite element limit analysis. In addition, since the new upper bound formulation is capable of computing the stability factors of slopes of any arbitrary shape, the stability of a slope whose shape is varying during excavation process can be assessed. Moreover, the influence of the presence of pre-existing cracks, non-homogeneity and anisotropy of the ground on the optimal profiles is studied. Finally, the optimal profiles corresponding to slopes made of rock obeying the Hoek-Brown failure criterion are investigated. Special consideration is given in the discussion to the blast-induced damage.

### 5.1 Introduction

In nature, slopes present different shapes, such as concave, convex and S-shaped profiles (see Figure 5-1). In a variety of geotechnical problems concerning slope stability such as the design of embankments and open cast mines, man-made slopes are excavated. It is important to optimize the shape of slope profile in order to

maximize slope stability under certain geometry constraints. For instance, when the allowable height ( $H$ ) and width ( $L$ ) of an excavation are assigned, i.e., slope crest and toe are fixed points, the planar profile  $AC$  (see Figure 5-2) is widely adopted in engineering practice, but it has been proved not to be the best one in terms of stability (Hoek and Bray 1981; Utili and Nova 2007; Jeldes et al. 2013; Jeldes et al. 2014).

There is limited literature about the stability of non-planar slopes. Jenike and Yen (1962) presented the results of slope stability analyses in axial symmetry using the slip-line theory formulated by Sokolovskiĭ (1960). They found out that S-shaped critical profiles are able to describe the theoretical failure shape. Hoek and Bray (1981) argued for plain strain slopes that concave slopes are more stable than convex slopes. However, they did not produce any detailed investigation to underpin their claim.

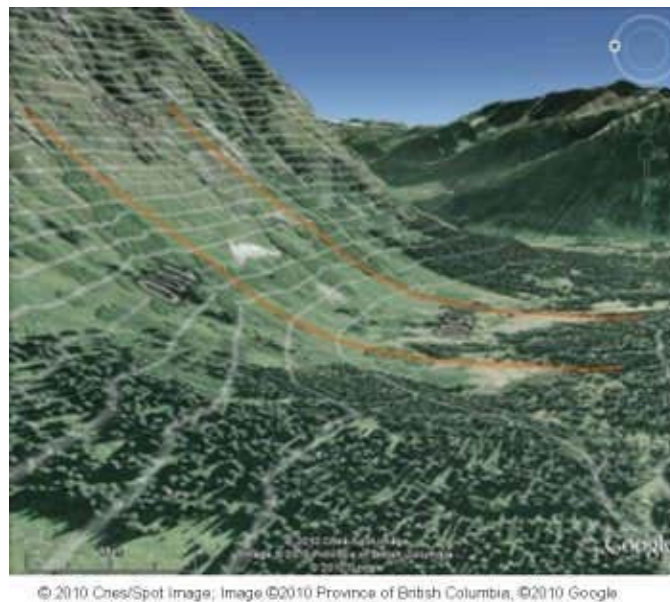
Considering logarithmic spiral curves only, Utili and Nova (2007) derived a new upper bound limit analysis formulation to compute the external work made by the weight of a double logarithmic spiral shaped soil region sliding away. The optimal logarithmic spiral profiles were determined by maximizing the stability factor  $\frac{\gamma H}{c}$ . Compared with slopes with planar profile, the percentage of increase provided by the best spiral in terms of stability factor can reach as high as 30.5% (depending on the ground properties).

Theoretical and experimental findings (such as Stefano et al. 2000, Rieke-Zapp and Nearing 2005) seem to indicate that slopes of concave profiles are more capable of resisting erosion. Therefore, based on the optimal profiles found for weightless and frictionless slopes by Sokolovskiĭ (1960) and Sokolovskii (1965), Jeldes et al. (2013) and Jeldes et al. (2014) derived an approximate solution for slopes with  $\gamma > 0$  and  $\phi > 0$  to determine the geometry of optimal concave slopes,

having restricted the choice of slope profiles to a certain class compatible with the slip line method requirements (see Sokolovskii, 1965).

The above studies attempted to find the best slope profile among certain pre-determined classes of shapes, but none of them considered the more general and fundamental problem of determining the optimal profile of a slope of any arbitrary shape. Moreover, the analyses of previous authors are limited to some restricted slope features. This is the first study to systematically attempt to find the most stable slope shape for various geometrical constraints and ground properties.

In this chapter, the optimal profile of a slope is investigated by means of the kinematic approach of limit analysis. The slope is treated as a continuum obeying the Mohr-Coulomb failure criterion (soil slope) or the Hoek-Brown failure criterion (rock slope). By discretizing the slope face into several linear piece-wise points, slopes of any arbitrary profiles can be examined (see Figure 5-3). Two global optimization techniques, i.e., genetic algorithm and pattern search are adopted to search for the optimal profile.



(a) A concave slope in Canada



(b) Wave rock (convex slope) in Perth, Western Australia



(c) A S-shaped slope in Rio de Janeiro, Brazil

Figure 5-1. Slopes of different shapes.



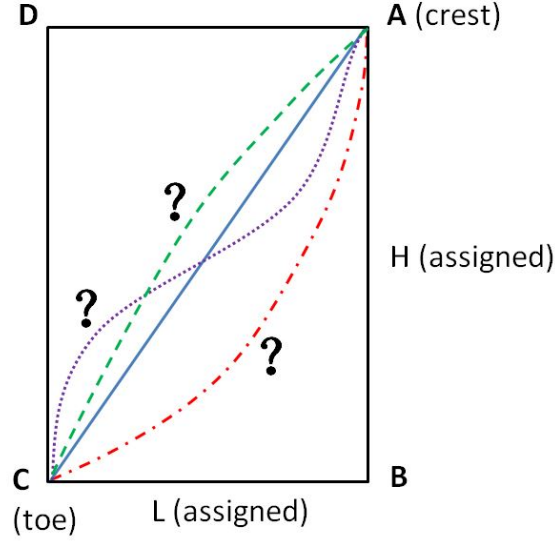


Figure 5-2. Different slope profiles under given geometry constraints.

## 5.2 Upper bound formulation for a slope of an arbitrary profile

In the following, the upper bound formulation for a slope of an arbitrary profile under the constraint of fixed crest and toe is specified. By fixing these two points, the average slope inclination  $\beta = \arctan \frac{H}{L}$  is prescribed. No other geometrical constraint on the slope profile is imposed. The stability factor, defined as  $\frac{\gamma H}{c}$ , corresponding to a given slope of an arbitrary shape is determined by the discretization of the slope profile. In Figure 5-3, the rectangle region of  $ABCD$  is discretized into  $n$  horizontal rows. For each horizontal line  $M_i Q_i$ , a nodal point  $P_i$  lies between  $M_i$  and  $Q_i$ .  $k_i$  is here defined as  $k_i = \frac{P_i Q_i}{M_i Q_i} = \frac{P_i Q_i}{L}$ , with  $0 \leq k_i \leq 1$ ,  $i = 1, 2, 3 \dots n + 1$ .  $k_i$  gives the relative position of  $P_i$  on  $M_i Q_i$  and can be regarded as the coordinate of  $P_i$  on  $M_i Q_i$ . Slope profile  $\widehat{AC}$  is represented by piecewise linearization through all the nodal points  $P_i$  on each horizontal line  $M_i Q_i$ . By increasing  $n$ , the discretization of the slope profile becomes more refined. In order



to seek the optimal profile, under the constraint of fixed crest and toe, by changing  $k_i$  on each horizontal line, slopes with different shapes are to be examined. Among all candidate profiles, the optimal one provides the highest stability, which corresponds to the largest stability factor having fixed ground properties. Considering the slope under investigation is made of a homogeneous rigid perfectly plastic continuum, obeying the Mohr-Coulomb failure criterion, the mass **ACFE** rigidly sliding away about the centre of rotation **O**, the validity of the normality flow rule of the material is assumed to hold true and  $\widehat{EF}$  is assumed to be a logarithmic spiral failure line. It is important to point out that the logarithmic spiral failure line is the most critical failure mechanism within the framework of the kinematic approach of limit analysis regardless of slope shapes (Chen 1975, Baker and Garber 1978, Baker and Frydman 1983, Zhang and Chen 1987). The following geometrical relationships are obtained according to Figure 5-3:

$$r_h = r_0 e^{\tan \phi (\theta_h - \theta_0)} \quad (5-1)$$

$$\beta = \arctan \left( \frac{H}{L} \right) \quad (5-2)$$

$$\frac{H}{r_0} = \frac{\sin \beta'}{\sin(\beta' - \alpha)} \left[ e^{\tan \phi (\theta_h - \theta_0)} \sin(\theta_h + \alpha) - \sin(\theta_0 + \alpha) \right] = f_H(\theta_0, \theta_h) \quad (5-3)$$

$$\begin{aligned} \frac{L_0}{r_0} &= \frac{\sin(\theta_h - \theta_0)}{\sin(\theta_h + \alpha)} \\ &- \frac{\sin(\theta_h + \beta')}{\sin(\theta_h + \alpha) \sin(\beta' - \alpha)} \left[ e^{\tan \phi (\theta_h - \theta_0)} \sin(\theta_h + \alpha) - \sin(\theta_0 + \alpha) \right] \end{aligned} \quad (5-4)$$

where  $\phi$  is the friction angle at failure,  $L_0$  is the length of  $\mathbf{AE}$ . The rate of work done by the weight of  $\mathbf{ACFE}$  is calculated as the work done by the fictitious weight of the region  $\mathbf{OEF}$  ( $\dot{W}_1$ ) minus the work done by the fictitious weight of the regions  $\mathbf{OEA}$  ( $\dot{W}_2$ ),  $\mathbf{OAC}$  ( $\dot{W}_{3,n}$ ) and  $\mathbf{OCF}$  ( $\dot{W}_4$ ). Therefore, the total rate of external work due to the material weight is expressed as:

$$\dot{W}_\gamma = \dot{W}_1 - \dot{W}_2 - \dot{W}_{3,n} - \dot{W}_4 = \omega \gamma r_0^3 (f_1 - f_2 - f_{3,n} - f_4) \quad (5-5)$$

The expressions of  $\dot{W}_1$  and  $\dot{W}_2$  are found in Chen (1975), and here only the final expressions are given:

$$\begin{aligned} \dot{W}_1 &= \omega \gamma r_0^3 \frac{e^{3 \tan \phi (\theta_h - \theta_0)} (3 \tan \phi \cos \theta_h + \sin \theta_h) - 3 \tan \phi \cos \theta_0 - \sin \theta_0}{3(1 + 9 \tan^2 \phi)} \\ &= \omega \gamma r_0^3 f_1(\theta_0, \theta_h) \end{aligned} \quad (5-6)$$

$$\dot{W}_2 = \omega \gamma r_0^3 \left[ \frac{1}{6} \sin(\theta_0 + \alpha) \frac{L_0}{r_0} \left( 2 \cos \theta_0 - \frac{L_0}{r_0} \cos \alpha \right) \right] = \omega \gamma r_0^3 f_2(\theta_0, \theta_h, \beta') \quad (5-7)$$

where  $\gamma$  is the unit weight of the ground material,  $\omega$  is the angular velocity of the sliding mass. Considering the region of  $\mathbf{OFC}$ , the rate of external work is calculated by:

$$\begin{aligned} \dot{W}_4 &= \omega |x_{G4} - x_0| \gamma A_4 \\ &= \omega \gamma r_0^3 \frac{H}{6r_0} \left( \frac{1}{\tan \beta'} - \frac{1}{\tan \beta} \right) \left( \frac{H}{\tan \beta} + \frac{L_0}{r_0} \sin \alpha + \sin \theta_0 \right) \\ &\quad \times \left( 2 \cos \theta_0 - 2 \frac{L_0}{r_0} \cos \alpha - \frac{H}{r_0 \tan \beta'} - \frac{H}{r_0 \tan \beta} \right) \\ &= \omega \gamma r_0^3 f_4(\theta_0, \theta_h, \beta') \end{aligned} \quad (5-8)$$

where  $x_{G4}$  and  $x_0$  are the horizontal coordinates of the gravity center of the soil region and the center of rotation  $\mathbf{O}$  respectively.  $A_4$  is the area of  $\mathbf{OCF}$ .

With the discretization of the slope profile  $\widehat{AC}$ , the rate of work  $\dot{W}_{3,n}$  is divided into  $n$  segments (see Figure 5-3). Each of them can be expressed in terms of the coordinates of  $P_i$  and  $P_{i+1}$ .  $P_1$  is point  $A$  and  $P_{n+1}$  is point  $C$ . In a Cartesian coordinate system with  $\mathbf{O}$  as its origin, the coordinates of  $P_i$  and  $P_{i+1}$  are written as  $P_i(l_i \cos \theta_i, l_i \sin \theta_i)$  and  $P_{i+1}(l_{i+1} \cos \theta_{i+1}, l_{i+1} \sin \theta_{i+1})$ , with

$$l_i = \sqrt{\left[ r_0 \sin \theta_0 + L_0 \sin \alpha + H \cdot \frac{i-1}{n} \right]^2 + \left[ r_0 \cos \theta_0 - L_0 \cos \alpha - k_i \cdot L \right]^2} \quad (5-9)$$

$$\theta_i = \arccos \left( \frac{r_0 \cos \theta_0 - L_0 \cos \alpha - k_i \cdot L}{r_i} \right) \quad (5-10)$$

The area of a segment  $OP_iP_{i+1}$  is expressed as:

$$A_i = \frac{1}{2} |l_i \cos \theta_i \cdot l_{i+1} \sin \theta_{i+1} - l_{i+1} \cos \theta_{i+1} \cdot l_i \sin \theta_i| \quad (5-11)$$

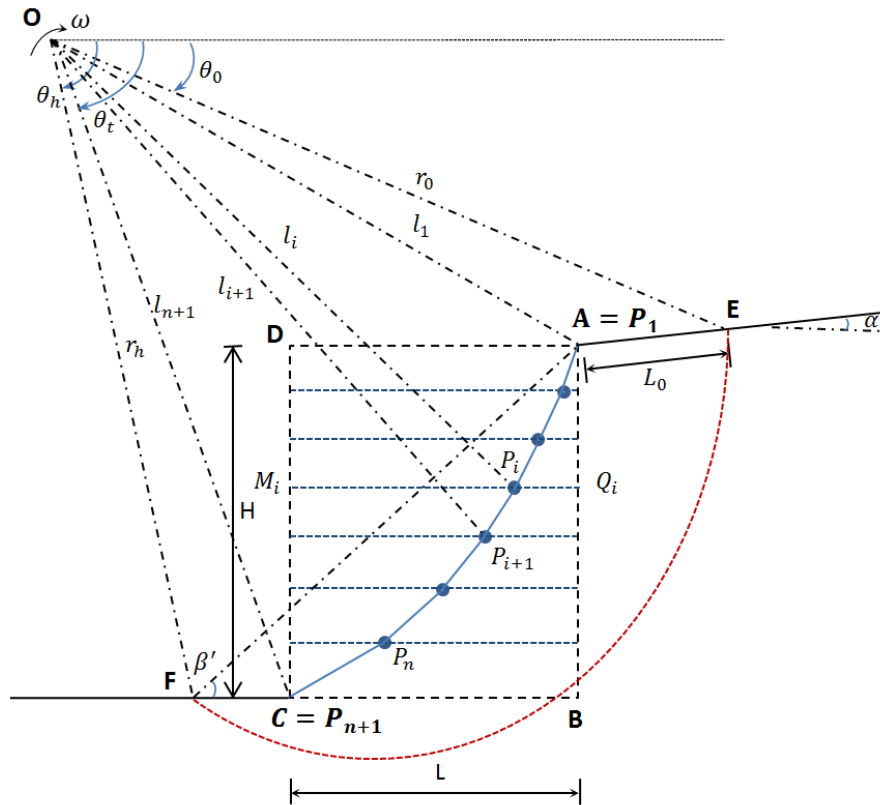
Then the rate of work done by the weight of  $\mathbf{OAC}$  is obtained as the summation of each segment:

$$\begin{aligned} \dot{W}_{3,n} &= \sum_{i=1}^{n+1} \omega |x_{Gi} - x_0| \gamma A_i \\ &= \omega \gamma r_0^3 \sum_{i=1}^{n+1} \left( \frac{l_i \cos \theta_i + l_{i+1} \cos \theta_{i+1}}{3} \cdot \frac{A_i}{r_0^3} \right) = \omega \gamma r_0^3 f_{3,n}(\theta_0, \theta_h, \beta') \end{aligned} \quad (5-12)$$

where  $x_{Gi}$  is the horizontal coordinate of the gravity centre of each segment.

For planar slopes,  $\dot{W}_{3,n}$  becomes:

$$\begin{aligned} \dot{W}_{3,n} = & \omega \gamma r_0^3 \frac{e^{\tan \phi (\theta_h - \theta_0)}}{6} \left[ \sin(\theta_h - \theta_0) - \frac{L_0}{r_0} \sin(\theta_h + \alpha) \right] \\ & \times \left[ \cos \theta_0 - \frac{L_0}{r_0} \cos \alpha + \cos \theta_h e^{\tan \phi (\theta_h - \theta_0)} \right] \end{aligned} \quad (5-13)$$



The rate of internal energy dissipation along the logarithmic spiral  $\widehat{EF}$  has been calculated by Chen (1975):

$$\dot{W}_{d-\log} = \frac{c\omega r_0^2}{2 \tan \phi} \left[ e^{2 \tan \phi (\theta - \theta_0)} - 1 \right] = c\omega r_0^2 f_{d-\log}(\theta_0, \theta_h) \quad (5-14)$$

Equating the rate of external work to the rate of energy dissipation, leads to:

$$\dot{W}_\gamma = \omega \gamma r_0^3 (f_1 - f_2 - f_{3,n} - f_4) = \dot{W}_{d-\log} = c \omega r_0^2 f_{d-\log} \quad (5-15)$$

Dividing by  $\omega$  and  $r_0^2$  and rearranging, the upper bound on the stability factor  $N_{M-C}$  of a slope of any arbitrary profile is obtained:

$$N_{M-C} = \frac{\gamma H}{c} = \frac{f_{d-\log} \times f_H}{f_1 - f_2 - f_{3,n} - f_4} \quad (5-16)$$

The least upper bound is found as the minimum value of Eq. (5-16) which has to be determined by evaluating repeatedly Eq. (5-16) over the three geometric variables  $\theta_0, \theta_h$  and  $\beta'$ . The most critical logarithmical spiral failure mechanism is the one associated to be the least upper bound.

So far, it has been implicitly assumed that the logarithmic spiral failure line passes through or below the slope toe. But for a slope of a non-planar profile, the most critical failure mechanism may pass above the slope toe (see Figure 5-4). In this case, each nodal point  $P_i$  can be regarded as a potential slip toe of a sub-slope whose height  $h_i$  is shorter than the total height  $H$ . The most critical failure mechanism for the entire slope is then determined by finding the minimum value of  $N_{M-C,Sub} \cdot \frac{H}{H_i}$  among all the potential above-toe failure mechanisms, with  $N_{M-C,Sub}$  the stability factor of sub-slope  $\widehat{P_1 P_i}$ . For each potential failure mechanism,  $N_{M-C,Sub}$  is calculated by using Eq. (5-16) and replacing  $H$  with  $H_i$ . Note that the corresponding inclination  $\beta_i$  and  $k'_i$  of the sub-slope  $\widehat{P_1 P_i}$  must be updated according to the coordinate of the potential slip toe  $P_i$ :

$$\beta_i = \arctan \frac{H_i}{L_i} \quad (5-17)$$

$$k'_i = \frac{k_i}{L_i/L} \quad (5-18)$$

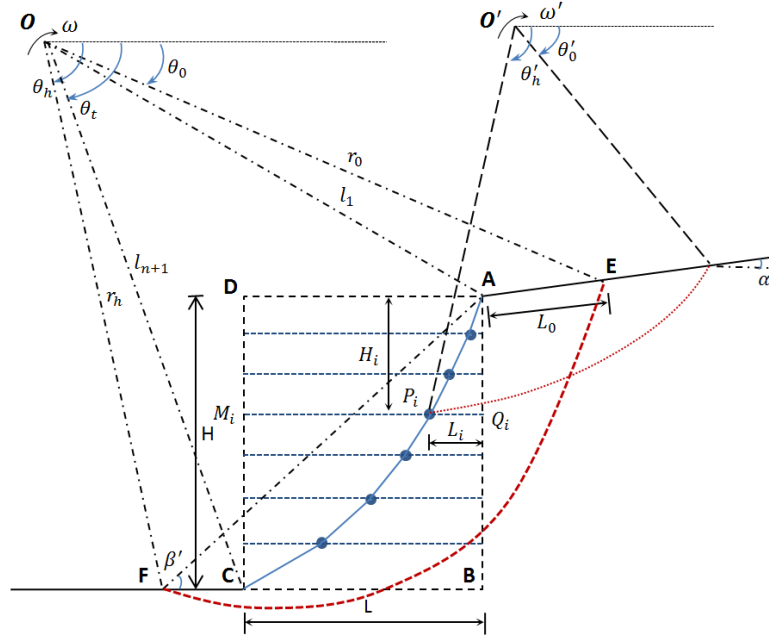


Figure 5-4. Failure mechanism passing above slope toe.

### 5.3 Optimization algorithms to determine the optimal profile

The shape of any arbitrary profile is represented by the coordinates of the nodal points  $P_i$  (see Figure 5-3). The coordinates of  $P_i$  are determined by the number of rows ( $n$ ) the rectangle area of  $ABCD$  is discretized into and the relative position  $k_i$ . In searching of the optimal profile, by changing the values of  $k_i$  of each nodal point  $P_i$  along the horizontal line, different shapes can be evaluated. Among all the candidate profiles, the optimal one providing the highest stability is sought. For each candidate profile to be evaluated, it can be mathematically expressed by an array:  $\mathbf{P} = [n, k_1, k_2, k_3 \dots k_i]$ .  $k_1, k_2, k_3 \dots k_i$  are variables to be optimized. The

optimal profile searching process is then transformed into a typical optimization problem. The objective function to be maximized is the stability factor defined in Eq. (5-16). The optimization process proceeds to find a profile that provides the maximum stability factor among all the available ones:

$$\max N_{M-C}(\mathbf{P}) \quad (5-19)$$

where  $N_{M-C}$  is the stability factor defined in Eq. (5-16). It is worth noting that for each candidate profile, the stability factor of the slope has to be sought by a minimization process according to the upper bound theorem. Thus, finding the optimal profile for a given  $\frac{H}{L}$  is a minimization-maximization process. The constraints for this optimization problem are given by prescribing that each nodal point  $P_i$  stays in the rectangle area of **ABCD**, i.e.,  $0 \leq k_i \leq 1$ . Moreover, in order to exclude some physically infeasible profiles,  $k_i \geq k_{i+1}$ ,  $i = 1, 2, 3, \dots, n$  (see Figure 5-5). Thus, the constrained maximization can then be expressed as:

$$\begin{aligned} & \max N_{M-C}(\mathbf{P}) \\ & \text{subject to} \quad 0 \leq k_i \leq 1 \quad i=1, 2, 3, \dots, n \\ & \quad \quad \quad k_i \geq k_{i+1} \end{aligned} \quad (5-20)$$

The objective function of the stability factor is highly nonlinear due to the presence of several products between exponential and trigonometric functions. Hence traditional gradient-type optimization methods such as gradient descent and conjugate gradient (Hestenes and Stiefel 1952) are not suited to this type of function. In these methods, an initial trial/guess value is needed. Suitable values are difficult to determine. Using these methods, local maximum/minimum close to the initial guess value employed may be found instead of the global maximum/minimum (Chen and Shao 1988, Cheng et al. 2007c).

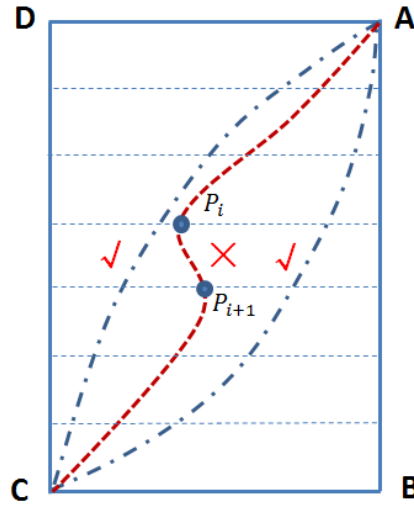


Figure 5-5. Selection of feasible profiles.

Global optimization methods are powerful tools to search for the most critical failure surface within the framework of limit equilibrium. As summarized in Cheng and Lau (2014), there are six global optimization methods, i.e., simulated annealing algorithm (Cheng 2003, Cheng 2007), genetic algorithms (McCombie and Wilkinson 2002), particle swarm algorithm (Cheng et al. 2007b), Tabu search algorithm (Cheng et al. 2007c), harmony search algorithm (Cheng et al. 2008) and ant colony algorithm (Kahatadeniya et al. 2009, Gao 2014). According to Cheng et al. (2007c), no single method can outperform all the other methods under all scenarios, and a genetic algorithm is considered to be an efficient approach when the system variables are less than 20. In this chapter, genetic algorithm and pattern search were selected as the global optimization algorithms to determine the optimal profile, since they exhibit a proven track record in slope stability analyses: e.g., genetic algorithm being employed by McCombie and Wilkinson (2002), Zolfaghari et al. (2005), Sun et al. (2008), Li et al. (2010), Jurado-Piña and Jimenez (2015) and pattern search by Mo et al. (1999). In addition, these two algorithms are already implemented in the Optimization Toolbox of MATLAB R2014b



(Mathworks 2014). In the following, the main principles underpinning these two methods are illustrated briefly.

Genetic algorithm (GA) is derived from Darwin's theory of survival of the fittest. The algorithm starts with a set of possible solutions called the "population". Each possible solution within the "population" is called a "chromosome". A new chromosome outgrows its predecessor and evolves to be a fitter chromosome (fitter means a higher value of the objective function is found). This evolution is repeated until the best chromosome representing the optimal solution is found when some termination criteria are met. The genetic algorithm is the most widely adopted method in determining the critical slip surfaces in the literature and the flowchart of the algorithm is provided in Figure 5-6.

Pattern search (PS) is a direct search method which does not require any information about the gradient of the objective function. At each step, the algorithm looks for a set of solutions, called a mesh, around the current solution (the solution computed at the previous step). The mesh is formed by adding the current solution to a scalar multiple of a set of vectors called a pattern. If the pattern search algorithm finds a solution in the mesh that improves the objective function, the new solution becomes the current solution for the next step of the algorithm. The flowchart for the pattern search algorithm is illustrated in Figure 5-7.

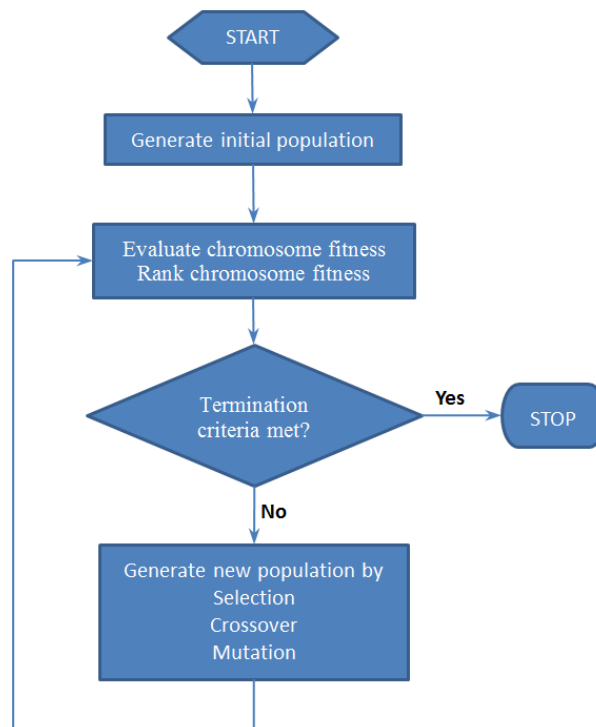


Figure 5-6. Flowchart for genetic algorithm.

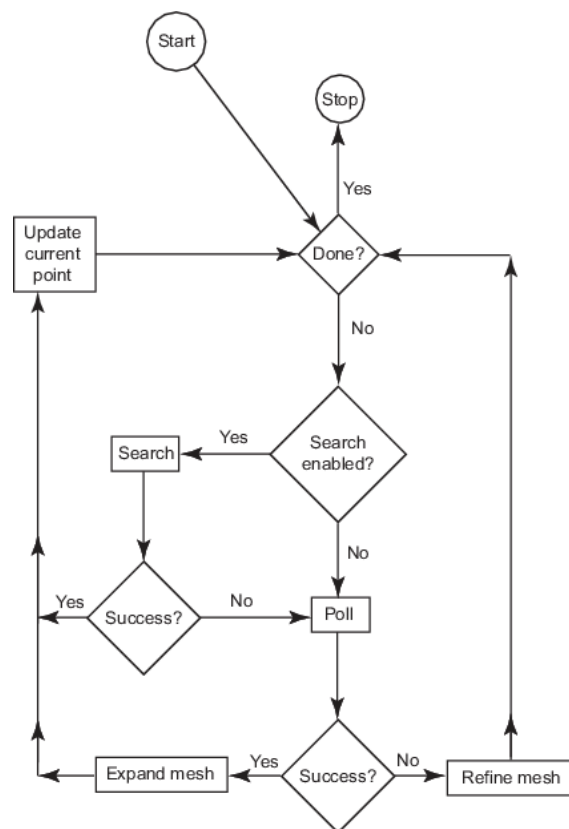
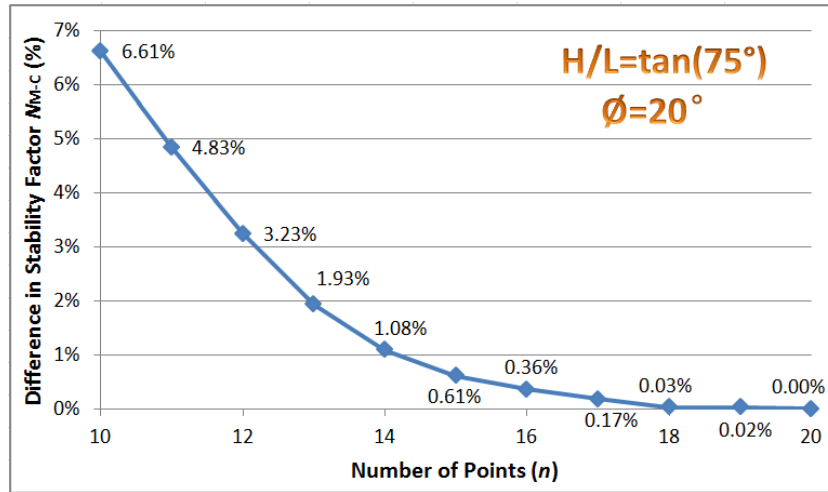


Figure 5-7. Flowchart for pattern search (MATLAB R2014b).

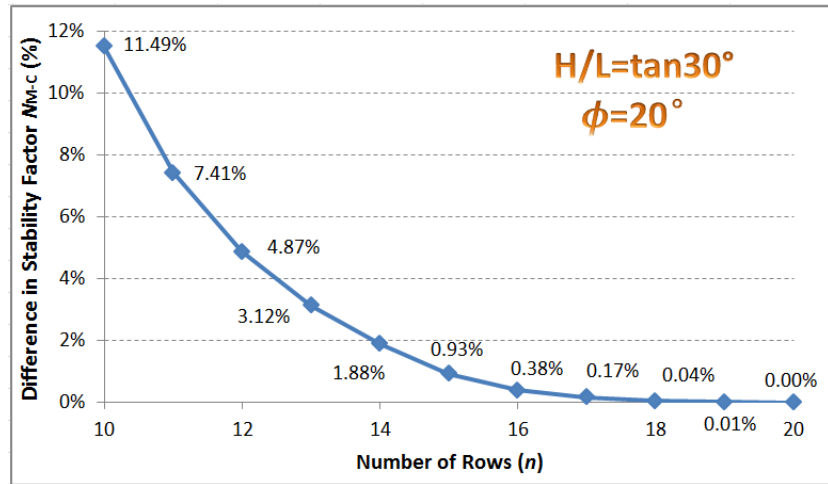
The optimization parameters for the applications of genetic algorithm and pattern search are listed in Table 5-1. For the sake of simplicity, here the case of horizontal upper slope ( $\alpha = 0$ ) is considered. To obtain the results reported here, parallel optimization was performed on an 8-core workstation (CPU: Xeon 5110, RAM: 16GB). Optimizations were run for various discretizations of the slope profile. As may be expected, the accuracy of the result increases with the number of piecewise segments  $n$  employed to discretize the profile. It turns out that the improvement of results becomes less than 1% for  $n > 20$ , as shown in Figure 5-8. Therefore to keep the computation time within reasonable limits,  $n = 20$  was adopted as a standard discretization.

Table 5-1. Optimization parameters for genetic algorithm and pattern search.

<b>Genetic Algorithm</b>		
<b>Parameters</b>	<b>Description</b>	<b>Value</b>
CrossoverFraction	The fraction of the population at the next generation, not including elite children.	0.8
EliteCount	Positive integer specifying how many individuals in the current generation are guaranteed to survive to the next generation.	10
Generations	Positive integer specifying the maximum number of iterations before the algorithm halts	$100n$
PopulationSize	Size of the population	200
StallGenLimit	Positive integer. The algorithm stops if the average relative change in the best fitness function value over StallGenLimit generations is less than or equal to TolFun.	50
TolFun	Positive scalar. The algorithm stops if the average relative change in the best fitness function value over StallGenLimit generations is less than or equal to TolFun.	$10^{-6}$
<b>Pattern Search</b>		
<b>Parameters</b>	<b>Description</b>	<b>Value</b>
InitialMeshSize	Initial mesh size for pattern algorithm	1.0
MaxFunEvals	Maximum number of objective function evaluations	$2000n$
MaxIter	Maximum number of iterations	$100n$
MeshContraction	Mesh contraction factor, used when iteration is unsuccessful	0.5
MeshExpansion	Mesh expansion factor, expands mesh when iteration is successful	2.0
TolFun	Tolerance on function, stop if both the change in function value and the mesh size are less than TolFun	$10^{-6}$



(a)  $\frac{H}{L} = \tan 75^\circ, \phi = 20^\circ$



(b)  $\frac{H}{L} = \tan 30^\circ, \phi = 20^\circ$

Figure 5-8. Influence of number of rows ( $n$ ) on results, based on genetic algorithm. The

difference in stability factor  $N_{M-C}$  is defined as  $\left(1 - \frac{N_{M-C}(n)}{N_{M-C}(n-1)}\right) \times 100\%$ .

In Table 5-2, the optimization results obtained by using both genetic algorithm and pattern search for different values of  $H/L$  and friction angle  $\phi$  are presented and compared. For the selection of the employed parameters, the recommended default values in MATLAB R2014b were adopted (see Table 5-1). Values of the parameters other than the recommended default values were also examined, but the difference in results is less than 1%. The planar profile is selected as the

initial/guess profile to initiate the optimization process in pattern search. The results from both algorithms are almost identical to each other and the difference is within 1% in terms of both the stability factors (defined in Eq. (5-16)) and coordinates of nodal points  $P_i$ .

Table 5-2–Comparison of the optimal profiles obtained using genetic algorithm and pattern search,  $\alpha = 0^\circ$

	$\frac{H}{L} = \tan 75^\circ$ $\phi = 40^\circ$		$\frac{H}{L} = \tan 75^\circ$ $\phi = 30^\circ$		$\frac{H}{L} = \tan 75^\circ$ $\phi = 20^\circ$	
	GA	PS	GA	PS	GA	PS
$k_{21}$	0.000	0.000	0.000	0.000	0.000	0.000
$k_{20}$	0.122	0.121	0.147	0.146	0.178	0.178
$k_{19}$	0.239	0.238	0.286	0.285	0.342	0.342
$k_{18}$	0.351	0.351	0.417	0.417	0.493	0.493
$k_{17}$	0.458	0.458	0.538	0.538	0.630	0.630
$k_{16}$	0.559	0.559	0.649	0.649	0.754	0.754
$k_{15}$	0.654	0.653	0.752	0.751	0.862	0.861
$k_{14}$	0.741	0.740	0.848	0.847	0.948	0.948
$k_{13}$	0.822	0.822	0.926	0.926	1.000	1.000
$k_{12}$	0.898	0.898	0.976	0.976	1.000	1.000
$k_{11}$	0.957	0.956	1.000	0.999	1.000	1.000
$k_{10}$	0.988	0.988	1.000	1.000	1.000	1.000
$k_9$	1.000	1.000	1.000	1.000	1.000	1.000
$k_8$	1.000	1.000	1.000	1.000	1.000	1.000
$k_7$	1.000	1.000	1.000	1.000	1.000	1.000
$k_6$	1.000	1.000	1.000	1.000	1.000	1.000
$k_5$	1.000	1.000	1.000	1.000	1.000	1.000
$k_4$	1.000	1.000	1.000	1.000	1.000	1.000
$k_3$	1.000	1.000	1.000	1.000	1.000	1.000
$k_2$	1.000	1.000	1.000	1.000	1.000	1.000
$k_1$	1.000	1.000	1.000	1.000	1.000	1.000
$N_{M-C}$	17.8041	17.8014	11.7492	11.7465	8.4105	8.4102
	$\frac{H}{L} = \tan 60^\circ$ $\phi = 40^\circ$		$\frac{H}{L} = \tan 60^\circ$ $\phi = 30^\circ$		$\frac{H}{L} = \tan 60^\circ$ $\phi = 20^\circ$	
	GA	PS	GA	PS	GA	PS
$k_{21}$	0.000	0.000	0.000	0.000	0.000	0.000
$k_{20}$	0.010	0.011	0.026	0.025	0.047	0.046
$k_{19}$	0.022	0.023	0.083	0.083	0.083	0.083
$k_{18}$	0.050	0.049	0.179	0.178	0.224	0.223
$k_{17}$	0.095	0.094	0.283	0.282	0.371	0.371

$k_{16}$	0.197	0.199	0.378	0.378	0.488	0.488
$k_{15}$	0.313	0.311	0.466	0.466	0.586	0.586
$k_{14}$	0.418	0.416	0.552	0.552	0.679	0.679
$k_{13}$	0.507	0.505	0.635	0.635	0.764	0.764
$k_{12}$	0.585	0.582	0.712	0.712	0.838	0.838
$k_{11}$	0.656	0.658	0.782	0.782	0.902	0.901
$k_{10}$	0.727	0.724	0.845	0.845	0.960	0.960
$k_9$	0.788	0.787	0.902	0.902	0.998	0.998
$k_8$	0.838	0.834	0.953	0.953	1.000	1.000
$k_7$	0.883	0.881	0.988	0.988	1.000	1.000
$k_6$	0.926	0.923	1.000	1.000	1.000	1.000
$k_5$	0.952	0.955	1.000	1.000	1.000	1.000
$k_4$	0.974	0.975	1.000	1.000	1.000	1.000
$k_3$	0.987	0.986	1.000	1.000	1.000	1.000
$k_2$	0.995	0.993	1.000	1.000	1.000	1.000
$k_1$	1.000	1.000	1.000	1.000	1.000	1.000
$N_{M-C}$	41.5634	41.5602	21.8677	21.8654	12.9896	12.9879
	$\frac{H}{L} = \tan 45^\circ$ $\phi = 40^\circ$		$\frac{H}{L} = \tan 45^\circ$ $\phi = 30^\circ$		$\frac{H}{L} = \tan 45^\circ$ $\phi = 20^\circ$	
	<b>GA</b>	<b>PS</b>	<b>GA</b>	<b>PS</b>	<b>GA</b>	<b>PS</b>
$k_{21}$	0.000	0.000	0.000	0.000	0.000	0.000
$k_{20}$	0.015	0.017	0.013	0.013	0.008	0.008
$k_{19}$	0.054	0.052	0.035	0.032	0.020	0.020
$k_{18}$	0.097	0.099	0.102	0.100	0.052	0.052
$k_{17}$	0.154	0.151	0.170	0.171	0.119	0.118
$k_{16}$	0.210	0.207	0.229	0.230	0.225	0.225
$k_{15}$	0.269	0.267	0.288	0.287	0.342	0.342
$k_{14}$	0.335	0.331	0.359	0.358	0.437	0.437
$k_{13}$	0.394	0.399	0.434	0.434	0.524	0.525
$k_{12}$	0.475	0.470	0.505	0.505	0.602	0.602
$k_{11}$	0.538	0.534	0.572	0.572	0.684	0.684
$k_{10}$	0.601	0.603	0.638	0.638	0.761	0.761
$k_9$	0.658	0.654	0.702	0.702	0.829	0.829
$k_8$	0.713	0.717	0.763	0.764	0.888	0.888
$k_7$	0.764	0.760	0.822	0.823	0.937	0.937
$k_6$	0.811	0.815	0.878	0.877	0.976	0.976
$k_5$	0.855	0.857	0.927	0.927	1.000	1.000
$k_4$	0.896	0.898	0.968	0.970	1.000	1.000
$k_3$	0.934	0.938	0.997	1.000	1.000	1.000
$k_2$	0.969	0.965	1.000	1.000	1.000	1.000
$k_1$	1.000	1.000	1.000	1.000	1.000	1.000
$N_{M-C}$	198.044	198.039	49.6545	49.6515	22.4191	22.4175

## 5.4 Results and comparisons

In Figure 5-10, the optimal profiles obtained by genetic algorithm corresponding to various assigned values of  $\frac{H}{L}$  and  $\phi$  are plotted. For steep slopes with  $\frac{H}{L} = \tan 75^\circ$ , the optimal profiles turn out to be entirely concave for low  $\phi$  values (see Figure 5-10 (a),(b) ). Instead, for slopes with  $\frac{H}{L} = \tan 60^\circ$  and  $\frac{H}{L} = \tan 45^\circ$ , the optimal profiles exhibit both a concave and a convex part. These profiles look different from those obtained in Utili and Nova (2007) and Jeldes et al. (2013), which assume the optimal profiles to be completely concave. A more detailed investigation of the geometrical properties of the optimal profiles can be found in the following sections (5.6 and 5.7).

The stability factors defined in Eq. (5-16) for slopes of both planar and optimal profiles are also reported in Figure 5-10. Compared with the planar slopes, there is a significant increase in terms of the stability factor of the optimal slopes. In order to have quantitative measurements, the percentage of increase of the stability factor is defined as  $\left(\frac{N_{optimal}}{N_{planar}} - 1\right) \times 100$ , with  $N_{planar}$  and  $N_{optimal}$  the stability factors of planar and optimal slopes respectively. The percentage of increase is plotted against  $\beta$  for  $\phi = 20^\circ, 30^\circ$  and  $40^\circ$  in Figure 5-11. The percentage of increase rises from 0 corresponding to the case of vertical slope to a maximum value and then drops to 0 for  $\frac{H}{L}$  approaching  $\tan \phi$ . In both cases (i.e., vertical slope and  $\frac{H}{L} = \tan \phi$ ), the optimal profiles coincide with planar profiles. In fact,  $\beta = 90^\circ$  and  $\phi$  are singular cases for the optimization process where physical considerations alone suffice to conclude that no non-linear profile can outperform the linear (planar) one. The maximum value of the percentage in Figure 5-11 can reach up to 49% when  $\phi = 40^\circ, \beta = 65^\circ$ .

The obtained optimal profiles are superior to the optimal logarithmic spiral profiles found by Utili and Nova (2007) in all the cases considered. The percentage of increase of the stability factor on the optimal logarithmic spiral profiles of Utili and Nova (2007) are plotted in Figure 5-11(b). The maximum value of the percentage in Figure 5-11(b) climbs up to 25% when  $\phi = 40^\circ, \beta = 65^\circ$ .

Jeldes et al. (2013) and Jeldes et al. (2014) proposed an approximate solution to define the geometry of concave slope based on slip-line field method. The obtained concave profiles can be expressed analytically as:

$$x(y) = \begin{cases} 0 & -h_{cr} \leq y \leq 0 \\ A[\gamma y(B-1)(\csc \phi - 1) + c \cot \phi \cdot B(\csc \phi + 1)] & y > 0 \end{cases} \quad (5-21)$$

where

$$A = \frac{\cos \phi}{2\gamma(1 - \sin \phi)} \quad (5-22)$$

$$B = \ln \left[ \frac{\gamma y}{c \cot \phi} \left( \frac{1 - \sin \phi}{1 + \sin \phi} \right) + 1 \right] \quad (5-23)$$

The directions of  $x$  and  $y$  is illustrated in Figure 5-9. According to Jeldes et al. (2013), the obtained optimal concave profile consists of a vertical tension crack zone whose height is assumed to be:

$$h_{cr} = \frac{2c \cos \phi}{\gamma(1 - \sin \phi)} \quad (5-24)$$



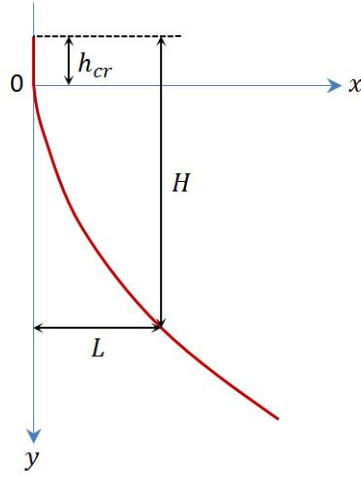
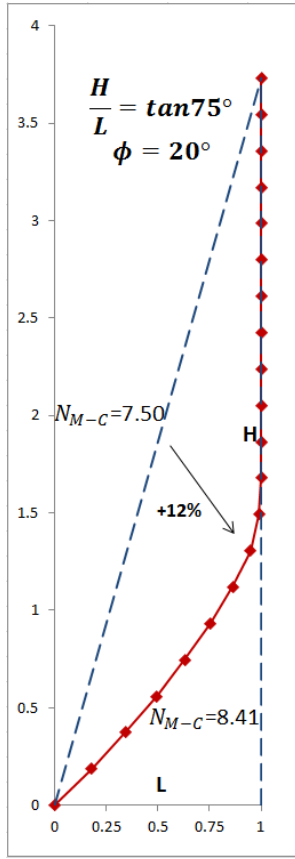


Figure 5-9. Optimal concave profile according to Jeldes et al. (2013).

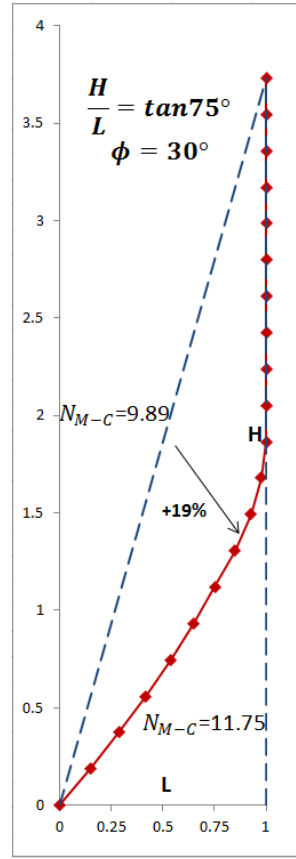
The stability factor of the optimal concave profile is then found as:

$$N_{concave} = \frac{\gamma(h_{cr} + y)}{c} \quad (5-25)$$

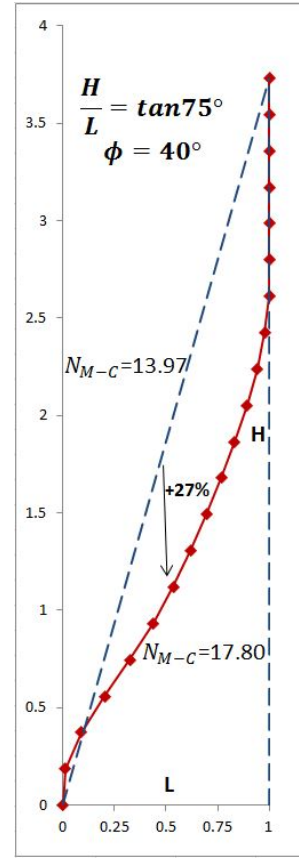
In all cases considered the optimal profiles here found are superior to the profiles determined by Jeldes et al. (2013). In Figure 5-11(c), the increase of the stability factor in percent of the obtained optimal profiles over the ones from Jeldes et al. (2013) is plotted. The maximum percentage is as high as 26% when  $\phi = 40^\circ$ ,  $\beta = 60^\circ$ . Note that the profiles from Utili and Nova (2007) are marginally better than the ones from Jeldes et al. (2013). The advantage of optimal slopes in improving the stability factor is more prominent for high friction angles cases in Figure 5-11.



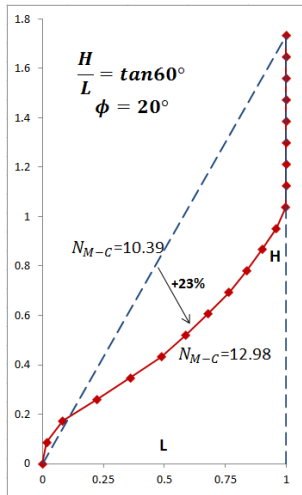
(a)  $\frac{H}{L} = \tan 75^\circ, \phi = 20^\circ$



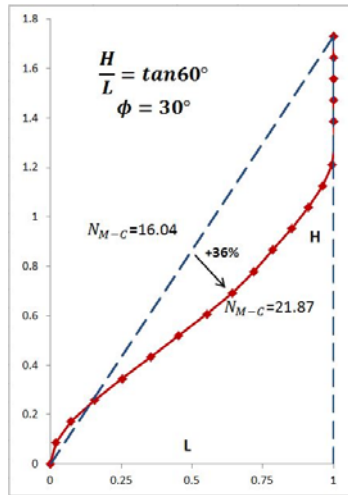
(b)  $\frac{H}{L} = \tan 75^\circ, \phi = 30^\circ$



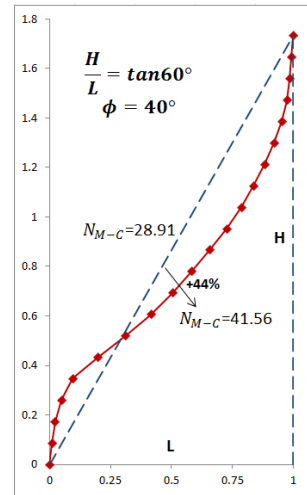
(c)  $\frac{H}{L} = \tan 75^\circ, \phi = 40^\circ$



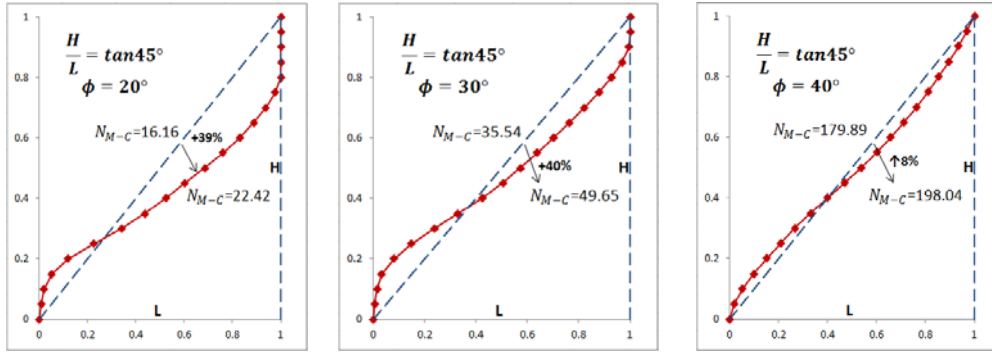
(d)  $\frac{H}{L} = \tan 60^\circ, \phi = 20^\circ$



(e)  $\frac{H}{L} = \tan 60^\circ, \phi = 30^\circ$



(f)  $\frac{H}{L} = \tan 60^\circ, \phi = 40^\circ$

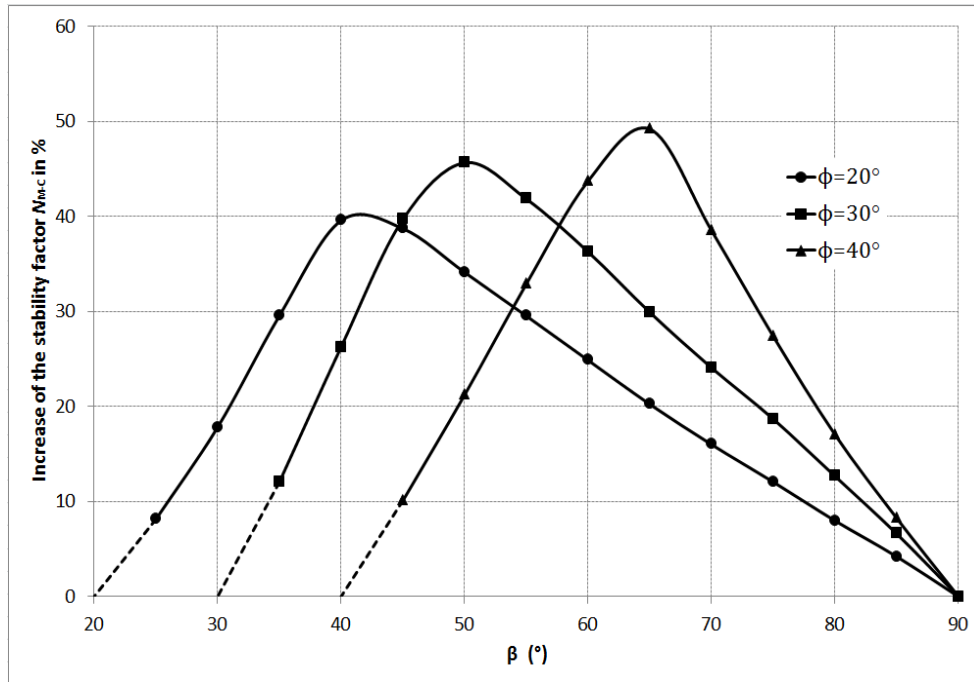


(g)  $\frac{H}{L} = \tan 45^\circ, \phi = 20^\circ$

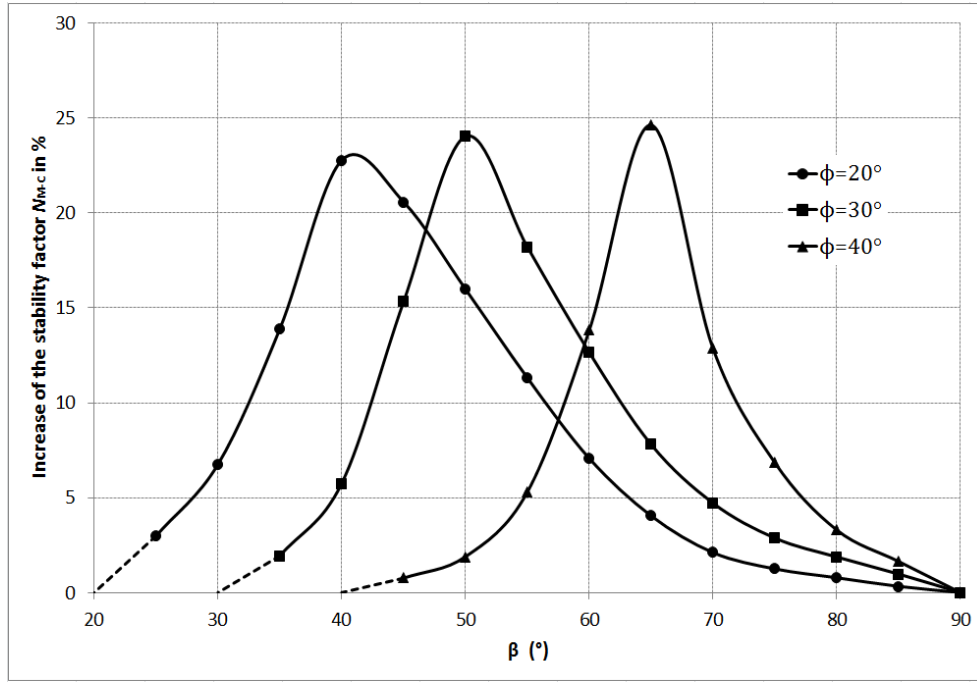
(h)  $\frac{H}{L} = \tan 45^\circ, \phi = 30^\circ$

(i)  $\frac{H}{L} = \tan 45^\circ, \phi = 40^\circ$

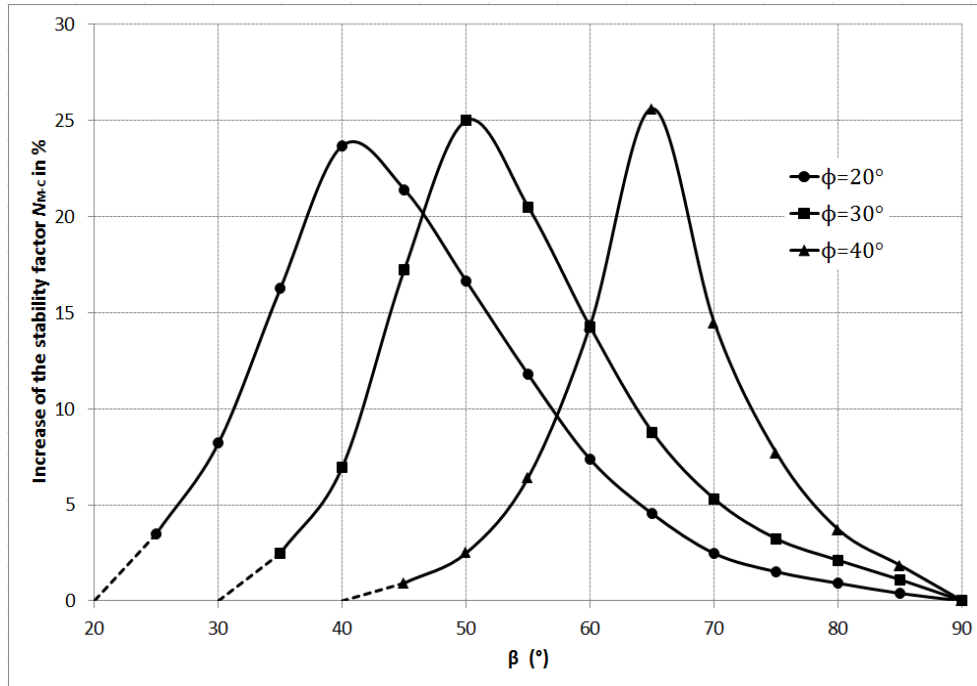
Figure 5-10. Optimal profiles for  $c - \phi$  slopes corresponding to different assigned  $\frac{H}{L}$  and friction angles.



(a) Increase of stability factor over traditional planar profiles



(b) Increase of stability factor over optimal log-spiral profiles (Utili and Nova 2007)



(c) Increase of stability factor over optimal concave profiles (Jeldes et al. 2013)

Figure 5-11. Increase of stability factor in percent for the obtained optimal profiles over the corresponding planar, optimal log-spiral and optimal concave profiles. Case (a): increase of stability factor over traditional planar profiles calculated as  $\left(\frac{N_{optimal}}{N_{planar}} - 1\right) \times 100$ , with  $N_{planar}$  and  $N_{optimal}$  the stability factors of planar and optimal slopes respectively; Case

(b): increase of stability factor over optimal log-spiral profiles calculated as  $\left(\frac{N_{optimal}}{N_{log-spiral}} - 1\right) \times 100$ , with  $N_{log-spiral}$  being the stability factor of the optimal logarithmic spiral profile: Case (c): increase of stability factor over optimal concave profiles calculated as  $\left(\frac{N_{optimal}}{N_{concave}} - 1\right) \times 100$ , with  $N_{concave}$  being the stability factor of the optimal concave profile.

## 5.5 Validation by numerical analyses

Let us recall that the obtained results are based on the upper bound theorem of limit analysis, which provide by definition an overestimation of the slope stability. Therefore, it is desirable to investigate the stability of the optimal profiles found by the analytical approach described using other methods such as the numerical lower/upper bound limit analysis and displacement-based finite element method with strength reduction technique. The software Optum G2 (OptumCE 2013) was used for numerical finite element limit analysis while Phase 2 (Rocscience 2015) for finite element analyse with strength reduction technique. The input values of Optum G2 and Phase2 are given in Table 5-3 and mesh discretization techniques employed in the two types of software are illustrated in Figure 5-12.

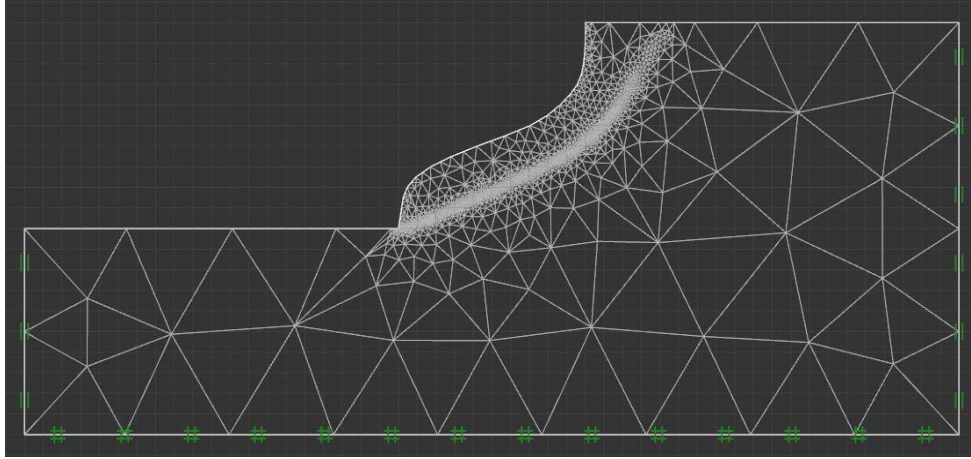
Finite element lower bound and upper bound results of the stability factors obtained from Optum G2 are listed in Table 5-4. For all the optimal profiles found in the previous section 5.4, comparing the analytical findings corresponding to different values of  $\beta$  and friction angles, the biggest difference, defined as  $\left(\frac{N_{UB}}{N_{FELB}} - 1\right) \times 100$ , is around 6%, with  $N_{FELB}$  being the stability factor obtained from finite element lower bound analysis and  $N_{UB}$  the analytical stability factor defined in Eq. (5-16).

Additionally, we may note that the upper bound theorem is based on the assumption of an associative flow rule (i.e. dilatancy angle  $\psi = \phi$ ). However, in reality, the dilatancy angle  $\psi$  varies within the range  $0 \leq \psi < \phi$ . In this section, the stability of optimal slopes is examined by shear strength reduction technique via Phase 2. Elastoplastic analyses following both associative flow rule ( $\phi = \psi$ , as assumed in limit analysis) and non-associative flow rule ( $\psi = \frac{\phi}{4}$ ) were conducted and compared. Slopes were discretized into uniform 6 noded triangular meshes. The results obtained from the stability factors are given in Table 5-5. The analytical upper bound solution provides an estimate very close to the collapse value from the finite element method. The influence of dilatancy on the results is small (less than 5%).

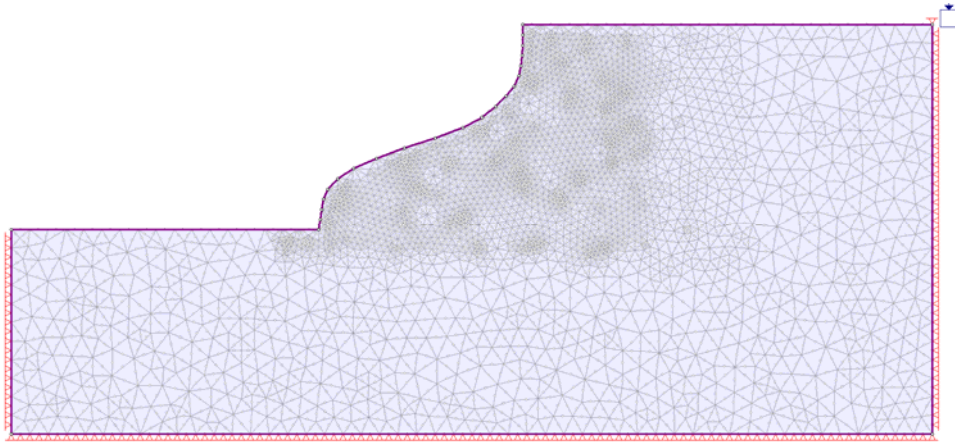
In Figure 5-13, yielded elements ( $\times$  points) within the slope of both planar and optimal profiles on the verge of failure are exhibited for different inclinations ( $\beta = 45^\circ, 60^\circ, 75^\circ$ ) using Phase 2. Having the same material strength, the area of yielded elements within optimal slopes is notably much larger than that within the planar slopes, which means the ground strength is better utilized in the optimal slopes.

Table 5-3. Input values in Optum G2 and Phase2.

Unit Weight $\gamma$	$19 \text{ kN/m}^3$
Young's Modulus	$3000 \text{ MPa}$
Poisson's Ratio	0.3
Slope Height $H$	$20 \text{ m}$
Cohesion $c$	$\frac{\gamma H}{N_{M-C}}$ ( $N_{M-C}$ is defined in Eq. (5-16))
Mesh Density (see Figure 5-12)	Adaptive (Optum G2) Approximately $50/\text{m}^2$ (Phase 2)



(a) Optum G2



(b) Phase 2

Figure 5-12. Mesh discretization.

Table 5-4. Validation with finite element limit analysis (Optum G2).

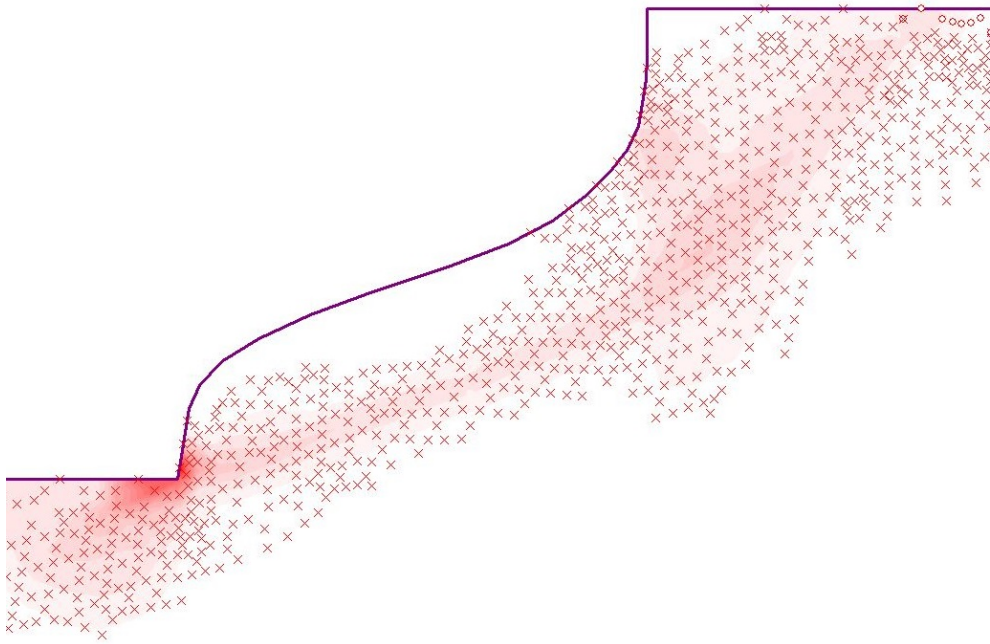
$\beta$	75°				70°			
$\phi$	$N_{FELB}$	$N_{FEUB}$	$N_{UB}$	$\left(\frac{N_{UB}}{N_{FELB}} - 1\right) \times 100\%$	$N_{FELB}$	$N_{FEUB}$	$N_{UB}$	$\left(\frac{N_{UB}}{N_{FELB}} - 1\right) \times 100\%$
20°	8.12	8.26	8.41	3.55%	9.25	9.45	9.61	3.85%
25°	9.66	9.82	9.98	3.37%	11.16	11.31	11.53	3.31%
30°	11.30	11.53	11.75	3.86%	13.60	14.00	14.25	4.70%
35°	13.91	14.07	14.27	2.62%	17.09	17.36	17.58	2.87%
40°	17.08	17.47	17.80	4.23%	22.74	23.29	23.76	4.60%
$\beta$	65°				60°			
$\phi$	$N_{FELB}$	$N_{FEUB}$	$N_{UB}$	$\left(\frac{N_{UB}}{N_{FELB}} - 1\right) \times 100\%$	$N_{FELB}$	$N_{FEUB}$	$N_{UB}$	$\left(\frac{N_{UB}}{N_{FELB}} - 1\right) \times 100\%$
20°	10.70	10.94	11.13	4.01%	12.45	12.76	12.98	4.25%
25°	13.11	13.48	13.74	4.77%	15.82	16.29	16.64	5.22%
30°	16.64	17.25	17.46	4.99%	20.78	21.42	21.87	5.21%
35°	21.87	22.30	22.68	3.68%	28.55	29.29	29.86	4.57%
40°	30.57	31.66	32.20	5.33%	39.47	40.87	41.56	5.45%
$\beta$	55°				50°			
$\phi$	$N_{FELB}$	$N_{FEUB}$	$N_{UB}$	$\left(\frac{N_{UB}}{N_{FELB}} - 1\right) \times 100\%$	$N_{FELB}$	$N_{FEUB}$	$N_{UB}$	$\left(\frac{N_{UB}}{N_{FELB}} - 1\right) \times 100\%$
20°	14.57	15.03	15.29	5.00%	17.27	17.81	18.28	5.80%

25°	19.32	19.82	20.22	4.67%	24.37	25.00	25.70	5.45%
30°	26.52	27.33	27.80	4.96%	35.01	36.11	37.02	5.57%
35°	36.78	38.03	38.89	5.73%	59.26	61.09	62.62	5.67%
40°	52.65	54.31	55.67	5.74%	80.74	82.47	85.56	5.97%
$\beta$	45°				40°			
$\phi$	$N_{FELB}$	$N_{FEUB}$	$N_{UB}$	$\left(\frac{N_{UB}}{N_{FELB}} - 1\right) \times 100\%$	$N_{FELB}$	$N_{FEUB}$	$N_{UB}$	$\left(\frac{N_{UB}}{N_{FELB}} - 1\right) \times 100\%$
20°	21.28	21.91	22.42	5.22%	26.50	27.27	27.91	5.13%
25°	32.52	33.44	34.20	5.17%	47.73	49.10	50.27	5.32%
30°	46.94	48.57	49.65	5.77%	69.56	71.87	73.57	5.77%
35°	89.10	91.01	93.29	5.90%	112.57	116.06	119.30	5.98%
40°	186.79	192.40	198.04	6.02%				
$\beta$	35°				30°			
$\phi$	$N_{FELB}$	$N_{FEUB}$	$N_{UB}$	$\left(\frac{N_{UB}}{N_{FELB}} - 1\right) \times 100\%$	$N_{FELB}$	$N_{FEUB}$	$N_{UB}$	$\left(\frac{N_{UB}}{N_{FELB}} - 1\right) \times 100\%$
20°	32.71	33.72	34.53	5.55%	45.44	46.90	48.20	6.08%
25°	79.30	81.32	83.54	5.34%	128.52	131.78	136.39	6.12%
30°	149.40	153.11	158.20	5.89%				
$N_{FELB}$ ---- Stability factor (finite element lower bound) $N_{FEUB}$ ---- Stability factor (finite element upper bound) $N_{UB}$ ---- Stability factor (defined in Eq. (5-16)) $\tan\beta = H/L$ $\phi$ --- friction angle								

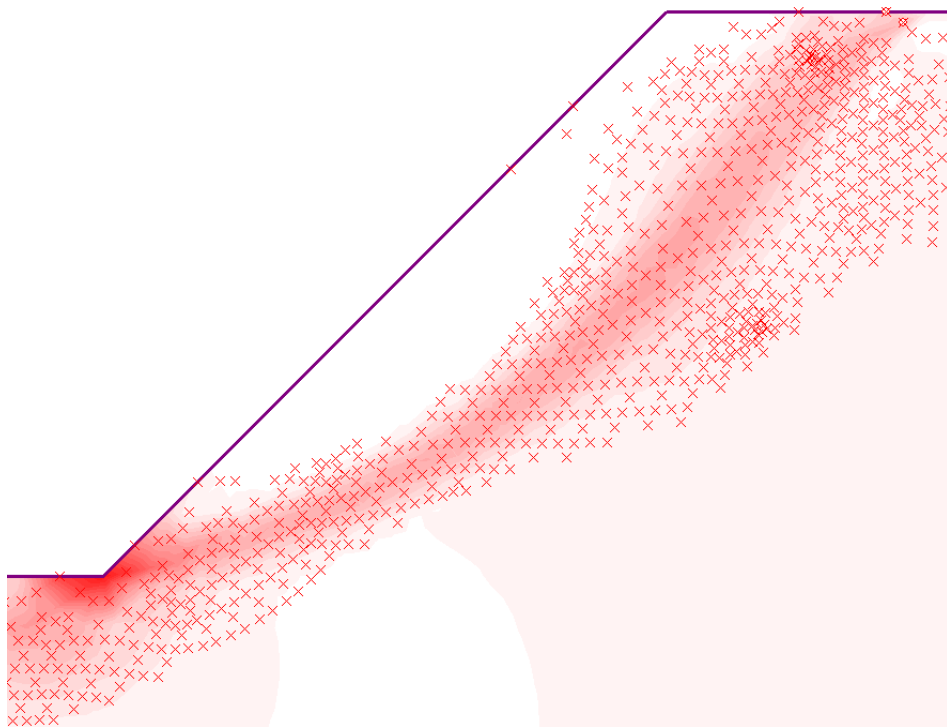
Table 5-5. Validation by displacement-based finite element method with strength reduction technique (Phase 2).

$\beta = 75^\circ$	$\phi = 20^\circ$		$\phi = 25^\circ$			$\phi = 30^\circ$			$\phi = 35^\circ$			$\phi = 40^\circ$		
$N_{UB}$	$N_{\phi=\psi}^{F.E}$	$N_{\phi=\frac{1}{4}\psi}^{F.E}$	$N_{UB}$	$N_{\phi=\psi}^{F.E}$	$N_{\phi=\frac{1}{4}\psi}^{F.E}$	$N_{UB}$	$N_{\phi=\psi}^{F.E}$	$N_{\phi=\frac{1}{4}\psi}^{F.E}$	$N_{UB}$	$N_{\phi=\psi}^{F.E}$	$N_{\phi=\frac{1}{4}\psi}^{F.E}$	$N_{UB}$	$N_{\phi=\psi}^{F.E}$	$N_{\phi=\frac{1}{4}\psi}^{F.E}$
8.41	8.16 3.1%	8.06 4.3%	9.98	9.66 3.2%	9.49 4.9%	11.75	11.35 3.4%	11.23 4.5%	14.27	14.21 0.4%	14.07 1.4%	17.80	17.61 1.1%	17.30 2.9%
$\beta = 60^\circ$	$\phi = 20^\circ$		$\phi = 25^\circ$			$\phi = 30^\circ$			$\phi = 35^\circ$			$\phi = 40^\circ$		
$N_{UB}$	$N_{\phi=\psi}^{F.E}$	$N_{\phi=\frac{1}{4}\psi}^{F.E}$	$N_{UB}$	$N_{\phi=\psi}^{F.E}$	$N_{\phi=\frac{1}{4}\psi}^{F.E}$	$N_{UB}$	$N_{\phi=\psi}^{F.E}$	$N_{\phi=\frac{1}{4}\psi}^{F.E}$	$N_{UB}$	$N_{\phi=\psi}^{F.E}$	$N_{\phi=\frac{1}{4}\psi}^{F.E}$	$N_{UB}$	$N_{\phi=\psi}^{F.E}$	$N_{\phi=\frac{1}{4}\psi}^{F.E}$
12.98	12.72 2.0%	12.63 2.8%	16.64	16.68 0.2%	16.39 1.5%	21.87	22.43 2.6%	21.85 0.2%	29.86	29.83 0.1%	29.26 2.0%	41.56	42.47 2.2%	41.11 1.1%
$\beta = 45^\circ$	$\phi = 20^\circ$		$\phi = 25^\circ$			$\phi = 30^\circ$			$\phi = 35^\circ$			$\phi = 40^\circ$		
$N_{UB}$	$N_{\phi=\psi}^{F.E}$	$N_{\phi=\frac{1}{4}\psi}^{F.E}$	$N_{UB}$	$N_{\phi=\psi}^{F.E}$	$N_{\phi=\frac{1}{4}\psi}^{F.E}$	$N_{UB}$	$N_{\phi=\psi}^{F.E}$	$N_{\phi=\frac{1}{4}\psi}^{F.E}$	$N_{UB}$	$N_{\phi=\psi}^{F.E}$	$N_{\phi=\frac{1}{4}\psi}^{F.E}$	$N_{UB}$	$N_{\phi=\psi}^{F.E}$	$N_{\phi=\frac{1}{4}\psi}^{F.E}$
22.42	22.49 0.3%	22.05 1.7%	34.20	34.54 1.0%	34.10 0.3%	49.65	50.89 2.5%	50.20 1.1%	93.29	95.90 2.8%	94.97 1.8%	198.04	203.39 2.7%	200.81 1.4%
$\beta = 30^\circ$	$\phi = 20^\circ$		$\phi = 25^\circ$			$N_{\phi=\psi}^{F.E}$ ---- Stability factor (FE SSR technique following associative flow rule) $N_{\phi=\frac{1}{4}\psi}^{F.E}$ ---- Stability factor (FE SSR technique following non-associative flow rule) $N_{UB}$ ---- Stability factor (defined in Eq. (5-16)) $\tan\beta=H/L$ $\phi$ --- friction angle								
$N_{UB}$	$N_{\phi=\psi}^{F.E}$	$N_{\phi=\frac{1}{4}\psi}^{F.E}$	$N_{UB}$	$N_{\phi=\psi}^{F.E}$	$N_{\phi=\frac{1}{4}\psi}^{F.E}$									
48.20	48.92 1.5%	48.39 0.4%	136.39	139.80 2.5%	138.16 1.3%									

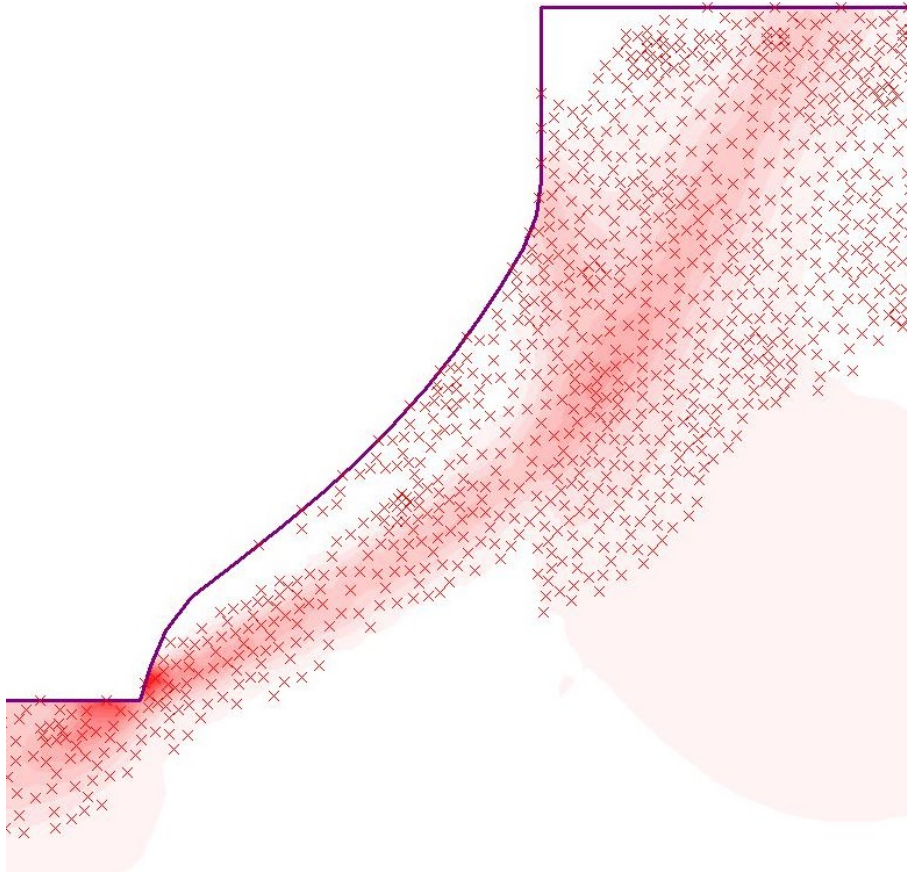




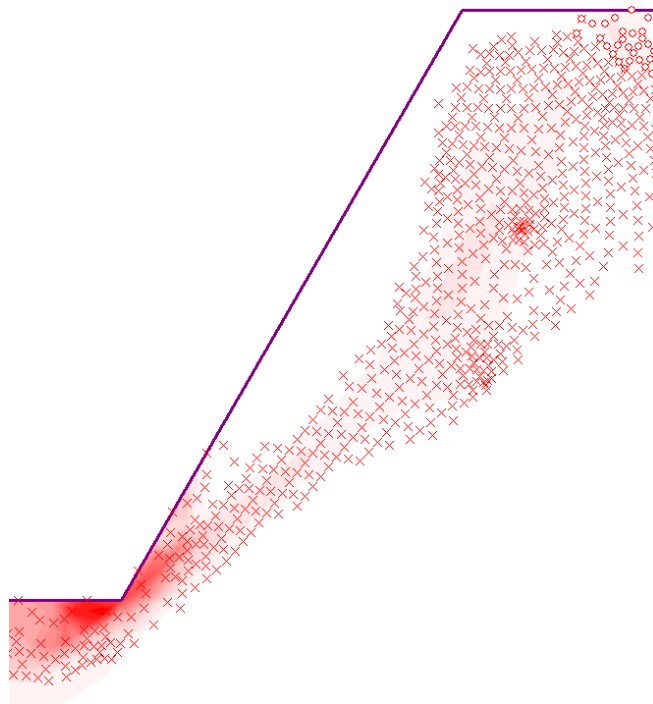
(a)  $\beta = 45^\circ, \phi = 20^\circ$ , optimal slope



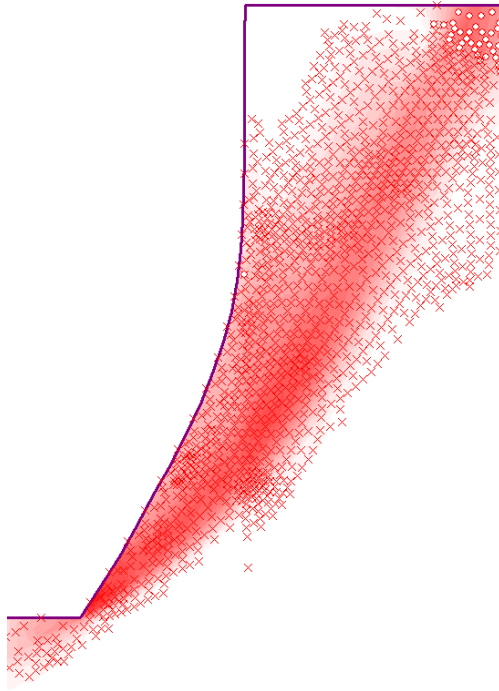
(b)  $\beta = 45^\circ, \phi = 20^\circ$ , planar slope



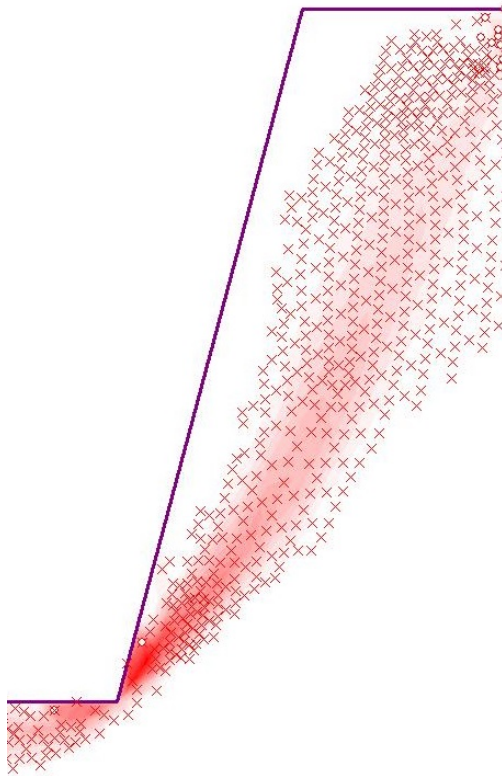
(c)  $\beta = 60^\circ, \phi = 30^\circ$ , optimal slope



(d)  $\beta = 60^\circ, \phi = 30^\circ$ , planar slope



(e)  $\beta = 75^\circ, \phi = 40^\circ$ , optimal slope



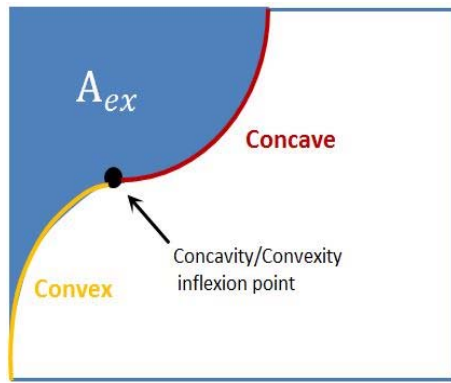
(f)  $\beta = 75^\circ, \phi = 40^\circ$ , planar slope

Figure 5-13. Yielded elements at failure for slopes of planar and optimal profiles.

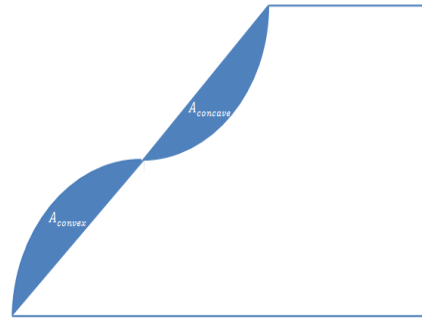
## 5.6 Study of the geometrical and physical properties of the optimal profile

The advantage of finding the optimal profiles is illustrated above to show their capacity to increase the stability factor by up to 49%. In terms of geometry, the optimal profile exhibits both a concave and a convex part, see Figure 5-14. The convex part vanishes when the assigned value of  $\frac{H}{L}$  is high or friction angle is small. In Figure 5-15, the optimal profiles of slopes with various assigned values of  $\frac{H}{L}$  corresponding to friction angles  $\phi = 20^\circ$  and  $40^\circ$  are reported. The curved bold lines represent the concavity/convexity inflexion point of each optimal profile, whose equations are obtained by 3<sup>rd</sup> order polynomial fit.

The excavation area  $A_{ex}$  of a man-made slope is the shaded region in Figure 5-14(a). So far the optimal and planar profiles have been compared given the same average slope inclination ( $\beta = \arctan \frac{H}{L}$ ). Instead, in Figure 5-16,  $A_{ex}/H^2$  is plotted against the stability factor  $N_{M-C}$  defined in Eq. (5-16) for both planar and optimal slopes corresponding to friction angles  $\phi = 20^\circ, 30^\circ$  and  $40^\circ$ . The average slope inclination of an optimal slope is always higher than that of a planar slope, given the same stability factor. The amount of ground excavated away for the optimal profile can be as little as 50% of that for a planar profile when  $\phi = 40^\circ, \frac{H}{L} = \tan 70^\circ$ .

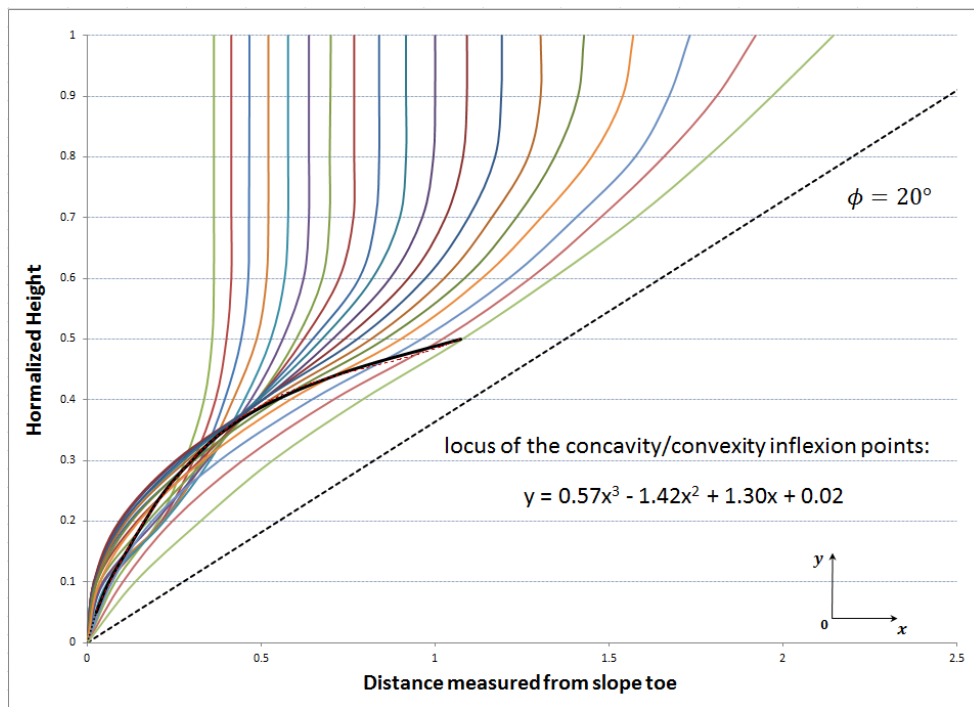


(a) excavated area  $A_{ex}$

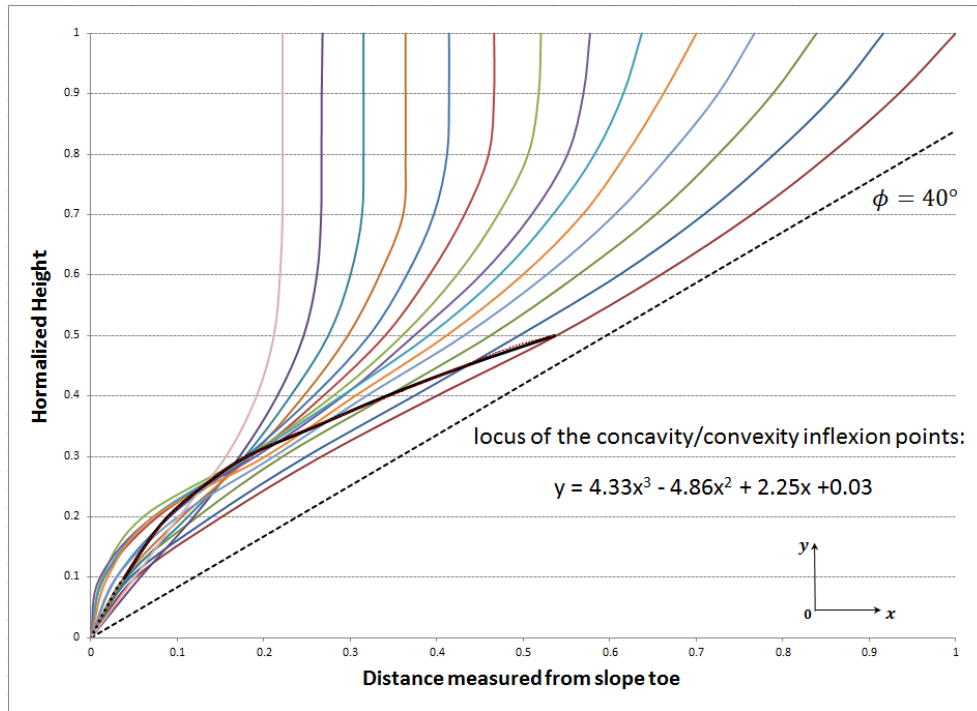


(b) convex/concave areas  $A_{convex}/A_{concave}$

Figure 5-14. Concavity and convexity of the optimal profile.

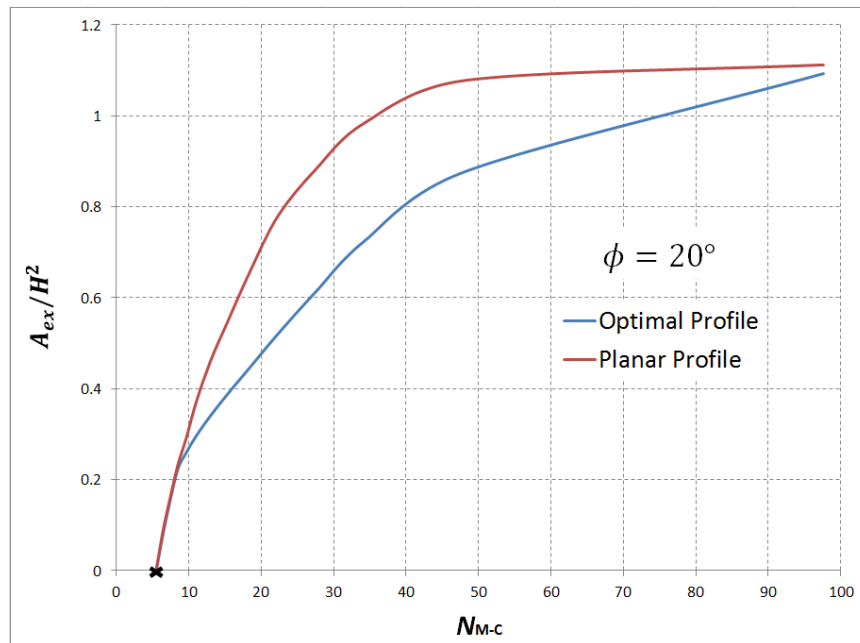


(a)  $\phi = 20^\circ$

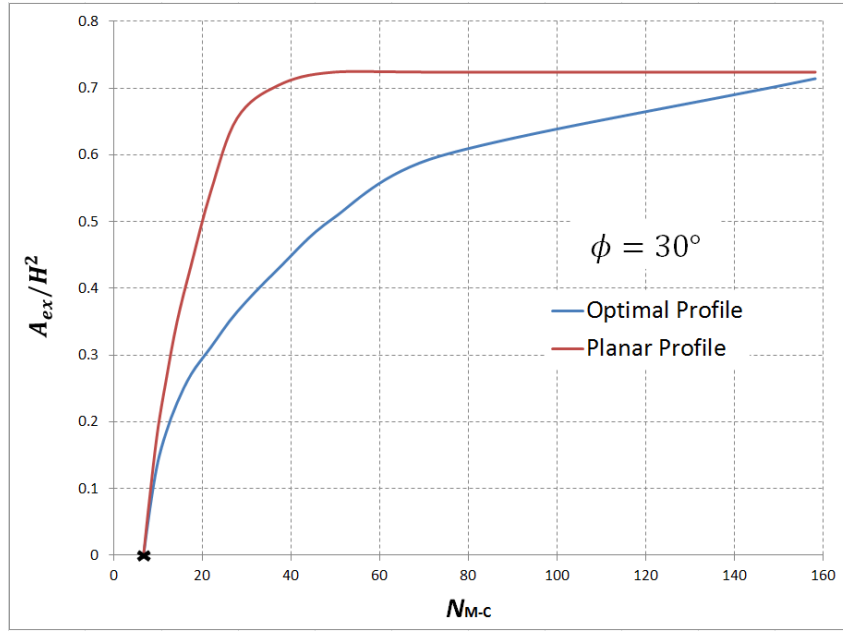


(b)  $\phi = 40^\circ$

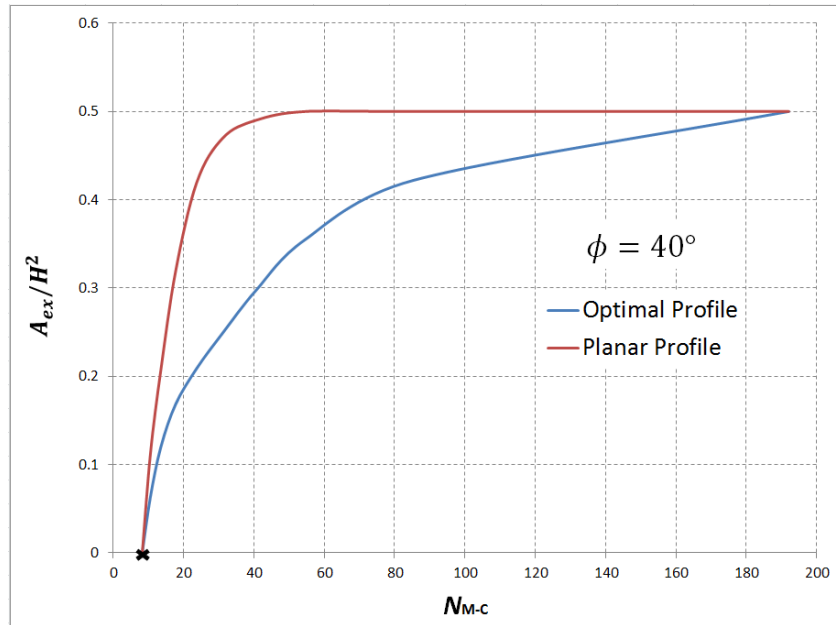
Figure 5-15. Optimal profiles for various assigned  $\frac{H}{L}$  and concavity/convexity inflexion point curves.



(a)  $\phi = 20^\circ$



(b)  $\phi = 30^\circ$



(c)  $\phi = 40^\circ$

Figure 5-16. Excavation area against the stability factor  $N_{M-C}$  (× indicates the vertical profile).

In Figure 5-17, the area of the concave part plus the area of the convex part ( $A_{cc} = A_{concave} + A_{convex}$ , as shown in Figure 5-14 (b)), is plotted against  $\beta$  corresponding to  $\phi = 20^\circ, 30^\circ$  and  $40^\circ$ .  $A_{cc}$  starts from 0 for  $\beta = \phi$  to a maximum

value and then decreases to 0 for  $\beta = 90^\circ$ . This area represents the amount of ground to be excavated to re-profile a planar slope into an optimal profile maintaining the average slope inclination. In section 5.7, it will be shown that this type of re-profiling may well be enough to stabilize planar slope showing signs of distress (impending failure). In addition, the length of the concave part of the optimal profile over the total length of the profile is plotted against  $\beta$  in Figure 5-18, from which the average inclination corresponding to when the optimal profile becomes entirely concave can be obtained.

Since the shapes of the optimal profiles are highly non-linear, it is necessary to abstract some key geometric parameters of the optimal profiles for practical use in excavation design. To this end, the following variables can be employed:  $z_v$  (the vertical distance starting from slope crest),  $h_u$  (the horizontal distance from the midpoint of  $\overline{AD}$  to the optimal profile),  $h_l$  (the horizontal distance from the midpoint of  $\overline{DC}$  to the optimal profile) and  $x_{PI}/y_{PI}$  (horizontal/vertical coordinates of inflexion point  $D, C$  as the origin), as illustrated in Figure 5-19. Table 5-6~Table 5-8 list the five key geometric parameters of the optimal profiles for different values of  $\beta$  corresponding to  $\phi = 20^\circ, 30^\circ$  and  $40^\circ$ .

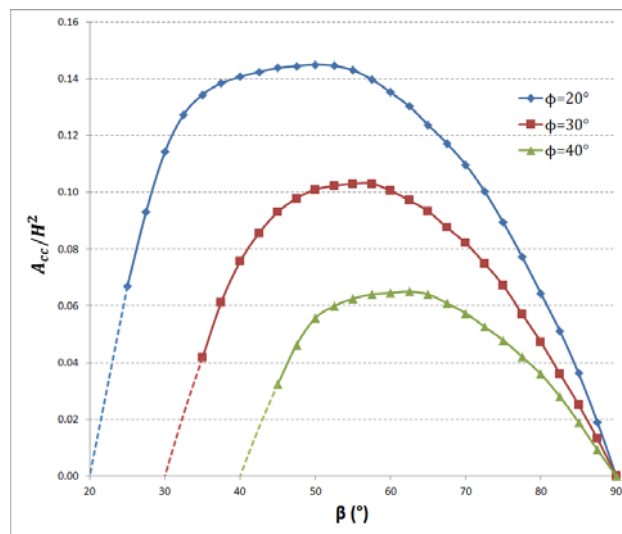


Figure 5-17. Area of concave part plus convex part against  $\beta$ .



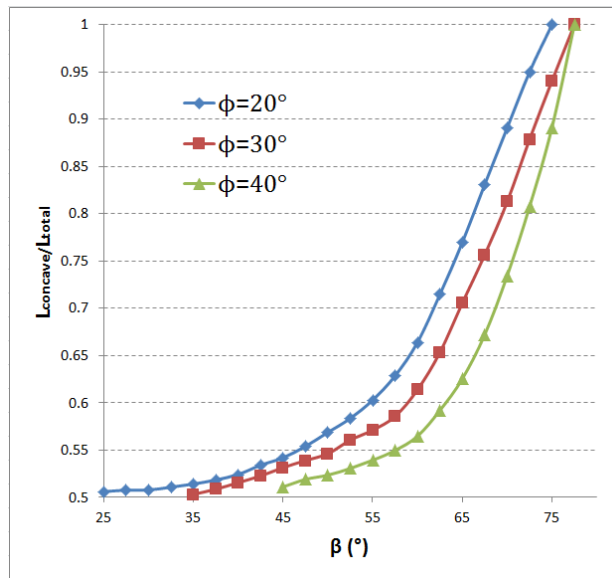


Figure 5-18. Length of concave part over length of the entire profile against  $\beta$ .

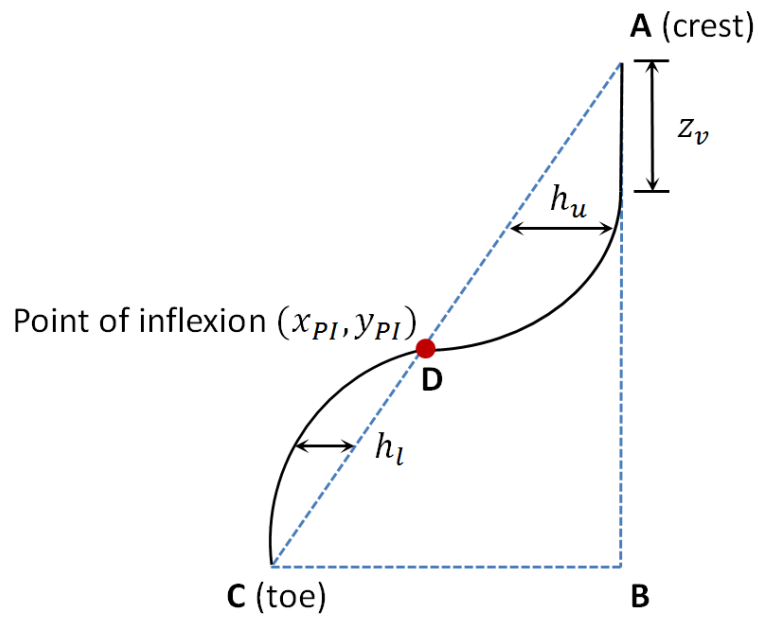


Figure 5-19. Key geometric parameters of an optimal profile.

Table 5-6. Geometric parameters defining the optimal profiles, for soil slope of  $\phi = 20^\circ$

$\beta$	$\frac{z_v}{H}$	$\frac{x_{PI}}{H}$	$\frac{y_{PI}}{H}$	$\frac{h_u}{H}$	$\frac{h_l}{H}$
$75^\circ$	0.600	0.000	0.000	1.850	0.000
$70^\circ$	0.525	0.000	0.000	1.375	0.000

65°	0.475	0.150	0.050	0.975	0.050
60°	0.425	0.300	0.150	0.700	0.100
55°	0.375	0.500	0.250	0.500	0.175
50°	0.300	0.475	0.325	0.350	0.175
45°	0.225	0.450	0.375	0.250	0.175
40°	0.150	0.375	0.400	0.175	0.100
35°	0.100	0.300	0.425	0.100	0.050
30°	0.050	0.250	0.450	0.050	0.025

Table 5-7. Geometric parameters defining the optimal profiles, for soil slope of  $\phi = 30^\circ$

$\beta$	$\frac{z_v}{H}$	$\frac{x_{PI}}{H}$	$\frac{y_{PI}}{H}$	$\frac{h_u}{H}$	$\frac{h_l}{H}$
75°	0.500	0.000	0.000	1.675	0.000
70°	0.400	0.275	0.000	1.175	0.150
65°	0.300	0.425	0.125	0.800	0.225
60°	0.275	0.425	0.225	0.525	0.300
55°	0.200	0.575	0.325	0.350	0.350
50°	0.150	0.475	0.375	0.250	0.225
45°	0.100	0.400	0.425	0.150	0.150
40°	0.025	0.325	0.450	0.100	0.100

Table 5-8. Geometric parameters defining the optimal profiles, for soil slope of  $\phi = 40^\circ$

$\beta$	$\frac{z_v}{H}$	$\frac{x_{PI}}{H}$	$\frac{y_{PI}}{H}$	$\frac{h_u}{H}$	$\frac{h_l}{H}$
75°	0.300	0.000	0.000	1.575	0.000
70°	0.250	0.350	0.125	1.025	0.150
65°	0.125	0.600	0.250	0.700	0.325
60°	0.075	0.550	0.300	0.425	0.400
55°	0.025	0.500	0.350	0.275	0.225
50°	0.000	0.450	0.400	0.175	0.125

## 5.7 Applications of the optimal slope

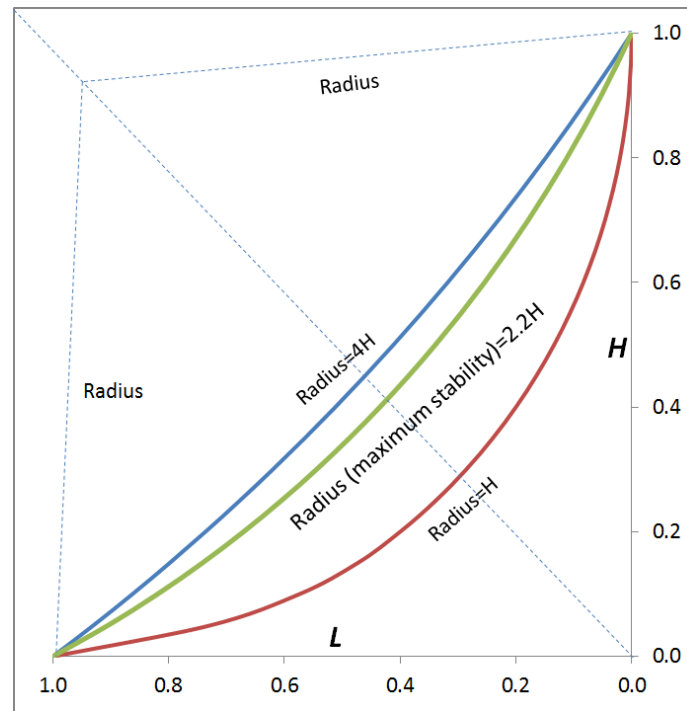
### 5.7.1. Safety monitoring during excavation

The analytical formulation described in section 5.2 can be used to calculate the stability factors of slopes of any arbitrary shapes. For instance, for slopes with

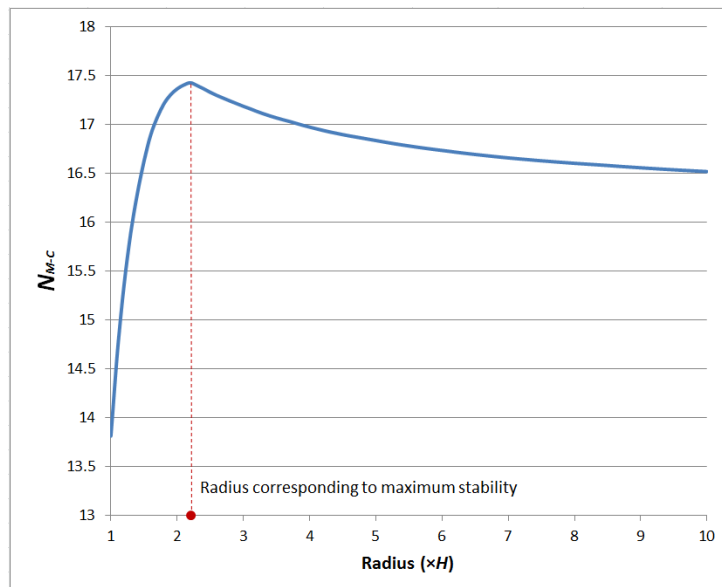
$\frac{H}{L} = \tan 45^\circ$  and  $\phi = 20^\circ$ , the shapes of different circular slopes are plotted in

Figure 5-20 (a). The corresponding stability factors (defined in Eq. (5-16)) of

different circular slopes are plotted against their radii in Figure 5-20 (b). Hoek and Bray (1981) investigated the stability of circular slopes; however, they did not tackle optimality, i.e. which one is optimal. The optimal circular profile (having the highest stability factor) is determined in Figure 5-20 (b).



(a) different circular slopes



(b) stability factor against radius of curvature,  $\phi = 20^\circ, \frac{H}{L} = \tan 45^\circ$

Figure 5-20. Optimal circular profile.

In the case of man-made slope excavation, since the slope profile varies with the excavation steps, it is important to monitor the evolving stability status during the whole construction period. The stability factor of the excavated part is here defined as  $N_{M-C}(H_i) \frac{H_{total}}{H_i}$ , with  $N_{M-C}$  the stability factor defined in Eq. (5-16).  $H_i$  is the current excavation height and  $H_{total}$  is the final excavation height to be undertaken. In Figure 5-21, the stability factors of engineered slopes of the optimal logarithmic spiral profile (Utili and Nova 2007), the optimal concave profile (Jeldes et al. 2013), the optimal circular profile and the optimal profile are plotted against excavation steps  $\frac{H_i}{H_{total}}$ . The optimal slope is the one providing the highest stability.

In Figure 5-22, the stability factors of the excavated part are plotted against  $\frac{H_i}{H_{total}}$  for different values of  $\frac{H}{L}$  and friction angles  $\phi$  from the start until the end of excavation. It merges that the stability factor of an optimal slope tends to remain almost constant after reaching a critical excavation depth, which is one of the key features of the optimal profile. However, it should be noted that the calculated value  $N_{M-C} \frac{H_{total}}{H_i}$  may increase during the excavation process in some cases when the failure line daylighting above the excavation toe point.

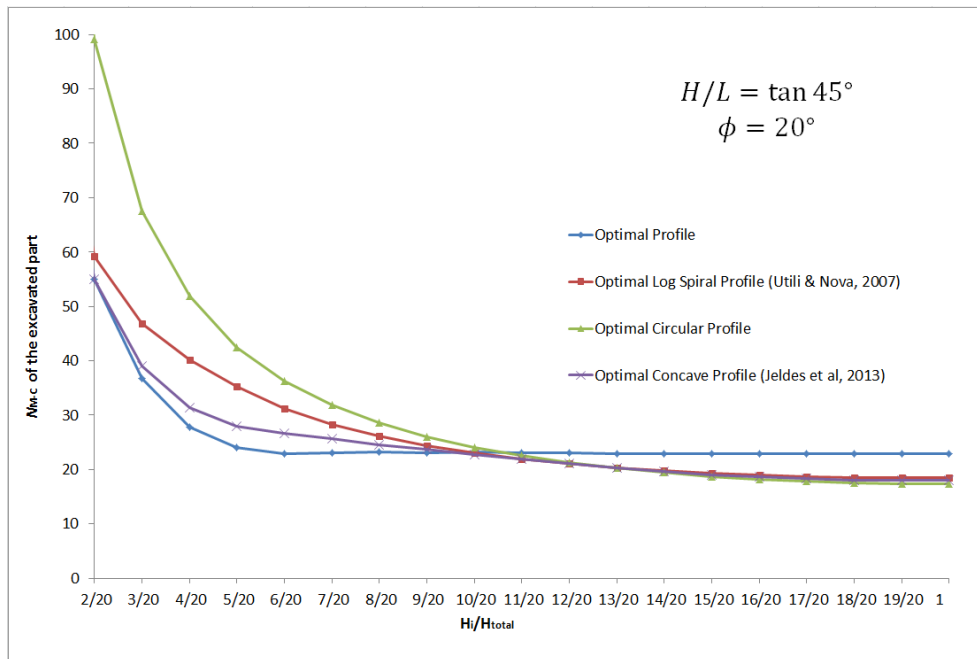
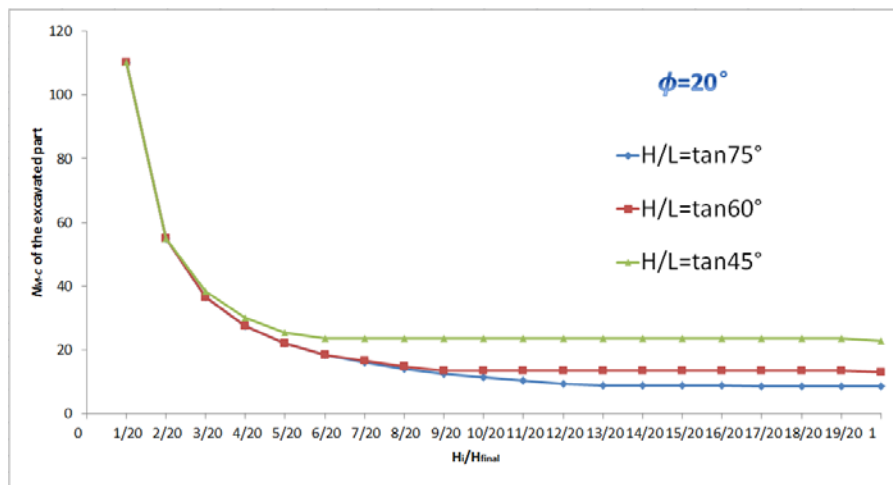
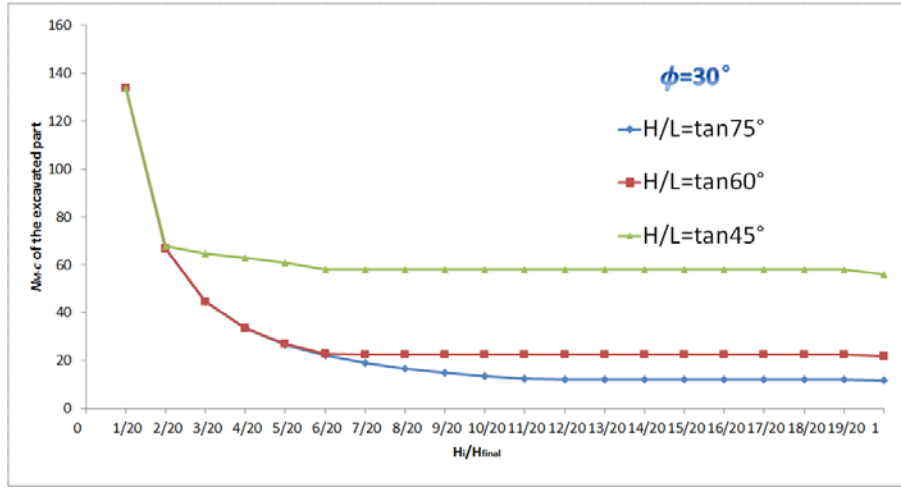


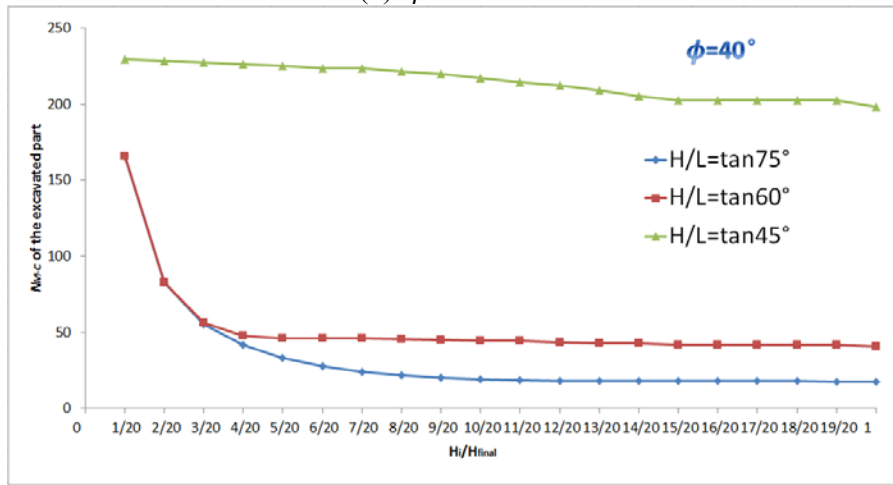
Figure 5-21. Slope stability factor of the excavated part of profile against excavation step.



(a)  $\phi = 20^\circ$



(b)  $\phi = 30^\circ$



(c)  $\phi = 40^\circ$

Figure 5-22. Stability factor of the excavated part of profile during excavation for various

friction angles and values of  $\frac{H}{L}$ .

### 5.7.2. Re-profiling/profiling a slope to maximize the factor of safety

In the design of engineered slopes, often there are unavoidable space constraints (see Figure 5-23). It is desirable to find the optimal profile providing the maximum factor of safety for a slope of assigned  $\frac{H}{L}$  and prescribed ground strength properties (cohesion  $c_g$  and friction angle  $\phi_g$ ). In Figure 5-24, each point corresponds to a different optimal profile found for the assigned  $\frac{H}{L}$  and  $\phi$ .  $\frac{c}{\gamma H}$  is plotted against  $\tan\phi$  by the least square polynomial function fitting. The trend line function

$\frac{c}{\gamma H} = g(\tan\phi)$  and coefficient of determination  $R^2$  of each curve is reported alongside.

The maximum factor of safety can be determined via a graphic method. For example, in Figure 5-24,  $M$  is the point known corresponding to the values of  $c_g$  and  $\phi_g$  of the ground material.  $A$  is the unknown point to be found on the curve for  $\beta = 45^\circ$  in Figure 5-24. According to the definition of the factor of safety in Eq. (3-22), i.e. the same factor applied on both cohesion and internal  $\phi$ :

$$F = \frac{\tan\phi_g}{\tan\phi_f} = \frac{c_g}{c_f} = \frac{g(\tan\phi_g)}{g(\tan\phi_f)} \quad (5-26)$$

where  $c_f$  and  $\phi_f$  are cohesion and internal friction angle at failure,  $g$  being the trend line function.

The graphic interpretation of Eq. (5-26) is written as follows:

$$\frac{AC}{ME} = \frac{AD}{MF} \quad (5-27)$$

After rearranging Eq. (5-26),  $\tan\phi_f$  is obtained:

$$\tan\phi_f = \frac{g(\tan\phi_f)}{g(\tan\phi_g)} \tan\phi_g \quad (5-28)$$

Note that there is some approximation in finding the maximum factor of safety according to Eqs. (5-26) and (5-28) due to the use of interpolation functions used. If needed, a more accurate result can be obtained by running a search for the optimal profile corresponding to the  $\phi_f$  and assigned  $\frac{H}{L}$  obtained from Eq. (5-28). In this case, the error on the maximum factor of safety due to interpolation can be





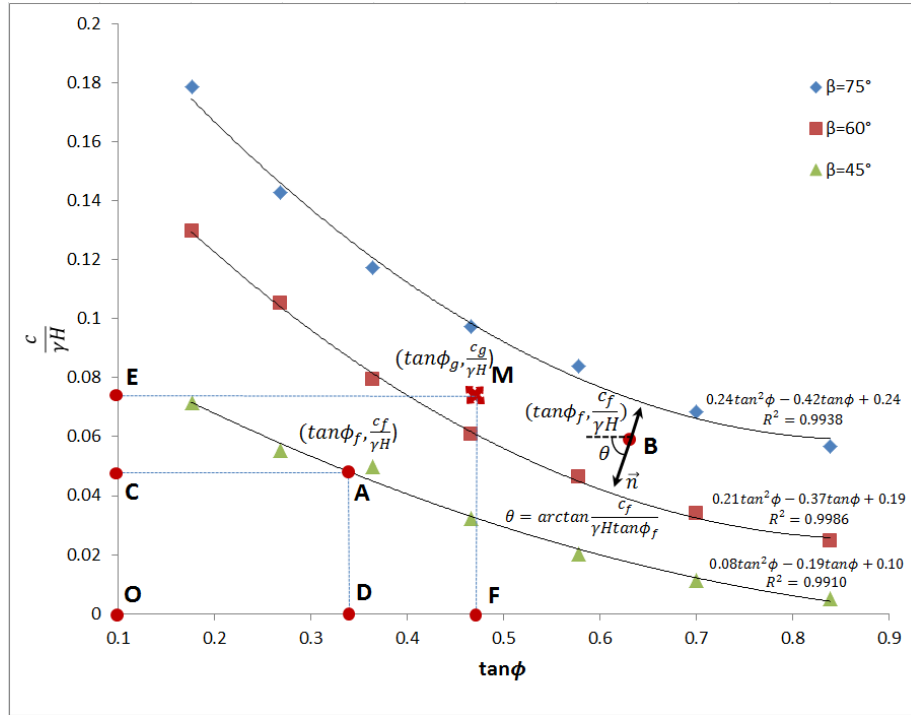


Figure 5-24.  $\frac{c}{\gamma H}$  against  $\tan\phi$  by interpolation.

## 5.8 The effect of the presence of pre-existing cracks on soil slopes

In Chapter 3 and Chapter 4, the effect of the presence of cracks has been investigated for planar slopes. It turns out that the presence of cracks reduces the stability factor significantly. In this section, the influence of the presence of pre-existing cracks on the stability of optimal slopes and how the optimal profiles should be modified to be still optimal when cracks are present is examined.

In Figure 5-25, considering the presence of pre-existing crack  $GH$ , the following geometrical relationships are found:

$$L_c = r_0 \left\{ \frac{\sin(\theta_c - \theta_0)}{\sin(\theta_c + \alpha)} - \frac{\cos \theta_c}{\sin(\theta_c + \alpha) \cos \alpha} \cdot \left[ e^{\tan \phi (\theta_c - \theta_0)} \sin(\theta_c + \alpha) - \sin(\theta_0 + \alpha) \right] \right\} \quad (5-30)$$

$$\delta = r_0 \frac{1}{\cos \alpha} \left[ e^{\tan \phi (\theta_c - \theta_0)} \sin(\theta_c + \alpha) - \sin(\theta_0 + \alpha) \right] \quad (5-31)$$

with  $L_c$  the length of  $\mathbf{AG}$  and  $\delta$  being the crack depth.

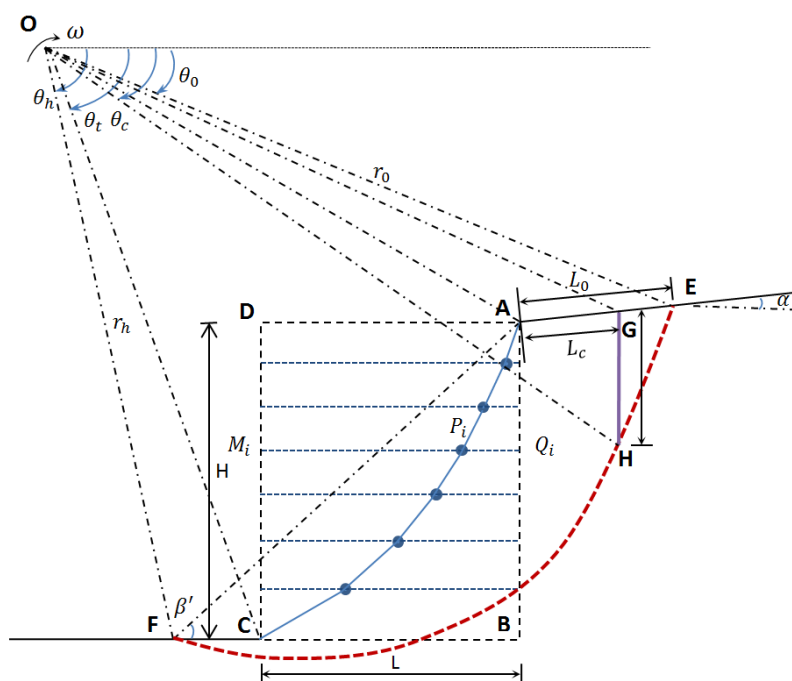


Figure 5-25. Failure mechanism for a slope subject to a pre-existing crack.

Considering the block **ACFHG** rigidly rotating away about a centre of rotation **O**, the remaining part is bounded by a crack **GH** and a logarithmic spiral failure surface  $\widehat{FH}$ . The rate of external work due to the weight of region **ACFHG** is computed as the work done by region **OFE** minus the work of region **OEA**, region **OAC**, region **OFC** and region **GEH**. And the rate of external work for region **GEH** is the result of work done by **OEH** subtract **OEG** and **OGH**.  $\dot{W}_1, \dot{W}_2, \dot{W}_{3,n}, \dot{W}_4,$

$\dot{W}_5$ ,  $\dot{W}_6$ , and  $\dot{W}_7$  indicate the work done by **OFE**, **OEA**, **OAC**, **OFC**, **OEH**, **OEG** and **OGH** respectively.  $\dot{W}_1, \dot{W}_2, \dot{W}_{3,n}, \dot{W}_4$  are given in Eqs. (5-6), (5-7), (5-12), (5-8).  $\dot{W}_5$ ,  $\dot{W}_6$ , and  $\dot{W}_7$  are calculated by Utili (2013) and are written as follows:

$$\begin{aligned}\dot{W}_5 &= \omega \gamma r_0^3 \frac{e^{3 \tan \phi (\theta_c - \theta_0)} (3 \tan \phi \cos \theta_c + \sin \theta_c) - 3 \tan \phi \cos \theta_0 - \sin \theta_0}{3(1 + 9 \tan^2 \phi)} \\ &= \omega \gamma r_0^3 f_5(\theta_0, \theta_c)\end{aligned}\quad (5-32)$$

$$\dot{W}_6 = \omega \gamma r_0^3 \frac{1}{6} \sin \theta_0 \frac{L_c}{r_0} \left( 2 \cos \theta_0 - \frac{L_c}{r_0} \right) = \omega \gamma r_0^3 f_6(\theta_0, \theta_c) \quad (5-33)$$

$$\begin{aligned}\dot{W}_7 &= \omega \gamma r_0^3 \frac{1}{3} e^{2 \tan \phi (\theta_c - \theta_0)} \frac{\cos^2 \theta_c}{\cos \alpha} \left[ e^{\tan \phi (\theta_c - \theta_0)} \sin(\theta_c + \alpha) - \sin(\theta_0 + \alpha) \right] \\ &= \omega \gamma r_0^3 f_7(\theta_0, \theta_c)\end{aligned}\quad (5-34)$$

Internal energy is dissipated only along the spiral  $\widehat{HF}$ . The rate of the energy dissipation is expressed as:

$$\begin{aligned}\dot{W}_{d-\log}'' &= \int_{\widehat{HF}} c \dot{u} \cos \phi \frac{r d\theta}{\cos \phi} = c \omega \int_{\widehat{HF}} r^2 d\theta = c \omega r_0^2 \int_{\theta_h}^{\theta_c} e^{2 \tan \phi (\theta - \theta_0)} d\theta \\ &= \frac{c \omega r_0^2}{2 \tan \phi} \left[ e^{2 \tan \phi (\theta_h - \theta_0)} - 1 \right] e^{2 \tan \phi (\theta_c - \theta_0)} = c \omega r_0^2 f_{d-\log}''(\theta_0, \theta_c, \theta_h)\end{aligned}\quad (5-35)$$

Equating the rate of external work to the rate of energy dissipation leads to:

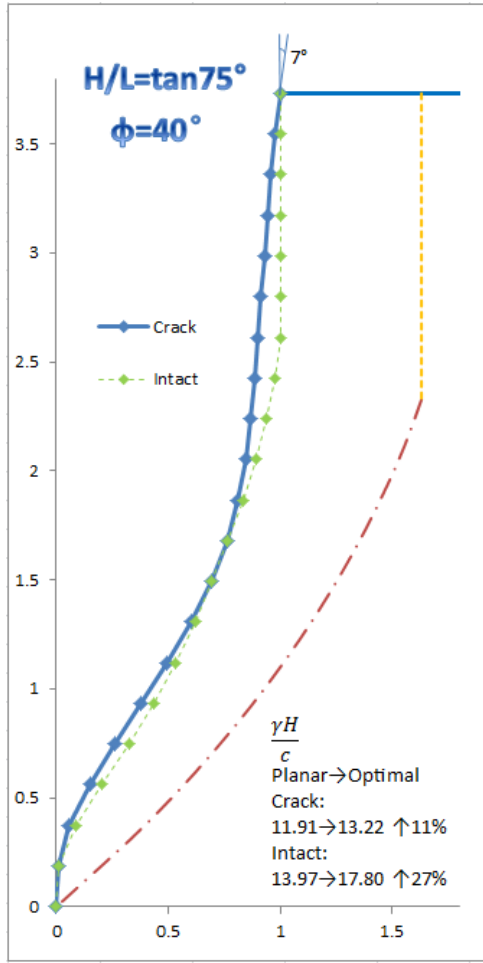
$$\dot{W}_\gamma = \omega \gamma r_0^3 (f_1 - f_2 - f_{3,n} - f_4 - f_5 + f_6 + f_7) = \dot{W}_{d-\log}'' = c \omega r_0^2 f_{d-\log}'' \quad (5-36)$$

After rearranging, the stability factor of a slope of an arbitrary profile considering the presence of cracks is derived:

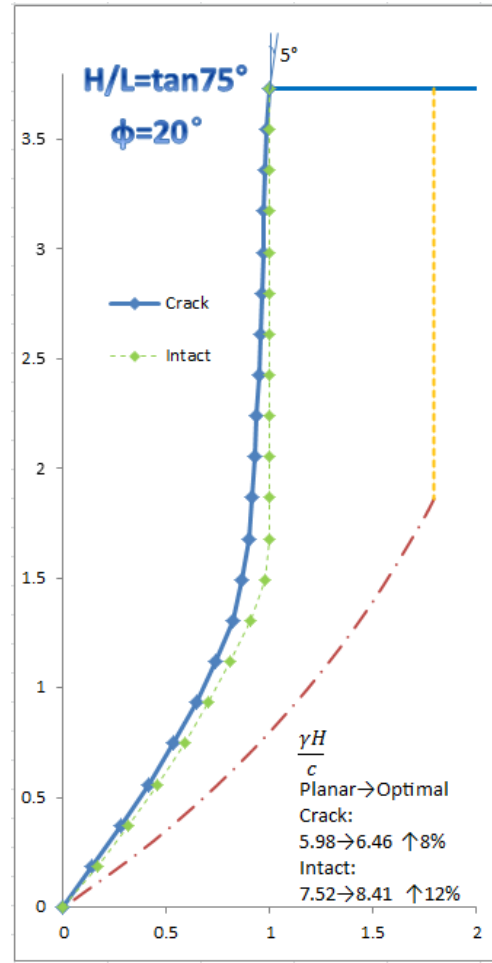
$$\frac{\gamma H}{c} = \frac{f_{d-\log}'' \times f_H}{f_1 - f_2 - f_{3,n} - f_4 - f_5 + f_6 + f_7} \quad (5-37)$$

The least upper bound is minimized over all possible values of  $\theta_0, \theta_h, \theta_c$  and  $\beta'$  of engineering interests. In the following calculation, the case of horizontal upper slope ( $\alpha = 0$ ) and the most adverse pre-existing cracks are considered.

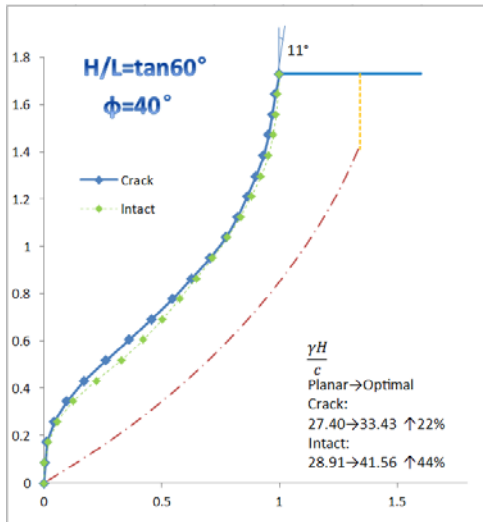
The optimal profiles of cracked slopes are obtained by the genetic algorithm described in section 5.3. The objective function to be maximized is the stability factor defined in Eq. (5-37). In Figure 5-26, the optimal profiles considering the presence of pre-existing cracks corresponding to various values of  $\frac{H}{L}$  and friction angles are presented. The optimal profiles of intact slopes are also plotted in Figure 5-26 as reference. The presence of cracks alters the shape of the optimal profiles in such a way that the profile near the crest is no longer vertical but becomes sub-vertical. This is because the presence of cracks makes the upper part of the slopes more prone to failure. From the results obtained, it emerges that the presence of cracks reduces the improvement given by adopting an optimal profile over a planar one. For instance, for intact slopes, optimal profiles increase the stability factors by up to 39% ( $\frac{H}{L} = \tan 45^\circ, \phi = 20^\circ$ ) and 27% ( $\frac{H}{L} = \tan 75^\circ, \phi = 40^\circ$ ) over planar ones. However, if the presence of cracks is considered, the optimal profiles of cracked slopes can only improve the stability factor by 36% ( $\frac{H}{L} = \tan 45^\circ, \phi = 20^\circ$ ) and 11% ( $\frac{H}{L} = \tan 75^\circ, \phi = 40^\circ$ ) in comparison with cracked planar slopes, less than the improvement in the intact case.



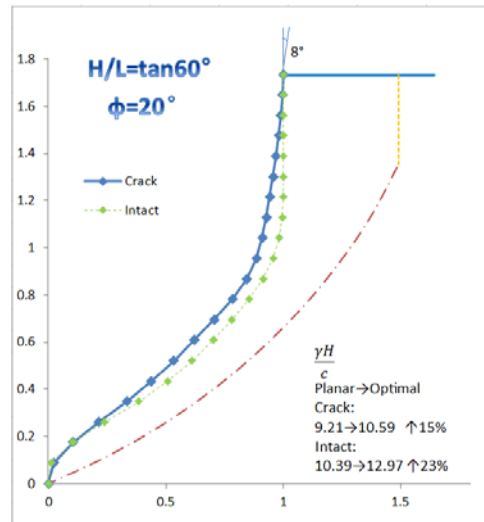
(a)  $\frac{H}{L} = \tan 75^\circ, \phi = 40^\circ$



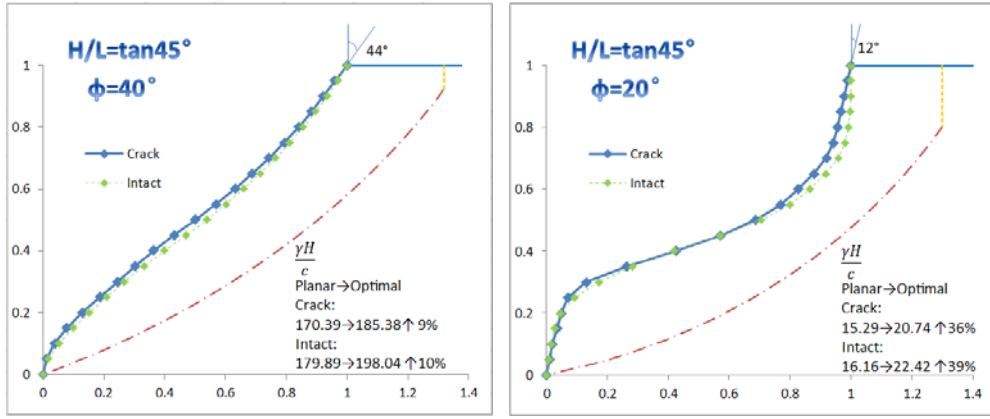
(b)  $\frac{H}{L} = \tan 75^\circ, \phi = 20^\circ$



(c)  $\frac{H}{L} = \tan 60^\circ, \phi = 40^\circ$

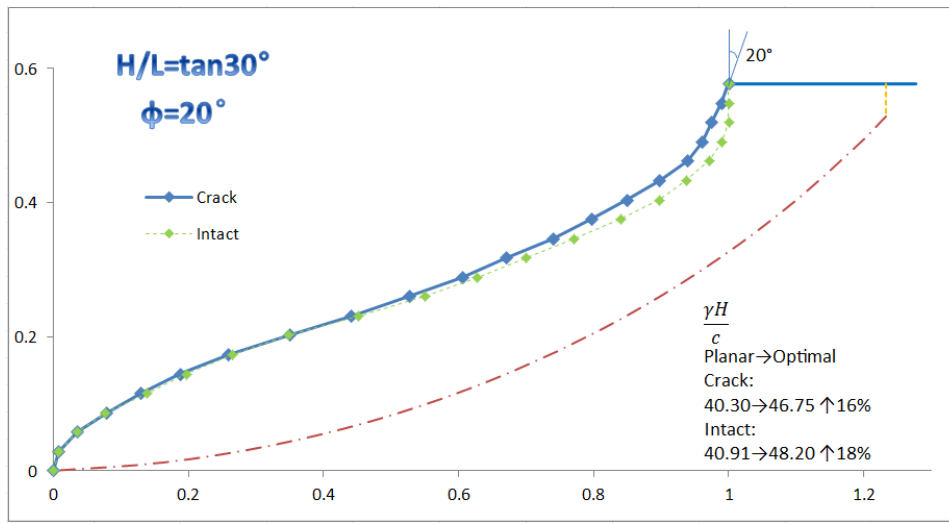


(d)  $\frac{H}{L} = \tan 60^\circ, \phi = 20^\circ$



$$(e) \frac{H}{L} = \tan 45^\circ, \phi = 40^\circ$$

$$(f) \frac{H}{L} = \tan 45^\circ, \phi = 20^\circ$$



$$(g) \frac{H}{L} = \tan 30^\circ, \phi = 20^\circ$$

Figure 5-26. Optimal profiles for cracked slopes.

## 5.9 The effect of non-homogeneity and anisotropy of the ground on optimal slopes

In practice, slopes are excavated in different ground conditions. In this section, the influence of ground strength anisotropy and spatial non-homogeneity in the vertical direction on the optimal profiles is investigated, using the methodology presented in section 3.4. The stability factor  $N_{M-C}$  defined in Eq. (5-16) is extended to accommodate the different expressions for the energy dissipation along the failure

surface caused by the spatially varying cohesion (according to Eq. (3-73)) and is rewritten as:

$$\frac{\gamma H}{c} = \frac{(q_1 + q_2 + q_3) \times f_H}{f_1 - f_2 - f_{3,n} - f_4} \quad (5-38)$$

where  $q_1 \sim q_3$  are defined in Eqs. (3-64) ~ (3-66).

Optimal profiles accounting for ground non-homogeneity and anisotropy are determined by the genetic algorithms described in section 5.3. The objective function to be maximized is the stability factor defined in Eq. (5-38). In Figure 5-28, the optimal profiles corresponding to four different cases of linearly varying cohesion (see Figure 5-27 (b),  $n_0 = 0, 0.25, 0.5, 0.75$ ) and uniform cohesion within soil slopes are illustrated. Comparing slopes featured by the same value of  $\phi$ , but different spatial distributions of cohesion, it emerges that the optimal profiles for all cases are similar to each other. In other words, the optimal profiles obtained in section 5.3 are applicable to slopes made of non-homogenous and anisotropic materials, which is another important characteristic of optimal profiles. It appears that the shapes of optimal profiles are predominately governed by the ground internal friction angle rather than the spatially distribution of cohesion.

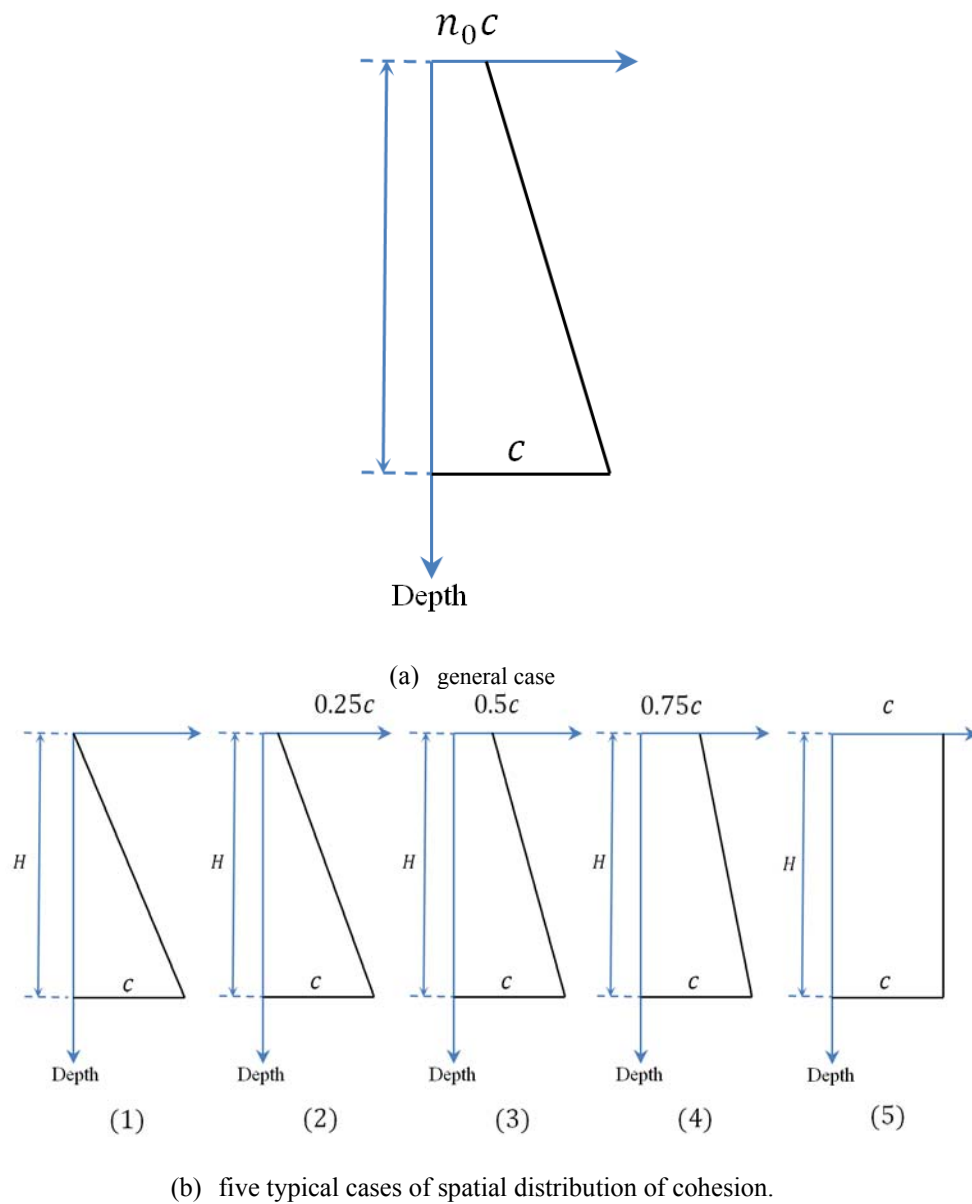
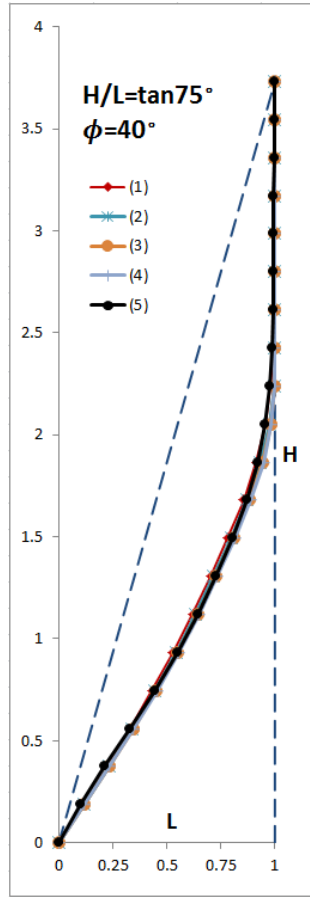
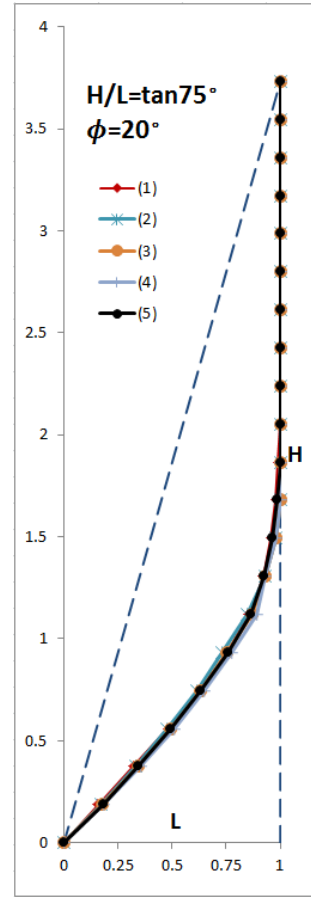


Figure 5-27. Spatial distribution of cohesion varying linearly with depth.

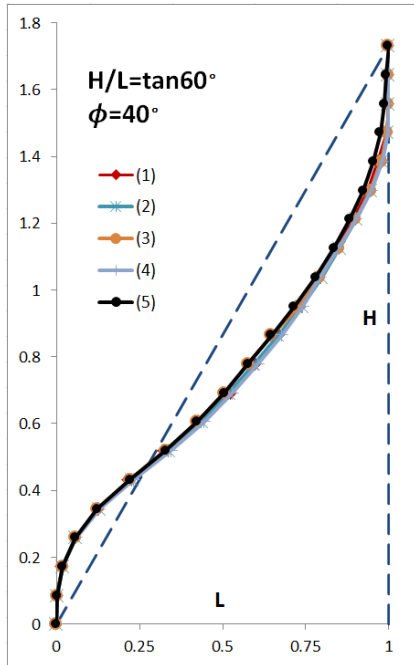




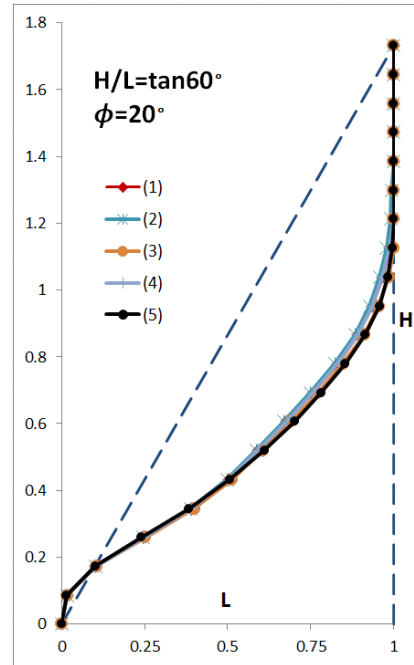
(a)  $\frac{H}{L} = \tan 75^\circ, \phi = 40^\circ$



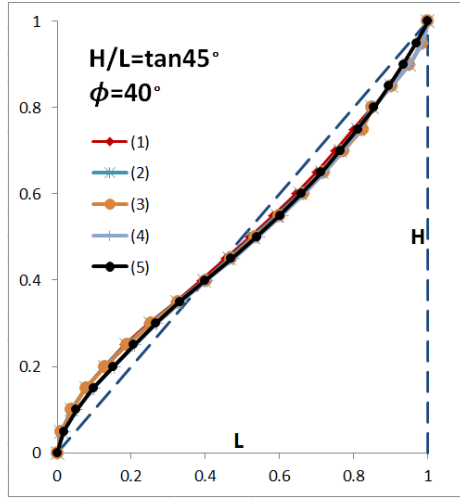
(b)  $\frac{H}{L} = \tan 75^\circ, \phi = 20^\circ$



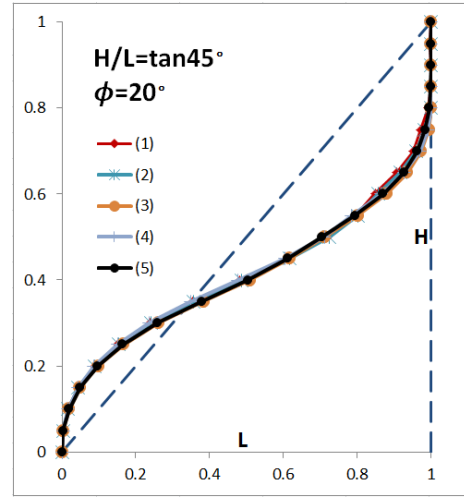
(c)  $\frac{H}{L} = \tan 60^\circ, \phi = 40^\circ$



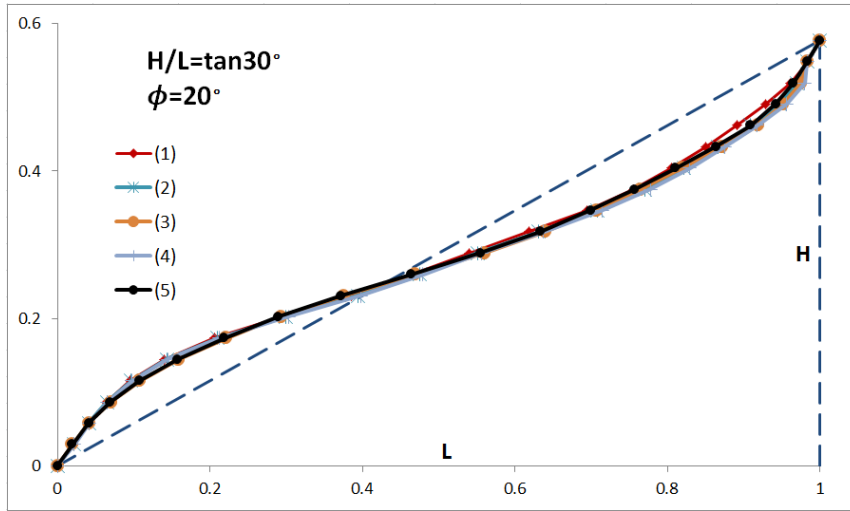
(d)  $\frac{H}{L} = \tan 60^\circ, \phi = 20^\circ$



(e)  $\frac{H}{L} = \tan 45^\circ, \phi = 40^\circ$



(f)  $\frac{H}{L} = \tan 45^\circ, \phi = 20^\circ$



(g)  $\frac{H}{L} = \tan 30^\circ, \phi = 20^\circ$

Figure 5-28. Optimal profiles in non-homogenous and anisotropic grounds for various  $\frac{H}{L}$  and  $\phi$ . Five typical cases of spatial distributions correspond to those in Figure 5-27 (b).

## 5.10 The optimal profiles of slopes made of rock obeying the Hoek-Brown failure criterion

In this section, the continuum equivalent approach is employed to characterize rock slopes obeying the Hoek-Brown failure criterion. Using the tangential technique described in section 4.3, the stability factor of a rock slope of any arbitrary profile

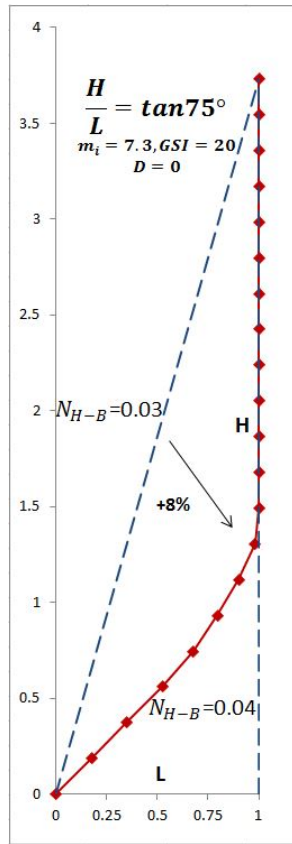
is obtained by extending the solutions corresponding to the Mohr-Coulomb failure criterion. Referring to Eqs.(5-16) and (4-8), the stability factor of a rock slope is defined as:

$$\begin{aligned}
 N_{H-B} &= \frac{\gamma H}{\sigma_{ci}} = \frac{\gamma H}{c_t} \cdot \frac{c_t}{\sigma_{ci}} = N_{M-C} \Big|_{\phi=\phi_t} \cdot \frac{c_t}{\sigma_{ci}} \\
 &= \frac{f_{d-\log} \times f_H}{f_1 - f_2 - f_{3,n} - f_4} \\
 &\quad \times \left\{ \frac{\cos \phi_t}{2} \left[ \frac{mn(1 - \sin \phi_t)}{2 \sin \phi_t} \right]^{n/(1-n)} \right. \\
 &\quad \left. - \frac{\tan \phi_t}{m} \left( 1 + \frac{\sin \phi_t}{n} \right) \left[ \frac{mn(1 - \sin \phi_t)}{2 \sin \phi_t} \right]^{1/(1-n)} + \frac{s}{m} \tan \phi_t \right\}
 \end{aligned} \tag{5-39}$$

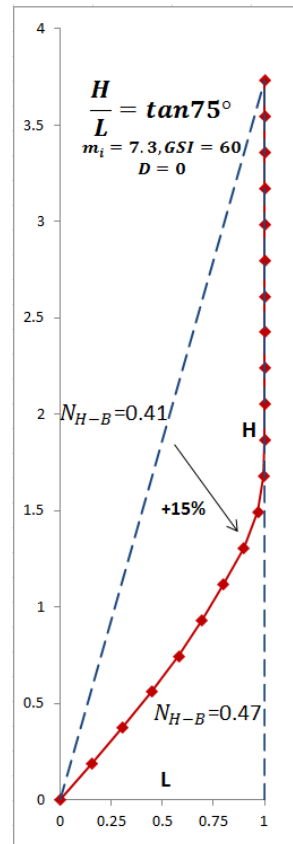
where  $\phi_t$  is the dip angle of the tangent to the Hoek-Brown failure envelope in  $(\tau, \sigma)$  stress space.  $m$ ,  $s$  and  $n$  are material parameters defined in Eqs. (4-2)-(4-4).  $\sigma_{ci}$  is the uniaxial compression strength for intact rock. The minimization of Eq. (5-39) is now carried out over the same valuables as in Eq. (5-16) with the addition of  $\phi_t$ .

The optimal profiles of slopes made of rock obeying the Hoek-Brown failure criterion are obtained by the genetic algorithm described in section 5.3. The objective function to be maximized is the stability factor defined in Eq. (5-39). In Figure 5-29, the shapes of the optimal profiles with various assigned  $\frac{H}{L}$  are present. How the optimal profiles evolve with different rock types is illustrated in Figure 5-29. Compared with soil slopes in section 5.4, the optimal profiles of rock slopes present similar trends. For steep slopes made of weak rock with  $\frac{H}{L} = \tan 75^\circ$ , the optimal profiles turn out to be all concave in the cases of (a) ~ (c) in Figure 5-29. However, for all other cases, the optimal profiles exhibit both a concave and a convex part. The stability factors defined in Eq. (5-39) for slopes of both the planar and the optimal profiles are reported in Figure 5-29 as well. Compared with the

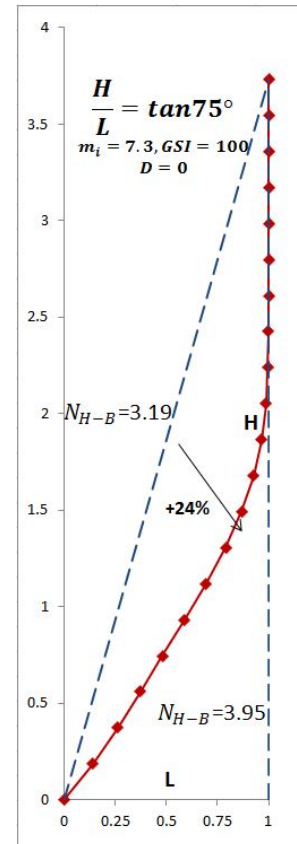
planar slopes, there is a significant increase in terms of the stability factor. The percentage of increase is plotted against  $\beta$  corresponding to different values of  $m_i$  and  $GSI$  in Figure 5-30 and Figure 5-31. The percentage of increase rises from 0 which corresponds to vertical slopes to a maximum value, and then drops. The maximum value of the percentage in Figure 5-30 can reach up to 55% when  $m_i = 26.2, GSI = 100, \beta = 60^\circ$ .



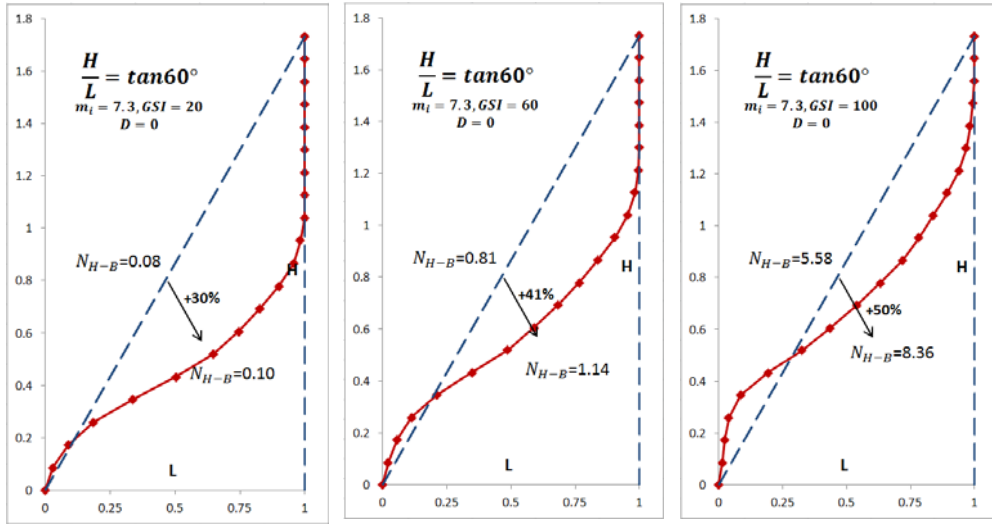
(a)  $\frac{H}{L} = \tan 75^\circ, GSI = 20$



(b)  $\frac{H}{L} = \tan 75^\circ, GSI = 60$



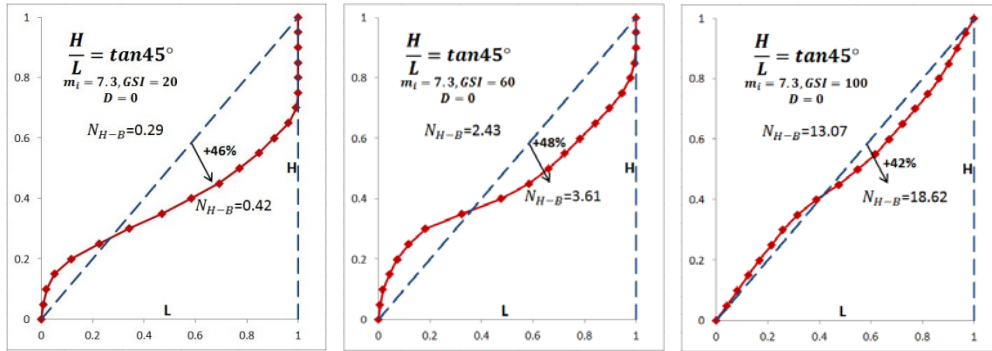
(c)  $\frac{H}{L} = \tan 75^\circ, GSI = 100$



(d)  $\frac{H}{L} = \tan 60^\circ, GSI = 20$

(e)  $\frac{H}{L} = \tan 60^\circ, GSI = 60$

(f)  $\frac{H}{L} = \tan 60^\circ, GSI = 100$



(g)  $\frac{H}{L} = \tan 45^\circ, GSI = 20$

(h)  $\frac{H}{L} = \tan 45^\circ, GSI = 60$

(i)  $\frac{H}{L} = \tan 45^\circ, GSI = 100$

Figure 5-29. Optimal profiles of different rock slopes with different assigned  $\frac{H}{L}$ .

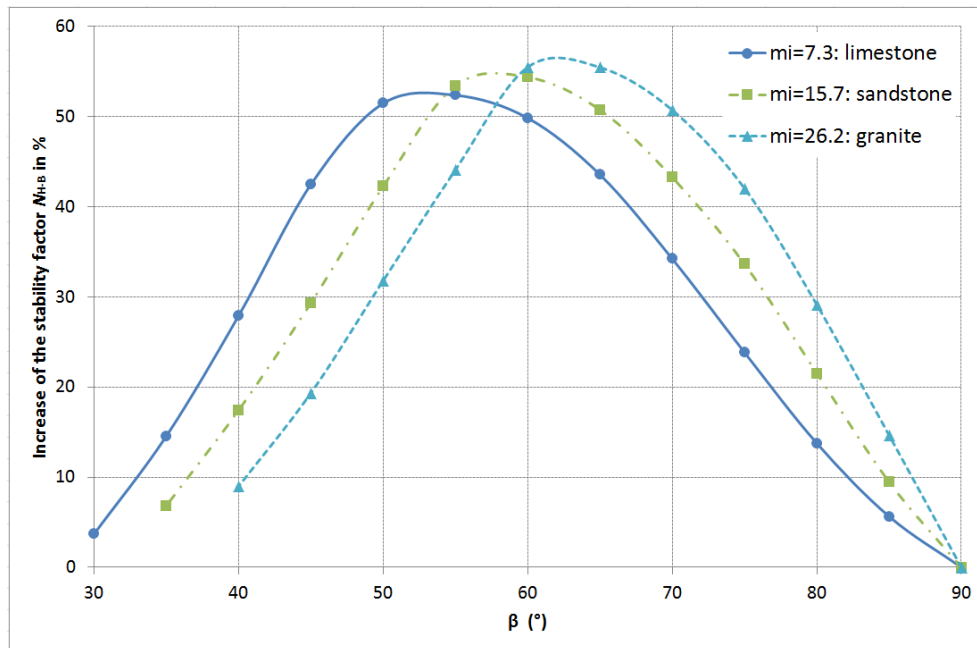


Figure 5-30. Percentage of increase of stability factor against  $\beta$  for different values of  $m_i$ ,

$$GSI = 100.$$

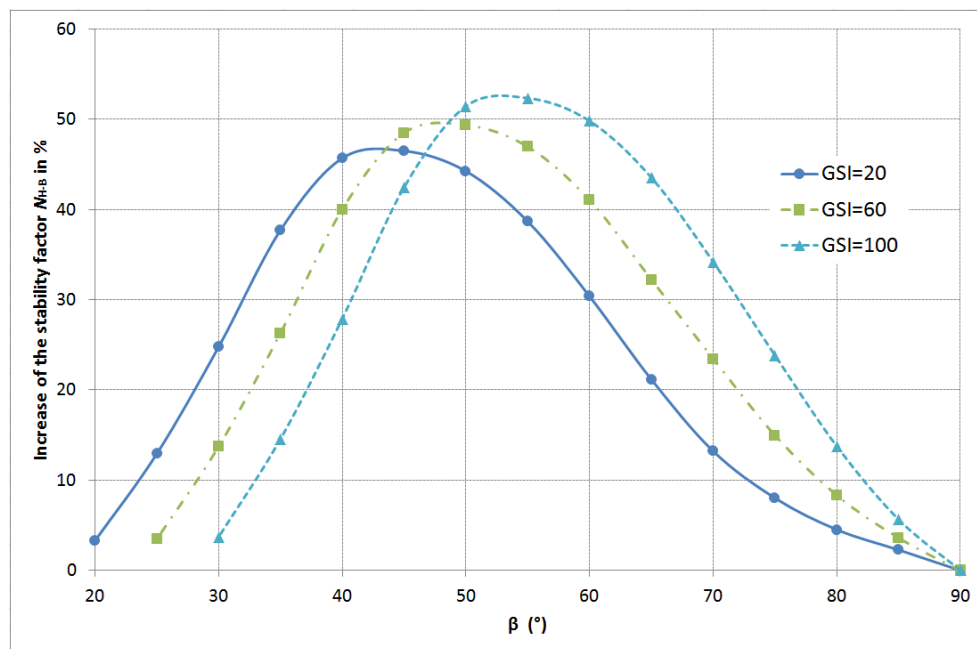


Figure 5-31. Percentage of increase of stability factor against  $\beta$  for different values of  $GSI$ ,

$$m_i = 7.3.$$

### 5.11 The effect of blast-induced damage on rock slopes

In geotechnical problems involving man-made slope excavations such as open cast mine, rock slopes are routinely excavated with controlled blasting, which inevitably causes damage to the rock strength. In this section, the optimal profiles of slopes made of rock obeying the Hoek-Brown failure criterion subjected to blast-induced damage are investigated. Recalling section 4.3, the tangential technique is employed.

Consistent with the assumptions adopted in section 4.6, the disturbance coefficient  $D_d$  along the excavation face is assumed to be constant. The rock strength of each point within the rock mass is assumed to vary linearly proportional with its distance to the excavation face (Marinos et al., 2005; Li et al., 2011). The spatial distribution of the blast-induced damage in the rock is illustrated in Figure 5-32. The affected area due to blasting can be divided into three zones. In Zone 1, the disturbance factor  $D$  varies linearly along the horizontal direction, from  $D_d$  at the crest to  $D_i$  (the value for undamaged rock, in most cases  $D_i = 0$ ) at a distance of  $H$ . In Zone 2, the disturbance factor  $D$  varies linearly along a direction  $(\frac{\pi}{2} - \beta$  to the horizontal), from  $D_d$  on the slope face to  $D_i$  at a distance of  $H$  from the slope profile. In Zone 3, the disturbance factor  $D$  varies linearly with depth, from  $D_d$  on the surface to  $D_i$  at the depth of  $H \times \cos \beta$ .

To include the non-homogeneity of rock strength within slopes caused by blasting in the limit analysis upper bound approach, the disturbance coefficient at each angle along the potential failure surface (governed by  $\theta_0$  and  $\theta_h$ , see Figure 5-32) can be expressed as:

$$D(\theta) = \begin{cases} \frac{H - r_0 \cdot x(\theta)}{H} \cdot (D_d - D_i) + D_i, \\ \text{if } y(\theta) > \frac{H}{r_0} \cdot \left(1 + \frac{1}{\tan^2 \beta}\right) - \frac{x(\theta)}{\tan \beta} \quad (\text{zone 1}) \\ \frac{H - [r_0 \cdot e^{\tan \phi_i (\theta - \theta_0)} - P(\theta)] \cdot \sin(\beta + \theta)}{H} \cdot (D_d - D_i) + D_i, \\ \text{if } y(\theta) < -\frac{x(\theta)}{\tan \beta} \quad (\text{zone 2}) \\ \frac{H + r_0 \cdot y(\theta) \cdot \cos \beta}{H} \cdot (D_d - D_i) + D_i, \\ \text{zone 3} \end{cases} \quad (5-40)$$

where  $y(\theta)$  and  $x(\theta)$  are defined in Eqs. (4-43) and (4-44) respectively.  $P(\theta)$  represents the geometry of the optimal profile in the polar coordinates with  $O$  as its center.

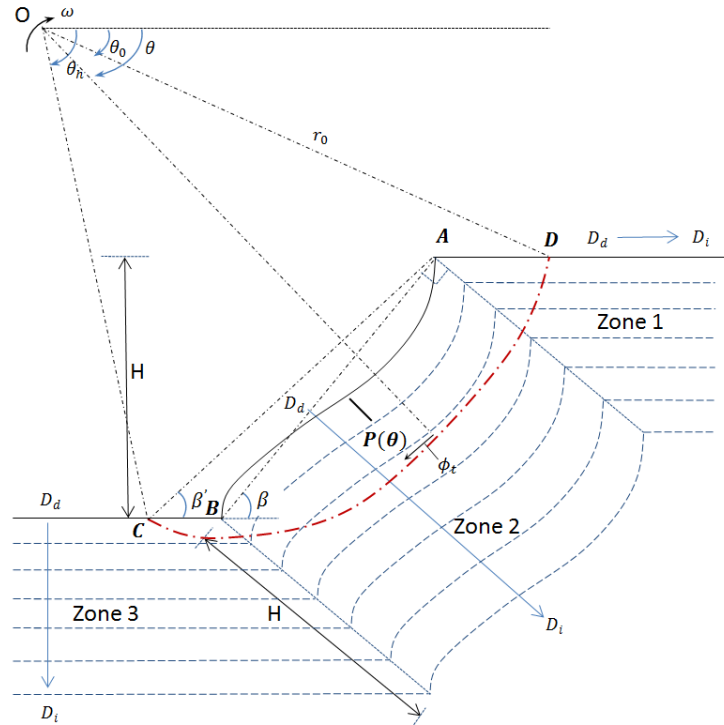


Figure 5-32. The distribution of the disturbance coefficient  $D$  in a non-homogeneous rock slope subjected to blasting.



For rock slopes subjected to blasting, the material parameters obeying the Hoek-Brown failure criterion are no longer constants within the slope but vary with  $\theta$ . They are written as follows:

$$m(\theta) = m_i \exp\left(\frac{GSI - 100}{28 - 14D(\theta)}\right) \quad (5-41)$$

$$s(\theta) = \exp\left(\frac{GSI - 100}{9 - 3D(\theta)}\right) \quad (5-42)$$

$$\begin{aligned} \frac{c_t(\theta)}{\sigma_{ci}} &= \frac{\cos \phi_t}{2} \left[ \frac{m(\theta)n(1 - \sin \phi_t)}{2 \sin \phi_t} \right]^{n/(1-n)} \\ &- \frac{\tan \phi_t}{m(\theta)} \left( 1 + \frac{\sin \phi_t}{n} \right) \left[ \frac{m(\theta)n(1 - \sin \phi_t)}{2 \sin \phi_t} \right]^{1/(1-n)} + \frac{s(\theta)}{m(\theta)} \tan \phi_t \end{aligned} \quad (5-43)$$

where  $n$  is defined in Eq. (4-4).

The rate of the energy dissipation along the failure line  $\widehat{CD}$  is:

$$\int_{\widehat{CD}} c_t(\theta) \dot{u} \cos \phi_t \frac{rd\theta}{\cos \phi_t} = \omega r_0^2 \int_{\theta_0}^{\theta_h} c_t(\theta) e^{2 \tan \phi_t (\theta - \theta_0)} d\theta \quad (5-44)$$

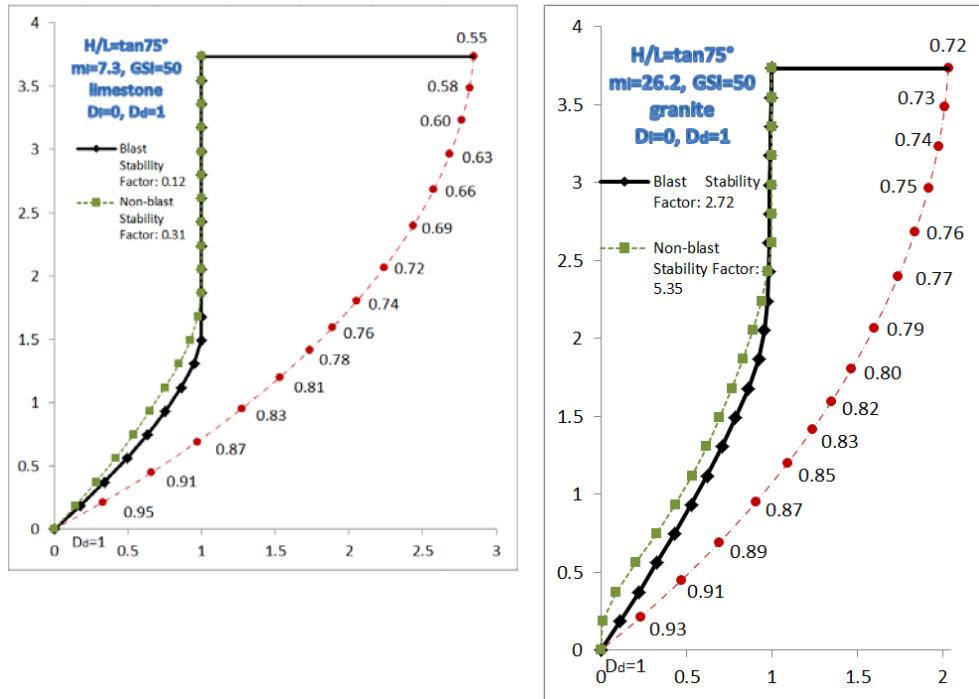
Equating the rate of external work (written in Eq. (5-5)) to the rate of energy dissipation, leads to:

$$\omega \gamma r_0^3 (f_1 - f_2 - f_{3,n} - f_4) = \omega r_0^2 \int_{\theta_0}^{\theta_h} c_t(\theta) e^{2 \tan \phi_t (\theta - \theta_0)} d\theta \quad (5-45)$$

Dividing by  $\omega$  and  $r_0^2$  and rearranging, the stability factor of rock slopes of any arbitrary profile subjected to blast-induced damage is obtained:

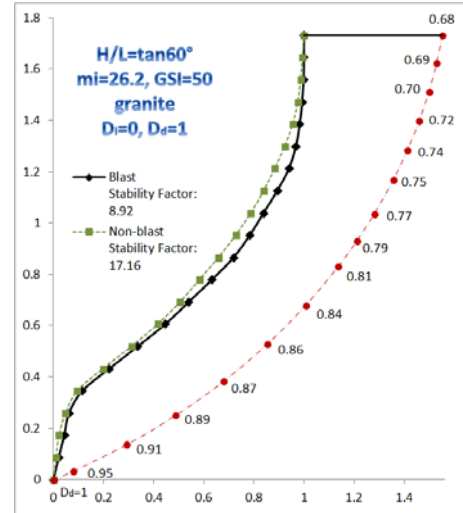
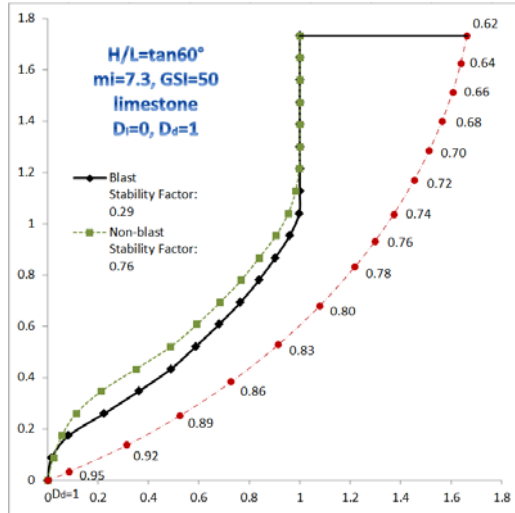
$$\frac{\gamma H}{\sigma_{ci}} = \frac{f_H}{(f_1 - f_2 - f_{3,n} - f_4)} \cdot \int_{\theta_0}^{\theta_h} \frac{c_i(\theta)}{\sigma_{ci}} \cdot e^{2 \tan \phi_i (\theta - \theta_0)} d\theta \quad (5-46)$$

The optimal profiles of slopes made of material obeying the Hoek-Brown failure criterion drilled by blasting are obtained by the genetic algorithm described in section 5.3. The objective function to be maximized is the stability factor defined in Eq. (5-46). In Figure 5-33, the optimal rock slopes with different assigned values of  $\frac{H}{L}$  are present. The disturbance coefficients along the failure surface are provided as reference. It turns out that blast-induced damage can significantly reduce the stability factor and alter the shape of the optimal profile. For example, for a rock slope whose  $\frac{H}{L} = \tan 45^\circ$ ,  $m_i = 7.3$ ,  $GSI = 50$ ,  $D_i = 0$  and  $D_d = 1$ , the stability factor defined in Eq. (5-46) is only 39% of a slope excavated without blasting.



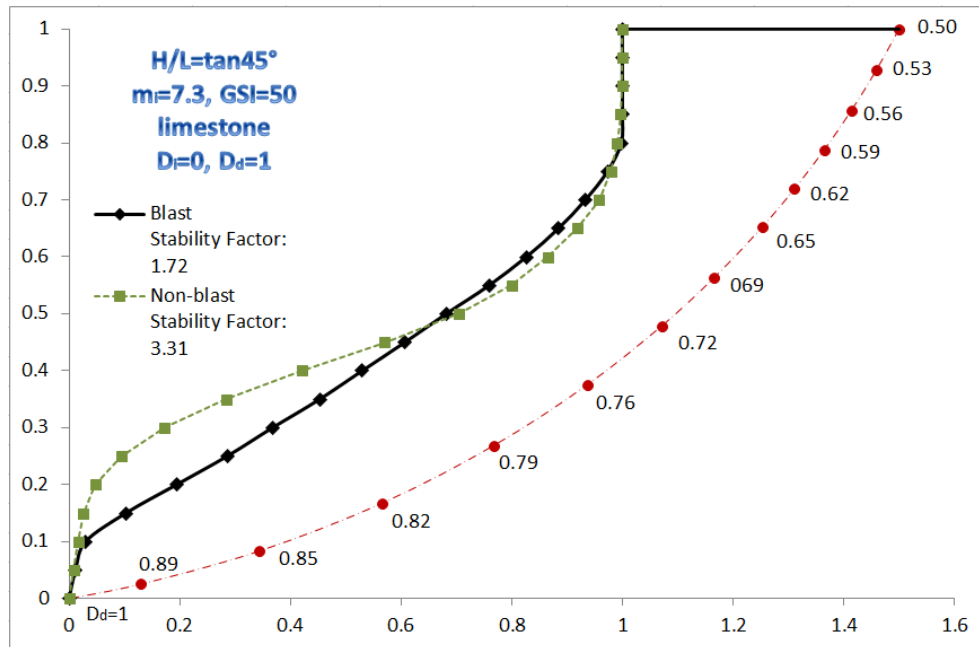
(a)  $\frac{H}{L} = \tan 75^\circ$ ,  $m_i = 7.3$ : limestone

(b)  $\frac{H}{L} = \tan 75^\circ$ ,  $m_i = 26.2$ : granite

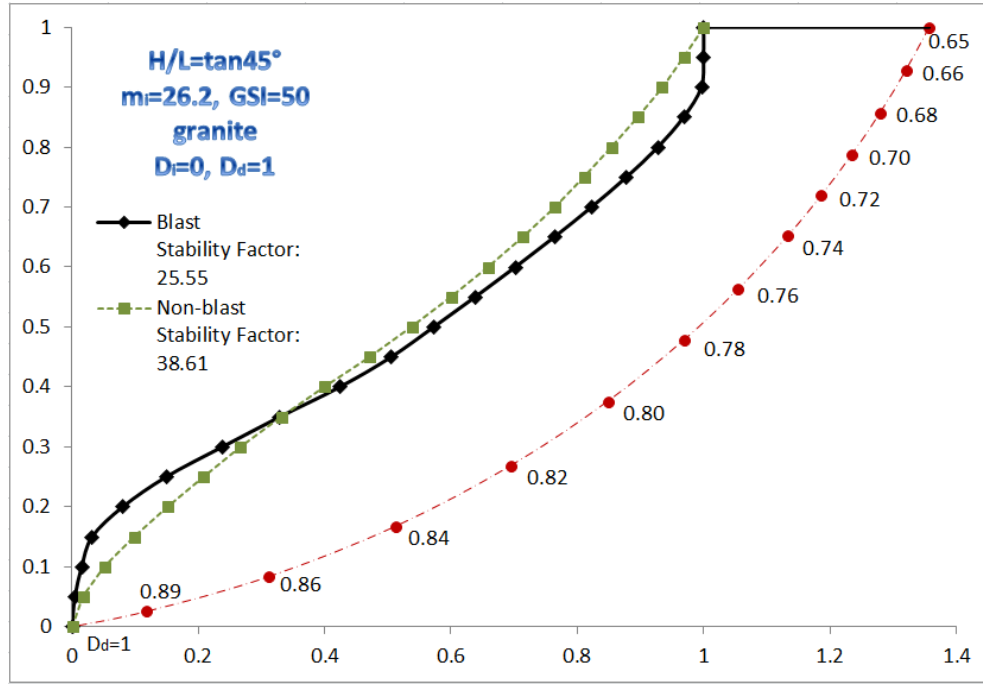


(c)  $\frac{H}{L} = \tan 60^\circ, m_i = 7.3$ : limestone

(d)  $\frac{H}{L} = \tan 60^\circ, m_i = 26.2$ : granite



(e)  $\frac{H}{L} = \tan 45^\circ, m_i = 7.3$ : limestone



$$(f) \frac{H}{L} = \tan 45^\circ, m_i = 26.2: \text{granite}$$

Figure 5-33. Optimal profiles of rock slopes under blasting.  $GSI = 50, D_i = 0, D_d = 1$ .

## 5.12 Conclusions

In this chapter, arbitrary slope profiles are represented by piecewise lines between nodal points determined by an equally spaced discretization along the horizontal direction. Under the constraint of fixed crest and toe, genetic algorithm and pattern search were adopted for locating the optimal profile among all possible candidate profiles. The following conclusions can be drawn:

(a) Previous literature (e.g., Utili and Nova 2007, Jeldes et al. 2013) searched for the optimal profile among concave types of slopes. From this study instead, it turns out that the optimal profiles of  $c - \phi$  slopes exhibit both a concave and a convex part. In comparison with the traditional planar profiles, the percentage of increase of the stability factor can reach up to 49%. In addition, given the same stability factor, the average slope inclination of an optimal slope is always higher

than that of a planar slope. The amount of ground excavated for the optimal profile can be as little as 50% of that for a planar profile.

(b) For all the average slope inclinations considered, the optimal slopes turn out to be better than the optimal logarithmic spiral slopes (Utili and Nova 2007) and the optimal concave slopes (Jeldes et al. 2013 and Jeldes et al. 2014) in terms of their stability. This can be explained by the fact that for the first time the search for the optimal shape is not constrained to any particular class of shapes.

(c) Potential overestimation of slope stability due to use of a semi-analytical approach to assess the slope stability factor based upon upper bound limit analysis, and the assumption of associative flow rule were examined. The error is estimated within 6% according to the validations performed by finite element limit analysis and displacement-based finite element method with strength reduction technique.

(d) The geometrical properties of the optimal profiles including the average inclination corresponding to when the convex part of an optimal profile vanishes are investigated. Key geometric parameters to abstract the highly non-linear optimal profiles are provided. The area of yielded elements (in finite element strength reduction modelling) within optimal slopes is much larger than that within the planar slopes, which means the ground strength is better utilized in optimal slopes.

(e) Since the new upper bound formulation is capable of computing the stability factors of slopes of any arbitrary shape, the stability of the profile to be excavated can be monitored during the whole construction period. Optimal profiles exhibit a peculiar property: near full mobilization of the ground strength occurs in a large region within the slope rather than a thin shear band only. The stability factor of the excavated part after reaching a critical depth tends to remain constant with the progression of the excavation.

(f) A method to find the maximum factor of safety for engineered slopes for prescribed ground properties and assigned  $\frac{H}{L}$ , as well as the maximum inclination of slopes under prescribed factors of safety is provided.

(g) An analytical approach to calculating the optimal slope profiles in the presence of cracks is provided. The presence of cracks can alter the shapes of optimal slopes and reduce its capacity to increase slope stability.

(h) An analytical approach to account for the optimal slope profiles in non-homogenous and anisotropic grounds is put forward. The optimal profiles obtained for uniform  $c - \phi$  slopes are also applicable for anisotropic slopes whose cohesion varies linearly with depth.

(i) For slopes made of rock obeying the Hoek-Brown failure criterion, the optimal profiles have both a concave and a convex part as well. An analytical approach to tackle the impact of blast-induced damage is laid out. If rock slopes are excavated by blasting, the damage caused will inevitably alter the shapes of the optimal profiles.

## Chapter 6 Optimal Design of Pile Reinforcement

When the factor of safety of a slope is considered to be insufficient, reinforcement measures will take place. In Chapter 5, finding the optimal profiles provides a solution to improve slope stability. However, excavating slopes following the optimal profiles requires sophisticated land-forming techniques such as auto-guidance construction equipment and advanced mapping technology. When they are not available, other reinforcement measures should be considered. Anti-sliding piles are widely implemented to stabilize slopes in practice. The slope-pile system brings new challenges to the existing slope stability assessment procedures considering the complexity of soil-pile interaction.

In the literature review in section 2.4, the results of all numerical analyses show that the optimal position of a row of piles is close to the middle of the slope. However, by using the combined limit equilibrium analysis and Ito-Matsui's formula (Ito and Matsui 1975), the optimal position approaches the top of the slope. Moreover, according to the results obtained by means of the analytical limit analysis method, the optimal position is near the toe of the slope. The discrepancies are ascribed to how the resistance force provided by the anti-sliding piles is considered and what type of the failure mechanism is assumed in the formulations. The presence of piles is treated as an equivalent force and a moment in the analytical solutions such as Hassiotis et al. (1997), Ausilio et al. (2001) and Li et al. (2012) but the influence of the soil-pile interaction is neglected. As pointed out by Wei and Cheng (2009), the critical failure surface is divided into two sections when the pile spacing is small, and these two sections will gradually connect with the increase of pile spacing until a clear single critical failure surface is formed. However, in all the analytical solutions (limit equilibrium method and limit

analysis), the failure surfaces are assumed beforehand as a continuous circular or logarithmic spiral line.

As stated in Li et al. (2012), the investigation of the optimal position of a row of piles in slope stabilization can be divided into two categories: the most effective pile location and the location of the pile ensuring the maximum factor of safety.

In Ausilio et al. (2001), Nian et al. (2008) and Li et al. (2012), the most effective pile location is defined as the place where the stabilizing force needed to increase factor of safety to a desired value takes the minimum value. All the above studies conclude that the most effective pile location is somewhere around the slope toe. However, for piles placed near the toe, it is entirely possible that the buried depth is so small that the capacity of piles cannot be fully utilized or above-pile failure can happen, which makes the pile installation completely ineffective as shown in Figure 6-1. In this chapter, the most effective location of the stabilizing piles is reappraised by considering both the above-pile and pass-through-pile failure mechanisms. It turns out that the stabilizing piles have to be installed within certain range to avoid above-pile failure.

According to Hassiotis et al. (1997), Li et al. (2009c) and Li et al. (2012), by assuming that the piles are long enough, built with prescribed materials, installed with certain diameter and spacing, the stabilizing force that a row of piles can provide is proportional to their buried depth. In this case, given a row of piles, the optimal position corresponds to the location yielding maximum factor of safety.

For the sake of conciseness, the most effective pile location will be referred as case 1 and the location of the pile ensuring the maximum stability factor will be referred as case 2 in the following. In this chapter, design charts illustrating both case 1 and case 2 are provided based on the kinematic approach of limit analysis. The effect of the presence of pre-existing cracks, pore water pressure and seismic actions is discussed. Finally, the optimal position of piles corresponding to the



location yielding the minimum accumulative displacement during an earthquake is evaluated.

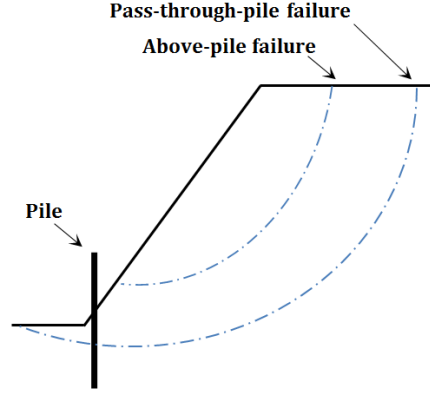


Figure 6-1. Above-pile and pass-through-pile failure mechanisms.

## 6.1 The most effective pile location

The stability of slopes without pile reinforcement is assessed in Chapter 3 and Chapter 4. In this section, slopes reinforced with a row of piles are investigated. In the two dimensional plain strain case, one pile is inserted into the slope to provide stabilization (see Figure 6-2). The failure surface is still assumed to be a logarithmic spiral line, and the following geometrical relationship can be found in Figure 6-2:

$$r_p = r_0 e^{\tan \phi (\theta_p - \theta_0)} \quad (6-1)$$

$$L_t = H \frac{\sin(\beta - \beta')}{\sin \beta \sin \beta'} \quad (6-2)$$

$$x_p = r_p \cos \theta_p - r_h \cos \theta_h - L_t \quad (6-3)$$

$x_p$  is the pile location measured from the slope toe. The total height of buried depth

$h_b$  of the piles varies with  $x_p$  and is written as:

$$h_b = \begin{cases} r_p \sin \theta_p - r_h \sin \theta_h & -L_t \leq x_p < 0 \\ r_p \sin \theta_p - r_h \sin \theta_h + x_p \tan \beta & 0 \leq x_p < H \cot \beta \\ r_p \sin \theta_p - r_h \sin \theta_h + H + (x_p - H \cot \beta) \tan \alpha & x_p > H \cot \beta \end{cases} \quad (6-4)$$

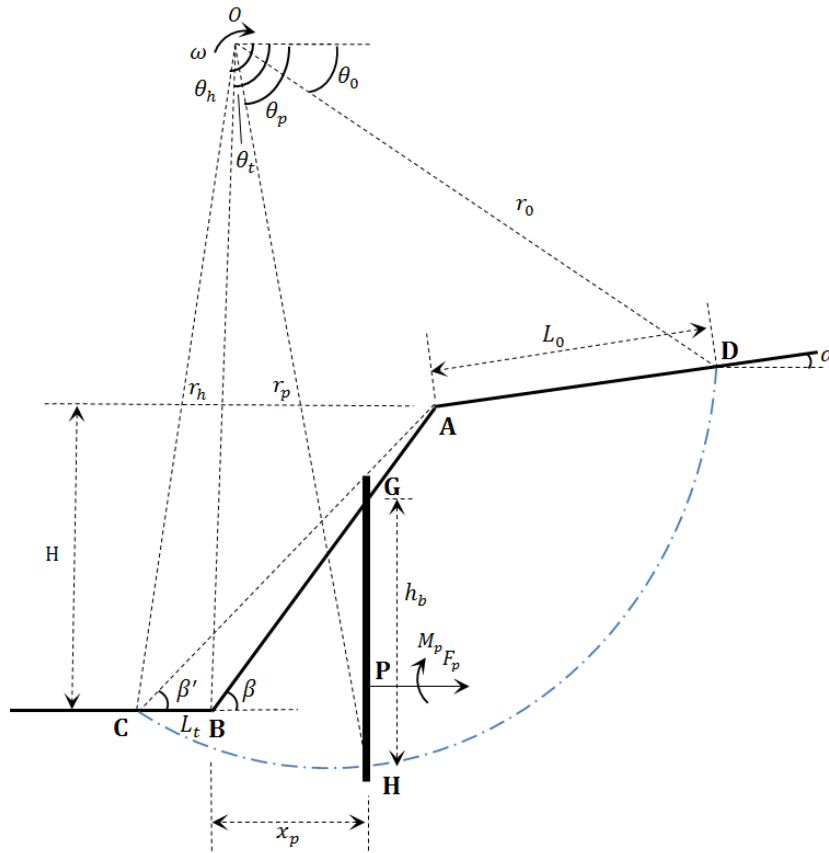


Figure 6-2. Failure mechanism for a slope reinforced with a row of piles (plain strain case).

Considering the mass **ABCD** rigidly sliding away about the centre of rotation **O**, the energy dissipation of the pile-slope system includes both the dissipated energy along the failure mechanism **CD** and the stabilizing work brought from pile

reinforcement (represented by an equivalent horizontal lateral force per unit width and a moment).

The rate of additional stabilizing work is expressed as:

$$\dot{W}_{p,1} = \omega F_{p,1} \left[ \sin \theta_p r_0 e^{\tan \phi (\theta_p - \theta_0)} - M_{p,1} \right] = \omega F_{p,1} f_{p,1} \quad (6-5)$$

where  $F_{p,1}$  and  $M_{p,1}$  are the equivalent lateral force and moment which are found by:

$$F_{p,1} = K_{pl} \frac{\gamma H^2}{2} \quad (6-6)$$

$$M_{p,1} = F_{p,1} m_F h_b \quad (6-7)$$

with  $K_{pl}$  a dimensionless coefficient indicating the magnitude of the stabilizing force.  $m_F$  is a coefficient representing the type of lateral pressure distribution along the pile, and  $m_F = \frac{PH}{GH}$  (see Figure 6-2). When lateral pressure is assumed to be linearly varying along the depth,  $m_F = 1/3$ . For rectangular distribution,  $m_F = 1/2$ . According to Poulos (1995), when  $m_F = 0$ , only the resistance force  $F_{p,1}$  is considered,  $M_{p,1} = 0$ .

Equating the rate of external work done by the material weight to the rate of internal energy dissipation due to cohesion and pile reinforcement, leads to:

$$\dot{W}_\gamma = \omega \gamma r_0^3 (f_1 - f_2 - f_3 - f_4) = \dot{W}_{d-\log} + \dot{W}_{p,1} = c \omega r_0^2 f_{d-\log} + \omega F_{p,1} f_{p,1} \quad (6-8)$$

where  $f_1, f_2, f_3, f_4$  are found in Eqs. (5-6), (5-7), (5-13) and (5-8).

After rearranging, the stability factor for a slope reinforced with a row of piles is expressed as:

$$N_{p,1} = \frac{\gamma H}{c} = \frac{f_H \times f_{d-\log}}{f_1 - f_2 - f_3 - f_4 - \frac{f_H^2}{2} K_{pl} f_{p,1}} \quad (6-9)$$

with  $f_H$  defined in Eq. (5-3),  $f_{d-\log}$  defined in Eq. (5-35). The least upper bound is found by the minimization of Eq. (6-9) with  $\theta_0$ ,  $\theta_h$  and  $\beta'$  denoting the most critical failure mechanism.

To achieve the desired value of factor of safety, the stabilizing force needed can be derived from Eq. (6-9):

$$K_{pl} = \frac{2 \left( f_1 - f_2 - f_3 - f_4 - \frac{f_H \times f_{d-\log}}{N_{p,1}} \right)}{f_H^2 \times f_{p,1}} \quad (6-10)$$

In Ausilio et al. (2001), Nian et al. (2008) and Li et al. (2012), the most effective pile location is found near the slope toe where the stabilizing force needed to increase the factor of safety to a desired value takes the minimum value. This conclusion can be restated that given the same magnitude of stabilizing force, the stability factor for a reinforced slope reaches a maximum value when the piles are placed near the slope toe. However, it is completely possible that for piles located at around the slope toe, the buried depth is so small that the capacity of piles cannot be fully utilized or above-pile failure can happen, which makes the pile installation completely ineffective. Thus, in this section, both above-pile and pass-through-pile failure mechanisms are considered, as shown in Figure 6-1. The stability factor corresponding to above-pile failure can be obtained by considering the sliding of an

unreinforced slope just above the piles whose height is  $H - h_p$ . It is worth noting that  $F_{p,1}$  is routinely assumed to act horizontally (e.g., Ausilio et al. 2001, Li et al. 2012). The case that  $F_{p,1}$  is tangent to the failure surface at the point  $H$  (where the piles intersect with the potential sliding surface) is investigated as well. The difference in terms of the stability factor defined in Eq. (6-9) is within 3%, thus  $F_{p,1}$  is still assumed to be horizontal in this section.

In Figure 6-3, by changing the pile location ( $x_p$ ), the stability factors defined in Eq. (6-9) are plotted against  $x_p$  of a slope reinforced with a row of piles whose  $K_{p1} = 0.1, \beta = 45^\circ$ . For illustrative purposes, the case of horizontal upper slope ( $\alpha = 0^\circ$ ) is considered, the friction angle of the material is specified as  $20^\circ$  and the lateral force distribution is assumed to be triangular ( $m_F = 1/3$ ). In Figure 6-3, the solid line represents the stability factors obtained by imposing failure mechanisms passing through the piles. The dotted line stands for the stability factors of the unreinforced slope just above the piles. The stability factors corresponding to the above-pile failure mechanisms are more critical than those corresponding to the pass-through-pile failure mechanisms until  $x_p = 0.46$ , which means that the slope is more likely to slide above the pile making the presence of piles completely ineffective when  $0 < x_p < 0.46$ . Ausilio et al. (2001), Nian et al. (2008) and Li et al. (2012) neglect the above-pile failure mechanism, which turns out to be critical for both slope-pile interaction analysis and the determination of the optimal pile position. The point where the solid line and dotted line intersects can be regarded as the most effective pile location, which yields the highest possible stability factor.

Design charts illustrating the most effective pile location are provided in Figure 6-4 for various slope inclinations and friction angles. For example, let a 15m tall slope with a  $30^\circ$  inclination be comprised of soil whose  $\phi = 15^\circ, c = 20 \text{ kN/m}^2$  and  $\gamma = 19.40 \text{ kN/m}^3$ . The desired factor of safety  $F$  is set to be 1.5.

The friction angle at failure is  $\arctan\left(\frac{\tan 15^\circ}{F}\right) \approx 10^\circ$ . Using the chart in Figure 6-4 (a), the value of  $\gamma H F / c = 21.83$ , its corresponding  $K_{pl}=0.15$ . The stabilizing force needed is determined by  $F_{p,1}=K_{pl}\frac{\gamma H^2}{2} = 327.38 \text{ kN/m}$ . The most effective pile location is  $x_p \times \frac{H}{\tan 30^\circ} = 10.39 \text{ m}$  measured from slope toe. It is worth noting that with the increase of  $K_p$  and friction angle, the most effective pile location shifts towards the upper-middle part of a slope.

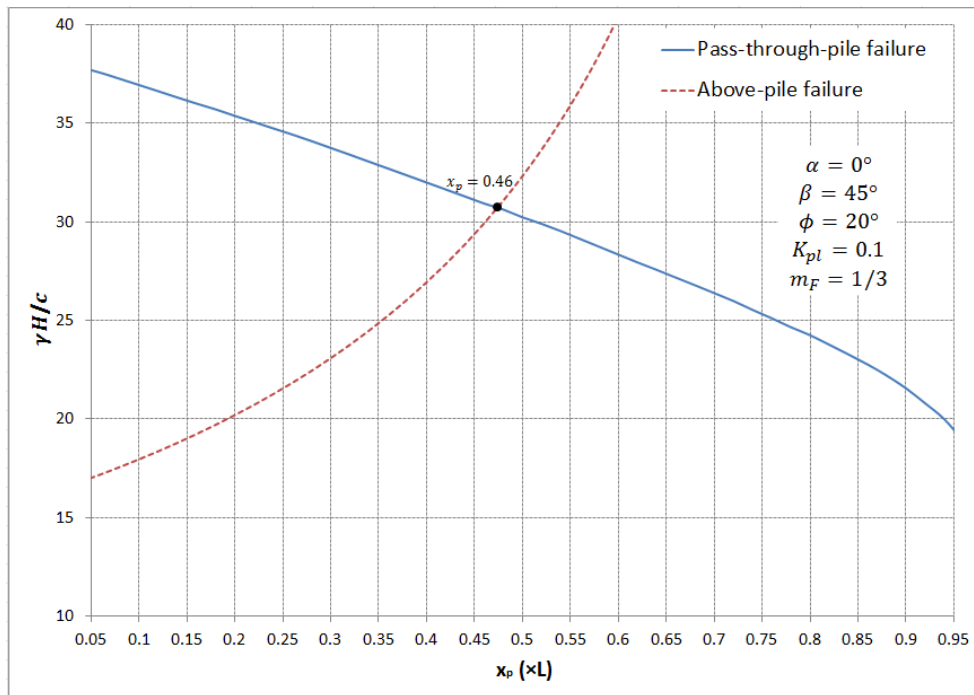
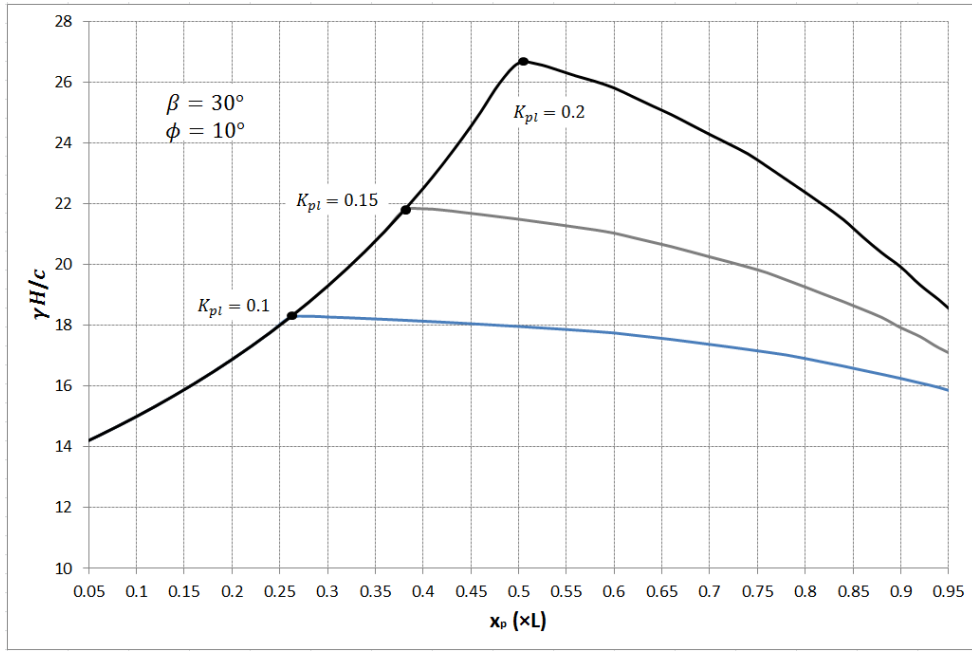
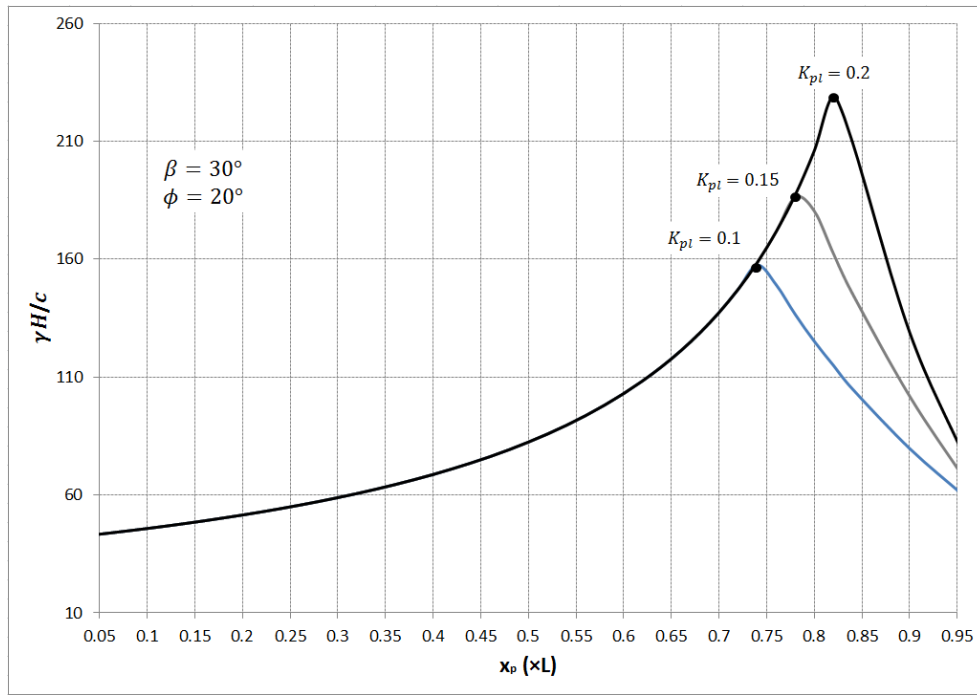


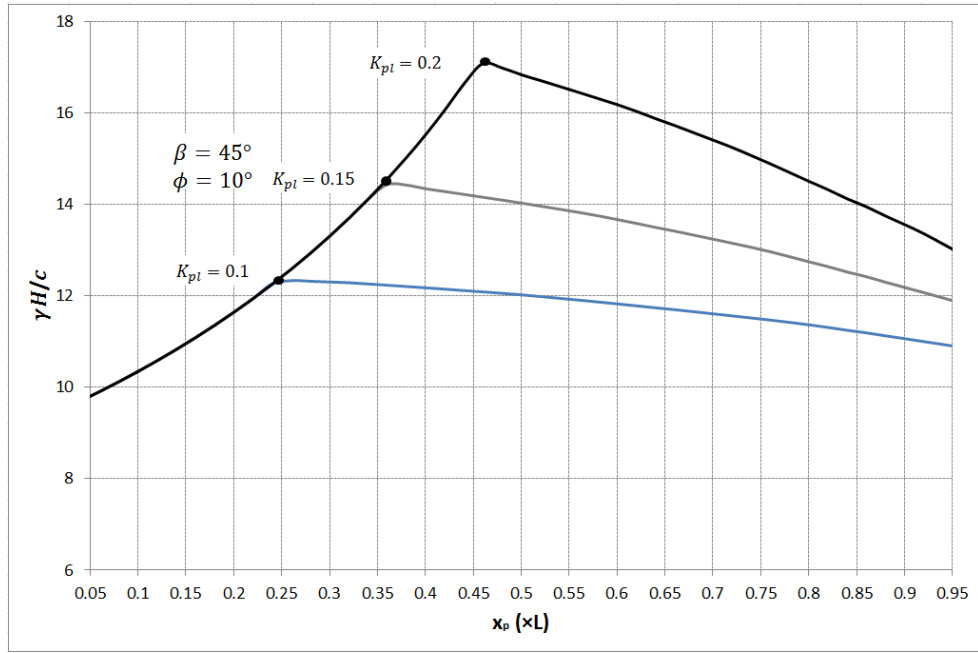
Figure 6-3. Stability factors against pile location considering both pass-through-pile and above-pile failure mechanisms,  $\alpha = 0^\circ, \beta = 45^\circ, \phi = 20^\circ, K_{pl} = 0.1, m_F = 1/3$ .



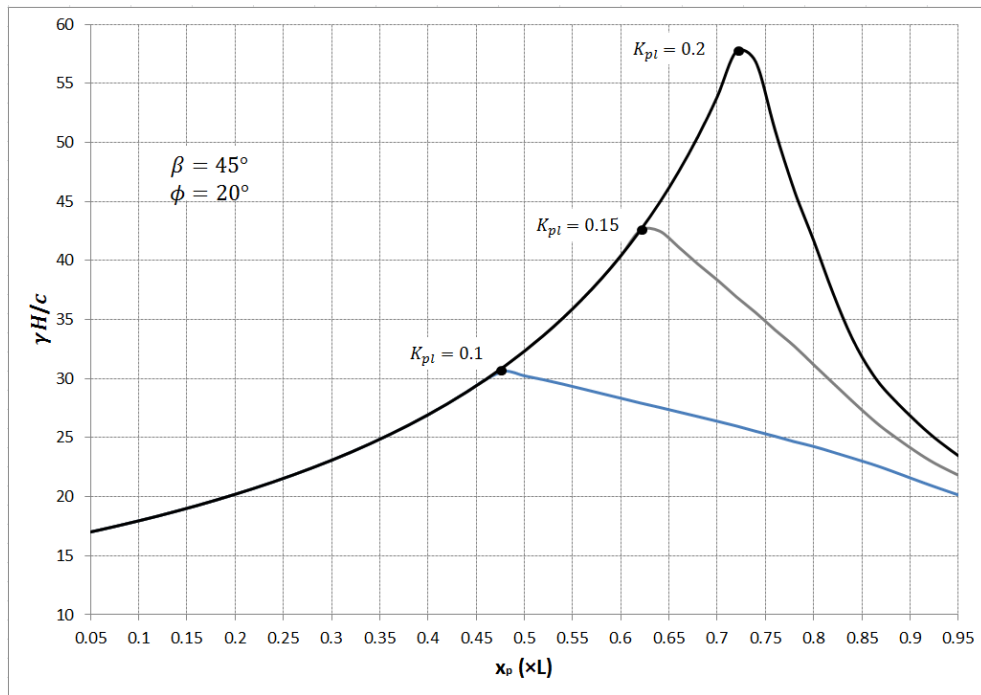
(a)  $\beta = 30^\circ, \phi = 10^\circ$



(b)  $\beta = 30^\circ, \phi = 20^\circ$

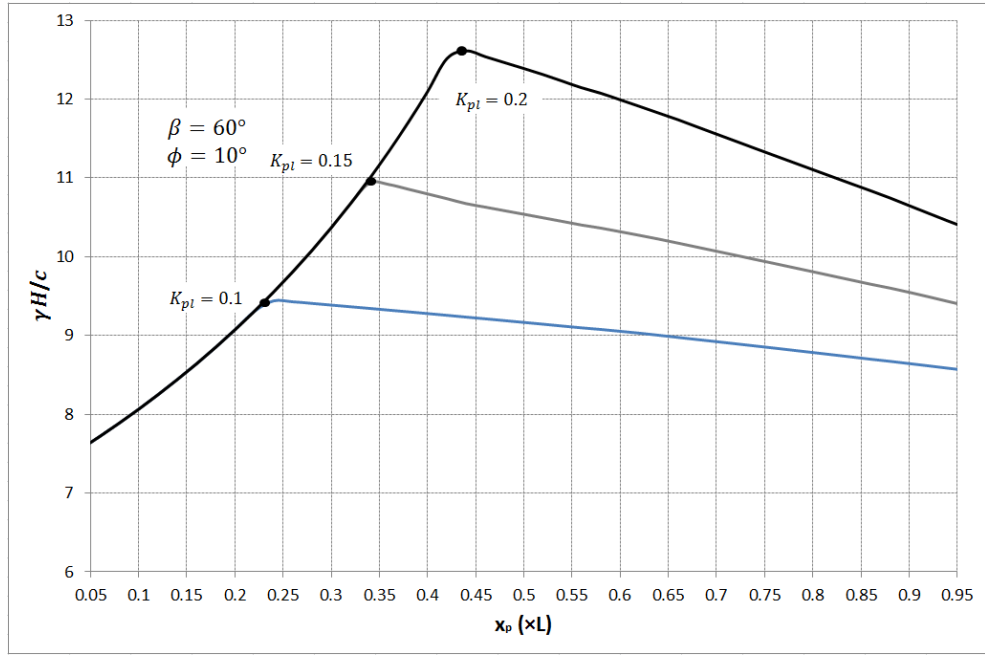


(c)  $\beta = 45^\circ, \phi = 10^\circ$

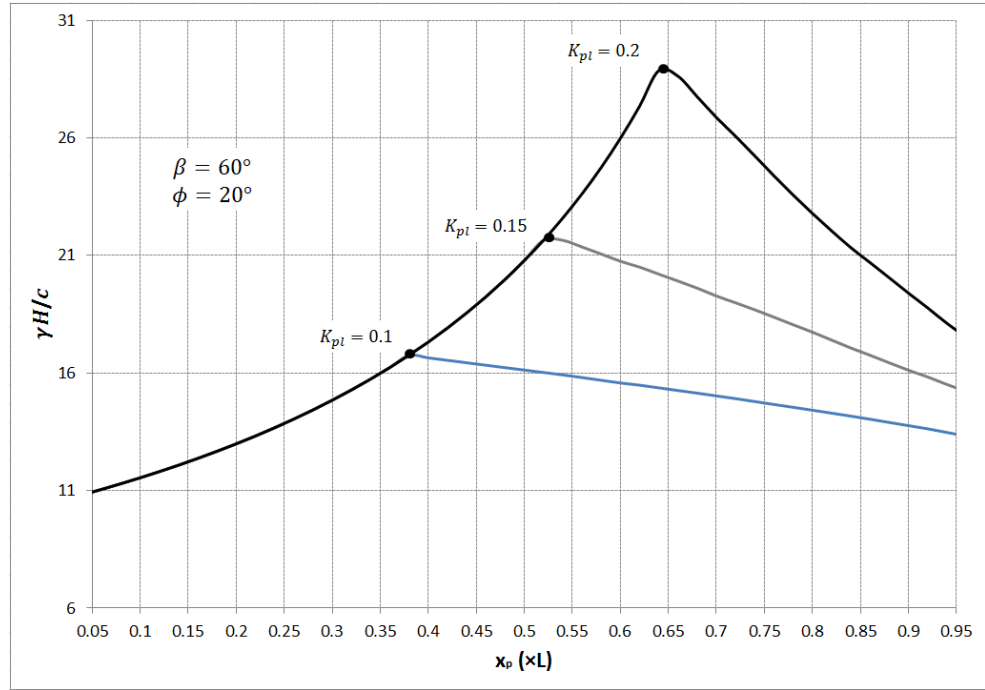


(d)  $\beta = 45^\circ, \phi = 20^\circ$

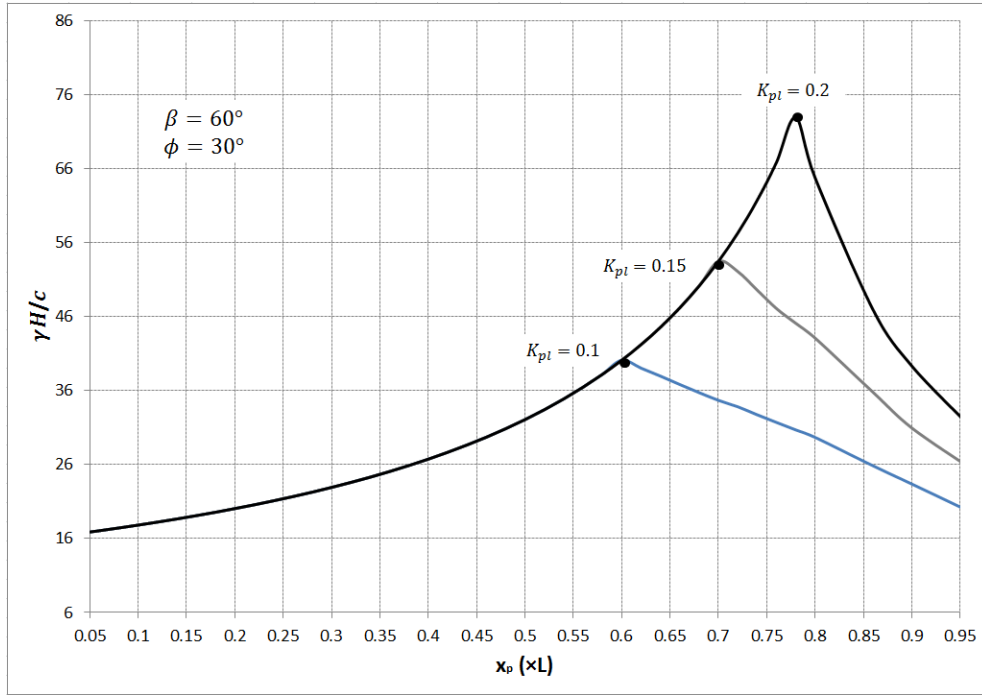




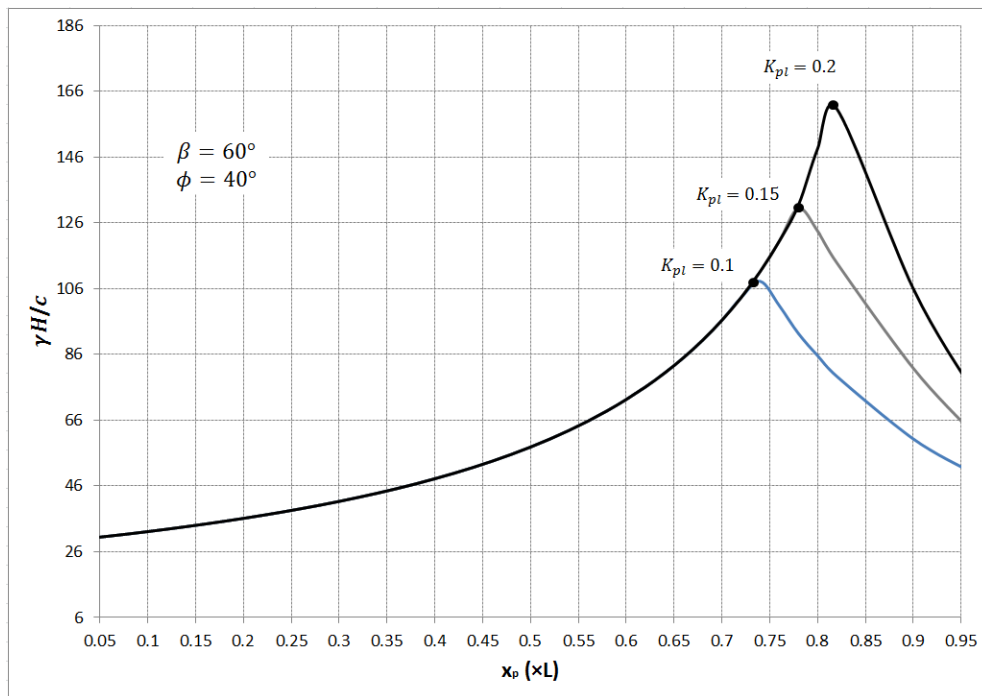
(e)  $\beta = 60^\circ, \phi = 10^\circ$



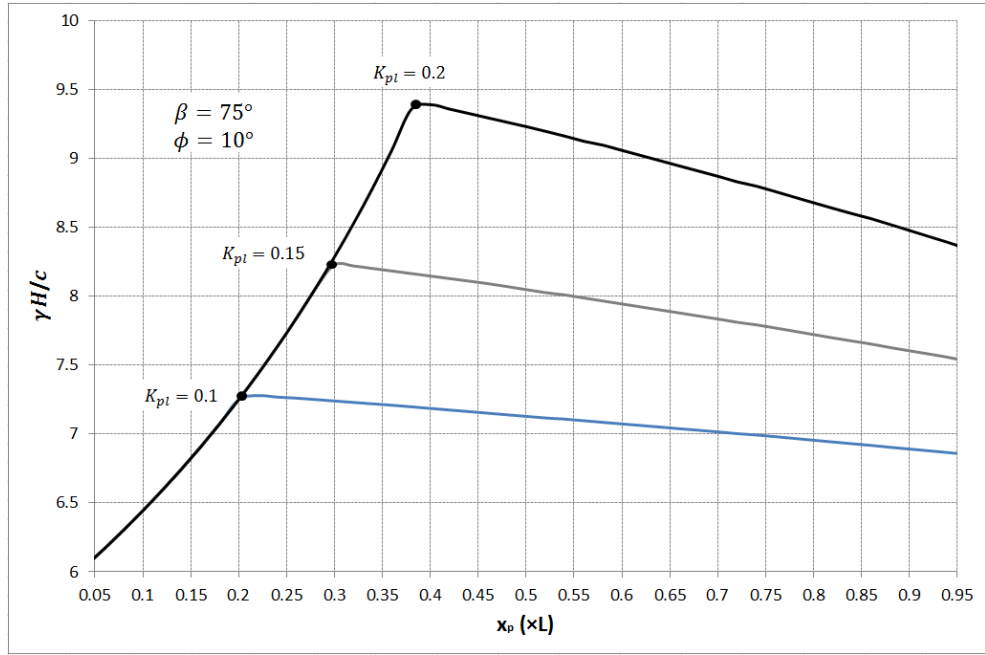
(f)  $\beta = 60^\circ, \phi = 20^\circ$



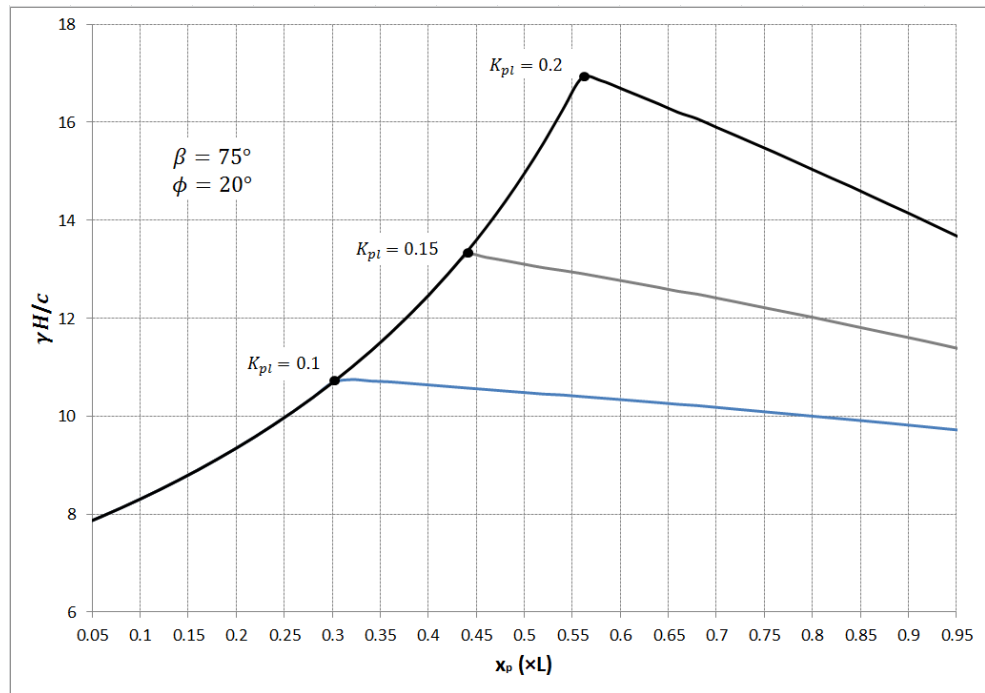
(g)  $\beta = 60^\circ, \phi = 30^\circ$



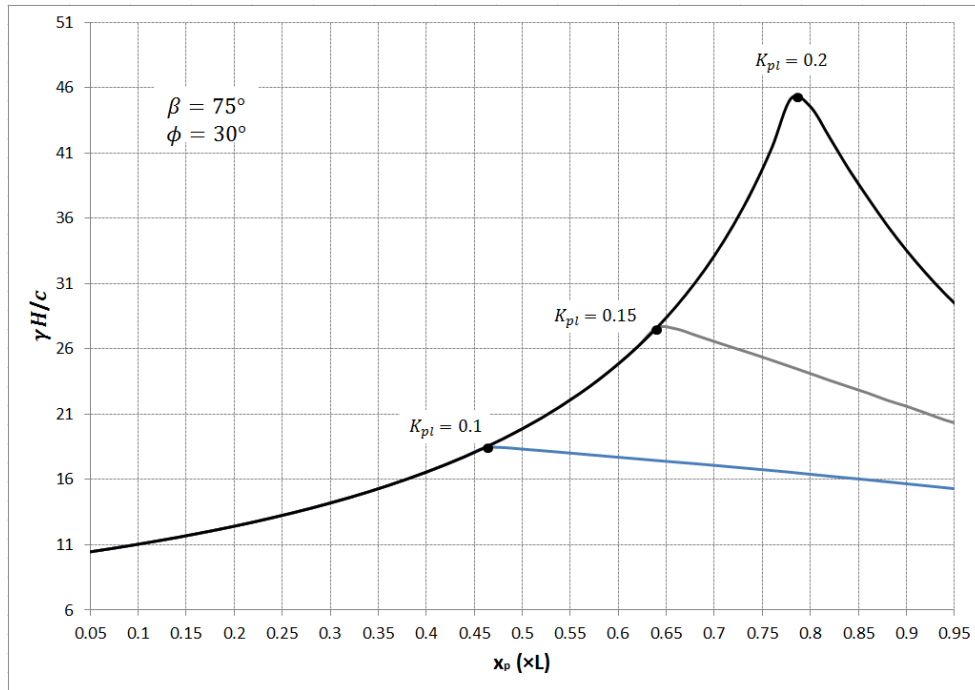
(h)  $\beta = 60^\circ, \phi = 40^\circ$



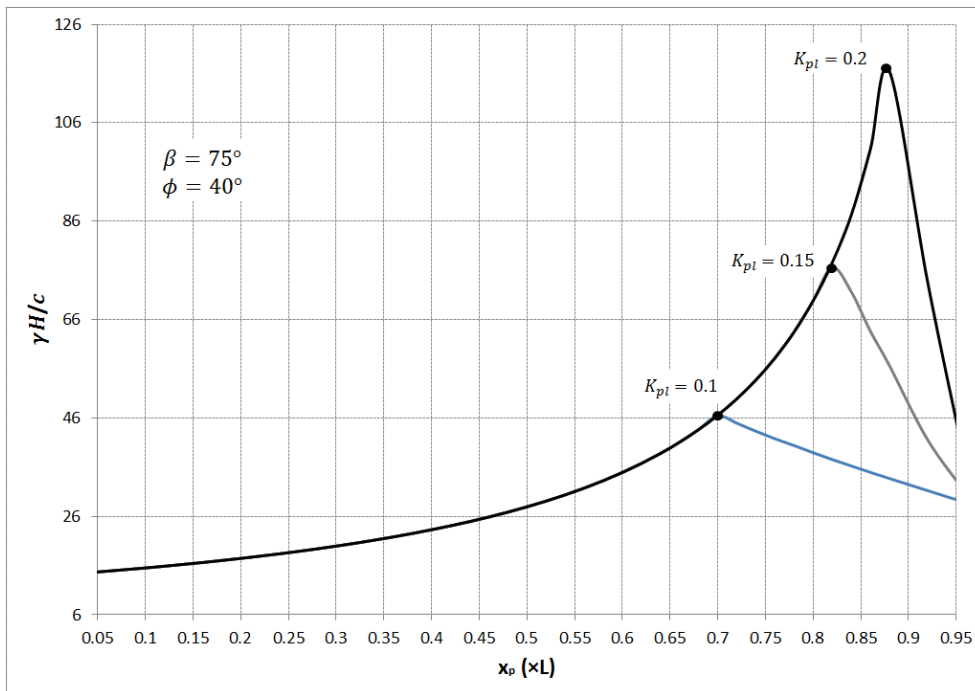
(i)  $\beta = 75^\circ, \phi = 10^\circ$



(j)  $\beta = 75^\circ, \phi = 20^\circ$



(k)  $\beta = 75^\circ, \phi = 30^\circ$



(l)  $\beta = 75^\circ, \phi = 40^\circ$

Figure 6-4. Design charts corresponding to the most effective pile location for various slope inclinations and friction angles,  $\alpha = 0^\circ, m_F = 1/3$ .

## 6.2 Location of the pile ensuring maximum stability factor for the slope

According to Hassiotis et al. (1997), Li et al. (2009c) and Li et al. (2012), by assuming that the piles are long enough, built with prescribed materials, installed with certain diameter and spacing, the stabilizing force that a row of piles can provide is proportional to their buried depth. The location of the pile ensuring the largest factor of safety given a row of piles is investigated in this section.

There is no universally accepted lateral pressure distribution mode around the piles. However, according to previous studies such as Ito and Matsui (1975), Ito et al. (1981), Hassiotis et al. (1997) and Zeng and Liang (2002), the lateral pressure distribution can be simplified with a triangular mode as shown in Figure 6-5.

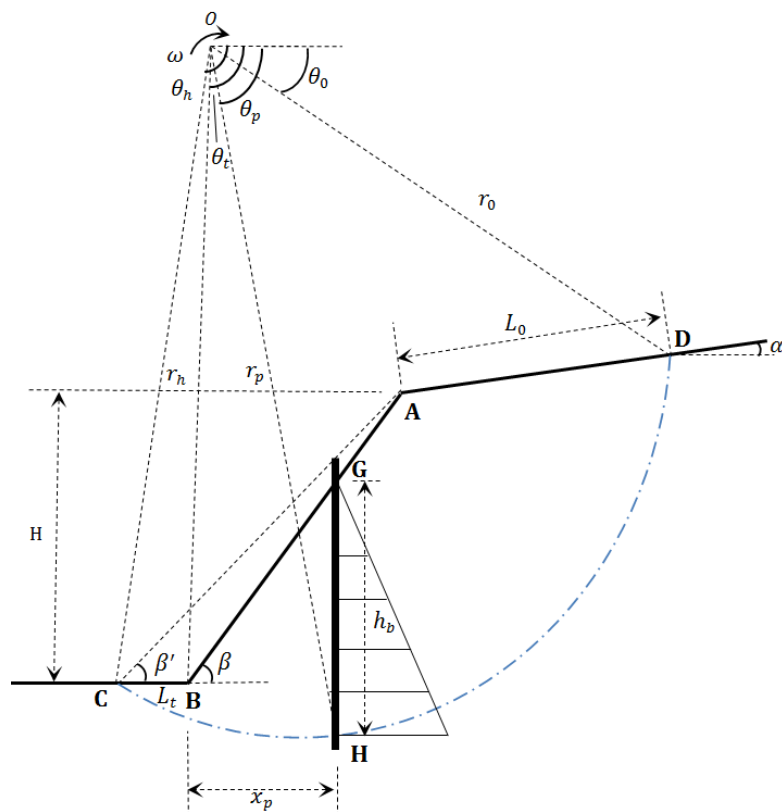


Figure 6-5. Lateral pressure distribution along the pile.

Ito and Matsui (1975) proposed a formula to simplify the magnitude of lateral pressure based on active earth pressure on a row of passive piles. The soil around the pile is assumed to be in plastic equilibrium, satisfying the Mohr-Coulomb failure criterion. The lateral force per unit thickness of soil layer acting on the piles is estimated by:

$$p(z) = cA \left( \frac{e^{\frac{D_1-D_2}{D_2} N_\phi \tan \phi \tan \left( \frac{\pi}{8} + \frac{\phi}{4} \right)} - 2N_\phi^{(1/2)} \tan \phi - 1}{N_\phi \tan \phi} + \frac{2 \tan \phi + 2N_\phi^{(1/2)} + N_\phi^{-(1/2)}}{N_\phi^{(1/2)} \tan \phi + N_\phi - 1} \right) \quad (6-11)$$

$$- c \left( D_1 \frac{2 \tan \phi + 2N_\phi^{(1/2)} + N_\phi^{-(1/2)}}{N_\phi^{(1/2)} \tan \phi + N_\phi - 1} - 2D_2 N_\phi^{-(1/2)} \right) + \frac{\gamma z}{N_\phi} \left[ A e^{\frac{D_1-D_2}{D_2} N_\phi \tan \phi \tan \left( \frac{\pi}{8} + \frac{\phi}{4} \right)} - D_2 \right]$$

with

$$N_\phi = \tan^2 \left( \frac{\pi}{4} + \frac{\phi}{2} \right) \quad (6-12)$$

$$A = D_1 \cdot \left( \frac{D_1}{D_2} \right)^{N_\phi^{1/2} \tan \phi + N_\phi - 1} \quad (6-13)$$

where  $D_1$  is the centre-to-centre piles spacing,  $D_2$  is the opening between piles,  $z$  is the depth of the soil layer from ground surface, as shown in Figure 6-6. Note that the lateral pressure along the pile will increase as the pile spacing decreases according to Eq. (6-11). However, the pressure on the pile would be expected to increase with pile spacing as each pile has to support a greater width of the slope (Hayward et al. 2000, Smethurst and Powrie 2007). Eq. (6-11) is regarded as an available estimation of lateral pressure to provide an analytical solution.

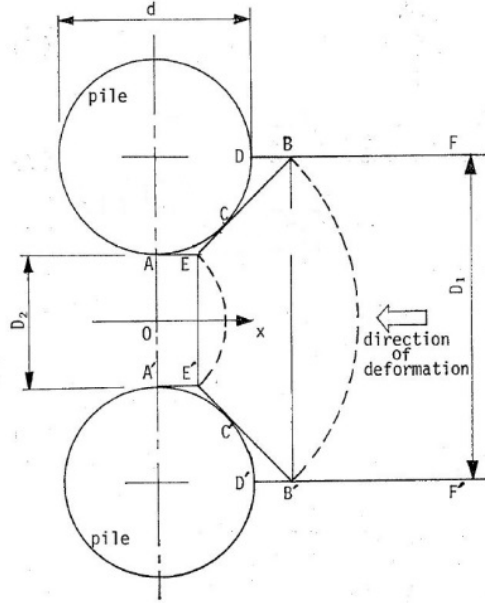


Figure 6-6. Plan view of piles in a row (Ito and Matsui 1975).

Considering the mass **ABCD** rigidly sliding away about the centre of rotation **O**, once the pressure along the pile/slope interface is postulated, the presence of pile reinforcement is incorporated by adding an additional stabilizing work term in the energy balance equation. In other words, the internal energy dissipation of the pile-slope system includes both the dissipated energy along the failure mechanism **CD** and the work done by the resistance pressure applied on the falling mass along **GH**.

As suggested by Hassiotis et al. (1997) and Li et al. (2009c), the total lateral force acting on a pile is obtained by integrating Eq. (6-11) along the buried depth of the pile inserted into the sliding slope mass. Thus, the resistance force ( $F_p$ ) per unit width of soil provided by the pile is expressed as:

$$F_{p,2} = \int_0^{h_b} \frac{p(z)}{D_1} dz \quad (6-14)$$

After integration, we obtain:

$$F_{p,2} = ch_b P_1(D_1, D_2) + \frac{\gamma h_b^2}{2} P_2(D_1, D_2) \quad (6-15)$$

where  $P_1$  and  $P_2$  are functions of  $D_1$ ,  $D_2$ , which are written as:

$$P_1(D_1, D_2) = \frac{A}{D_1} \left[ \frac{e^{\frac{D_1 - D_2}{D_2} N_\phi \tan \phi \tan \left( \frac{\pi}{8} + \frac{\phi}{4} \right)} - 2N_\phi^{(1/2)} \tan \phi - 1}{N_\phi \tan \phi} + \frac{2 \tan \phi + 2N_\phi^{(1/2)} + N_\phi^{-(1/2)}}{N_\phi^{(1/2)} \tan \phi + N_\phi - 1} \right] \quad (6-16)$$

$$- \frac{2 \tan \phi + 2N_\phi^{(1/2)} + N_\phi^{-(1/2)}}{N_\phi^{(1/2)} \tan \phi + N_\phi - 1} + 2 \frac{D_2}{D_1} N_\phi^{-(1/2)}$$

$$P_2(D_1, D_2) = \frac{Ae^{\frac{D_1 - D_2}{D_2} N_\phi \tan \phi \tan \left( \frac{\pi}{8} + \frac{\phi}{4} \right)} - D_2}{D_1 N_\phi} \quad (6-17)$$

$F_{p,2}$  acts horizontally on the point of  $\mathbf{P}$  at a height of  $\frac{h}{3}$  above the intersection point  $\mathbf{H}$  between the pile and the failure surface. Some literature such as Hassiotis et al. (1997) and Nian et al. (2008) assumes that  $F_p$  is parallel to the failure surface at the point  $\mathbf{H}$ . However, in order to be consistent with the theory proposed by Ito and Matsui (1975), it is assumed here that there is no shear traction along the slope-pile interface and  $F_{p,2}$  acts horizontally. The rate of additional stabilizing work due to pile reinforcement corresponding to case 2 is determined by:

$$\dot{W}_{p,2} = \omega F_{p,2} \left[ \sin \theta_p r_0 e^{\tan \phi (\theta_p - \theta_0)} - \frac{h_b}{3} \right] = \omega F_{p,2} f_{p,2} \quad (6-18)$$



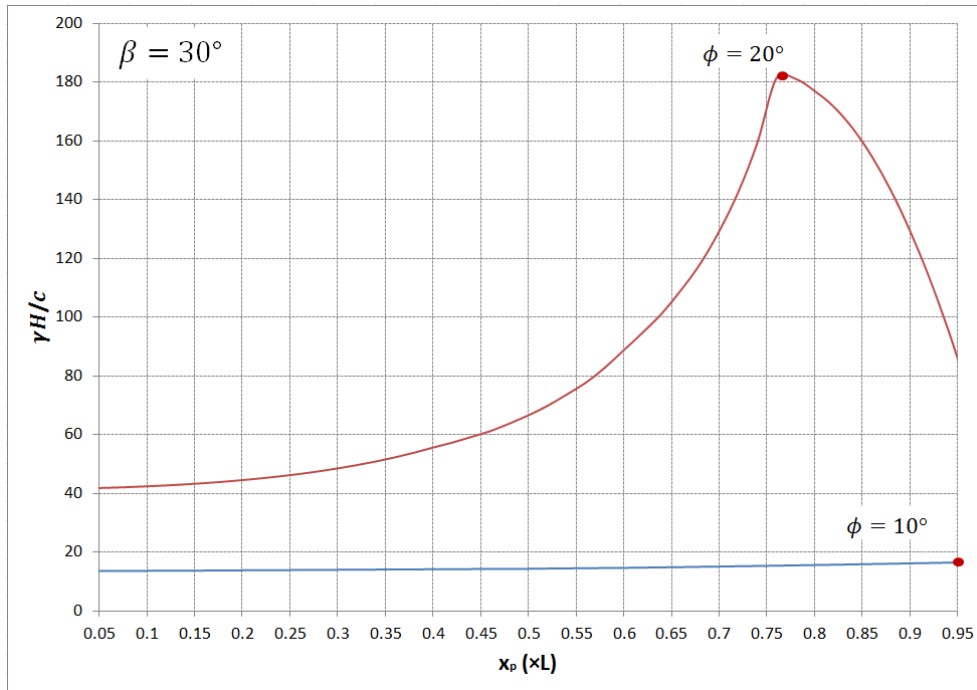
Equating the rate of external work to the rate of energy dissipation due to cohesion and pile reinforcement, leads to:

$$\dot{W}_\gamma = \omega \gamma r_0^3 (f_1 - f_2 - f_3 - f_4) = \dot{W}_{d-\log} + \dot{W}_{p,2} = c \omega r_0^2 f_{d-\log} + \omega F_{p,2} f_{p,2} \quad (6-19)$$

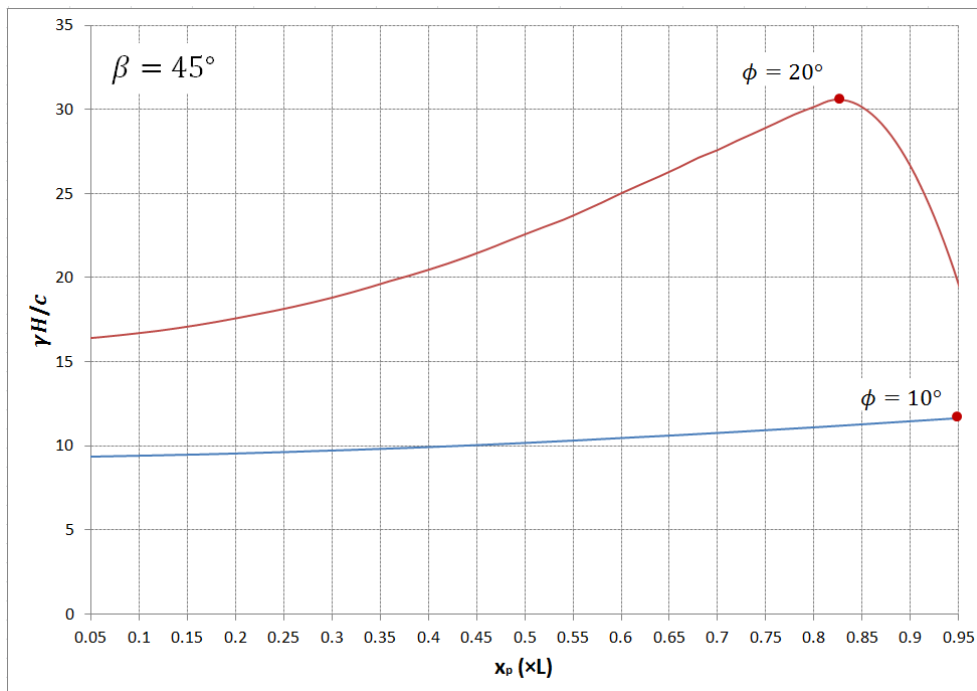
After rearranging, the stability factor for a reinforced slope corresponding to Ito and Matsui's theory (Ito and Matsui 1975) is given by:

$$N_{p,2} = \frac{\gamma H}{c} = \frac{f_H \times (f_{d-\log} + P_1 \times f_{p,2})}{f_1 - f_2 - f_3 - f_4 - P_2 \times f_{p,2} \times \frac{h_b^2}{2r_0^2}} \quad (6-20)$$

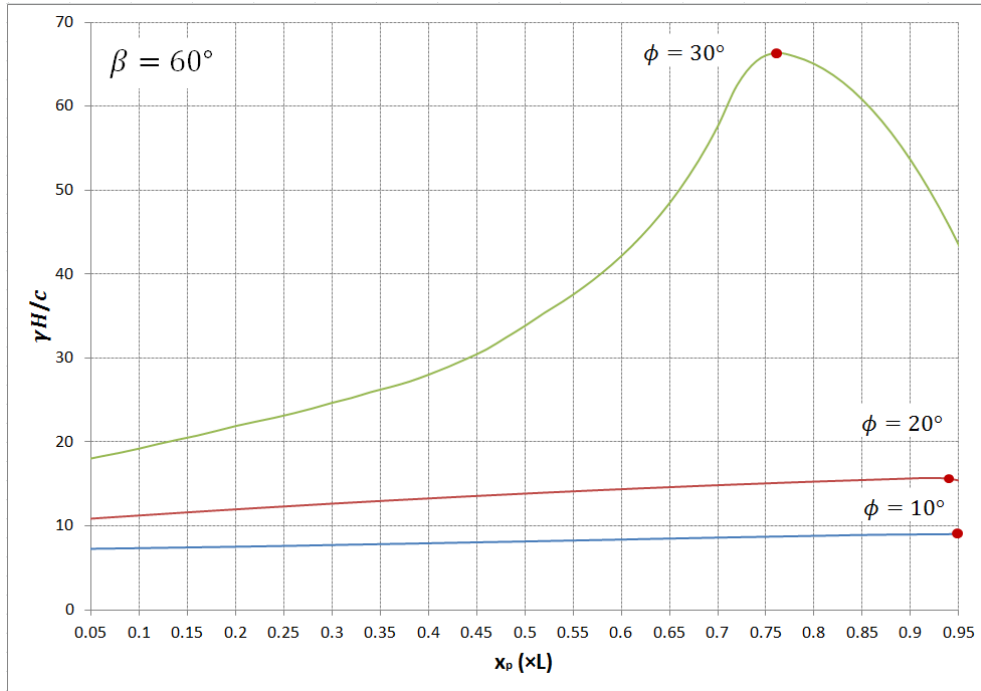
In Figure 6-7, by changing the pile location ( $x_p$ ), the stability factors  $N_{p,2}$  defined in (6-20) against  $x_p$  for slopes with different inclinations ( $\beta = 30^\circ, 45^\circ, 60^\circ, 75^\circ$ ) reinforced with a row of piles whose  $\frac{D_2}{D_1} = 0.6$  are illustrated. The friction angle of the material ranges from  $10^\circ$  to  $30^\circ$ . The locations of the pile ensuring maximum stability factor will shift downwards to the middle of slope face when the friction angle increases.



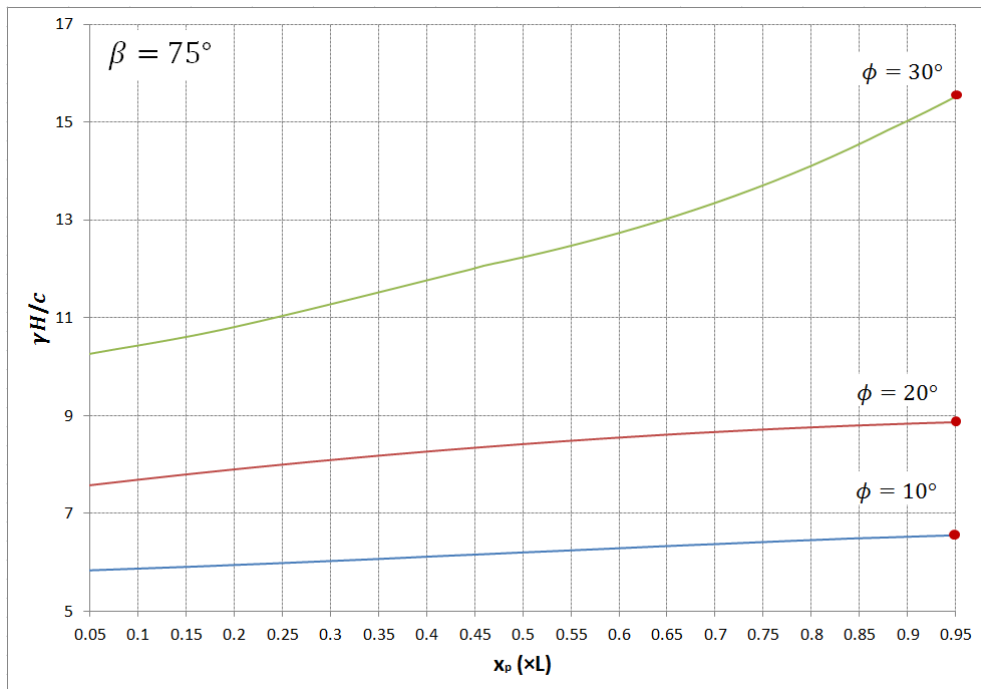
(a)  $\beta = 30^\circ$



(b)  $\beta = 45^\circ$



(c)  $\beta = 60^\circ$

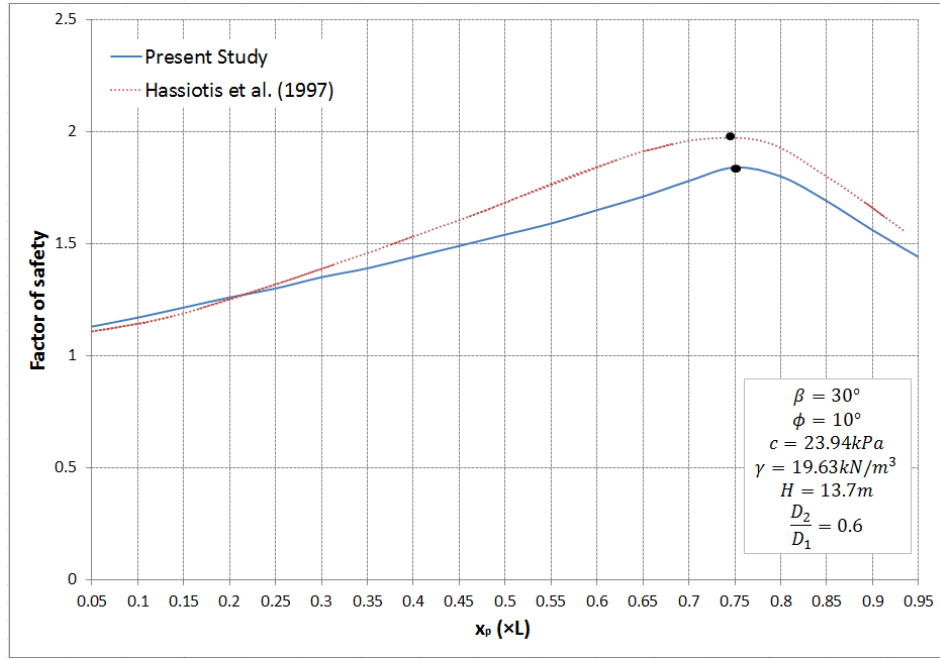


(d)  $\beta = 75^\circ$

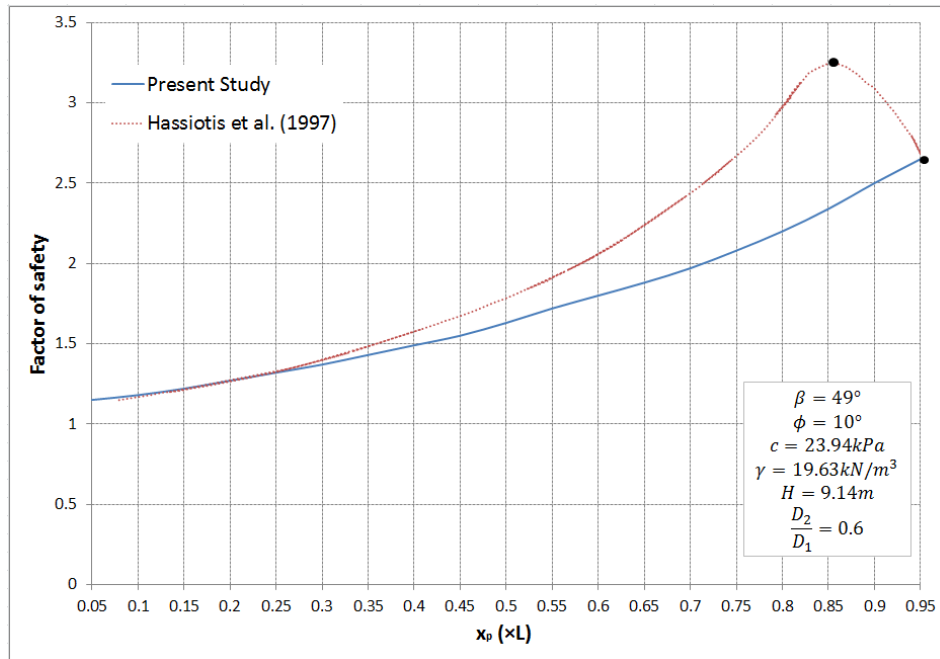
Figure 6-7. Design charts according to the Ito and Matsui (1975)'s theory for various slope inclinations and friction angles,  $\alpha = 0^\circ$ ,  $\frac{D_2}{D_1} = 0.6$ .

Once the stability factors of slopes reinforced with a row of piles are derived, the factor of safety  $F$  can be calculated by replacing  $c$  with  $c_s/F$  and  $\tan\phi$  with  $\tan\phi_s/F$  in Eq. (6-20).  $F$  is obtained by an iterative process since it appears in both side of Eq. (6-20). In order to validate the upper bound formulation in this section, the results obtained from Hassiotis et al. (1997) using limit equilibrium and from Wei and Cheng (2009) adopting finite element strength reduction technique are selected as reference.

In Figure 6-8, the factor of safety against pile location  $x_p$  is plotted for two sample slopes (used in Hassiotis et al. 1997). The two slopes have different inclination and height. The factors of safety obtained by using Eq. (6-20) are smaller/more critical than those from Hassiotis et al. (1997) except when piles are placed at around slope toe. The optimal pile positions obtained from the two methods are close to each other for slope I, but different for slope II. The discrepancy lies in the application of two distinct methods. As pointed out by the authors themselves, the results in Hassiotis et al. (1997) are quite sensitive to the pre-determined circular failure mechanisms. In addition, the direction of  $F_p$  is assumed differently in both methods.



(a) Slope I:  $\beta = 30^\circ, H = 13.7 \text{ m}$



(b) Slope II:  $\beta = 49^\circ, H = 9.14 \text{ m}$

Figure 6-8. Comparison with the results from Hassiotis et al. (1997).

In Figure 6-9, the factor of safety is plotted against six values of  $\frac{D_2}{D_1}$  corresponding to different cases of pile spacing. The sample slope is 10 m in height with a gradient of 1:1.5. The cohesive strength, friction angle and unit weight of

the material are 10 kPa, 20° and 20 kN/m<sup>3</sup>, respectively. The results obtained by using Eq. (6-20) are more conservative than those from Wei and Cheng (2009). The maximum discrepancy is around 10%.

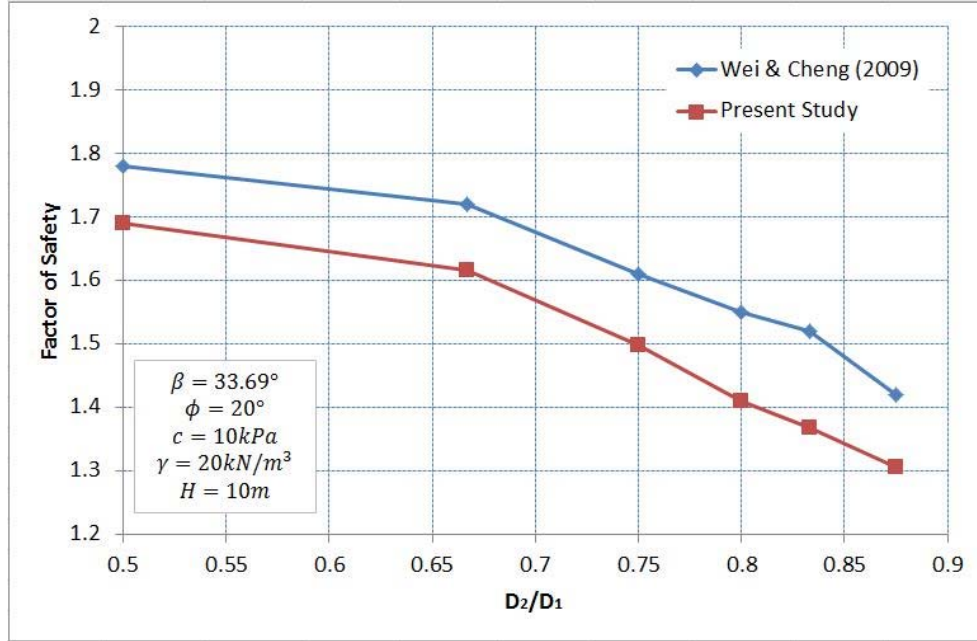


Figure 6-9. Comparison with the results from Wei and Cheng (2009).

### 6.3 The effect of cracks on optimal pile position

The upper bound formulations to include the presence of cracks in slope stability analyses are detailed in Chapter 3 and Chapter 5. As shown in Figure 6-10, the external work done by the weight of sliding mass **ABCDE** is calculated by the work done by the fictitious weight of the region **ABCF** minus the work done by that of the region **EDF**. Equating the rate of external work to the rate of energy dissipation due to cohesion and pile reinforcement leads to:

$$\begin{aligned}\dot{W}_\gamma &= \dot{W}_1 - \dot{W}_2 - \dot{W}_3 - \dot{W}_4 - \dot{W}_5 + \dot{W}_6 + \dot{W}_7 = \omega \gamma r_0^3 (f_1 - f_2 - f_3 - f_4 - f_5 + f_6 + f_7) \\ &= \dot{W}_{d-\log}'' + \dot{W}_p = c \omega r_0^2 f_{d-\log}'' + \omega F_p f_p\end{aligned}\quad (6-21)$$

where  $f_5, f_6, f_7$  are defined in Eqs. (5-32), (5-33) and (5-34).  $f''_{d-log}$  is defined in Eq. (5-35). And

$$\dot{W}_p, F_p, f_p = \begin{cases} \dot{W}_{p,1}, F_{p,1}, f_{p,1} & \text{case 1} \\ \dot{W}_{p,2}, F_{p,2}, f_{p,2} & \text{case 2} \end{cases} \quad (6-22)$$

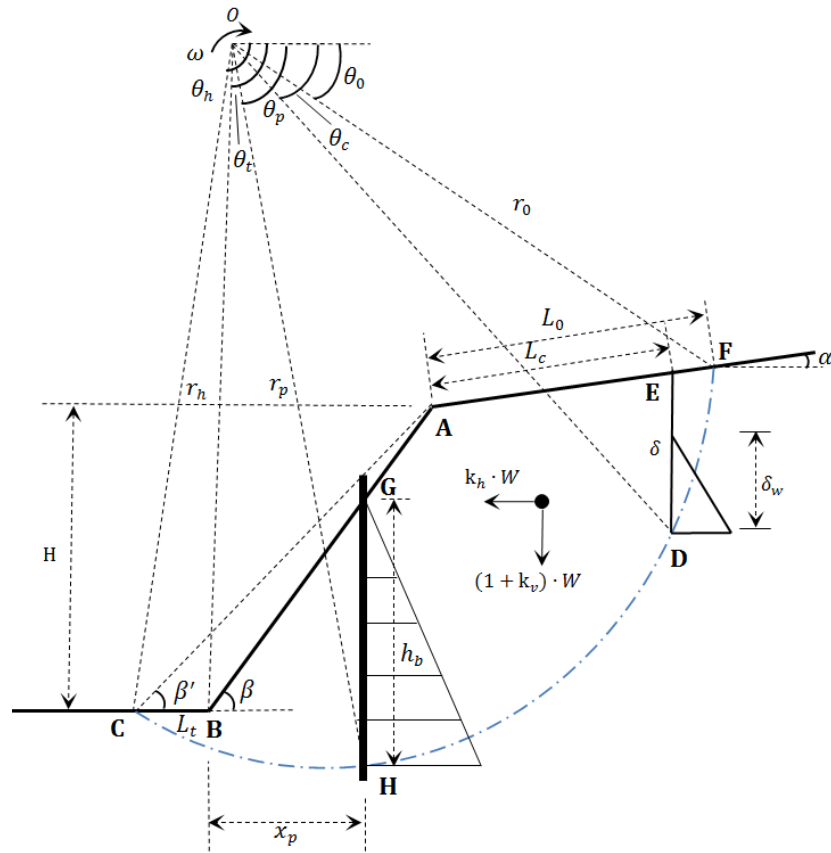


Figure 6-10. Failure mechanism for cracked slope reinforced with piles.

After rearranging, the stability factors for a cracked slope reinforced with piles corresponding to both case 1 and case 2 are obtained:

$$N_{p,1,c} = \frac{\gamma H}{c} = \frac{f_H \times f_{d-\log}''}{f_1 - f_2 - f_3 - f_4 - f_5 + f_6 + f_7 - \frac{f_H^2}{2} K_{pl} f_{p,1}} \quad (6-23)$$

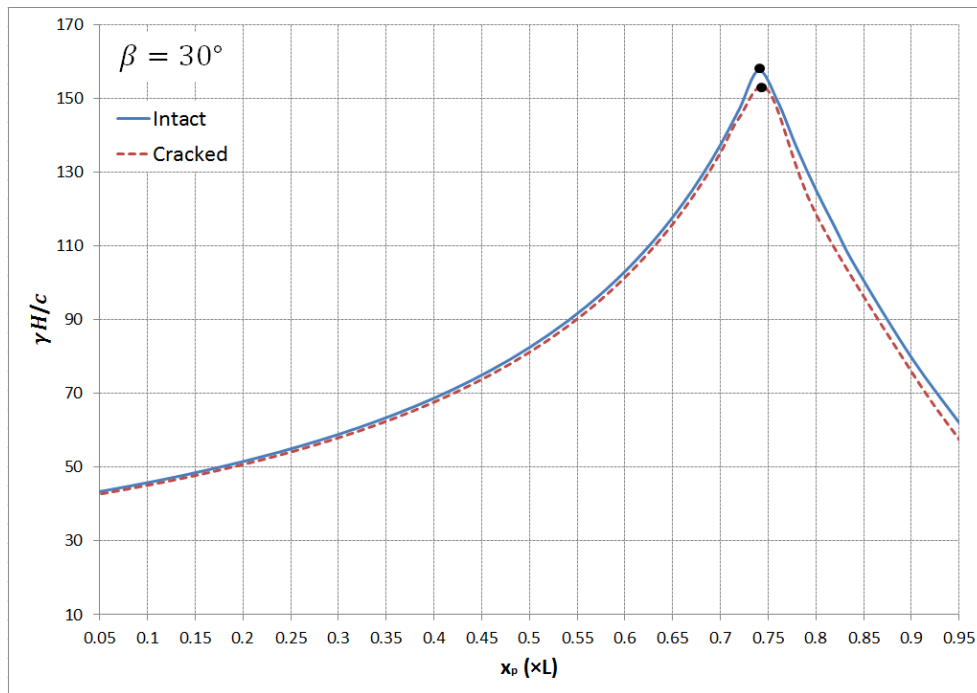
$$N_{p,2,c} = \frac{\gamma H}{c} = \frac{f_H \times (f_{d-\log}'' + P_1 \times f_{p,2})}{f_1 - f_2 - f_3 - f_4 - f_5 + f_6 + f_7 - P_2 \times f_{p,2} \times \frac{h_b^2}{2r_0^2}} \quad (6-24)$$

The least upper bound is found by minimization of Eq. (6-23) and (6-24) with  $\theta_0$ ,  $\theta_c$ ,  $\theta_h$  and  $\beta'$  denoting the most critical failure mechanism.

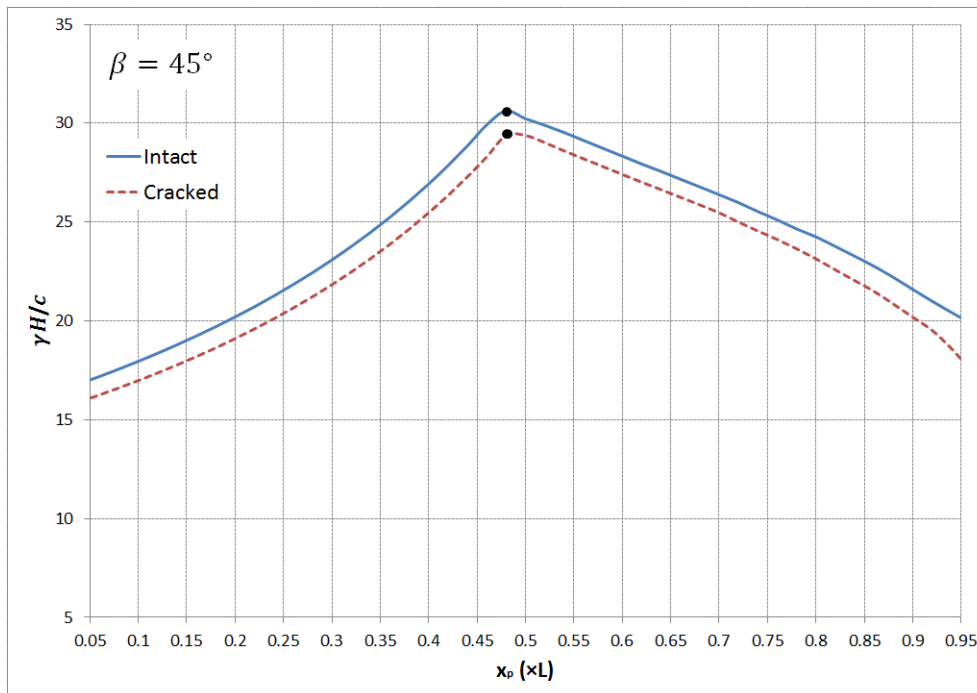
In Figure 6-11, the stability factors defined in Eq. (6-23) corresponding to case 1 are plotted against  $x_p$  for both intact and cracked cases. For illustrative purposes, the case of horizontal upper slope ( $\alpha = 0^\circ$ ) is considered. The friction angle of the material is specified as  $20^\circ$ . Slopes with different inclinations ( $\beta = 30^\circ, 45^\circ, 60^\circ, 75^\circ$ ) reinforced with a row of piles whose  $K_{p1} = 0.1$  are illustrated. For cracked slopes, the most adverse pre-existing cracks are considered. It is expected that the stability factors of intact slope is higher than those of the cracked one. However, the difference of the most effective pile location between intact and cracked cases is marginal. The biggest difference is  $0.05L$  when  $\beta = 75^\circ$ .

In Figure 6-12, the stability factors defined in Eq. (6-24) corresponding to case 2 are plotted against  $x_p$  for both intact and cracked cases. Slopes with different inclinations ( $\beta = 30^\circ, 45^\circ, 60^\circ, 75^\circ$ ) reinforced with a row of piles whose  $\frac{D_1}{D_2} = 0.6$  are illustrated. In Figure 6-12, for gentle slopes ( $\beta = 30^\circ, 45^\circ$ ), the locations of the pile ensuring maximum stability factor are within the upper-middle part of the slope for both intact and cracked cases. For steep slopes ( $\beta = 60^\circ, 75^\circ$ ), the locations approach the slope crest. Moreover, it is important to know the presence of cracks has little influence on the optimal pile position.

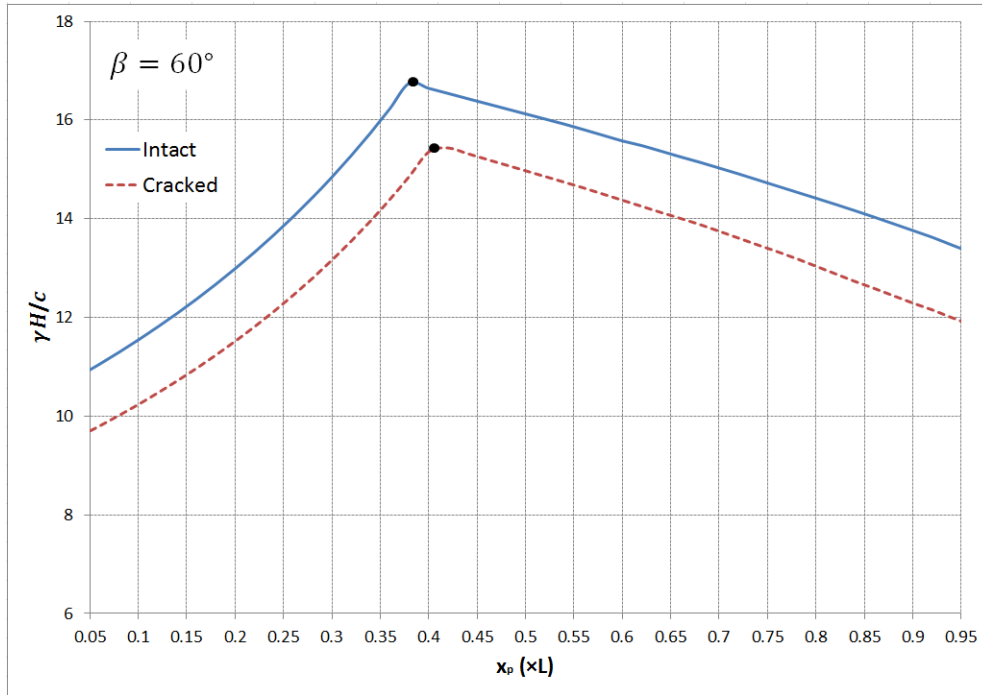




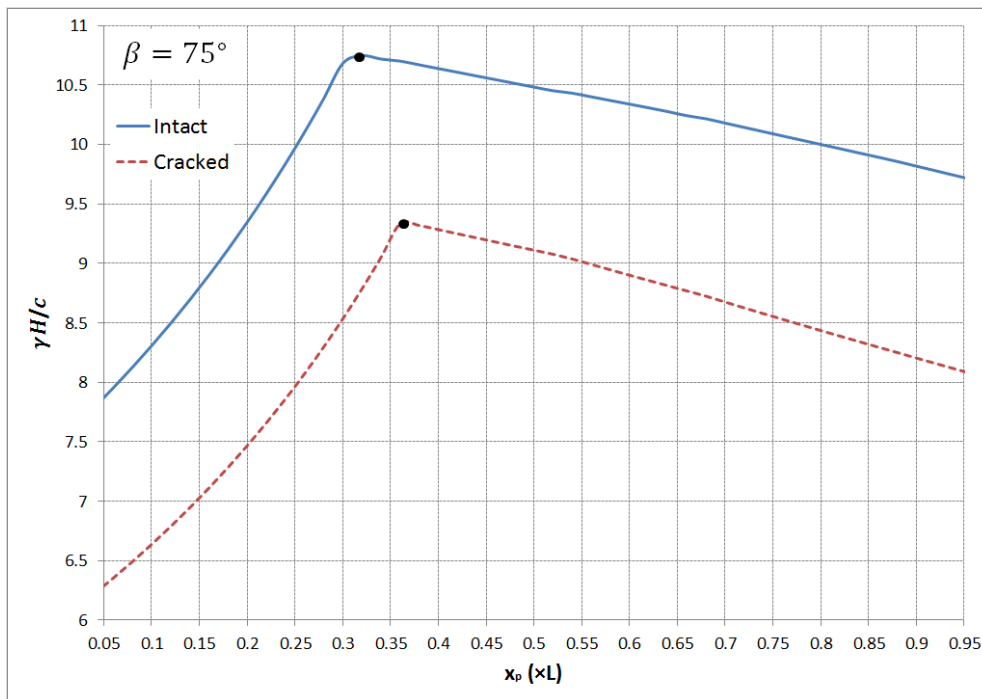
(a)  $\beta = 30^\circ$



(b)  $\beta = 45^\circ$

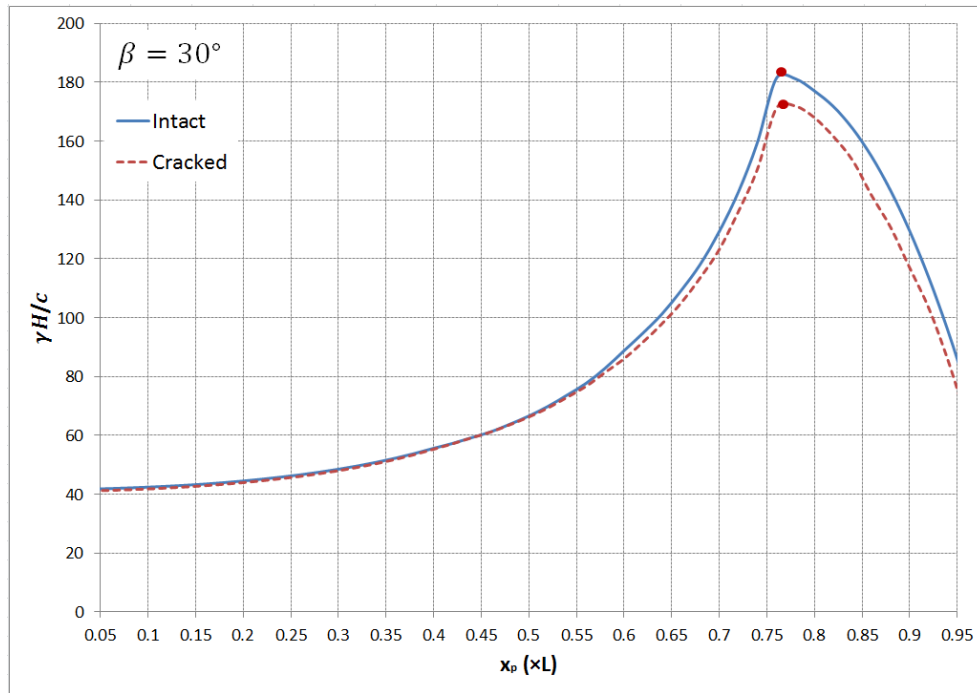


(c)  $\beta = 60^\circ$

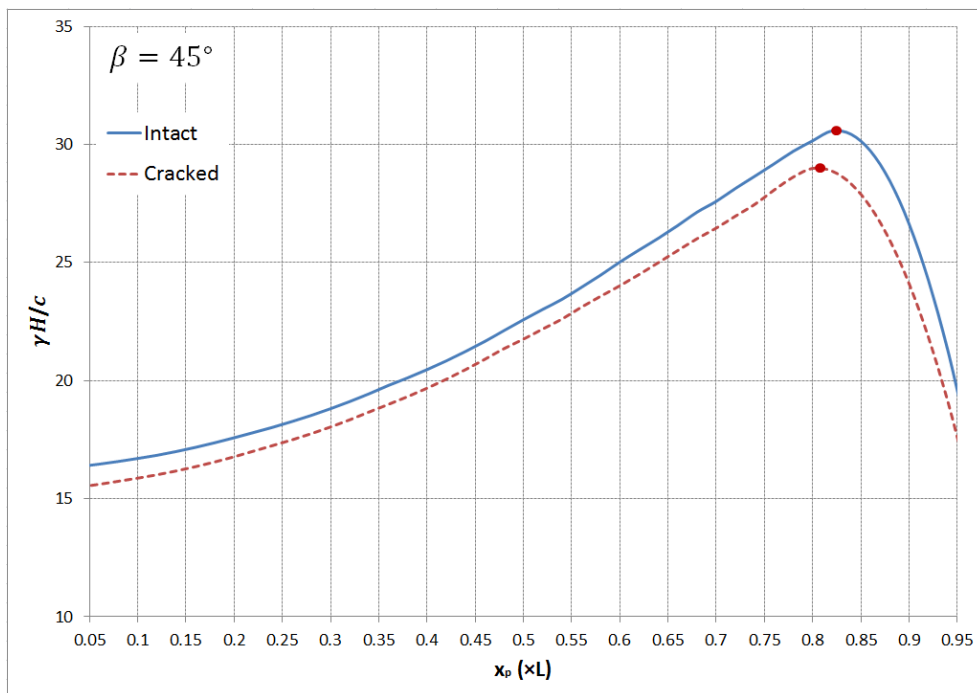


(d)  $\beta = 75^\circ$

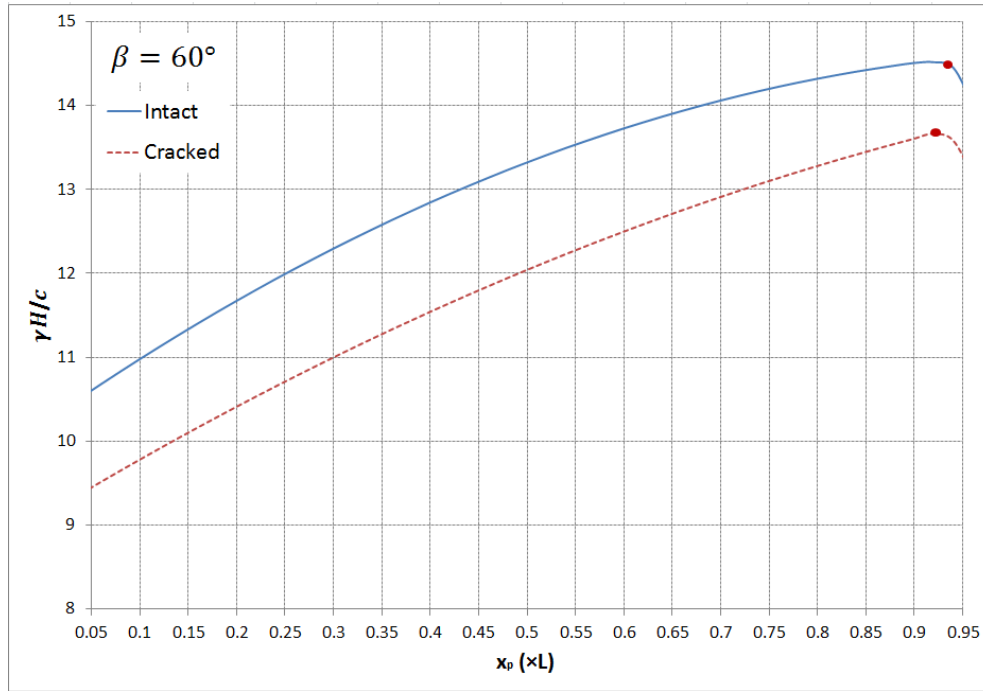
Figure 6-11. Stability factor corresponding to case 1 against pile position for slopes with various inclinations,  $\alpha = 0^\circ$ ,  $\phi = 20^\circ$ ,  $K_{pl} = 0.1$ .



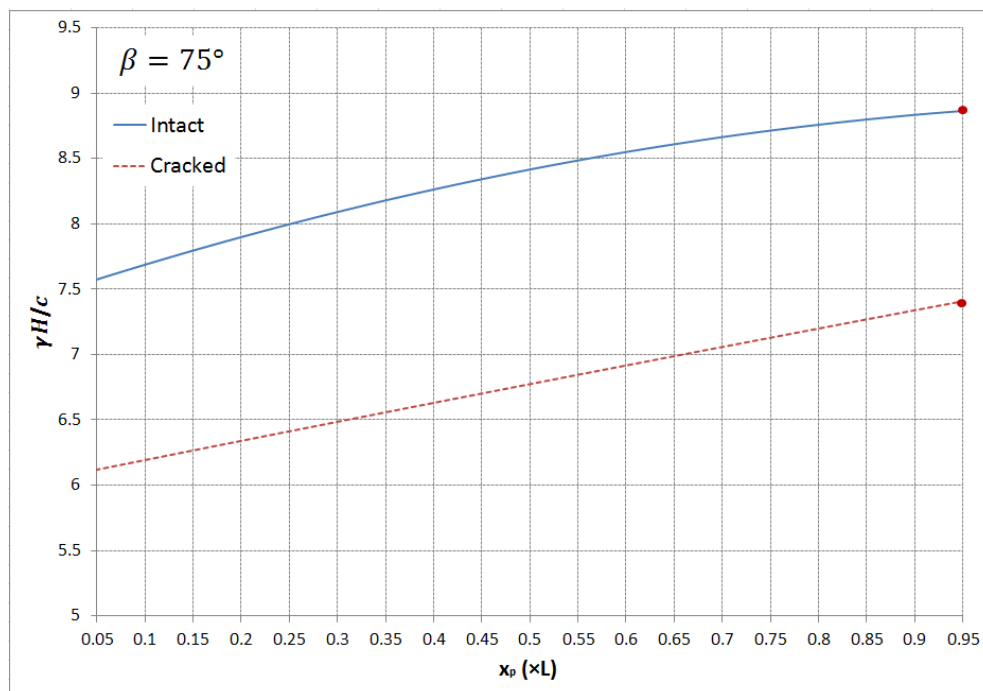
(a)  $\beta = 30^\circ$



(b)  $\beta = 45^\circ$



(c)  $\beta = 60^\circ$



(d)  $\beta = 75^\circ$

Figure 6-12. Stability factor corresponding to case 2 against pile position for slopes with various inclinations,  $\alpha = 0^\circ$ ,  $\phi = 20^\circ$ ,  $\frac{D_2}{D_1} = 0.6$ .

## 6.4 The effect of pore water pressure on optimal pile position

The influence of water acting on both the crack and the failure surface is evaluated in this section.  $r_u$  is imposed to describe the general pore water pressure distribution as that in section 3.2.

The external work of the soil-pile system contains both the work done by the material weight and pore water pressure. Equating the rate of external work to the rate of energy dissipation, leads to:

$$\dot{W}_\gamma + \dot{W}_w = \dot{W}_{d-\log}'' + \dot{W}_p \quad (6-25)$$

After rearranging, the stability factors defined in Eqs. (6-23) and (6-24) corresponding to case 1 and case 2 for dry slopes are extended to include the presence of pore water pressure:

$$\begin{aligned} N_{p,w,1} &= \frac{\gamma H}{c} \\ &= \frac{f_H \times f_{d-\log}''}{f_1 - f_2 - f_3 - f_4 - f_5 + f_6 + f_7 + p_{w-c} + p_{w-\log} - \frac{f_H^2}{2} K_{pl} f_{p,1}} \end{aligned} \quad (6-26)$$

$$\begin{aligned} N_{p,w,2} &= \frac{\gamma H}{c} \\ &= \frac{f_H \times (f_{d-\log}'' + P_1 \times f_{p,2})}{f_1 - f_2 - f_3 - f_4 - f_5 + f_6 + f_7 + p_{w-c} + p_{w-\log} - P_2 \times f_{p,2} \times \frac{h_b^2}{2r_0^2}} \end{aligned} \quad (6-27)$$

where  $p_{w-c}$  and  $p_{w-\log}$  are obtained by the revision of Eqs. (3-31) and (3-38) and written as follows:

$$p_{w-c}(\theta_0, \theta_h, \beta') = \frac{1}{2} \frac{\gamma_w}{\gamma} \left( \frac{K_w \delta}{r_0} \right)^2 \left( \sin \theta_c e^{\tan \phi (\theta_c - \theta_0)} - \frac{1}{3} \frac{K_w \delta}{r_0} \right) \quad (6-28)$$

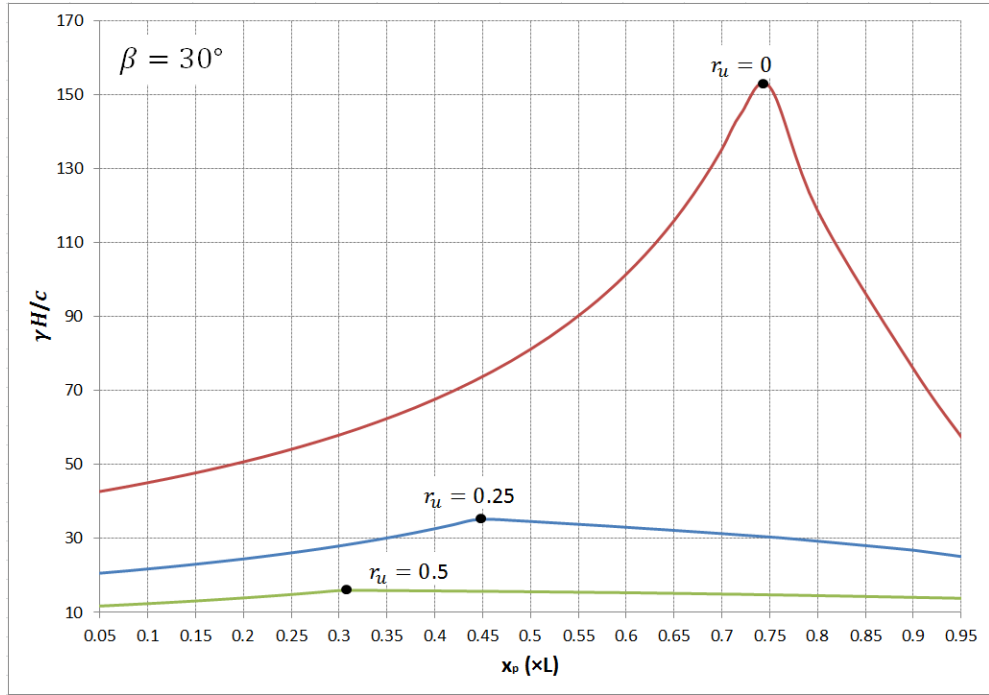
and

$$p_{w-\log}(\theta_0, \theta_h, \beta') = r_u \tan \phi \left[ \int_{\theta_c}^{\theta_1} \frac{z_1}{r_0} e^{2 \tan \phi (\theta - \theta_0)} d\theta + \int_{\theta_1}^{\theta_2} \frac{z_2}{r_0} e^{2 \tan \phi (\theta - \theta_0)} d\theta + \int_{\theta_2}^{\theta_h} \frac{z_3}{r_0} e^{2 \tan \phi (\theta - \theta_0)} d\theta \right] \quad (6-29)$$

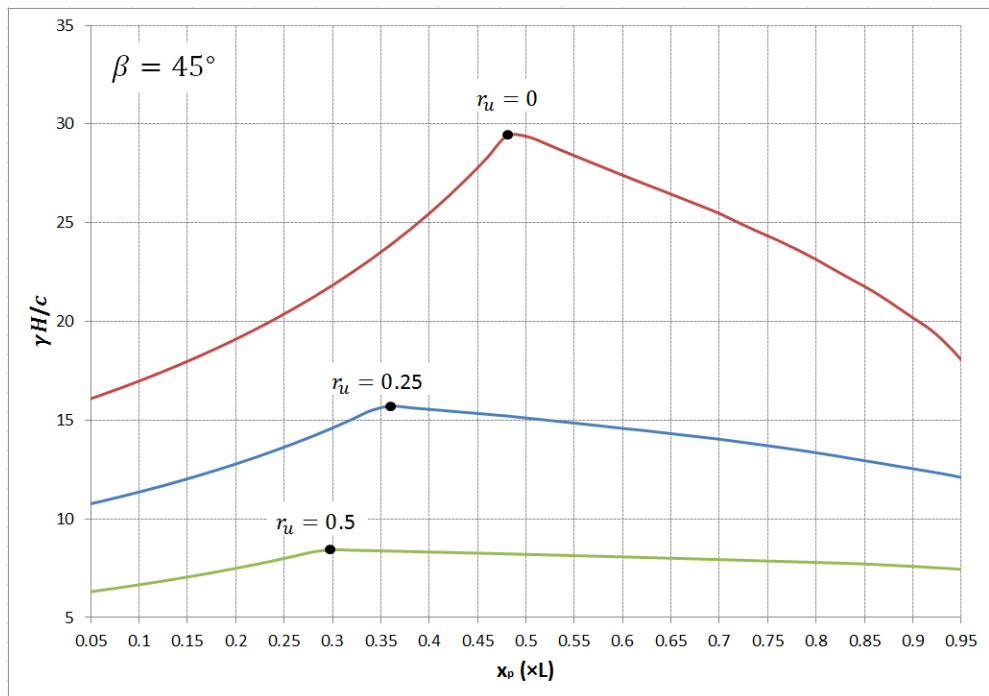
where  $\theta_1$ ,  $\theta_2$ ,  $z_1$ ,  $z_2$  and  $z_3$  are found in Eqs. (3-39) ~ (3-43).

In Figure 6-13, the stability factors defined in Eq. (6-26) are plotted against pile location  $x_p$  for slopes with different inclinations ( $\beta = 30^\circ, 45^\circ, 60^\circ, 75^\circ$ ) subjected to pore water pressure. Slopes are reinforced by a row of piles whose  $K_{pl} = 0.1$ . For illustrative purposes, the case of horizontal upper slope ( $\alpha = 0^\circ$ ) is considered. The friction angle of the material is specified as  $20^\circ$ . Two pore water pressure distributions, i.e.,  $r_u = 0.25$  and  $r_u = 0.5$  are investigated. It is worth noting that the presence of pore water pressure not only lowers the stability factors of slopes but changes the behaviour of pile reinforcement in the way that the most effective pile location shifts downwards with the increasing magnitude of  $r_u$ .

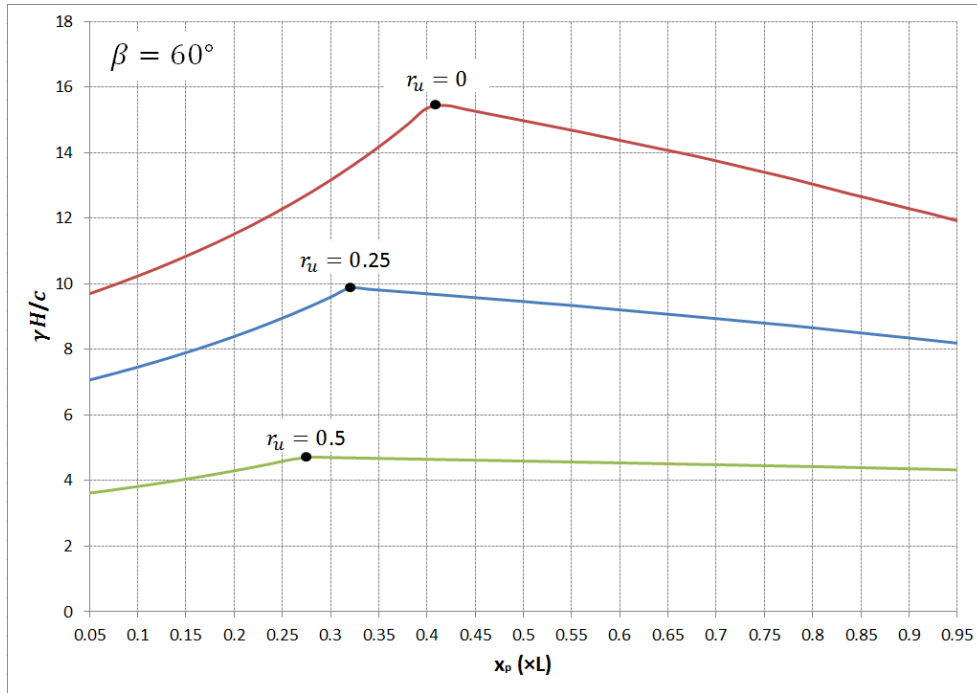
Stability factors defined in Eq. (6-27) are plotted against pile location  $x_p$  for slopes with different inclinations ( $\beta = 30^\circ, 45^\circ, 60^\circ, 75^\circ$ ) in Figure 6-14. Slopes are reinforced by a row of piles whose  $\frac{D_2}{D_1} = 0.6$ . Compared with the dry case ( $r_u = 0$ ), the locations of the pile ensuring maximum stability factor for saturated slope are at the crest of the slope.



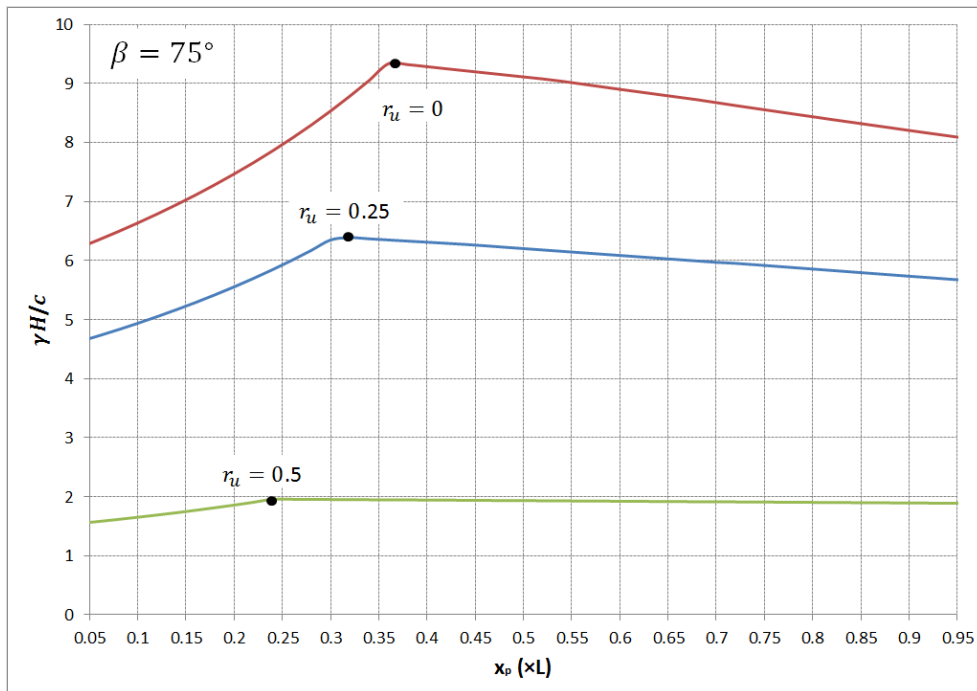
(a)  $\beta = 30^\circ$



(b)  $\beta = 45^\circ$



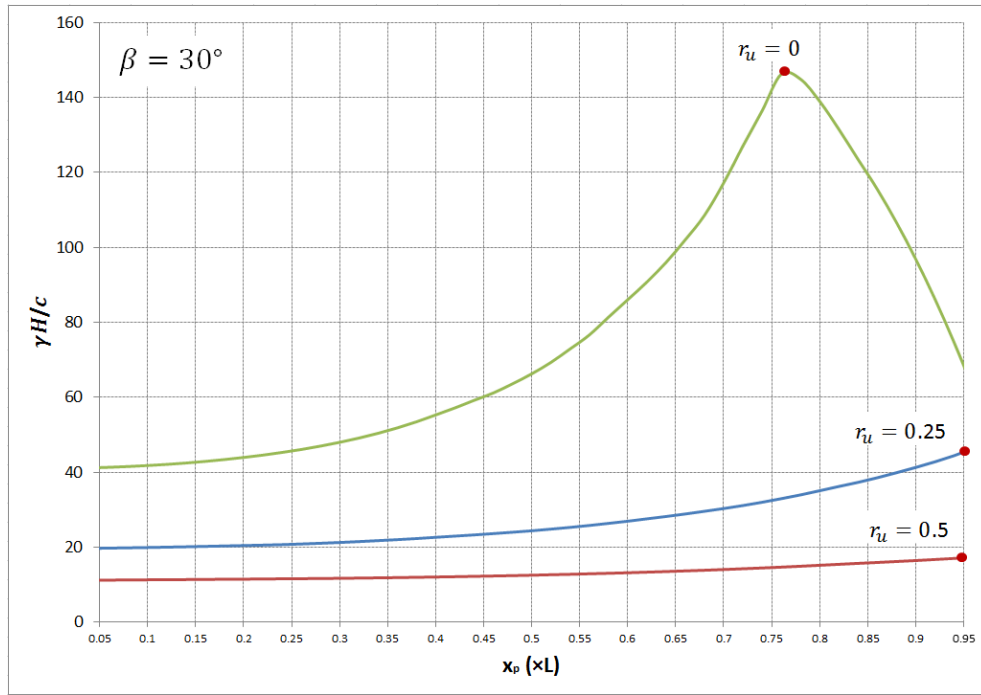
(c)  $\beta = 60^\circ$



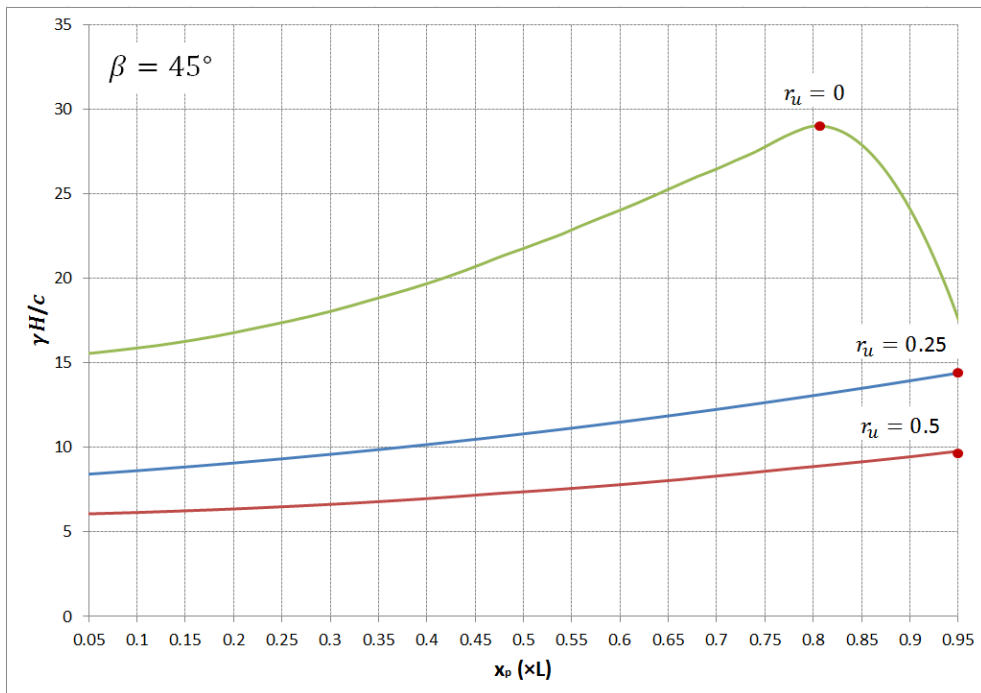
(d)  $\beta = 75^\circ$

Figure 6-13. Stability factor corresponding to case 1 against pile location for slopes subjected to pore water pressure with various inclinations,  $\alpha = 0^\circ$ ,  $\phi = 20^\circ$ ,  $K_{pl} = 0.1$ .

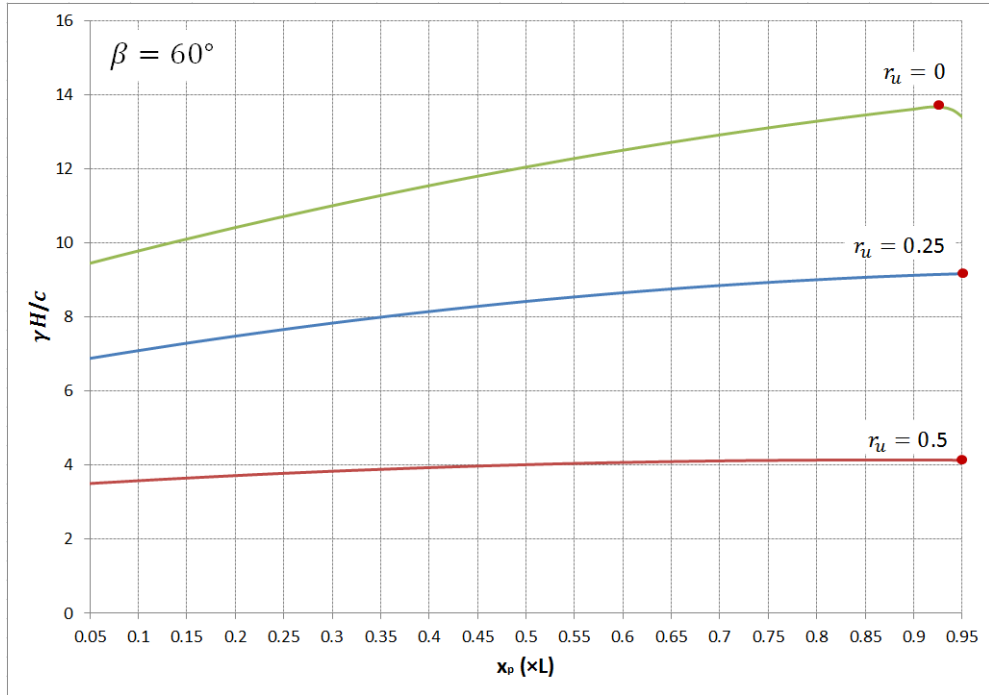




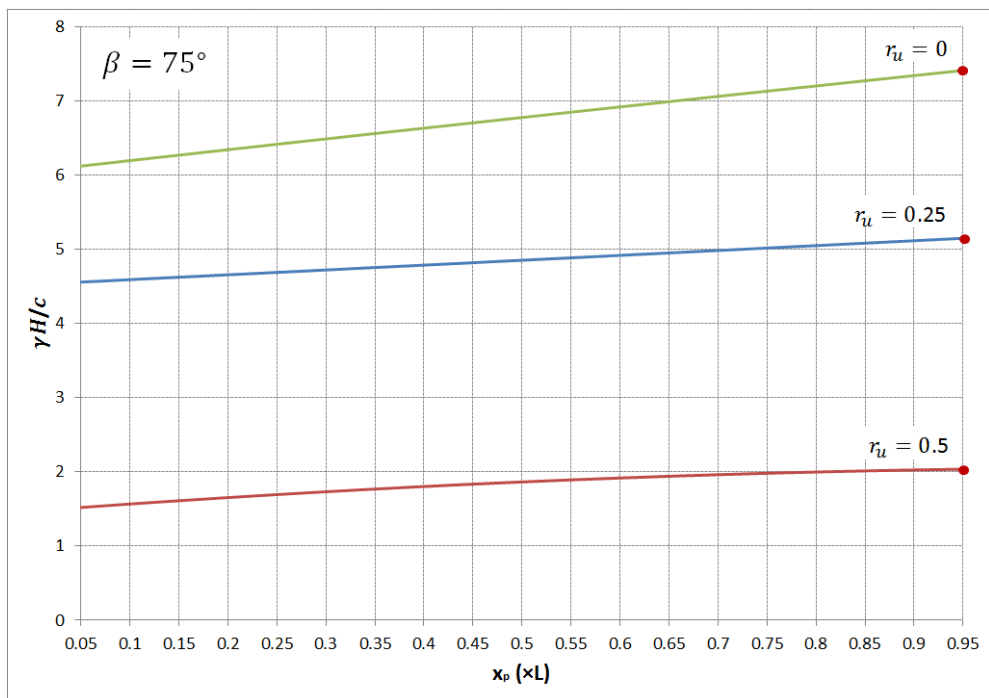
(a)  $\beta = 30^\circ$



(b)  $\beta = 45^\circ$



(c)  $\beta = 60^\circ$



(d)  $\beta = 75^\circ$

Figure 6-14. Stability factor corresponding to case 2 against pile location considering for slopes subjected to pore water pressure,  $\alpha = 0^\circ$ ,  $\phi = 20^\circ$ ,  $\frac{D_2}{D_1} = 0.6$ .

## 6.5 The effect of seismic action on optimal pile position

In this section, reinforced slopes subjected to seismic actions are investigated using the pseudo-static method as described in section 3.3. Coefficients  $k_h$  and  $k_v$  represents the intensity of horizontal and vertical acceleration as a fraction of the gravity acceleration.

The external work of the soil-pile system contains the work done by the material weight and horizontal/vertical seismic actions. Equating the rate of external work to the rate of energy dissipation, leads to:

$$\dot{W}_\gamma + \dot{W}_{s,v} + \dot{W}_{s,h} = \dot{W}_d + \dot{W}_p \quad (6-30)$$

where  $\dot{W}_{s,v}$  and  $\dot{W}_{s,h}$  are the rate of work done by vertical and horizontal seismic actions respectively.  $\dot{W}_{s,v}$  is calculated by:

$$\dot{W}_{s,v} = k_v \cdot \dot{W}_\gamma \quad (6-31)$$

$\dot{W}_{s,h}$  acting on the sliding region **ABCDE** (see Figure 6-10) is the summation of the rate of work done by seismic actions on the region **OCF** ( $\dot{W}_{1h}$ ) minus the work of **OAF** ( $\dot{W}_{2h}$ ), **OAB** ( $\dot{W}_{3h}$ ), **OBC** ( $\dot{W}_{4h}$ ) and **EDF** respectively. Similarly, the rate of work of region **EDF** is the result of work done by seismic actions on **ODF** ( $\dot{W}_{5h}$ ) subtract **OEF** ( $\dot{W}_{6h}$ ) and **ODE** ( $\dot{W}_{7h}$ ). For each term, it can be expressed uniformly as:

$$\dot{W}_{ih} = k_h \omega |y_{Gi} - y_0| \gamma A_i \quad (6-32)$$

where  $y_{Gi}$  and  $y_0$  are the vertical coordinates of the gravity center of the region and of the center of rotation  $O$  respectively.  $A_i$  is the area of each region. The expressions for  $\dot{W}_{1h} \sim \dot{W}_{3h}$  are found in Chen and Liu (1990):

$$\begin{aligned}\dot{W}_{1h} &= \omega\gamma r_0^3 \frac{e^{3\tan\phi(\theta_h - \theta_0)} (3\tan\phi \sin\theta_h - \cos\theta_h) - 3\tan\phi \sin\theta_0 + \cos\theta_0}{3(1+9\tan^2\phi)} \\ &= \omega\gamma r_0^3 f_{1h}(\theta_0, \theta_h)\end{aligned}\quad (6-33)$$

$$\begin{aligned}\dot{W}_{2h} &= \omega\gamma r_0^3 \left[ \frac{1}{6} \sin(\theta_0 + \alpha) \frac{L_0}{r_0} \left( 2\sin\theta_0 + \frac{L_0}{r_0} \sin\alpha \right) \right] \\ &= \omega\gamma r_0^3 f_{2h}(\theta_0, \theta_h, \beta')\end{aligned}\quad (6-34)$$

$$\begin{aligned}\dot{W}_{3h} &= \omega\gamma r_0^3 \frac{H}{6r_0 \tan\beta} \left( \frac{L_0}{r_0} \sin\alpha + \sin\theta_0 + \cos\theta_0 \tan\beta - \frac{L_0}{r_0} \cos\alpha \right) \times \\ &\left( 2\cos\theta_0 - 2\frac{L_0}{r_0} \cos\alpha - \frac{H}{r_0 \tan\beta} \right) = \omega\gamma r_0^3 f_{3h}(\theta_0, \theta_h, \beta')\end{aligned}\quad (6-35)$$

Considering the regions of **OBC**, **ODF**, **OEF** and **ODE**,

$$\begin{aligned}\dot{W}_{4h} &= \omega\gamma r_0^3 \frac{H}{6r_0} \left( \frac{1}{\tan\beta'} - \frac{1}{\tan\beta} \right) \left( \frac{H}{\tan\beta} + \frac{L_0}{r_0} \sin\alpha + \sin\theta_0 \right) \\ &\times \left( 2\cos\theta_0 - 2\frac{L_0}{r_0} \cos\alpha - \frac{H}{r_0 \tan\beta'} - \frac{H}{r_0 \tan\beta} \right) \\ &= \omega\gamma r_0^3 f_{4h}(\theta_0, \theta_h, \beta')\end{aligned}\quad (6-36)$$

$$\begin{aligned}\dot{W}_{5h} &= \omega\gamma r_0^3 \frac{e^{3\tan\phi(\theta_c - \theta_0)} (3\tan\phi \cos\theta_c + \sin\theta_c) - 3\tan\phi \cos\theta_0 - \sin\theta_0}{3(1+9\tan^2\phi)} \\ &= \omega\gamma r_0^3 f_{5h}(\theta_0, \theta_c)\end{aligned}\quad (6-37)$$

$$\dot{W}_{6h} = \omega \gamma r_0^3 \frac{1}{6} \sin \theta_0 \frac{L_c}{r_0} \left( 2 \cos \theta_0 - \frac{L_c}{r_0} \right) = \omega \gamma r_0^3 f_{6h}(\theta_0, \theta_c) \quad (6-38)$$

$$\begin{aligned} \dot{W}_{7h} &= \omega \gamma r_0^3 \frac{1}{3} e^{2 \tan \phi (\theta_c - \theta_0)} \frac{\cos^2 \theta_c}{\cos \alpha} \left[ e^{\tan \phi (\theta_c - \theta_0)} \sin(\theta_c + \alpha) - \sin(\theta_0 + \alpha) \right] \\ &= \omega \gamma r_0^3 f_{7h}(\theta_0, \theta_c) \end{aligned} \quad (6-39)$$

After rearranging Eq. (6-30), the stability factors corresponding to both case 1 and case 2 for reinforced slopes subjected to seismic actions are obtained:

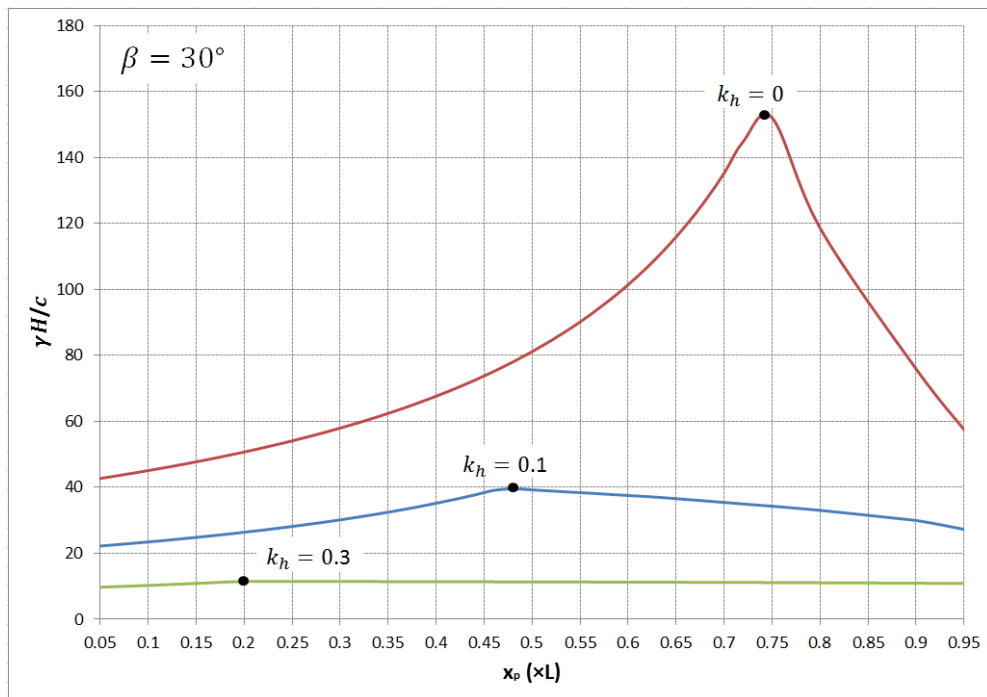
$$\begin{aligned} N_{p,1,s} &= \frac{\gamma H}{c} \\ &= \frac{f_H \times (f_{d-\log}'' + P_1 \times f_{p,1})}{(1 + k_v) \cdot (f_1 - f_2 - f_3 - f_4 - f_5 + f_6 + f_7)} \\ &\quad + k_h \cdot (f_{1h} - f_{2h} - f_{3h} - f_{4h} - f_{5h} + f_{6h} + f_{7h}) - \frac{f_H^2}{2} K_{pl} f_{p,1} \end{aligned} \quad (6-40)$$

$$\begin{aligned} N_{p,2,s} &= \frac{\gamma H}{c} \\ &= \frac{f_H \times (f_{d-\log}'' + P_1 \times f_{p,2})}{(1 + k_v) \cdot (f_1 - f_2 - f_3 - f_4 - f_5 + f_6 + f_7)} \\ &\quad + k_h \cdot (f_{1h} - f_{2h} - f_{3h} - f_{4h} - f_{5h} + f_{6h} + f_{7h}) - P_2 \times f_{p,2} \times \frac{h_b^2}{2r_0^2} \end{aligned} \quad (6-41)$$

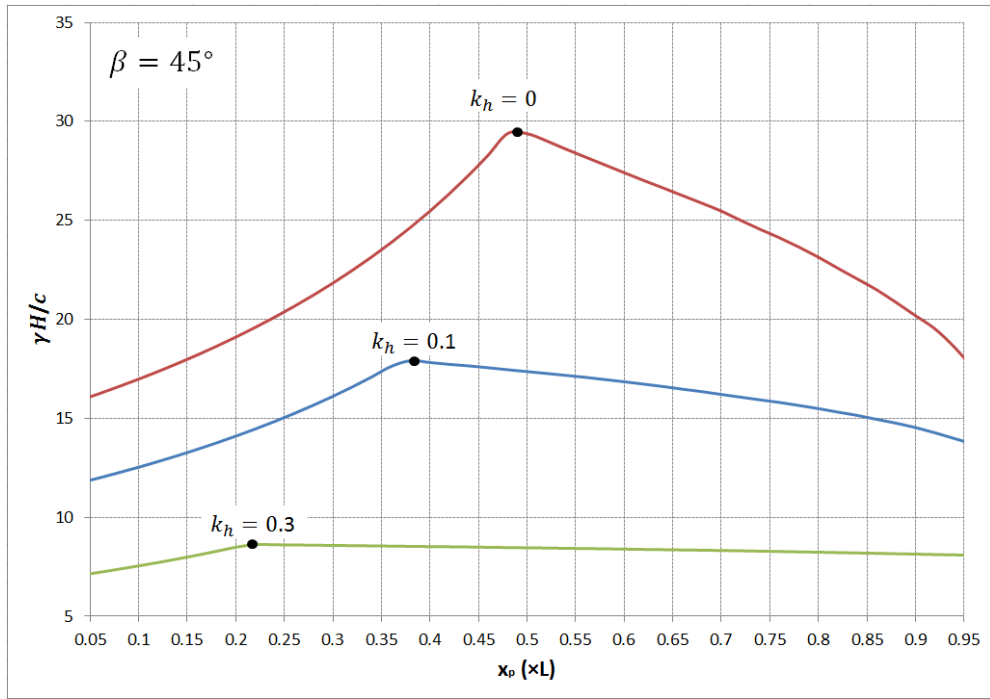
The optimal pile positions under seismic actions for slopes with different inclinations ( $\beta = 30^\circ, 45^\circ, 60^\circ, 75^\circ$ ) are revealed in Figure 6-15 and Figure 6-16. For illustrative purposes, the case of horizontal upper slope ( $\alpha = 0^\circ$ ) is considered. The friction angle of the material is specified as  $20^\circ$ . Vertical acceleration is disregarded. Stability factors defined in Eq. (6-40) against pile location  $x_p$  for two seismic actions ( $k_h = 0.1, 0.3$ ) are presented in Figure 6-15. Slopes are reinforced

by a row of piles whose  $K_{pl} = 0.1$ . The most effective pile location shifts downwards with the increasing magnitude of  $k_h$ .

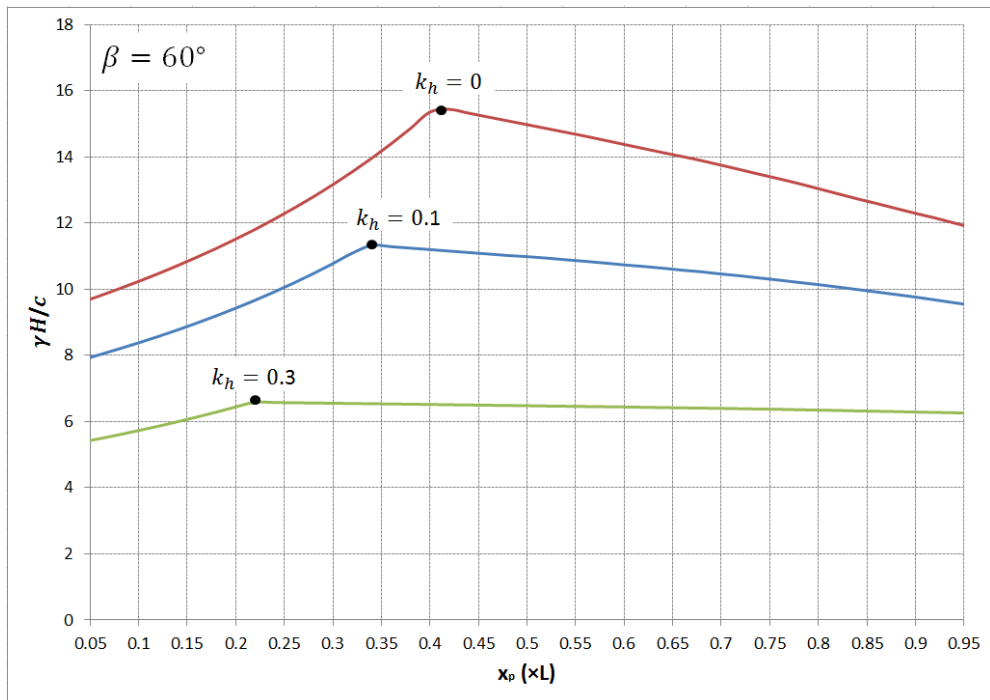
Stability factors defined in Eq. (6-41) are plotted against pile location  $x_p$  in Figure 6-16. Slopes are reinforced by a row of piles whose  $\frac{D_2}{D_1} = 0.6$ . For slopes subjected to gentle seismic action ( $k_h = 0.1$ ), the locations of the pile ensuring maximum stability factor are almost consistent with those for static cases. However, when violent earthquakes ( $k_h = 0.3$ ) occur, the locations convert to the crest of slopes.



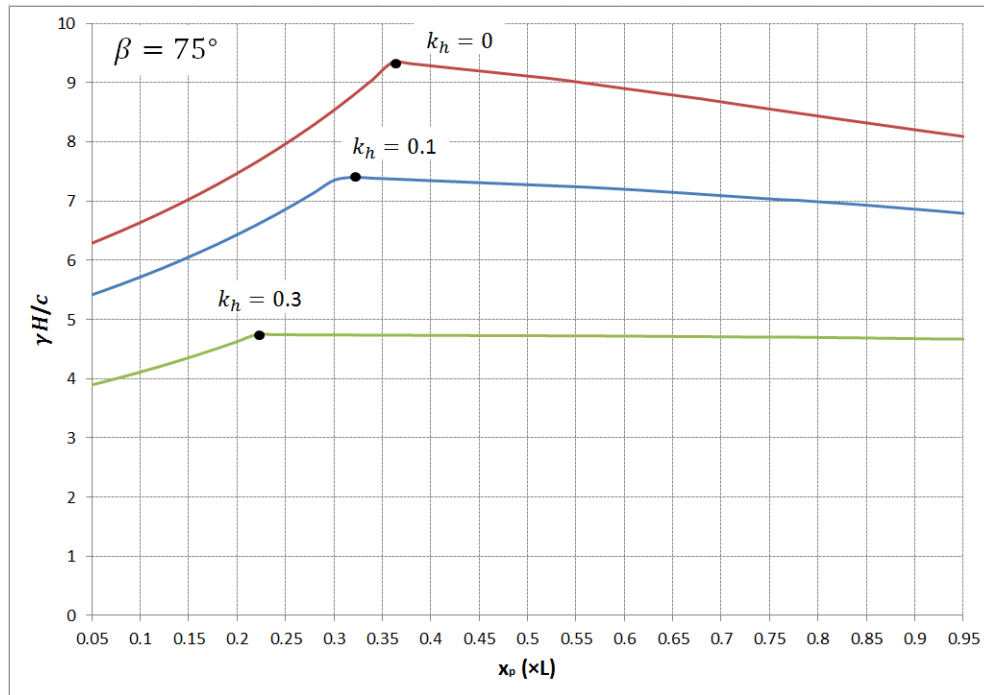
(a)  $\beta = 30^\circ$



(b)  $\beta = 45^\circ$

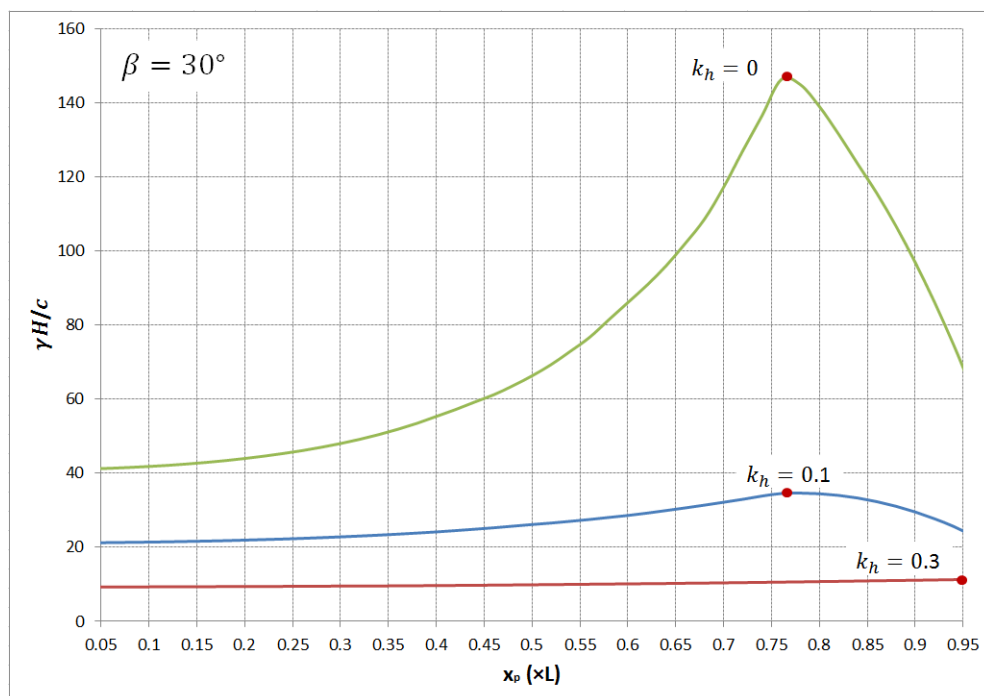


(c)  $\beta = 60^\circ$



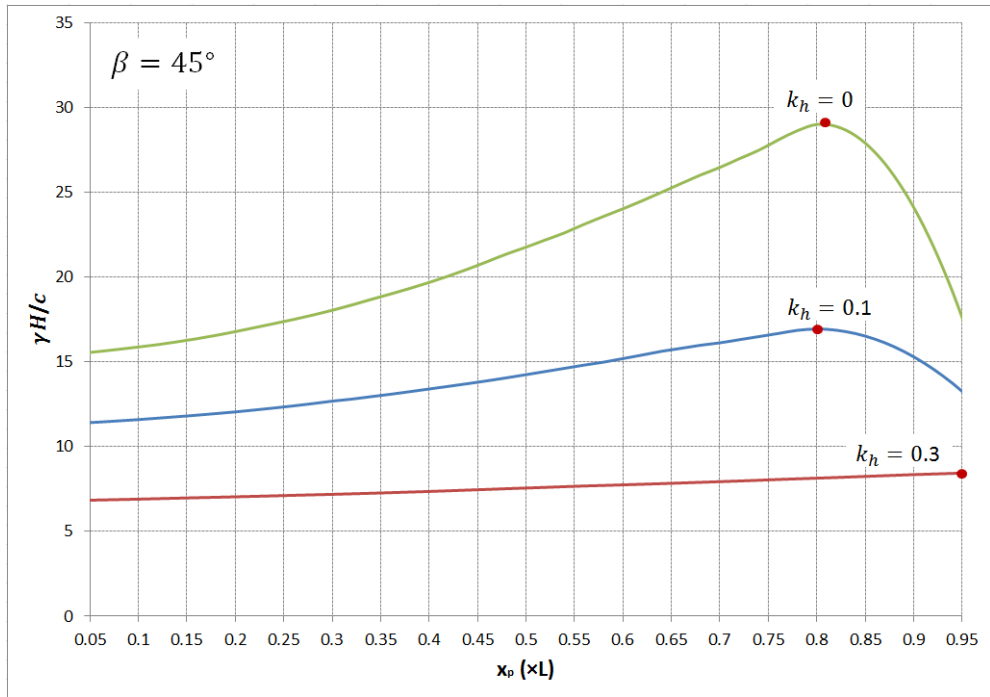
(d)  $\beta = 75^\circ$

Figure 6-15. Stability factor corresponding to case 1 against pile location subjected to seismic actions,  $\alpha = 0^\circ$ ,  $\phi = 20^\circ$ ,  $k_v = 0$ ,  $K_{pl} = 0.1$ .

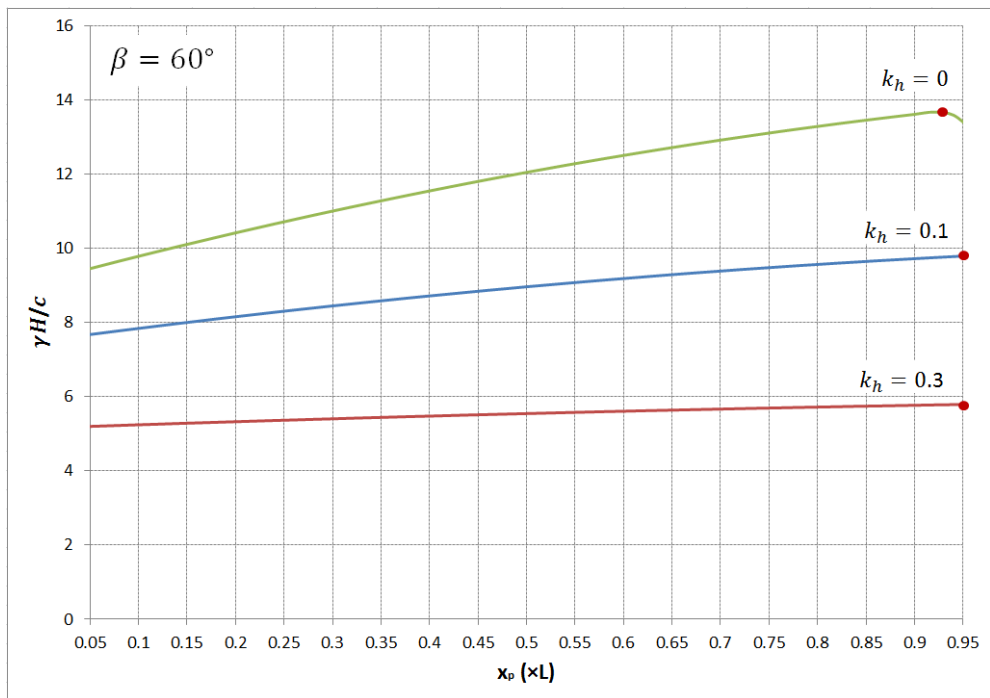


(a)  $\beta = 30^\circ$

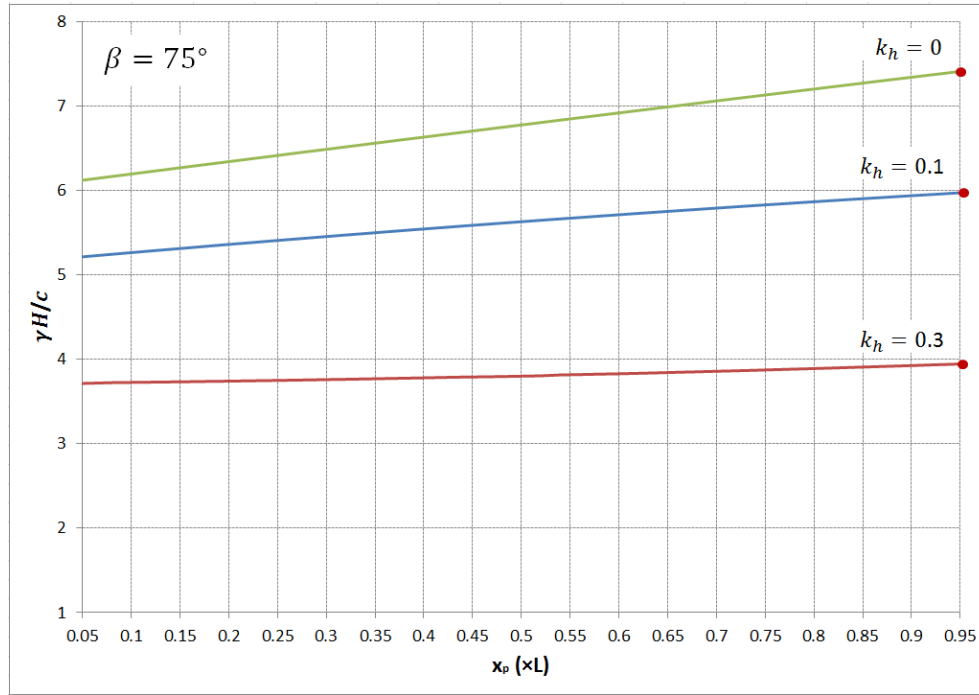




(b)  $\beta = 45^\circ$



(c)  $\beta = 60^\circ$



(d)  $\beta = 75^\circ$

Figure 6-16. Stability factor corresponding to case 2 against pile location subjected seismic

actions,  $\alpha = 0^\circ$ ,  $\phi = 20^\circ$ ,  $k_v = 0$ ,  $\frac{D_2}{D_1} = 0.6$ .

## 6.6 Performance-based optimal design of piles during earthquakes

Besides the stability factor, the stability of slopes can be measured according to the potential cumulative displacement during an earthquake. In this section, the optimal pile position corresponds to that yielding the minimum cumulative displacement during an earthquake is investigated. Seismic displacement calculation procedures proposed by Newmark (1965) and Chang et al. (1984) are adopted.

In Figure 6-10, when the rotational acceleration of the sliding block **ABCDE** about  $O$  is not zero, an additional moment due to inertial forces will appear.

According to Chang et al. (1984) and You and Michalowski (1999), the rotational acceleration of the block  $\ddot{\theta}$  is given by:

$$\ddot{\theta} = (k - k_c) \frac{\gamma r_0^3}{\frac{G}{g} l_g^2} (f_{1h} - f_{2h} - f_{3h} - f_{4h} - f_{5h} + f_{6h} + f_{7h}) \quad (6-42)$$

where  $G$  is the weight of the rotating block **ABCDE**. The total area of **ABCDE** is the summation of regions **OCF** ( $A_1$ ) minus **OAF** ( $A_2$ ), **OAB** ( $A_3$ ), **OBC** ( $A_4$ ) and **EFD** respectively. Similarly, the area of region **EFD** is the summation of **ODF** ( $A_5$ ) subtract **OEF** ( $A_6$ ) and **ODE** ( $A_7$ ). Thus,  $G$  is expressed as:

$$G = \gamma (A_1 - A_2 - A_3 - A_4 - A_5 + A_6 + A_7) \quad (6-43)$$

with

$$A_1 = \frac{1}{2} r_0^2 \frac{e^{2 \tan \phi (\theta_h - \theta_0)} - 1}{2 \tan \phi} \quad (6-44)$$

$$A_2 = \frac{1}{2} r_0^2 \frac{L_0}{r_0} \sin(\theta_0 + \alpha) \quad (6-45)$$

$$A_3 = \frac{1}{2} r_0^2 \frac{H}{r_0} \left( \cos \theta_0 - \frac{L_0}{r_0} \cos \alpha + \frac{\sin \theta_0 + \frac{L_0}{r_0} \sin \alpha}{\tan \beta} \right) \quad (6-46)$$

$$A_4 = \frac{1}{2} r_0^2 \frac{L_t}{r_0} r_h \sin \theta_h \quad (6-47)$$

$$A_5 = \frac{1}{2} r_0^2 \frac{e^{2 \tan \phi (\theta_c - \theta_0)} - 1}{2 \tan \phi} \quad (6-48)$$

$$A_6 = \frac{1}{2} r_0^2 \frac{L_c}{r_0} \sin(\theta_0 + \alpha) \quad (6-49)$$

$$A_7 = \frac{1}{2} r_0^2 \frac{\delta}{r_0} e^{\tan \phi (\theta_c - \theta_0)} \cos \theta_c \quad (6-50)$$

$l_g$  is the distance from point  $O$  to the centre of gravity of the block **ABCDE**, and is calculated by:

$$l_g = \frac{\gamma r_0^3}{G} \sqrt{\frac{(f_1 - f_2 - f_3 - f_4 - f_5 + f_6 + f_7)^2}{(f_{1h} - f_{2h} - f_{3h} - f_{4h} - f_{5h} + f_{6h} + f_{7h})^2}} \quad (6-51)$$

The permanent rotation increment  $\delta\theta$  is calculated by double integrating block acceleration  $\ddot{\theta}$  over time interval  $\delta t$ :

$$\delta\theta = \int_{\delta t} \int_{\delta t} \ddot{\theta} dt dt \quad (6-52)$$

The maximum horizontal displacement of slope toe is computed as:

$$\begin{aligned} \delta u_x &= r_h \delta\theta \sin \theta_h = \\ &= \frac{\gamma r_0^4}{G l_g^2} e^{\tan \phi (\theta_h - \theta_0)} \sin \theta_h (f_{1h} - f_{2h} - f_{3h} - f_{4h} - f_{5h} + f_{6h} + f_{7h}) \int_{\delta t} \int_{\delta t} g(k - k_c) dt dt \quad (6-53) \\ &= C \int_{\delta t} \int_{\delta t} g(k - k_c) dt dt \end{aligned}$$

where  $k_c$  is the yield acceleration coefficient, for slopes reinforced with piles, it can be obtained by rearranging Eq. (6-41) corresponding to case 2 and letting  $k_v = 0$ :

$$k_c = \frac{\frac{c}{\gamma H} \cdot f_H \cdot (f_{d-\log}'' + P_1 \times f_{p,2}) - (f_1 - f_2 - f_3 - f_4 - f_5 + f_6 + f_7) + P_2 \times f_{p,2} \times \frac{h_b^2}{2r_0^2}}{f_{1h} - f_{2h} - f_{3h} - f_{4h} - f_{5h} + f_{6h} + f_{7h}} \quad (6-54)$$

The maximum cumulative horizontal displacement during an earthquake can be calculated using Eq. (6-53) when the acceleration record of an earthquake is provided. The Northridge 1994 earthquake (Yegian et al. 1995) is selected as an example to illustrate the determination of the optimal pile positions corresponding to minimum displacement. The Northridge (Moorpark Station) record of horizontal ground acceleration is illustrated in Figure 6-17.

In Figure 6-18, the cumulative horizontal displacements at slope toe are plotted against different pile location  $x_p$  for slopes with various inclinations ( $\beta = 30^\circ, 45^\circ, 60^\circ, 75^\circ$ ) and values of  $\frac{\gamma H}{c}$ . Slopes are reinforced by a row of piles whose  $\frac{D_1}{D_2} = 0.6$ . For both intact slopes and cracked slopes, the optimal position for gentle slopes is within the upper-middle part of the slope. However, the optimal position switches to the crest for steep slopes. The observations are consistent with those in section 6.3, case 2. Thus, the determination of the optimal position of pile reinforcement based on the cumulative displacement during an earthquake yields similar results to that based on the stability factor.

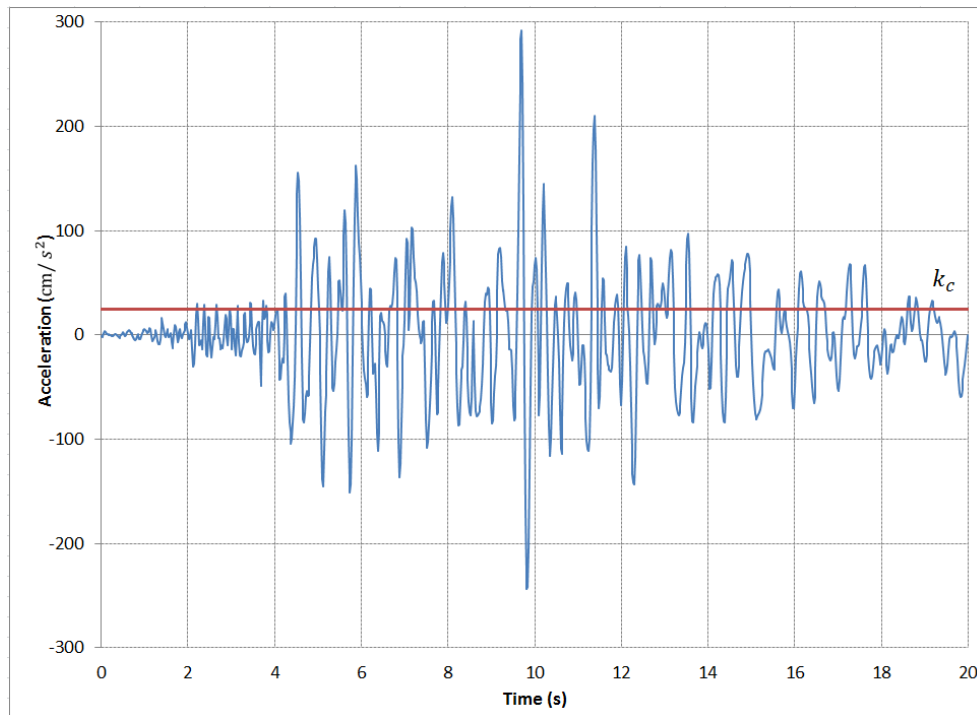
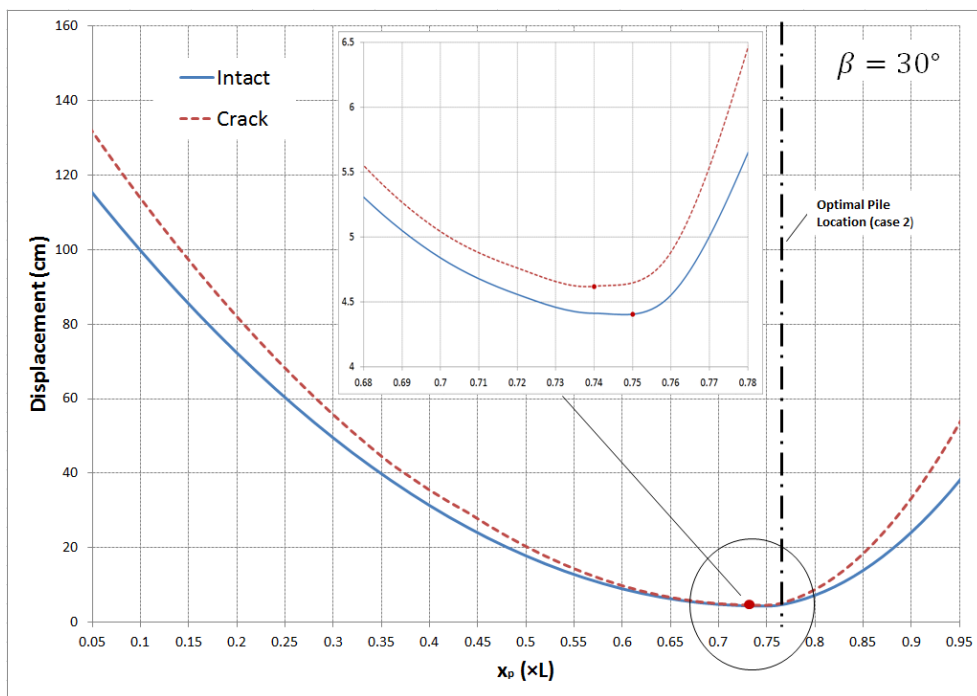
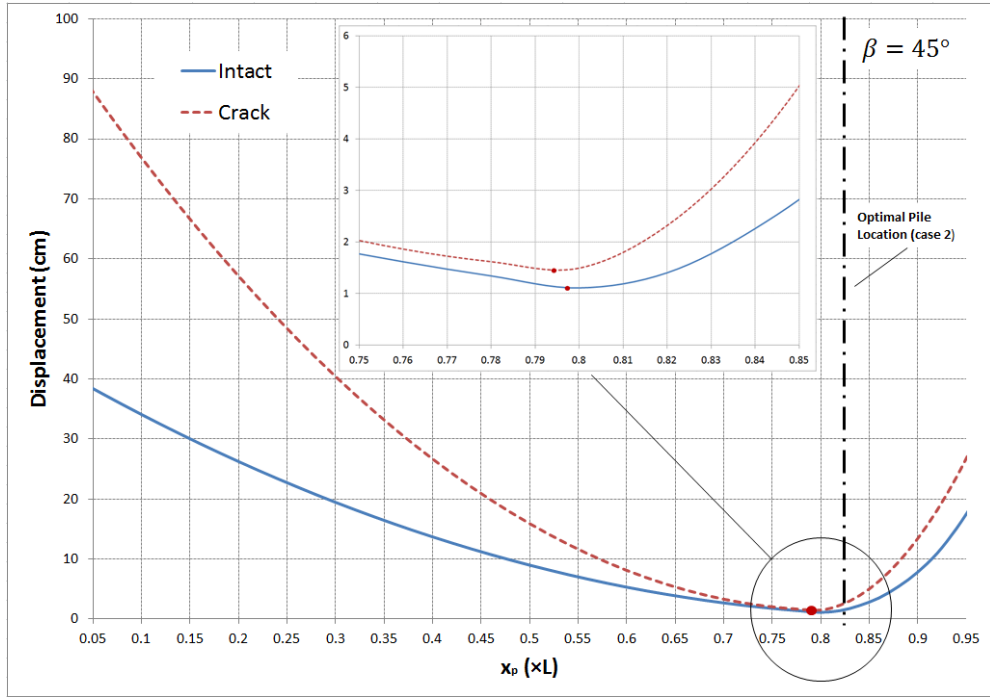


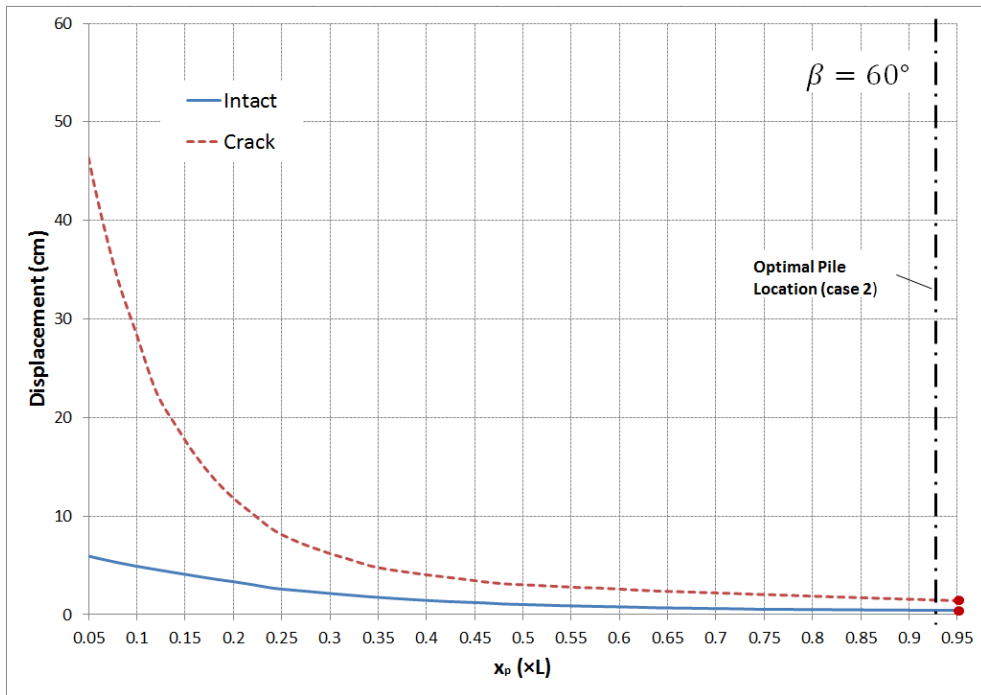
Figure 6-17. Northridge 1994 earthquake record (Moorpark Station), horizontal ground acceleration.



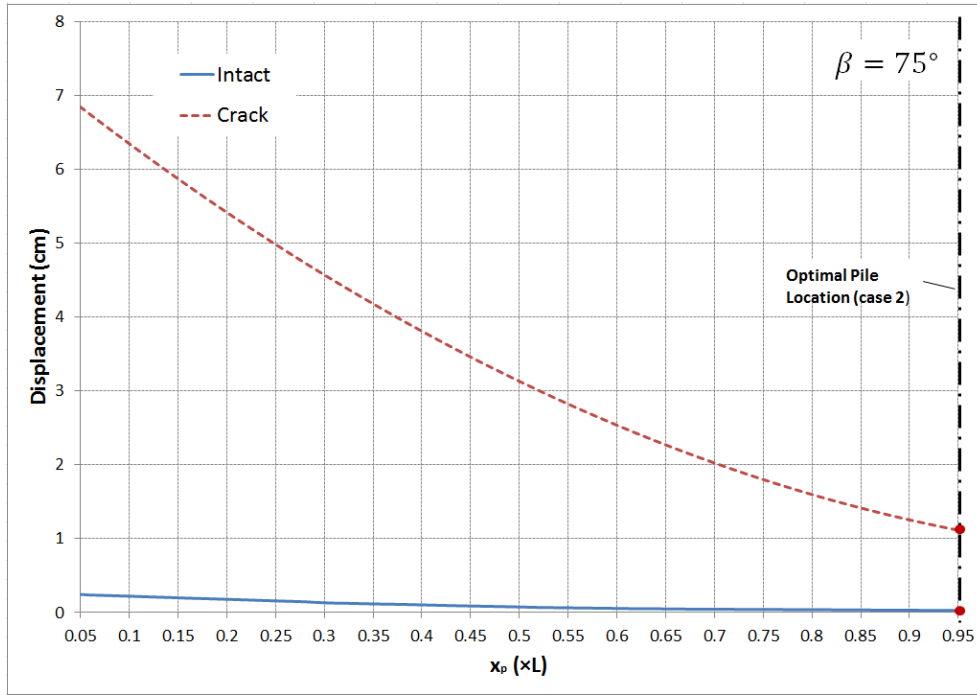
(a)  $\beta = 30^\circ, \frac{\gamma H}{c} = 40$



(b)  $\beta = 45^\circ, \frac{\gamma^H}{c} = 15$



(c)  $\beta = 60^\circ, \frac{\gamma^H}{c} = 9$



(d)  $\beta = 75^\circ, \frac{\gamma H}{c} = 5.5$

Figure 6-18. Displacement at slope toe against pile position for various slope inclinations,

$\alpha = 0^\circ, \phi = 20^\circ, k_v = 0, \frac{D_2}{D_1} = 0.6.$

## 6.7 Conclusions

In this chapter, the optimal pile positions corresponding to the most effective pile location, the location of the pile ensuring maximum stability factor and the location ensuring the minimum accumulative displacement during an earthquake are investigated using the kinematic approach of limit analysis. The effect of presence of crack, pore water pressure and seismic actions is evaluated. The following conclusions can be drawn:

(a) In the previous studies of Ausilio et al. (2001), Nian et al. (2008) and Li et al. (2012), the most effective pile location is found around the slope toe where the stabilizing force needed to increase factor of safety to a desired value takes the minimum value. However, the above-pile failure mechanism can make the



installation of piles completely ineffective. The most effective pile location is sought where the above-pile and pass-through-pile failure mechanisms yield the same stability factor. With the increase of  $K_p$  and friction angle, the most effective pile location shifts towards the upper-middle part of slope.

(b) In order to evaluate the location of the pile ensuring maximum stability factor, the presence of pile reinforcement is taken into account by integrating the dissipated energy along the slope-pile interface according to Ito and Matsui's theory (Ito and Matsui 1975). The locations will shift towards the middle of slope face when the friction angle increases.

(c) The presence of pre-existing cracks has little impact on the optimal position of a row of piles used in slope stabilization.

(d) The presence of pore water pressure changes the behavior of pile reinforcement. The most effective pile location shifts downwards to lower-middle part with the increasing magnitude of  $r_u$ . The locations of the pile ensuring maximum stability factor for saturated slope stay at the crest of the slope.

(e) For reinforced slopes subjected to seismic actions, the most effective pile location shifts downwards to the lower-middle part with the increasing magnitude of  $k_h$ . For slopes subjected to gentle seismic action ( $k_h = 0.1$ ), the locations ensuring maximum stability factor are almost consistent with those for static cases. However, when violent earthquakes ( $k_h = 0.3$ ) occur, the optimal locations convert to the crest of slopes.

(f) Besides the stability factor, the optimal pile position can be evaluated according to the potential cumulative displacement during an earthquake. The optimal pile position for gentle slopes is within the upper-middle part of the slope. However, it switches to the slope crest for steep slopes.

## **Chapter 7 Development of a Software Package for Slope Stability Assessment**

In Chapter 3 to Chapter 6, a great number of stability charts are provided for safety assessment and optimal design. However, it should be noted that the application of analytical limit analysis is still limited since most of the research findings are chart-based (e.g., Michalowski 1995, Uili 2013, Gao et al. 2012). Since no such stability chart is available to cover a wide range of material strength parameters, slope geometries and external loads, practitioners find it difficult to use the charts for a specific slope project. Nevertheless, the kinematic approach of limit analysis is still a powerful tool to assess slope stability for its theoretical rigor and simplicity. In comparison with plenty of existing commercial software based on limit equilibrium and FEM (e.g., Slide, Phase2, OptumG2, Plaxis, FLAC), the practical use of analytical limit analysis for individual projects is not yet available. In this chapter, the development of a software package for slope stability assessment based on the analytical upper bound method is introduced. The software package is nested in MATLAB R2014b (Mathworks 2014) using GUI (Graphical User Interfaces). An independent executable file (.exe) is also available by adopting the MATLAB Compiler toolbox. Illustrations of the software features and validations with other existing software are provided. The present software package turns out to be accurate and efficient in solving the factor of safety, failure mechanism and implementing sensitivity analysis.

### **7.1 Theoretical basis**

#### **7.1.1 Generalized formulation for homogeneous slopes**

According to Chen (1975, 1990), under the assumption that the slope under investigation is made of geomaterials obeying the Mohr-Coulomb failure criterion and normality flow rule, a logarithmic spiral failure mechanism (rigid-rotational type) is the most critical one among all kinematically admissible mechanisms regardless of the shape of the slope profile and the influence of external loads (e.g., pore water pressure and seismic actions).

In Figure 7-1, the slope is considered as a homogeneous rigid perfectly plastic continuum. It is subjected to the presence of pre-existing crack, vertical and horizontal seismic actions and pore water pressure, reinforced with a row of piles, a single block **ABCDE** rotates as a rigid body about  $O$  with angular velocity  $\omega$ , the remaining part is bounded by a vertical crack **DE** and a logarithmic spiral line  $\widehat{CD}$ . Similar to previous chapters, the rate of work due to the material weight and external loads can be expressed uniformly as:

$$\begin{aligned}\dot{W}_{external} &= \gamma r_0^3 \omega \left[ (1+k_v)(f_1 - f_2 - f_3 - f_4 - f_5 + f_6 - f_7) \right. \\ &\quad \left. + k_h(f_{1h} - f_{2h} - f_{3h} - f_{4h} - f_{5h} + f_{6h} - f_{7h}) + p_{w-c} + p_{w-log} \right] \quad (7-1) \\ &= \gamma r_0^3 \omega \left[ (1+k_v)f_v + k_h \cdot f_h + f_w \right]\end{aligned}$$

with  $k_h$  and  $k_v$ , the intensity of horizontal and vertical acceleration as a fraction of the gravity acceleration,  $\gamma$  being the unit weight of the material. The detailed expressions for  $f_1, f_2, f_4, f_5, f_6, f_7, f_{1h}, f_{2h}, f_{4h}, f_{5h}, f_{6h}, f_{7h}$  and  $p_{w-c}, p_{w-log}$  can be found in Chapter 6. For  $f_3$  and  $f_{3h}$ , since a non-planar slope profile is encountered, they are written into the forms:

$$f_3 = \frac{1}{3} \int_{\theta_c}^{\theta} P^3(\theta) \cos \theta d\theta \quad (7-2)$$

$$f_{3h} = \frac{1}{3} \int_{\theta_c}^{\theta_t} P^3(\theta) \sin \theta d\theta \quad (7-3)$$

where  $P(\theta)$  is the function of the slope profile  $AB$  in the polar coordinate system with  $O$  as its center.

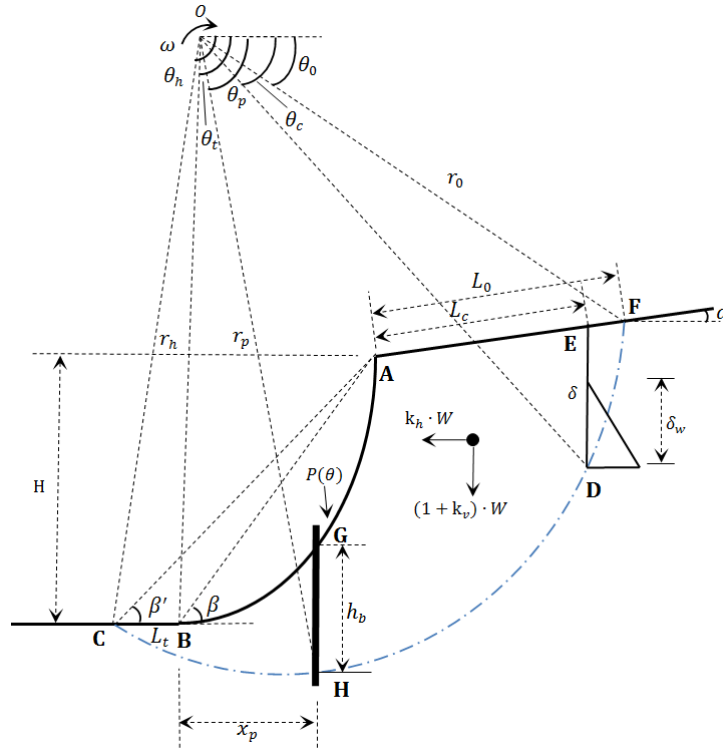


Figure 7-1. Slope geometry, loading conditions and failure mechanism.

The energy dissipation within the slope includes both the dissipated energy along the failure mechanism  $\widehat{CD}$  and the additional stabilizing work brought from pile reinforcement. The rate of internal energy dissipation is then expressed as:

$$\dot{W}_{\text{internal}} = c\omega r_0^2 f_{d-\log}'' + \omega F_p f_p \quad (7-4)$$

with  $f''_{d-log}$  and  $f_p$  defined in Eqs. (5-35) and (6-22). In order to calculate  $f_p$  corresponding to a non-planar slope profile,  $h_b$  defined in Eq. (6-4) has to be revised as:

$$h_b = P(\theta_G) \cos \theta_G - r_p \cos \theta_p \quad (7-5)$$

where  $\theta_G$  is determined by:

$$P(\theta_G) \sin \theta_G = r_p \sin \theta_p \quad (7-6)$$

By equating the rate of external work to the rate of internal energy dissipation, leads to:

$$\dot{W}_{external} = \gamma r_0^3 \omega \left[ (1 + k_v) f_v + k_h \cdot f_h + f_w \right] = \dot{W}_{internal} = c \omega r_0^2 f''_{d-log} + \omega F_p f_p \quad (7-7)$$

After rearranging, the generalized stability factor of a homogenous slope is defined as:

$$\frac{\gamma H}{c} = \frac{f_H \times (f''_{d-log} + P_1 \times f_p)}{(1 + k_v) f_v + k_h f_h + f_w - P_2 \times f_p \times \frac{h_b^2}{2r_0^2}} \quad (7-8)$$

where  $f_H$ ,  $P_1$  and  $P_2$  are found in Eqs. (5-3), (6-16) and (6-17).

The most critical failure mechanism is determined by four parameters  $\theta_0$ ,  $\theta_c$ ,  $\theta_h$  and  $\beta'$ , which are regarded as variables. The least upper bound is found through an optimization procedure where the minimum value of the stability factor defined in Eq. (7-8) is sought. By replacing  $c$  with  $c_s/F$  and  $\tan \phi$  with  $\tan \phi_s/F$ ,

the factor of safety  $F$  appears in both sides of the Eq. (7-8),  $F$  can be solved by an iterative procedure until the mobilized strength of the material are progressively reduced according to Eq. (3-22), until

$$\frac{\gamma H}{c_s / F} = \frac{f_H \times (f_{d-\log}'' + P_1 \times f_p)}{(1 + k_v) f_v + k_h f_h + f_w - P_2 \times f_p \times \frac{h_b^2}{2r_0^2}} \bigg|_{\phi = \arctan\left(\frac{\tan \phi_s}{F}\right)} \quad (7-9)$$

For slopes made of geomaterials obeying a non-linear failure criterion such as the Hoek-Brown failure criterion, Eq. (7-8) could be modified by using the equivalent cohesion and friction angle method or the tangential technique (see Chapter 4).

### 7.1.2 Generalized formulation for non-homogeneous slopes

In sections 3.4 and 5.9, the case of ground strength anisotropy and spatial non-homogeneity in the vertical direction has been investigated. The corresponding stability factors for non-homogenous slopes can be obtained by replacing  $f_{d-\log}''$  in Eq. (7-9) with  $q_1, q_2, q_3$  in Eqs. (3-64), (3-65), (3-66).

So far, the slope stability assessment procedure is based on the assumption that the slope will fail as a single rigid body rotating along a surface of velocity discontinuity. However, field observation (e.g., Xie et al. 2004, Huang et al. 2012) shows that the failure surfaces are sometimes not curvilinear especially for ground of complicated structures. For layered slopes, each layer shows different material parameters such as unit weight, cohesion, friction angle and seismic coefficients.

Donald and Chen (1997) developed a general framework for slope stability analysis, based on the kinematic approach of limit analysis. A slope is made up of

multiple rigid wedges obeying the linear Mohr-Coulomb failure criterion and normality flow rule. Hu et al. (2013) extended the theory of Donald and Chen (1997) by dividing the slope into several horizontal rows (see Figure 7-2) to account for layered slopes. Each layer is assumed to be a rigid body, but there is energy dissipation along the interfaces of layers when the slope is about to slice. The energy balance equation between the rates of external and internal work becomes:

$$D_L + D_S = WV^* + TV^* \quad (7-10)$$

where  $D_L$  is the energy dissipation between layers and  $D_S$  is the energy dissipation along the slip surface. The two terms on the right-hand side refer to the rates of work done by the weight of soil  $W$  and external loads  $T$  respectively.  $V^*$  is the velocity at the points where  $W$  and  $T^*$  apply. Detailed expression of Eq. (7-10) can be found in the Appendix A.

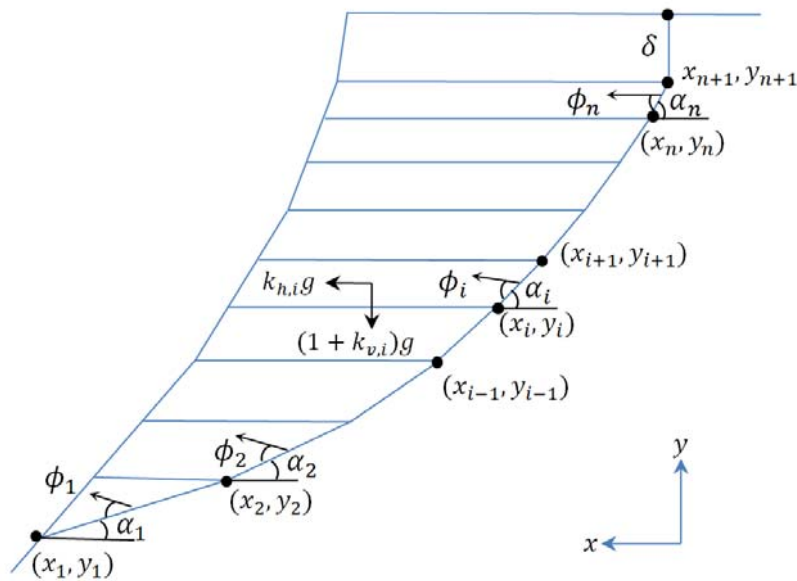


Figure 7-2. Layered slope analysis.

### 7.1.3 Sensitivity analysis

The stability of slopes is governed by a range of factors, such as material strength, slope geometry, external loads and reinforcement measures. All these factors are treated as known and deterministic variables in previous sections. In fact, most of the factors are stochastic, and each of them has a different degree of impact on the slope stability. Thus, it is important to implement sensitivity analysis, since it helps to establish the relationship of the factor of safety of a slope with each factor quantitatively. It is even more interesting to study the interaction between the factors and to determine the major/minor factors to cause slope failure.

Two types of sensitivity analysis will be adopted in this section. First, the one-at-a-time sensitivity analysis (Saltelli et al. 2009) is implemented by varying one factor at a time, while keeping other factors constant. Second, the multi-variable sensitivity analysis (Cannavó 2012) investigates the slope stability as a system of multiple factors and evaluates their correlations. The existing sensitivity analyses in slope stability assessment are mainly conducted with limit equilibrium method or FEM (e.g., Christian et al. 1994, Low et al. 1998, El-Ramly et al. 2002, Griffiths and Fenton 2004, Navarro et al. 2010, Jiang et al. 2014). In comparison with using limit analysis, long computational time and low efficiency make them less attractive to carry out a comprehensive sensitivity study. The present software is capable of running both one-at-a time and multi-variable sensitivity analysis to assess the distinct influence of each factor.

## 7.2 Framework of the software package

The framework of the software is explained in Figure 7-3. To begin with, users should input general information about the slope including its geometry, material



properties, external forces and pile reinforcement. The inputs of slope geometry include the total height, the inclination of the slope, the inclination of upper slope, the estimated position or depth of pre-existing cracks and the shape of slope profile (see Figure 7-4). Although the stability assessment of slopes of any arbitrary shape can be implemented according to Eq. (7-9), the input of complex slope shape requires sophisticated graphic processing, which is meant to be available in the following versions of the software. In the current version, slopes of circular profiles are allowed. The centre of the circular profile is located on the midperpendicular of  $AB$  in Figure 7-1. For slopes of planar profiles, the input value of the radius of slope face should be zero. It is worth mentioning that the software considers both the cases of cracks of known position and cracks of know depth and selects a more critical failure mechanism.

The ground parameters for a Mohr-Coulomb material include unit weight, cohesion and friction angle. For layered slopes, users should input the parameters for each layer (see Figure 7-5). In addition, for a Hoek-Brown material, the values of  $m_i$ , geological strength index ( $GSI$ ), disturbance coefficient ( $D$ ) and  $\sigma_{ci}$  must be assigned.

The inputs corresponding to external forces include the horizontal and vertical accelerations to be specified for seismic actions and  $r_u$  when pore water pressure is considered. Moreover, the position of pile reinforcement is yet another input.

Three different types of strength reduction techniques are available to choose from for materials obeying the Mohr-Coulomb failure criterion. The most routinely adopted way is to reduce both cohesion and friction angle at the same time. Isakov and Moryachkov (2014) proposed that cohesion and friction angle decrease at different rates, two-parameter factor of safety  $F_{double}$  is then defined as:

$$F_{double} = \frac{1}{1 - R / \sqrt{2}} \quad (7-11)$$

$$\text{where } R = \sqrt{\left(1 - \frac{1}{F_c}\right)^2 + \left(1 - \frac{1}{F_\phi}\right)^2}, \quad F_c = \frac{c_s}{c_f}, \quad F_\phi = \frac{\tan \phi_s}{\tan \phi_f}.$$

In addition, the factor of safety may apply to cohesion only. It should be noted that for rock obeying the Hoek-Brown failure criterion, the factor of safety applies to  $\sigma_{ci}$  only:

$$F_{\text{single}} = \frac{\sigma_{ci}}{\sigma_{ci,f}} \quad (7-12)$$

where  $\sigma_{ci,f}$  is the uniaxial compression strength at failure.

The interfaces of the input control panel are shown in Figure 7-4 and Figure 7-5. After the inputs of all information concerning the slope project are ready, the software will calculate the factor of safety for the given slope iteratively according to Eq. (7-8) and manifest the failure mechanism at collapse (see Figure 7-6). Moreover, the software can carry out one-at-a time and multi-variables sensitivity analysis. For instance, let a slope be made of material obeying the Mohr-Coulomb failure criterion. The cohesion  $c$  and friction angle  $\phi$  of the geomaterial satisfy normal distribution. The mean values of  $c$  and  $\phi$  are 20 kPa and  $30^\circ$ . The variances of  $c$  and  $\phi$  are 2 kPa and  $3^\circ$  respectively. Other parameters such as  $r_u$ , crack depth, slope face radius,  $k_h$  and  $k_v$  satisfy uniform distribution as well. Their variation ranges are presented in Figure 7-7. Users can watch the variation of the factor of safety against one variable (e.g. the radius of slope face in Figure 7-7) or sensitivity coefficients of each variable.

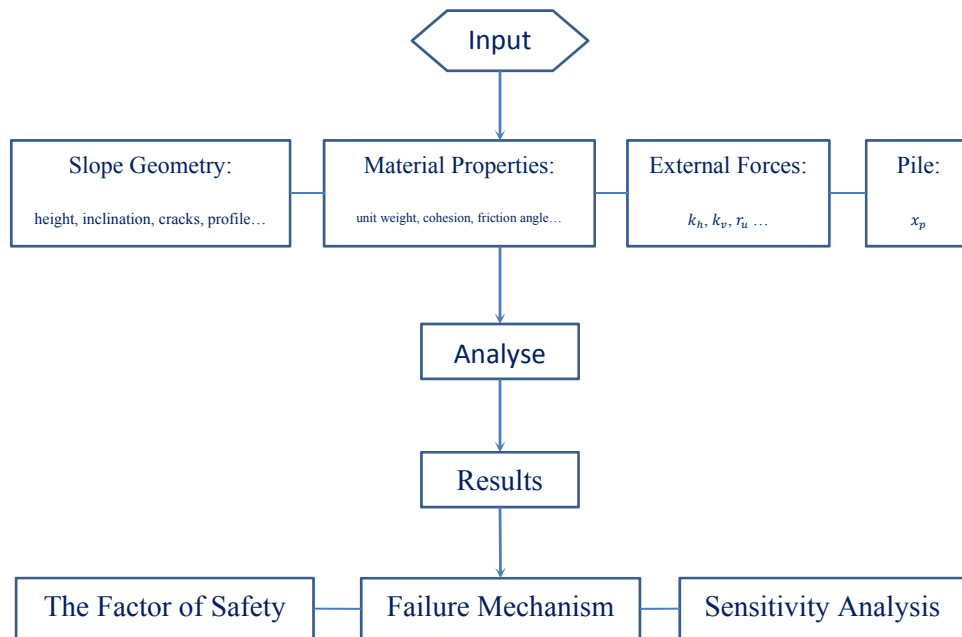


Figure 7-3. Framework of the software package.

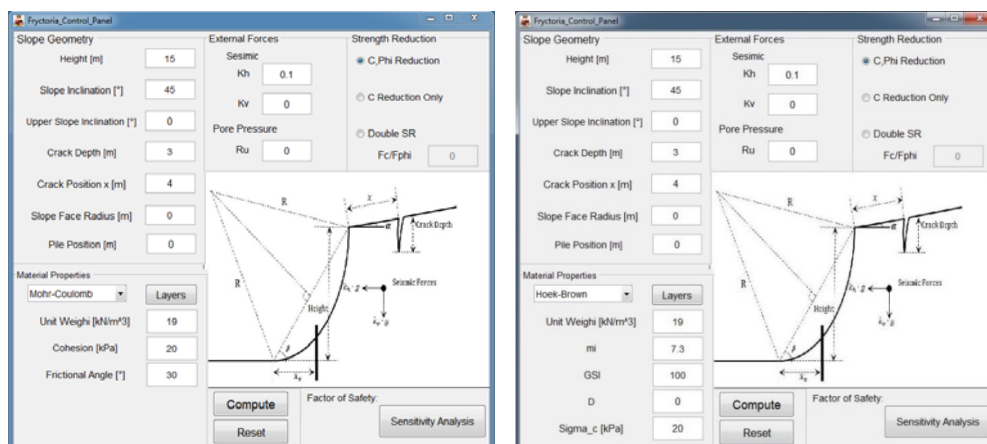


Figure 7-4. Input interface of the software.



(a) Mohr-Coulomb material

Layer	Unit Weight	mi	GSI	D	Sigma_c [kPa]
Layer 1	19	7.3	90	0	20
Layer 2	23	10.5	100	0	23
Layer 3	0	0	0	0	0
Layer 4	0	0	0	0	0
Layer 5	0	0	0	0	0

(b) Hoek-Brown material

Figure 7-5. Input interface for layered slope.

**Slope Geometry**

Height [m]: 15  
Slope Inclination [°]: 45  
Upper Slope Inclination [°]: 0  
Crack Depth [m]: 3  
Crack Position x [m]: 4  
Slope Face Radius [m]: 0  
Pile Position [m]: 0

**Material Properties**

Failure Criterion: Mohr-Coulomb  
Unit Weight [kN/m³]: 19  
Cohesion [kPa]: 20  
Frictional Angle [°]: 30

**External Forces**

Sesimic: Kh = 0.1, Kv = 0  
Pore Pressure: Ru = 0

**Strength Reduction**

☒ C, Phi Reduction  
☐ C Reduction Only  
☐ Double SR  
Fc/Fphi: 0

**Factor of Safety:** F=1.17

Figure 7-6. Result display.

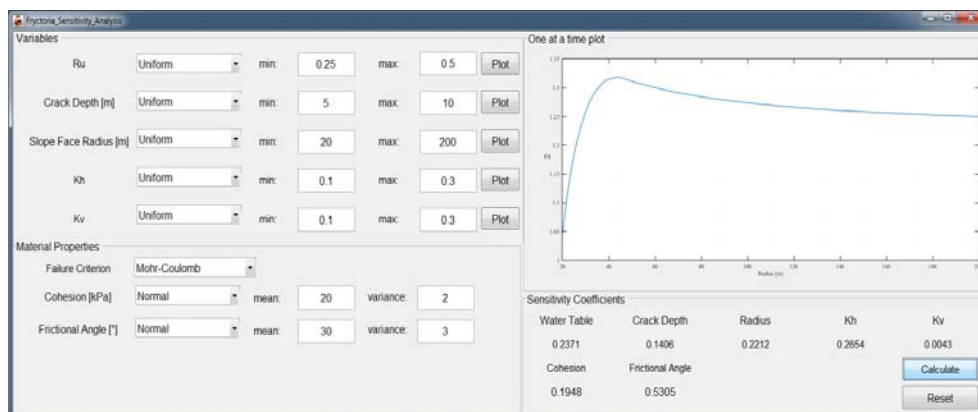


Figure 7-7. Sensitivity analysis.

### 7.3 Examples and validations

The reliability of the software package is examined and validated with two types of commercial finite-element software, i.e., Phase2 (Rocscience 2015) and Optum G2 (OptumCE 2013). The input values of Phase2 and Optum G2 are given in Table 7-1. The associated rule flow ( $\psi = \phi$ ) is implemented in both software to be consistent with the assumption in limit analysis. The influence of dilatancy angle ( $\psi < \phi$ ) is discussed in section 5.5 and Cheng and Lau (2014). The factors of safety obtained from associated-flow-rule analyses are very slightly greater (<5%) than those from non-associated-flow-rule analyses.

Table 7-1. Input values in Optum G2 and Phase2.

Unit Weight $\gamma$	$19 \text{ kN/m}^3$
Young's Modulus	$3000 \text{ MPa}$
Poisson's Ratio	0.3
Mesh Density (see Figure 5-12)	Adaptive (Optum G2) Approximately $50/\text{m}^2$ (Phase 2)

For intact slopes made of geomaterials obeying the Mohr-Coulomb failure criterion, the factors of safety of slopes with various values of inclinations, cohesions and friction angles are presented in Table 7-2 to Table 7-4. When one factor varies, the others keep constant. It turns out that the present software gives almost identical results in comparison with those obtained from both Phase2 and Optum G2.

Table 7-2. Verifications of slopes with different inclinations.

slope height $H = 20m$ , unit weight $\gamma = 19kN/m^3$ , cohesion $c = 20kPa$ , friction angle $\phi = 20^\circ$								
$\beta(^{\circ})$	30		40		50		60	
$F$	Present Work	1.27	Present Work	1.03	Present Work	0.85	Present Work	0.73
	Phase2	1.27	Phase2	1.02	Phase2	0.85	Phase2	0.73
	Optum	1.27	Optum	1.02	Optum	0.85	Optum	0.73
$\beta(^{\circ})$	70		80		90			
$F$	Present Work	Present Work	Present Work	Present Work	Present Work	0.52		
	Phase2	Phase2	Phase2	Phase2	Phase2	0.52		
	Optum	Optum	Optum	Optum	Optum	0.52		

Table 7-3. Verifications of slopes with different cohesions.

slope height $H = 20m$ , slope inclination $\beta = 45^\circ$ , unit weight $\gamma = 19kN/m^3$ , friction angle $\phi = 20^\circ$								
$c(kPa)$	10		15		20		25	
$F$	Present Work	0.72	Present Work	0.83	Present Work	0.93	Present Work	1.03
	Phase2	0.71	Phase2	0.83	Phase2	0.93	Phase2	1.03
	Optum	0.71	Optum	0.83	Optum	0.93	Optum	1.03
$c(kPa)$	30		35		40			
$F$	Present Work	1.13	Present Work	1.22	Present Work	1.32		
	Phase2	1.12	Phase2	1.22	Phase2	1.31		
	Optum	1.12	Optum	1.22	Optum	1.31		

Table 7-4. Verifications of slopes with different friction angles.

slope height $H = 20m$ , slope inclination $\beta = 45^\circ$ , unit weight $\gamma = 19kN/m^3$ , cohesion $c = 20kPa$								
$\phi(^{\circ})$	10		15		20		25	
	Present	0.64	Present	0.80	Present	0.93	Present	1.08

$F$	Work		Work		Work		Work	
	Phase2	0.64	Phase2	0.79	Phase2	0.93	Phase2	1.08
	Optum	0.64	Optum	0.79	Optum	0.93	Optum	1.08
$\phi(^{\circ})$	30		35		40			
$F$	Present Work	1.24	Present Work	1.40	Present Work	1.58		
	Phase2	1.23	Phase2	1.40	Phase2	1.57		
	Optum	1.23	Optum	1.40	Optum	1.57		

Table 7-5. Verifications of slopes subjected to different seismic actions.

slope height $H = 10m$ , slope inclination $\beta = 45^\circ$ , unit weight $\gamma = 19kN/m^3$ , cohesion $c = 20kPa$ , friction angle $\phi = 20^\circ$												
$k_h$	0.05		0.1		0.15		0.2		0.25		0.3	
$F$	Present Work	1.21	Present Work	1.13	Present Work	1.05	Present Work	0.98	Present Work	0.91	Present Work	0.85
	Phase2	1.21	Phase2	1.12	Phase2	1.05	Phase2	0.97	Phase2	0.90	Phase2	0.84
	Optum	1.21	Optum	1.12	Optum	1.05	Optum	0.97	Optum	0.89	Optum	0.83

Table 7-6. Verifications of slopes subjected to different levels of pore water pressure.

slope height $H = 10m$ , slope inclination $\beta = 45^{\circ}$ , unit weight $\gamma = 19kN/m^3$ , cohesion $c = 20kPa$ , friction angle $\phi = 20^{\circ}$										
$r_u$	0.1		0.2		0.3		0.4		0.5	
$F$	Present Work	1.23	Present Work	1.15	Present Work	1.07	Present Work	0.99	Present Work	0.91
	Phase2	1.22	Phase2	1.13	Phase2	1.04	Phase2	0.96	Phase2	0.87

In Table 7-5 and Table 7-6, the presence of seismic forces and pore water pressure are inspected respectively. The present software provides almost the same results with different values of seismic accelerations. The difference in terms of pore water pressure is more visible than any other factors. However, the largest

discrepancy in the factors of safety among different software when  $r_u = 0.5$  is within 5%.



## Chapter 8 Conclusions and Recommendations for

### Future Work

In this thesis, the analytical upper bound method of limit analysis was employed to derive generalized formulations for assessing the stability of slopes made of geomaterials obeying both the linear Mohr-Coulomb failure criterion and the non-linear Hoek-Brown failure criterion. The thesis is aimed at seeking slope profiles of optimal stability and enhancing the optimal design of pile reinforcement. The influence of the presence of cracks, water pressure, seismic actions, non-homogeneous anisotropic ground and blast-induced damage is investigated. An extensive parametrical study was carried out. A large number of stability charts and design charts are provided for the benefit of practitioners. A software package to evaluate the safety of slopes was created to overcome the limitations of chart-based design using analytical methods. The design of a software package to evaluate the safety of slope based on the kinematic approach of limit analysis is introduced. In this chapter, the findings of previous chapters are summarized and recommendations for future works are proposed.

### 8.1 Summary

#### (i) Optimal profiles of slopes

- Previous literature (e.g., Utili and Nova 2007, Jeldes et al. 2013) searched for the optimal profile among concave types of slopes. From this study instead, it turns out that the optimal profiles of  $c - \phi$  slopes exhibit both a concave and a convex part. In comparison with the traditional planar profiles, the percentage of

increase of the stability factor can reach up to 49%. In addition, given the same stability factor, the average slope inclination of an optimal slope is always higher than that of a planar slope. The amount of ground excavated for the optimal profile can be as little as 50% of that for a planar profile.

- For all the average slope inclinations considered, the optimal slopes turn out to be better than the optimal logarithmic spiral slopes (Utili and Nova 2007) and the optimal concave slopes (Jeldes et al. 2013 and Jeldes et al. 2014) in terms of their stability. This can be explained by the fact that for the first time the search for the optimal shape is not constrained to any particular class of shapes.
- Potential overestimation of slope stability due to use of a semi-analytical approach to assess the slope stability factor based upon upper bound limit analysis, and the assumption of associative flow rule were examined. The error is estimated within 6% according to the validations performed by finite element limit analysis and displacement-based finite element method with strength reduction technique.
- The geometrical properties of the optimal profiles including the average inclination corresponding to when the convex part of an optimal profile vanishes are investigated. Key geometric parameters to abstract the highly non-linear optimal profiles are provided. The area of yielded elements (in finite element strength reduction modelling) within optimal slopes is much larger than that within the planar slopes, which means the ground strength is better utilized in optimal slopes.
- Since the new upper bound formulation is capable of computing the stability factors of slopes of any arbitrary shape, the stability of the profile to be excavated can be monitored during the whole construction period. Optimal profiles exhibit a peculiar property: near full mobilization of the ground strength occurs in a large region within the slope rather than a thin shear band only. The stability factor

of the excavated part after reaching a critical depth tends to remain constant with the progression of the excavation.

- A method to find the maximum factor of safety for engineered slopes for prescribed ground properties and assigned  $\frac{H}{L}$ , as well as the maximum inclination of slopes under prescribed factors of safety is provided.
- An analytical approach to calculating the optimal slope profiles in the presence of cracks is provided. The presence of cracks can alter the shapes of optimal slopes and reduce its capacity to increase slope stability.
- An analytical approach to account for the optimal slope profiles in non-homogenous and anisotropic grounds is put forward. The optimal profiles obtained for uniform  $c - \phi$  slopes are also applicable for anisotropic slopes whose cohesion varies linearly with depth.
- For slopes made of rock obeying the Hoek-Brown failure criterion, the optimal profiles have both a concave and a convex part as well. An analytical approach to tackle the impact of blast-induced damage is laid out. If rock slopes are excavated by blasting, the damage caused will inevitably alter the shapes of the optimal profiles.

(ii) Optimal design of pile reinforcement

- In the previous studies of Ausilio et al. (2001), Nian et al. (2008) and Li et al. (2012), the most effective pile location is found around the slope toe where the stabilizing force needed to increase factor of safety to a desired value takes the minimum value. However, the above-pile failure mechanism can make the installation of piles completely ineffective. The most effective pile location is sought where the above-pile and pass-through-pile failure mechanisms yield the

same stability factor. With the increase of  $K_p$  and friction angle, the most effective pile location shifts towards the upper-middle part of slope.

- In order to evaluate the location of the pile ensuring maximum stability factor, the presence of pile reinforcement is taken into account by integrating the dissipated energy along the slope-pile interface according to Ito and Matsui's theory (Ito and Matsui 1975). The locations will shift towards the middle of slope face when the friction angle increases.
- The presence of pre-existing cracks has little impact on the optimal position of a row of piles used in slope stabilization.
- The presence of pore water pressure changes the behavior of pile reinforcement. The most effective pile location shifts downwards to lower-middle part with the increasing magnitude of  $r_u$ . The locations of the pile ensuring maximum stability factor for saturated slope stay at the crest of the slope.
- For reinforced slopes subjected to seismic actions, the most effective pile location shifts downwards to the lower-middle part with the increasing magnitude of  $k_h$ . For slopes subjected to gentle seismic action ( $k_h = 0.1$ ), the locations ensuring maximum stability factor are almost consistent with those for static cases. However, when violent earthquakes ( $k_h = 0.3$ ) occur, the optimal locations convert to the crest of slopes.
- Besides the stability factor, the optimal pile position can be evaluated according to the potential cumulative displacement during an earthquake. The optimal pile position for gentle slopes is within the upper-middle part of the slope. However, it switches to the slope crest for steep slopes.

(iii) Stability assessment of slopes made of rocks obeying the Hoek-Brown failure criterion

- The results obtained by the tangential technique are still upper bound solutions, which is an overestimation of the material strength and the safety of slopes. Compared with the more rigorous (both equilibrium equations and kinematic constraints are satisfied, see Chen and Liu 1990) variational approach, it is important to learn the difference of results between these two methods. It was reported by Drescher and Christopoulos (1988) that the adoption of the tangential technique only overestimates the stability factor of slopes made of geomaterials obeying the power-law failure criterion by less than 1%. However, it is illustrated in section 4.6 that the disparity between the tangential technique and the variational approach for the Hoek-Brown failure criterion can be as high as 9.66% when the rock mass is weak. Nevertheless, the application of the tangential technique is still an acceptable and convenient tool for evaluating the stability of slopes for the Hoek-Brown failure criterion. It is worth noting that the use of the equivalent  $c - \phi$  method according to Li et al. (2008) yields satisfactory results, with the biggest difference being 12.04% for low  $GSI$  values.
- The minimization process in finding the least upper bound for the stability factor defined in Eqs. (4-9) and (4-50) has to be conducted under the constraint of  $-\frac{s}{m} < \frac{\sigma}{\sigma_{ci}} < 1$  to avoid unrealistic selection of  $\phi_t$ . However, Collins et al. (1988) and Yang et al. (2004) overlooked the constraint and arrived at some unrealistic results, e.g., Table II in Collins et al. (1988) and Table II in Yang et al. (2004). The critical heights obtained from these two papers can be more than 50% less than those from Hoek et al. (2002) and Li et al. (2008).
- The analytical upper bound formulation for rock slopes subject to blast-induced damage (disturbance factor  $D$  varying linearly according to the distance to the excavation face) was derived for the first time.

(iv) Development of a software package for slope stability assessment

- The limitation of chart-based design using analytical methods can be overcome by the creation of a software package which can solve the factors of safety and the failure mechanisms of slopes automatically. The present software is proved to be accurate by providing almost identical results with those obtained from Phase2 and OptumG2. Thanks to its high computation efficiency, the software makes parametric design and sensitivity analysis much easier.

(v) Stability assessment of slopes made of geomaterials obeying the Mohr-Coulomb failure criterion

- The upper bound formulations illustrated in this chapter can be regarded as extension and clarification of the work done by Utili (2013) and Michalowski (2013), and are the basis of stability assessment of slopes made of geomaterials obeying the non-linear failure criterion. The issues regarding slopes made of frictionless soil, maximum stable crack depth, different ground and water conditions and the influence of seismic loading are tackled. Stability charts ( $\frac{F}{\tan\phi_g}$  against  $\frac{c_g}{\gamma H \tan\phi_g}$ ) for uniform slopes with water only present in the crack, uniform slopes subjected to different seismic actions and non-homogenous slopes with anisotropic strength are provided for the first time considering the most adverse pre-existing cracks being present in the slope.

- It is import to note that in order to seek the most adverse crack depth and location, the stability factor  $\frac{\gamma H}{c}$  is minimized over the angles denoting the failure mechanism and the normalized crack depth. To avoid the potential local failure (sliding of the soil/rock mass behind the crack), the minimization process should be done under the constraint of maximum stable crack depth defined in Eqs. (3-21), (3-45), (3-54) and (3-74).

## 8.2 Recommendations for future work

- (i) Two-dimensional plane strain analysis is predominately adopted and is regarded as a more conservative estimation of slope stability. However, in certain cases when the width of a slope is clearly defined and the three-dimensional effect cannot be neglected, a 3D stability analysis is required. The biggest challenge to implement analytical three-dimensional limit analysis is to construct kinematically admissible 3D failure mechanisms especially when the presence of cracks is considered.
- (ii) The most adverse crack depth and location are obtained by a mathematical minimization process in Chapter 3 and Chapter 4. They may be further validated by modern numerical analysis such as fracture mechanics (Scavia 1990, Ning et al. 2011).
- (iii) The optimal design of anti-sliding piles requires more medium-large scale experimental validations. The main concern is how to model the process from a stable status to the failure of the slope-pile system. Wang and Zhang (2014) designed an apparatus which has a load plate on the upper slope, however, it is difficult to simulate progressive failure only with local pressure on the top of slopes.
- (iv) The development of the software package in Chapter 7 needs subsequent refinement such as user interface optimization, the capability to tackle more complicated slope geometry and intelligent searching for the most critical failure mechanisms.

## Appendix A Layered slopes analysis

In Figure A-1, a piecewise linear model with  $n + 1$  nodes is adopted to represent the failure surface of a slope with  $n$  layers.  $x_1 \sim x_{n+1}$  are unknown variables to be optimized to find the most critical failure mechanism.  $y_1 \sim y_{n+1}$  are determined by the thickness  $h_i$  of each layer:

$$y_i = y_1 + \sum_2^{n+1} h_{i-1} \quad (i = 2, 3, 4, \dots, n) \quad (9-1)$$

The linear slip surface of each layer is

$$s_i = \sqrt{(y_{i+1} - y_i)^2 + (x_{i+1} - x_i)^2} \quad (i = 1, 2, 3, \dots, n) \quad (9-2)$$

having an inclination of  $\alpha_i$  to the horizontal axis.  $\alpha_i$  is given by

$$\alpha_i = \arctan\left(\frac{y_{i+1} - y_i}{x_i - x_{i+1}}\right), \quad (i = 2, 3, 4, \dots, n) \quad (9-3)$$

The length of the interface between the last two layers is

$$l_1 = \frac{h_1}{\tan \alpha_1} - \frac{h_1}{\tan \beta} \quad (9-4)$$

And the length of the interface between layer  $i$  and layer  $(i - 1)$  is

$$l_i = l_{i-1} + \frac{h_i}{\tan \alpha_i} - \frac{h_i}{\tan \beta} \quad (i = 2, 3, \dots, n) \quad (9-5)$$



Let the unit weight of layer  $i$  be  $\gamma_i$ , frictional angle be  $\phi_i$ , cohesion be  $c_i$ . According to the normality flow rule, the velocity of layer  $i$ ,  $V_i$  makes an angle of  $\phi_i$  to the linear base. The relative velocity between layer  $i$  and layer  $(i - 1)$  is  $V_{i,i-1}$ , making an angle of  $\phi_{i,i-1}$  to the layer interface. In order to establish a kinematically compatible velocity field within the slope, two adjacent layers must not move to cause overlap or indentation, which implies that the velocity hodograph must be closed. The velocities must satisfy:

$$V_i = V_{i-1} - V_{i,i-1} \quad (9-6)$$

with

$$V_i = V_{i-1} \frac{\sin(\alpha_{i-1} - \phi_{i-1} + \phi_{i,i-1})}{\sin(\alpha_i - \phi_i + \phi_{i,i-1})} \quad (i = 2, 3, 4, \dots, n) \quad (9-7)$$

$$V_{i,i-1} = V_{i-1} \frac{\sin(\alpha_i - \alpha_{i-1} - \phi_i + \phi_{i-1})}{\sin(\alpha_i - \phi_i + \phi_{i,i-1})} \quad (i = 2, 3, 4, \dots, n) \quad (9-8)$$

The weight of the bottom layer is

$$G_1 = \frac{1}{2} \gamma_1 l_1 h_1 \quad (9-9)$$

For each layer above, the weight is found by

$$G_i = \frac{1}{2} \gamma_i (l_i + l_{i-1}) h_i \quad (i = 2, 3, 4, \dots, n) \quad (9-10)$$

Thus, the rate of work done by the total weight of the slope sliding away is expressed as

$$\dot{W}_\gamma = \sum_{i=1}^n G_i V_i \sin(\alpha_i - \phi_i) \quad (9-11)$$

It is possible to consider the seismic action on each layer, the rate of work done by the pseudo static seismic force is computed by

$$\dot{W}_s = \sum_{i=1}^n k_{h,i} G_i V_i \cos(\alpha_i - \phi_i) \quad (9-12)$$

where  $k_{h,i}$  is the horizontal seismic acceleration.

According to Eq. (7-10), the internal energy dissipation constitutes two parts, one is the energy dissipation along the slip surface  $D_S$  and another is that on the layers interface  $D_L$ . We have

$$D_S = \sum_{i=1}^n c_i s_i V_i \cos \varphi_i \quad (9-13)$$

$$D_L = \sum_{i=1}^n c_i s_i V_{i+1} \cos \varphi_{i,i+1} \quad (9-14)$$

By equating the rate of external work to the rate of energy dissipation, leads to

$$D_L + D_S = \dot{W}_\gamma + \dot{W}_s \quad (9-15)$$

Using the  $c - \phi$  strength reduction technique described in section 3.1.3, the shear strength parameters  $c_i, \phi_i$  of each layer are reduced to bring the whole slope into a critical state:

$$c_{m,i} = \frac{c_i}{F}, \quad \phi_{m,i} = \arctan\left(\frac{\tan \phi_i}{F}\right) \quad (9-16)$$

The factor of safety  $F$  has to be sought by an iterative process since it appears on both side of Eq. (7-10).

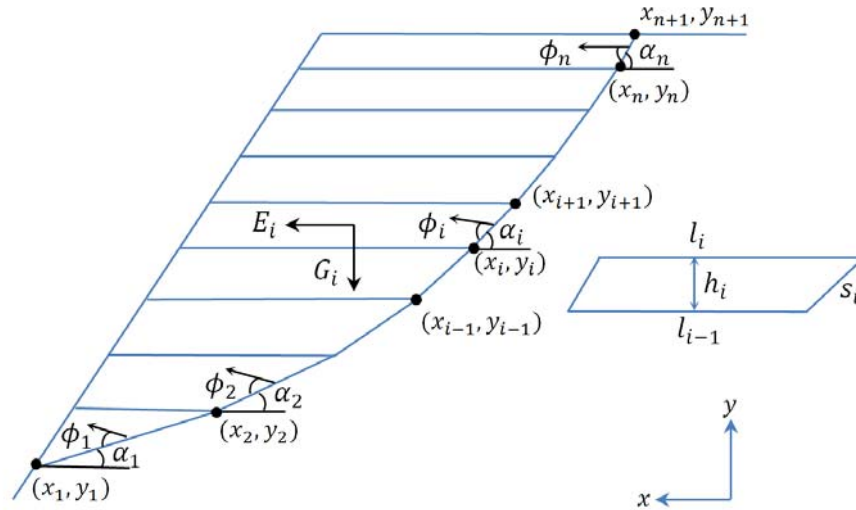


Figure A-1. Layered slope analysis.

## Appendix B Program Scripts (MATLAB R2014b)

### i. Chapter 3

```
% Main program: Stability factor of slopes subjected to the most adverse
% Crack (Mohr-Coulomb failure criterion)
% -----
clear;

% slope inclination [deg]
beta_grad=60;
% friction angle [deg]
phi_grad=20;
% initial slope inclination [deg]
alpha_grad=0;

% derived variables in radian
% -----
beta=beta_grad/180*pi;
alpha=alpha_grad/180*pi;
phi=phi_grad/180*pi;
b=tan(phi);

% indicate the magnitude of water filling in the crack
Kw=0;
% the ratio of water unit weight over ground unit weight
gamma_ratio=0;
% indicate crack formation
c_f=0;
% indicate the magnitude of seismic accelerations
Kh=0;
Kv=0;

% indicate the range of theta0, theta_c, theta_h, beta'
x_guess_grad=50;
y_guess_grad=88;
z_guess_grad=50;
x_delta_grad=24;
y_delta_grad=21;
z_delta_grad=24;
beta_delta_grad=18;
x_pass_grad=1;
y_pass_grad=1;
z_pass_grad=1;
beta_pass_grad=1;
x_range_grad=(-x_delta_grad+x_guess_grad):x_pass_grad:(x_delta_grad+x_guess_grad);
y_range_grad=(-y_delta_grad+y_guess_grad):y_pass_grad:(y_delta_grad+y_guess_grad);
z_range_grad=(-z_delta_grad+z_guess_grad):z_pass_grad:(z_delta_grad+z_guess_grad);
beta_range_grad=(beta_grad-beta_delta_grad):beta_pass_grad:beta_grad;
x_range=x_range_grad/180*pi;
y_range=y_range_grad/180*pi;
z_range=z_range_grad/180*pi;
beta_range=beta_range_grad/180*pi;

temp=size(x_range);
n1=temp(2);
temp=size(y_range);
n2=temp(2);
temp=size(z_range);
n3=temp(2);
temp=size(beta_range);
n4=temp(2);
MatrixN=zeros(n1,n2,n3,n4);

for i=1:n1
    for j=1:n2
        for k=1:n3
            for l=1:n4

                x=x_range(i);
                y=y_range(j);
                z=z_range(k);
                beta_f=beta_range(l);

                if (x>y-10e-6) || (x>z-10e-6) || (z>y-10e-6)
                    MatrixN(i,j,k,l)=NaN;
                else

MatrixN(i,j,k,l)=funXYZ_crack(alpha,beta,b,x,y,z,beta_f,Kw,gamma_ratio,c_f,Kh,Kv);
                end
            end
        end
    end
end
```

```

end
end
end
end

[N,BiI]=min(MatrixN(:));
[x_f,y_f,z_f,b_f]=ind2sub(size(MatrixN),BiI);
X(1)=x_range(x_f);
X(2)=y_range(y_f);
X(3)=z_range(z_f);
X(4)=beta_range(b_f);

function N=funXYZ_crack(alpha,beta,b,x,y,z,beta_f,Kw,gamma_ratio,c_f,Kh,Kv)

H=sin(beta_f)/sin(beta_f-alpha)*(exp(b*(y-x))*sin(y+alpha)-sin(x+alpha));
L1=sin(y-x)/sin(y+alpha)-sin(y+beta_f)/(sin(y+alpha)*sin(beta_f-alpha))*(exp(b*(y-x))*sin(y+alpha)-sin(x+alpha));
L2=sin(z-x)/sin(z+alpha)-cos(z)/sin(z+alpha)/cos(alpha)*(exp(b*(z-x))*sin(z+alpha)-sin(x+alpha));
D=1/cos(alpha)*(exp(b*(z-x))*sin(z+alpha)-sin(x+alpha));
flv=(exp(3*b*(y-x))*(sin(y)+3*b*cos(y))-3*b*cos(x)-sin(x))/(3*(1+9*b^2));
f2v=1/6*L1*sin(x+alpha)*(2*cos(x)-L1*cos(alpha));
f3v=1/6*exp(b*(y-x))*(sin(y-x)-L1*sin(y+alpha))*(cos(x)-L1*cos(alpha)+exp(b*(y-x))*cos(y));
f4v=(exp(3*b*(z-x))*(sin(z)+3*b*cos(z))-3*b*cos(x)-sin(x))/(3*(1+9*b^2));
f5v=1/6*L2*sin(x+alpha)*(2*cos(x+alpha)-L2);
f6v=1/3*D*exp(2*b*(z-x))*cos(z)*cos(z);
f7v=1/2*H^2*sin(beta-beta_f)/sin(beta)/sin(beta_f)*(cos(x)-L1*cos(alpha)-1/3*H*(1/tan(beta_f)+1/tan(beta)));

if Kh==0
    fh=0;
else
    flh=(exp(3*b*(y-x))*(-cos(y)+3*b*sin(y))-3*b*sin(x)+cos(x))/(3*(1+9*b^2));
    f2h=1/6*L1*(2*sin(x)+L1*sin(alpha))*sin(x+alpha);
    f3h=1/6*exp(b*(y-x))*(sin(y-x)-L1*sin(y+alpha))*(sin(x)+exp(b*(y-x))*sin(y));
    f4h=(exp(3*b*(z-x))*(-cos(z)+3*b*sin(z))-3*b*sin(x)+cos(x))/(3*(1+9*b^2));
    f5h=1/3*L2*sin(x+alpha)*sin(x+alpha);
    f6h=1/6*D*exp(b*(z-x))*cos(z)*(2*exp(b*(z-x))*sin(z)-D);
    fh=Kh*(flh-f2h-f3h-f4h+f5h+f6h);
end

tan_theta_c=sin(x)/((exp(b*(z-x))*cos(z)));
theta_c=atan(tan_theta_c);
if c_f==0 % pre-existing cracks
    fcf=0;
elseif c_f==1 % limited tensile strength
    int_fcf1 = integral(@(theta) (1-sin(theta))./(cos(theta)).^3,theta_c,z);
    int_fcf2 = integral(@(theta) (sin(theta)-b/sqrt(b^2+1))./(cos(theta)).^3,theta_c,z);
    fcf=((sin(x)/tan_theta_c)^2)*((1/sqrt(b^2+1))/(1-b/sqrt(b^2+1)))*int_fcf1+(1/sqrt(b^2+1)/((1-(b/sqrt(b^2+1)).^2)))*int_fcf2*(exp(b*(y-x))*sin(y)-sin(x));
elseif c_f==2 % tension cut-off
    int_fcf1 = integral(@(theta) (1-sin(theta))./(cos(theta)).^3,theta_c,z);
    int_fcf2 = 0;
    fcf=((sin(x)/tan_theta_c)^2)*((1/sqrt(b^2+1))/(1-b/sqrt(b^2+1)))*int_fcf1+(1/sqrt(b^2+1)/((1-(b/sqrt(b^2+1)).^2)))*int_fcf2*(exp(b*(y-x))*sin(y)-sin(x));
end

flag=1;
if gamma_ratio==0
    fw1=0;
    fw2=0;
    fw3=0;
else
    options = optimset('TolX',1e-5);
    [thetal,fval,exitflag,output] = fzero(@(thetal)cos(thetal)*exp(b*(thetal-x))-cos(x)+L1*cos(alpha),(z+y)/2,options);
    if (exitflag==1) && (thetal>z) && (thetal<y)
        fw1=integral(@(angle)funw1(angle,x,b),z,thetal);
        fw2=integral(@(angle)funw2(angle,x,y,b,beta),thetal,y);
        fw3=1/2*Kw*Kw*D*D*(exp(b*(z-x))*sin(z)-1/3*Kw*D);
    else
        flag=0;
    end
end

if flag==1
    % indicate the degree of non-homogeneity
    n0=0.5;
    ni=n0+D/H-D/H*n0;
    q1=ni/exp(2*x*b)*(funpsi(y,b)-funpsi(x,b));
    q2=(1-ni)/H/exp(3*x*b)*((funksi(y,b)-funpsi(y,b)*sin(x)*exp(x*b))-(funksi(x,b)-funpsi(x,b)*sin(x)*exp(x*b)));
end

```

```

        N=((q1+q2)*H+fcf)/((1+Kv)*(flv-f2v-f3v-f4v+f5v+f6v-
f7v)+(fw1+fw2+fw3)*gamma_ratio+fh);
        if N<1 || N>500
            N=NaN;
        end
    else
        N=NaN;
    end

function W=funw1(t,x,b)

W=b*(exp(b*(t-x)).*sin(t)-sin(x)).*exp(2*b*(t-x));

function W=funw2(t,x,y,b,beta)

W=b*(exp(b*(t-x)).*sin(t)-sin(y)).*exp(b*(y-x))+tan(beta)*(exp(b*(t-x)).*cos(t)-
cos(y)).*exp(b*(y-x))).*exp(2*b*(t-x));

function F=funpsi(theta,b)

F=exp(2*theta*b)/2/b;

function F=funksi(theta,b)

F=(3*b*sin(theta)-cos(theta)).*exp(3*theta*b)/(1+9*b*b);

```

## ii. Chapter 4

```

% Main program: Stability factor of slopes subjected to the most adverse
% Crack (Hoek-Brown failure criterion, tangential technique)
% -----
clear;

% slope inclination [deg]
beta_grad=60;
% initial slope inclination [deg]
alpha_grad=0;

% derived variables in radian
% -----
beta=beta_grad/180*pi;
alpha=alpha_grad/180*pi;

% input ground material strenght parameteres
mi=10;
GSI=50;
D=1;
m=mi*exp((GSI-100)/(28-14*D));
s=exp((GSI-100)/(9-3*D));
n=1/2+1/6*(exp(-GSI/15)-exp(-20/3));

% indicate the range of theta0, theta_c, theta_h, phi
x_guess_grad=50;
y_guess_grad=88;
z_guess_grad=50;
phi_guess_grad=24;
x_delta_grad=24;
y_delta_grad=21;
z_delta_grad=24;
phi_delta_grad=15;
x_pass_grad=1;
y_pass_grad=1;
z_pass_grad=1;
phi_pass_grad=1;

x_range_grad=(-x_delta_grad+x_guess_grad):x_pass_grad:(x_delta_grad+x_guess_grad);
y_range_grad=(-y_delta_grad+y_guess_grad):y_pass_grad:(y_delta_grad+y_guess_grad);
z_range_grad=(-z_delta_grad+z_guess_grad):z_pass_grad:(z_delta_grad+z_guess_grad);
phi_range_grad=(-phi_delta_grad+phi_guess_grad):phi_pass_grad:(phi_delta_grad+phi_guess_grad);

x_range=x_range_grad/180*pi;
y_range=y_range_grad/180*pi;
z_range=z_range_grad/180*pi;

```

```

phi_range=phi_range_grad/180*pi;

temp=size(x_range);
n1=temp(2);
temp=size(y_range);
n2=temp(2);
temp=size(z_range);
n3=temp(2);
temp=size(phi_range);
n4=temp(2);
MatrixN=zeros(n1,n2,n3,n4);

for i=1:n1
    for j=1:n2
        for k=1:n3
            for l=1:n4

                x=x_range(i);
                y=y_range(j);
                z=z_range(k);

                if (x>y-10e-6) || (x>z-10e-6) || (z>y-10e-6)
                    MatrixN(i,j,k,l)=NaN;
                else
                    phi=phi_range(l);
                    b=tan(phi);
                    strength_ratio=(cos(phi)/2*(m*n*(1-sin(phi))/2/sin(phi))^(n/(1-n))-
b/m*(1+sin(phi)/n)*(m*n*(1-sin(phi))/2/sin(phi))^(1/(1-n))+s/m*b)/(s^n);
                    sigma_ratio=(1/m+sin(phi)/m/n)*(m*n*(1-sin(phi))/2/sin(phi))^(1/(1-
n))-s/m;
                    if sigma_ratio>1
                        MatrixN(i,j,k,l)=NaN;
                    else

MatrixN(i,j,k,l)=s^n*strength_ratio*funXYZ_crack(alpha,beta,b,x,y,z,beta,0,0,0,0);
                        end
                    end
                end
            end
        end
    end

[N,BiI]=min(MatrixN(:));
[x_f,y_f,z_f,p_f]=ind2sub(size(MatrixN),BiI);
X(1)=x_range_grad(x_f);
X(2)=y_range_grad(y_f);
X(3)=z_range_grad(z_f);
X(4)=phi_range_grad(p_f);

% Main program: Critical height of slopes subjected to the most adverse
% Crack (Hoek-Brown failure criterion, variational approach)
clear

% slope inclination [deg]
beta_grad=60;

% input ground material strength parameteres
c=30; % uniaxial compression strength
GSI=100;
D=0;
mi=10;
m=mi*exp((GSI-100)/(28-14*D));
s=exp((GSI-100)/(9-3*D));
a=1/2+1/6*(exp(-GSI/15)-exp(-20/3));
gamma=19;

% indicate the range of theta0,theta_h
x_guess_grad=54;
y_guess_grad=94;
x_delta_grad=5;
y_delta_grad=5;
x_pass_grad=0.1;
y_pass_grad=0.1;
x_range_grad=(-x_delta_grad+x_guess_grad):x_pass_grad:(x_delta_grad+x_guess_grad);
y_range_grad=(-y_delta_grad+y_guess_grad):y_pass_grad:(y_delta_grad+y_guess_grad);
x_range=x_range_grad/180*pi;
temp=size(x_range);
n1=temp(2);
y_range=y_range_grad/180*pi;
temp=size(y_range);
n2=temp(2);
d_range=0.35:0.05:0.45;
temp=size(d_range);
n3=temp(2);
funH=zeros(n1,n2,n3);

```

```

for i=1:n1
    for j=1:n2
        for k=1:n3
            x=x_range(i);
            y=y_range(j);
            d=d_range(k);
            flag=1;
            options = optimset('TolX',1e-2);
            [p0,fval,exitflag,output] = fzero(@(p0)((1/m+sin(p0)/m/a)*(m*a*(1-
sin(p0))/2/sin(p0))^(1/(1-a))-s/m)*cos(x)+cos(p0)/2*(m*a*(1-sin(p0))/2/sin(p0))^(a/(1-
a))*(sin(x)+cos(x)*(tan(p0)*sin(x)+cos(x))/(sin(x)-tan(p0)*cos(x))),63/180*pi,options);
            if (exitflag~=1) || (p0>90/180*pi) || (p0<10/180*pi)
                flag=0;
            end
            if (x>y-0.1) || (flag==0)
                funH(i,j,k)=NaN;
            else
                funH(i,j,k)=H_critical(x,y,d,p0,beta,m,s,a,c,gamma);
            end
        end
    end
end

[Hc,BiI]=min(funH(:));
[x_f,y_f,d_f]=ind2sub(size(funH),BiI);
Theta0=x_range_grad(x_f);
ThetaH=y_range_grad(y_f);
ThetaC=d_range(d_f);

function Hc = H_critical(x,y,d,p0,beta,m,s,a,c,gamma)

[Theta, Phi] = ode45(@(theta,phi) PhiAlongTheta(theta,phi,c,m,a,x,gamma), [x y], p0);

Num=size(Phi);

Sigma=zeros(1,Num(1));
Tau=zeros(1,Num(1));
Radius=zeros(1,Num(1));
Cohesion=zeros(1,Num(1));
XX=zeros(1,Num(1));
YY=zeros(1,Num(1));

for i=1:Num(1)
    Sigma(i)=c/m*(2*sin(Phi(i))/m/a/(1-sin(Phi(i))))^(1/(a-1))*(sin(Phi(i))/a+1)-s*c/m;
    Tau(i)=c*cos(Phi(i))/2*(2*sin(Phi(i))/m/a/(1-sin(Phi(i))))^(a/(a-1));

    Radius(i)=exp(cos(Phi(i))*a*m/2/(sin(Phi(i))/a+1)*((m/c*Sigma(i)+s)/(sin(Phi(i))/a+1))^(
a-1)*(Theta(i)-x));
    Cohesion(i)=Tau(i)-Sigma(i)*tan(Phi(i));
    XX(i)=Radius(i)*cos(Theta(i));
    YY(i)=Radius(i)*sin(Theta(i));
end

h=YY2(Num(1))-YY2(1);
L=XX2(1)-XX2(Num(1))-h/tan(beta);

f1=0;
for i=1:(Num(1)-1)
    f1=f1+((Radius(i))^3*cos(Theta(i))+(Radius(i+1))^3*cos(Theta(i+1)))*(Theta(i+1)-
Theta(i))/6;
end

f2=sin(x)*L*(2*cos(x)-L)/6;
f3=Radius(Num(1))*(sin(y-x)-L*sin(y))*(cos(x)-L+cos(y)*Radius(Num(1)))/6;

g=0;
for i=1:(Num(1)-1)
    g=g+(Cohesion(i)*(Radius(i))^2+Cohesion(i+1)*(Radius(i+1))^2)*(Theta(i+1)-
Theta(i))/2;
end

D=d/(1-d)*h;

f4=1/6*(3*cos(x)-L+D/tan(beta))*(L-D/tan(beta))*D;
f5=1/6*(3*cos(x)-2*L+D/tan(beta))*L*D;

Hc=g*h/gamma/(f1-f2-f3+f4+f5)/(1-d);

if (Hc<c/gamma) || (Hc>100*c/gamma) || (L<0)
    Hc=NaN;
end

function dphi = PhiAlongTheta(theta,phi,c,m,a,x,gamma)

```



```

dphi=-((a-1)*a*m*(sin(phi)-1)*(2*sin(phi)/(a*m-a*m*sin(phi)))^(1/(1-a)))*(exp(a*(theta-
x)*sin(phi)*cos(phi)/(1-sin(phi)))/(a+sin(theta))*gamma*cos(theta)-
c*cos(phi)*(2*sin(phi)/(a*m-a*m*sin(theta)))^(a/(a-1))*tan(phi))/c/(a+a*sin(phi)-(a-
1)*sin(theta^2));

% Main program: Stability factor of slopes subjected to blasting, the most adverse
% Crack (Hoek-Brown failure criterion, tangential technique)
% -----
clear;

% slope inclination [deg]
beta_grad=60;
% initial slope inclination [deg]
alpha_grad=0;

% derived variables in radian
% -----
beta=beta_grad/180*pi;
alpha=alpha_grad/180*pi;

n_integral=20;

% input ground material strenght parameteres
mi=10;
GSI=50;
D0=0;
D1=1;
n=1/2+1/6*(exp(-GSI/15)-exp(-20/3));

% indicate the range of theta0, theta_c, theta_h, phi
x_guess_grad=50;
y_guess_grad=88;
z_guess_grad=50;
phi_guess_grad=24;
x_delta_grad=24;
y_delta_grad=20;
z_delta_grad=24;
phi_delta_grad=21;
x_pass_grad=1;
y_pass_grad=1;
z_pass_grad=1;
phi_pass_grad=1;

x_range_grad=(-x_delta_grad+x_guess_grad):x_pass_grad:(x_delta_grad+x_guess_grad);
y_range_grad=(-y_delta_grad+y_guess_grad):y_pass_grad:(y_delta_grad+y_guess_grad);
z_range_grad=(-z_delta_grad+z_guess_grad):z_pass_grad:(z_delta_grad+z_guess_grad);
phi_range_grad=(-
phi_delta_grad+phi_guess_grad):phi_pass_grad:(phi_delta_grad+phi_guess_grad);

x_range=x_range_grad/180*pi;
y_range=y_range_grad/180*pi;
z_range=z_range_grad/180*pi;
phi_range=phi_range_grad/180*pi;

temp=size(x_range);
n1=temp(2);
temp=size(y_range);
n2=temp(2);
temp=size(z_range);
n3=temp(2);
temp=size(phi_range);
n4=temp(2);
MatrixN=zeros(n1,n2,n3,n4);

for i=1:n1
    for j=1:n2
        for k=1:n3
            for l=1:n4
                x=x_range(i);
                y=y_range(j);
                z=z_range(k);
                if (x>y-10e-6) || (x>z-10e-6) || (z>y-10e-6)
                    MatrixN(i,j,k,l)=NaN;
                else
                    phi=phi_range(l);

MatrixN(i,j,k,l)=funXYZ_crack_D(alpha,beta,phi,x,y,z,beta,mi,GSI,n,D0,D1,0,0,n_integral
);
                    end
                end
            end
        end
    end

[N,BiI]=min(MatrixN(:));
[x_f,y_f,z_f,p_f]=ind2sub(size(MatrixN),BiI);

```

```

X(1)=x_range(x_f)/pi*180;
X(2)=y_range(y_f)/pi*180;
X(3)=z_range(z_f)/pi*180;
X(4)=phi_range(p_f)/pi*180;

function
F=funXYZ_crack_D(alpha,beta,phi,x,y,z,beta_f,mi,GSI,n,D0,D1,Kw,gamma_ratio,n_integral)

b=tan(phi);
H=sin(beta_f)/sin(beta_f-alpha)*(exp(b*(y-x))*sin(y+alpha)-sin(x+alpha));
L=H/tan(beta);
ry=exp(b*(y-x));
L1=sin(y-x)/sin(y+alpha)-sin(y+beta_f)/(sin(y+alpha)*sin(beta_f-alpha))*(exp(b*(y-x))*sin(y+alpha)-sin(x+alpha));
L2=sin(z-x)/sin(z+alpha)-cos(z)/sin(z+alpha)/cos(alpha)*(exp(b*(z-x))*sin(z+alpha)-sin(x+alpha));
D=1/cos(alpha)*(exp(b*(z-x))*sin(z+alpha)-sin(x+alpha));
flv=(exp(3*b*(y-x))*(sin(y)+3*b*cos(y))-3*b*cos(x)-sin(x))/(3*(1+9*b^2));
f2v=1/6*L1*sin(x+alpha)*(2*cos(x)-L1*cos(alpha));
f3v=1/6*exp(b*(y-x))*(sin(y-x)-L1*sin(y+alpha))*(cos(x)-L1*cos(alpha)+exp(b*(y-x))*cos(y));
f4v=(exp(3*b*(z-x))*(sin(z)+3*b*cos(z))-3*b*cos(x)-sin(x))/(3*(1+9*b^2));
f5v=1/6*L2*sin(x+alpha)*(2*cos(x+alpha)-L2);
f6v=1/3*D*exp(2*b*(z-x))*cos(z)*cos(z);
f7v=1/2*H^2*sin(beta-beta_f)/sin(beta)/sin(beta_f)*(cos(x)-L1-1/3*H*(1/tan(beta_f)+1/tan(beta)));

flag=1;

if gamma_ratio==0
    fw1=0;
    fw2=0;
    fw3=0;
else
    options = optimset('TolX',1e-5);
    [thetal,fval,exitflag,output] = fzero(@(thetal)cos(thetal)*exp(b*(thetal-x))-cos(x)+L1*cos(alpha),(z+y)/2,options);
    if (exitflag==1) && (thetal>z) && (thetal<y)
        fw1=integral(@(angle)funw1(angle,x,b),z,thetal);
        fw2=integral(@(angle)funw2(angle,x,y,b,beta),thetal,y);
        fw3=1/2*Kw*Kw*D*D*(exp(b*(z-x))*sin(z)-1/3*Kw*D);
    else
        flag=0;
    end
end

if flag==1
    t=zeros(1,n_integral+1);
    D=zeros(1,n_integral+1);
    c=zeros(1,n_integral+1);
    for i=1:(n_integral+1)
        t(i)=z+(y-z)/n_integral*(i-1);
        x_coord=exp(b*(t(i)-x))*cos(t(i))-ry*cos(y);
        y_coord=ry*sin(y)-exp(b*(t(i)-x))*sin(t(i));
        if (y_coord > (-L/H*x_coord+H+L^2/H))
            D(i)=(H-(exp(b*(t(i)-x))*sin(t(i))-sin(x))/sin(pi/2-beta))/H*(D1-D0)+D0;
        else
            D(i)=(H-(exp(b*(t(i)-x))*cos(pi/2-t(i)-beta)+ry*sin(pi-y-beta))/H*(D1-D0)+D0;
        end
        if D(i)<D0
            D(i)=D0;
        elseif D(i)>D1;
            D(i)=D1;
        end
        m=mi*exp((GSI-100)/(28-14*D(i)));
        s=exp((GSI-100)/(9-3*D(i)));
        sigma_ratio=(1/m+sin(phi)/m/n)*(m*n*(1-sin(phi))/2/sin(phi))^(1/(1-n))-s/m;
        c(i)=(cos(phi)/2*(m*n*(1-sin(phi))/2/sin(phi))^(n/(1-n))-tan(phi)/m*(1+sin(phi)/n)*(m*n*(1-sin(phi))/2/sin(phi))^(1/(1-n))+s/m*tan(phi));
    end
    q=0;
    for i=1:n_integral
        q=q+(c(i)*exp(2*b*(t(i)-x))+c(i+1)*exp(2*b*(t(i+1)-x)))*(y-z)/n_integral/2;
    end
    F=q*H/(f1v-f2v-f3v-f4v+f5v+f6v-f7v+(fw1+fw2+fw3)*gamma_ratio);
    if F<0 || F>500 || sigma_ratio>1
        F=NaN;
    end
else
    F=NaN;
end
end

```

### iii. Chapter 5

```
% Main program: Genetic Algorithm
% -----
clear;

% initialize parallel computing
CoreNum=8;
if matlabpool('size')<=0
    matlabpool('open','local',CoreNum);
else
    disp('Already initialized');
end

ObjectiveFunction = @Fun_MC; % objective function to maximize
n_points = 19; % Number of variables
LB = zeros(1,n_points); % Lower bound
UB = ones(1,n_points); % Upper bound

beta=60/180*pi;

opts = gaoptimset('PopulationSize',400, 'StallGenLimit',100, 'Generations',2000,
'UseParallel', 'always');

ConstraintFunction = @ConstraintR;
[R,Fval,exitFlag,Output] =
ga(ObjectiveFunction,n_points,[],[],[],[],LB,UB,ConstraintFunction,opts);

N=-Fval;
L_array=[0 (1-fliplr(R)) 1];
H_array=zeros(1,n_points+2);
for i=1:(n_points+2)
    H_array(i)=(i-1)/(n_points+1)*tan(beta);
end

matlabpool close

function [c, ceq] = ConstraintR(R)

n_points=19;
c=ones(1,n_points-1);

for i=1:(n_points-1)
    c(i)=R(i)-R(i+1);
end

c=c';

ceq = [];

% function to be maximized (Mohr-Coulomb failure criterion)
function N_=Fun_MC(R)

% slope inclination [deg]
beta_grad=60;
% friction angle [deg]
phi_grad=20;

% derived variables in radian
beta=beta_grad/180*pi;
phi=phi_grad/180*pi;
b=tan(phi);

n_points=19;

% indicate the range of theta0, theta_c, theta_h
x_guess_grad=50;
y_guess_grad=88;
z_guess_grad=50;
x_delta_grad=24;
y_delta_grad=20;
z_delta_grad=24;
x_pass_grad=1;
y_pass_grad=1;
z_pass_grad=1;
x_range_grad=(-x_delta_grad+x_guess_grad):x_pass_grad:(x_delta_grad+x_guess_grad);
y_range_grad=(-y_delta_grad+y_guess_grad):y_pass_grad:(y_delta_grad+y_guess_grad);
z_range_grad=(-z_delta_grad+z_guess_grad):z_pass_grad:(z_delta_grad+z_guess_grad);
x_range=x_range_grad/180*pi;
temp=size(x_range);
```

```

n1=temp(2);
y_range=y_range_grad/180*pi;
temp=size(y_range);
n2=temp(2);
z_range=z_range_grad/180*pi;
temp=size(z_range);
n3=temp(2);
MatrixN=zeros(n1,n2,n3);
N_all=zeros(1,n_points+1);
X_all=zeros(3,n_points+1);

H_R=zeros(1,n_points+1);
for k=1:(n_points+1)
    H_R(k)=(n_points+1)/(n_points+2-k);
end

R_new=R;
beta_new=beta;

for loop=1:(n_points+1)
    for i=1:n1
        for j=1:n2
            for k=1:n3
                x=x_range(i);
                y=y_range(j);
                z=z_range(k);
                if (x>y-10e-6) || (x>z-10e-6) || (z>y-10e-6)
                    MatrixN(i,j)=NaN;
                else
                    MatrixN(i,j)=funXY_Crack(x,y,beta_new,b,(n_points+1-loop),R_new);
                end
            end
        end
    end

    [N_all(loop),BiI]=min(MatrixN(:));
    [x_f,y_f]=ind2sub(size(MatrixN),BiI);
    X_all(1,loop)=x_range(x_f);
    X_all(2,loop)=y_range(y_f);
    X_all(3,loop)=z_range(z_f);

    R_temp=R_new;
    if (n_points+1-loop)==0
        R_new=NaN;
        beta_new=NaN;
    else
        if (n_points-loop)==0
            R_new=NaN;
        else
            R_new=zeros(1,n_points-loop);
            for k=1:(n_points-loop)
                R_new(k)=R_temp(k)/R_temp(n_points+1-loop);
            end
        end
        beta_new=atan(tan(beta_new)*(n_points+1-loop)/(n_points+2-loop)/R_temp(n_points+1-loop));
    end
end

N_all=H_R.*N_all;
[N_, toe]=min(N_all);
if toe==1
    flag=1;
    for i=1:(n_points+1)
        if isnan(N_all(i))
            flag=0;
        end
    end
    if flag==0;
        N_=1;
    else
        X(1)=X_all(1,toe);
        X(2)=X_all(2,toe);
        X(3)=X_all(3,toe);
        N_=-N_;
    end
else
    N_=1;
end

function N=funXY_Crack(x,y,z,beta,b,n_points,R)

flag=1;

H=exp(b*(y-x))*sin(y)-sin(x);
L=H/tan(beta);

```

```

Lrx=sin(x+beta)/sin(beta)-exp(b*(y-x))*sin(y+beta)/sin(beta);
rc=sqrt(sin(x)*sin(x)+(cos(x)-Lrx)^2);
sc=acos((cos(x)-Lrx)/rc);
ry=exp(b*(y-x));

H_points=zeros(1,n_points);
L_points=zeros(1,n_points);
ss=zeros(1,n_points);
rr=zeros(1,n_points);

for i=1:n_points
    H_points(i)=sin(x)+H*i/(n_points+1);
    L_points(i)=cos(x)-Lrx-R(i)*L;
    rr(i)=sqrt(H_points(i)*H_points(i)+L_points(i)*L_points(i));
    ss(i)=acos(L_points(i)/rr(i));
    if rr(i)>exp(b*(ss(i)-x))
        flag=0;
    end
    if ss(i)>y
        flag=0;
    end
end

if flag==1
    g=exp(2*b*(z-x))*(exp(2*b*(y-z))-1)*(exp(b*(y-x))*sin(y)-sin(x))/(2*b);
    f1=(exp(3*b*(y-x))*(sin(y)+3*b*cos(y))-3*b*cos(x)-sin(x))/(3*(1+9*b^2));
    f2=1/6*Lrx*sin(x)*(2*cos(x)-Lrx);
    f3=0;
    p1=(exp(3*b*(z-x))*(sin(z)+3*b*cos(z))-3*b*cos(x)-sin(x))/(3*(1+9*b^2));
    p2=1/6*sin(x)*((cos(x))^2-exp(2*b*(z-x))*(cos(z))^2);
    p3=1/3*exp(2*b*(z-x))*(cos(z))^2*(sin(z)*exp(b*(z-x))-sin(x));
    if n_points==0
        f3=fun3(rc,sc,ry,y);
    end
    if n_points==1
        f3=fun3(rc,sc,rr(1),ss(1))+fun3(rr(1),ss(1),ry,y);
    end
    if n_points>1
        f3=fun3(rc,sc,rr(1),ss(1));
        for i=1:(n_points-1)
            f3=f3+fun3(rr(i),ss(i),rr(i+1),ss(i+1));
        end
        f3=f3+fun3(rr(n_points),ss(n_points),ry,y);
    end

    N=g/(f1-f2-f3-p1+p2+p3);

    if N<1 || N>500
        N=NaN;
    end
else
    N=NaN;
end

% function to be maximized (Hoek-Brown failure criterion, Blasting)
function N_=Fun_HB(R)

% slope inclination [deg]
beta_grad=60;
% derived variables in radian
beta=beta_grad/180*pi;

n_points=19;
n_integral=20;

% input ground material strength parameteres
mi=10;
GSI=50;
D0=0;
D1=1;

% indicate the range of theta0, theta_c, theta_h, phi
x_guess_grad=50;
y_guess_grad=88;
z_guess_grad=50;
phi_guess_grad=24;
x_delta_grad=24;
y_delta_grad=20;
z_delta_grad=24;
phi_delta_grad=21;
x_pass_grad=1;
y_pass_grad=1;
z_pass_grad=1;
phi_pass_grad=1;
x_range_grad=(-x_delta_grad+x_guess_grad):x_pass_grad:(x_delta_grad+x_guess_grad);
y_range_grad=(-y_delta_grad+y_guess_grad):y_pass_grad:(y_delta_grad+y_guess_grad);

```

```

z_range_grad=(-z_delta_grad+z_guess_grad):z_pass_grad:(z_delta_grad+z_guess_grad);
phi_range_grad=(-
phi_delta_grad+phi_guess_grad):phi_pass_grad:(phi_delta_grad+phi_guess_grad);
x_range=x_range_grad/180*pi;
y_range=y_range_grad/180*pi;
z_range=z_range_grad/180*pi;
phi_range=phi_range_grad/180*pi;
temp=size(x_range);
n1=temp(2);
temp=size(y_range);
n2=temp(2);
temp=size(z_range);
n3=temp(2);
temp=size(phi_range);
n4=temp(2);
MatrixN=zeros(n1,n2,n3,n4);
N_all=zeros(1,n_points+1);
X_all=zeros(4,n_points+1);

H_R=zeros(1,n_points+1);
for l=1:(n_points+1)
    H_R(l)=(n_points+1)/(n_points+2-l);
end

R_new=R;
beta_new=beta;

for loop=1:(n_points+1)
    for i=1:n1
        for j=1:n2
            for k=1:n3
                for l=1:n4
                    x=x_range(i);
                    y=y_range(j);
                    z=z_range(k);
                    phi=phi_range(l);
                    if (x>y-10e-6) || (x>z-10e-6) || (z>y-10e-6)
                        MatrixN(i,j,k,l)=NaN;
                    else
MatrixN(i,j,k,l)=funXY_D(x,y,z,phi,beta_new,mi,GSi,D0,D1,(n_points+1-
loop),n_integral,R_new);
                    end
                end
            end
        end
    end

    [N_all(loop),BiI]=min(MatrixN(:));
    [x_f,y_f,z_f,p_f]=ind2sub(size(MatrixN),BiI);
    X_all(1,loop)=x_range(x_f);
    X_all(2,loop)=y_range(y_f);
    X_all(3,loop)=z_range(z_f);
    X_all(4,loop)=phi_range(p_f);

    R_temp=R_new;
    if (n_points+1-loop)==0
        R_new=NaN;
        beta_new=NaN;
    else
        if (n_points-loop)==0
            R_new=NaN;
        else
            R_new=zeros(1,n_points-loop);
            for k=1:(n_points-loop)
                R_new(k)=R_temp(k)/R_temp(n_points+1-loop);
            end
            beta_new=atan(tan(beta_new)*(n_points+1-loop)/(n_points+2-
loop))/R_temp(n_points+1-loop));
        end
    end

N_all=H_R.*N_all;
[N_, toe]=min(N_all);
if toe==1
    flag=1;
    for i=1:(n_points+1)
        if isnan(N_all(i))
            flag=0;
        end
    end
    if flag==0;
        N_=1;
    else
        X(1)=X_all(1,toe);
        X(2)=X_all(2,toe);
        X(3)=X_all(3,toe);
    end
end

```

```

        X(4)=X_all(4,toe);
        N_=-N_;
    end
else
    N_=1;
end

function F=fun3(r1,s1,r2,s2)

    x1=r1*cos(s1);
    y1=r1*sin(s1);
    x2=r2*cos(s2);
    y2=r2*sin(s2);
    S=1/2*abs(x1*y2-x2*y1);
    F=(x1+x2)/3*S;

function F=funXY_D(x,y,z,phi,beta,mi,GSI,D0,D1,n_points,n_integral,R)

b=tan(phi);
H=exp(b*(y-x))*sin(y)-sin(x);
L=H/tan(beta);
Lrx=sin(x+beta)/sin(beta)-exp(b*(y-x))*sin(y+beta)/sin(beta);

th=atan(sin(x)/(cos(x)-Lrx));
if th<0
    th=pi+atan(sin(x)/(cos(x)-Lrx));
end

rt=sqrt(sin(x)*sin(x)+(cos(x)-Lrx)^2);
ry=exp(b*(y-x));

H_points=zeros(1,n_points);
L_points=zeros(1,n_points);
tt=zeros(1,n_points);
rr=zeros(1,n_points);
DD=zeros(1,n_points);
cc=zeros(1,n_points);
flag=1;

for i=1:n_points
    H_points(i)=sin(x)+H*i/(n_points+1);
    L_points(i)=cos(x)-Lrx-R(i)*L;
    rr(i)=sqrt(H_points(i)*H_points(i)+L_points(i)*L_points(i));
    tt(i)=acos(L_points(i)/rr(i));
    if rr(i)>exp(b*(tt(i)-x))
        flag=0;
    end
    if tt(i)>y
        flag=0;
    end
    if flag==1
        x_coord=rr(i)*cos(tt(i))-ry*cos(y);
        y_coord=ry*sin(y)-rr(i)*sin(tt(i));
        if (y_coord > -L/H*x_coord+H+L^2/H)
            DD(i)=(H-(rr(i)*sin(tt(i))-sin(x))/sin(pi/2-beta))/H*(D0-D1)+D1;
        else
            DD(i)=(H-(exp(b*(tt(i)-x))-rr(i))*cos(pi/2-tt(i)-beta)/H*(D0-D1)+D1;
        end
        if DD(i)>D0
            DD(i)=D0;
        elseif DD(i)<D1;
            DD(i)=D1;
        end
        m=mi*exp((GSI-100)/(28-14*D(i)));
        s=exp((GSI-100)/(9-3*D(i)));
        n=1/2+1/6*(exp(-GSI/15)-exp(-20/3));
        cc(i)=(cos(phi)/2*(m*n*(1-sin(phi))/2/sin(phi))^n/(1-n))-
        b/m*(1+sin(phi)/n)*(m*n*(1-sin(phi))/2/sin(phi))^n/(1-n))+s/m*b/(s^n);
    end
end

if flag==1
    f1=(exp(3*b*(y-x))*(sin(y)+3*b*cos(y))-3*b*cos(x)-sin(x))/(3*(1+9*b^2));
    f2=1/6*Lrx*sin(x)*(2*cos(x)-Lrx);
    f4=(exp(3*b*(z-x))*(sin(z)+3*b*cos(z))-3*b*cos(x)-sin(x))/(3*(1+9*b^2));
    f5=1/6*L2*sin(x+alpha)*(2*cos(x+alpha)-L2);
    f6=1/3*D*exp(2*b*(z-x))*cos(z)*cos(z);
    f3=0;
    q=0;
    if n_points==0
        f3=fun3(rt,th,ry,y);
        t=zeros(1,n_integral+1);
        D=zeros(1,n_integral+1);
        c=zeros(1,n_integral+1);
    end
end

```

```

for i=1:(n_integral+1)
    t(i)=x+(y-x)/n_integral*(i-1);
    x_coord=exp(b*(t(i)-x))*cos(t(i))-ry*cos(y);
    y_coord=ry*sin(y)-exp(b*(t(i)-x))*sin(t(i));
    if (y_coord > -L/H*x_coord+H*L^2/H)
        D(i)=(H-(exp(b*(t(i)-x))*sin(t(i))-sin(x))/sin(pi/2-beta))/H*(D0-D1)+D1;
    else
        D(i)=(H-exp(b*(t(i)-x))*cos(t(i)-pi/2+beta)+ry*sin(pi-y-beta))/H*(D0-
D1)+D1;
    end
    m=mi*exp((GSI-100)/(28-14*D(i)));
    s=exp((GSI-100)/(9-3*D(i)));
    n=1/2+1/6*(exp(-GSI/15)-exp(-20/3));
    c(i)=(cos(phi)/2*(m*n*(1-sin(phi))/2/sin(phi))^(n/(1-n))-
b/m*(1+sin(phi)/n)*(m*n*(1-sin(phi))/2/sin(phi))^(1/(1-n))+s/m*b)/(s^n);
    end
    for i=1:(n_integral+1)
        q=q+(c(i)*exp(2*b*(t(i)-x))+c(i+1)*exp(2*b*(t(i+1)-x)))*(y-x)/n_integral/2;
    end
end
if n_points~=0
    if n_points==1
        f3=fun3(rt,th,rr(1),tt(1))+fun3(rr(1),tt(1),ry,y);
    else
        f3=fun3(rt,th,rr(1),tt(1));
        for i=1:(n_points-1)
            f3=f3+fun3(rr(i),tt(i),rr(i+1),tt(i+1));
        end
        f3=f3+fun3(rr(n_points),tt(n_points),ry,y);
    end
    t1=zeros(1,n_integral+1);
    D1=zeros(1,n_integral+1);
    c1=zeros(1,n_integral+1);
    for i=1:(n_integral+1)
        t1(i)=x+(th-x)/n_integral*(i-1);
        x_coord=exp(b*(t1(i)-x))*cos(t1(i))-ry*cos(y);
        y_coord=ry*sin(y)-exp(b*(t1(i)-x))*sin(t1(i));
        if (y_coord > -L/H*x_coord+H*L^2/H)
            D1(i)=(H-(exp(b*(t1(i)-x))*sin(t1(i))-sin(x))/sin(pi/2-beta))/H*(D0-
D1)+D1;
        else
            D1(i)=(H-exp(b*(t1(i)-x))*cos(t1(i)-pi/2+beta)+ry*sin(pi-y-
beta))/H*(D0-D1)+D1;
        end
        m=mi*exp((GSI-100)/(28-14*D(i)));
        s=exp((GSI-100)/(9-3*D(i)));
        n=1/2+1/6*(exp(-GSI/15)-exp(-20/3));
        c1(i)=(cos(phi)/2*(m*n*(1-sin(phi))/2/sin(phi))^(n/(1-n))-
b/m*(1+sin(phi)/n)*(m*n*(1-sin(phi))/2/sin(phi))^(1/(1-n))+s/m*b)/(s^n);
        end
        for i=1:n_integral
            q=q+(c1(i)*exp(2*b*(t(i)-x))+c1(i+1)*exp(2*b*(t(i+1)-x)))*(th-
x)/n_integral/2;
        end
        cc_start=c(n_integral+1);
        m=mi*exp((GSI-100)/(28-14*D0));
        s=exp((GSI-100)/(9-3*D0));
        n=1/2+1/6*(exp(-GSI/15)-exp(-20/3));
        cc_last=(cos(phi)/2*(m*n*(1-sin(phi))/2/sin(phi))^(n/(1-n))-
b/m*(1+sin(phi)/n)*(m*n*(1-sin(phi))/2/sin(phi))^(1/(1-n))+s/m*b)/(s^n);
        D2=zeros(1,n_points);
        c2=zeros(1,n_points);
        for i=1:n_points
            x_coord=exp(b*(tt(i)-x))*cos(tt(i))-ry*cos(y);
            y_coord=ry*sin(y)-exp(b*(tt(i)-x))*sin(tt(i));
            if (y_coord > -L/H*x_coord+H*L^2/H)
                D2(i)=(H-(exp(b*(tt(i)-x))*sin(tt(i))-sin(x))/sin(pi/2-beta))/H*(D0-
D1)+D1;
            else
                D2(i)=(H-(exp(b*(tt(i)-x))-rr(i))*cos(pi/2-tt(i)-beta))/H*(D0-D1)+D1;
            end
            m=mi*exp((GSI-100)/(28-14*D(i)));
            s=exp((GSI-100)/(9-3*D(i)));
            n=1/2+1/6*(exp(-GSI/15)-exp(-20/3));
            c2(i)=(cos(phi)/2*(m*n*(1-sin(phi))/2/sin(phi))^(n/(1-n))-
b/m*(1+sin(phi)/n)*(m*n*(1-sin(phi))/2/sin(phi))^(1/(1-n))+s/m*b)/(s^n);
            end
            q=q+(cc_start*exp(2*b*(th-x))+c2(1)*exp(2*b*(tt(1)-x)))*(tt(1)-th)/2;
            for i=1:(n_points-1)
                q=q+(c2(i)*exp(2*b*(tt(i)-x))+c2(i+1)*exp(2*b*(tt(i+1)-x)))*(tt(i+1)-
tt(i))/n_integral/2;
            end
            q=q+(c2(n_points)*exp(2*b*(th-x))+cc_last*exp(2*b*(y-x)))*(y-tt(n_points))/2;
        end
        F=q*(exp(b*(y-x))*sin(y)-sin(x))/(f1-f2-f3-f4+f5+f6);
        if F<1 || F>500
            F=NaN;
        end
    end
end

```



```

else
    F=NaN;
end

```

## iv. Chapter 6

```

% Main program: Case 2
% -----
clear;

% slope inclination [deg]
beta_grad=60;
% friction angle [deg]
phi_grad=20;
% initial slope inclination [deg]
alpha_grad=0;

% derived variables in radian
% -----
beta=beta_grad/180*pi;
alpha=alpha_grad/180*pi;
phi=phi_grad/180*pi;
b=tan(phi);

m=1/3;
Kw=1;
gamma_ratio=0;
Kh=0;
Kv=0;

x_guess_grad=50;
y_guess_grad=88;
z_guess_grad=50;
x_delta_grad=24;
y_delta_grad=20;
z_delta_grad=24;
beta_delta_grad=15;
x_pass_grad=1;
y_pass_grad=1;
z_pass_grad=1;
beta_pass_grad=1;
x_range_grad=(-x_delta_grad+x_guess_grad):x_pass_grad:(x_delta_grad+x_guess_grad);
y_range_grad=(-y_delta_grad+y_guess_grad):y_pass_grad:(y_delta_grad+y_guess_grad);
z_range_grad=(-z_delta_grad+z_guess_grad):z_pass_grad:(z_delta_grad+z_guess_grad);
beta_range_grad=(beta_grad-beta_delta_grad):beta_pass_grad:beta_grad;
x_range=x_range_grad/180*pi;
y_range=y_range_grad/180*pi;
z_range=z_range_grad/180*pi;
beta_range=beta_range_grad/180*pi;
position_left=0.04;
position_right=0.96;
position_step=0.02;

Position=position_left:position_step:position_right;

temp=size(Position);
n=temp(2);

X=zeros(n,4);
N=zeros(1,n);

for i=1:n
    [X(i,:),
    N(i)]=Grid_Fun_Pile(alpha,beta,b,x_range,y_range,z_range,beta_range,m,Position(i),Kw,gamma_ratio,Kh,Kv);
end

function [X,
N_]=Grid_Fun_Pile(alpha,beta,b,x_range,y_range,z_range,beta_range,m,p,Kw,gamma_ratio,Kh,Kv)

temp=size(x_range);
n1=temp(2);
temp=size(y_range);
n2=temp(2);
temp=size(z_range);
n3=temp(2);
temp=size(beta_range);
n4=temp(2);
MatrixN=zeros(n1,n2,n3,n4);

```

```

for i=1:n1
    for j=1:n2
        for k=1:n3
            for l=1:n4
                x=x_range(i);
                y=y_range(j);
                z=z_range(k);
                beta_f=beta_range(l);
                if (x>y-10e-6) || (x>z-10e-6) || (z>y-10e-6)
                    MatrixN(i,j,k,l)=NaN;
                else
                    MatrixN(i,j,k,l)=funXYZ_Pile(alpha,beta,b,x,y,z,beta_f,m,p,Kw,gamma_ratio,Kh,Kv);
                end
            end
        end
    end
end

[N_,BiI]=min(MatrixN(:));
[x_f,y_f,z_f,b_f]=ind2sub(size(MatrixN),BiI);
X(1)=x_range(x_f)/pi*180;
X(2)=y_range(y_f)/pi*180;
X(3)=z_range(z_f)/pi*180;
X(4)=beta_range(b_f)/pi*180;

function N=funXYZ_Pile(alpha,beta,b,x,y,z,beta_f,m,p,Kw,gamma_ratio,Kh,Kv)

H=sin(beta_f)/sin(beta_f-alpha)*(exp(b*(y-x))*sin(y+alpha)-sin(x+alpha));
L=H/tan(beta);
ry=exp(b*(y-x));
L1=sin(y-x)/sin(y+alpha)-sin(y+beta_f)/(sin(y+alpha)*sin(beta_f-alpha))*(exp(b*(y-x))*sin(y+alpha)-sin(x+alpha));
L2=sin(z-x)/sin(z+alpha)-cos(z)/sin(z+alpha)/cos(alpha)*(exp(b*(z-x))*sin(z+alpha)-sin(x+alpha));
D=1/cos(alpha)*(exp(b*(z-x))*sin(z+alpha)-sin(x+alpha));
g=exp(2*b*(z-x))*(exp(2*b*(y-z))-1)/(2*b);
f1v=(exp(3*b*(y-x))*(sin(y)+3*b*cos(y))-3*b*cos(x)-sin(x))/(3*(1+9*b^2));
f2v=1/6*L1*sin(x+alpha)*(2*cos(x)-L1*cos(alpha));
f3v=1/6*exp(b*(y-x))*(sin(y-x)-L1*sin(y+alpha))*(cos(x)-L1*cos(alpha)+exp(b*(y-x))*cos(y));
f4v=(exp(3*b*(z-x))*(sin(z)+3*b*cos(z))-3*b*cos(x)-sin(x))/(3*(1+9*b^2));
f5v=1/6*L2*sin(x+alpha)*(2*cos(x+alpha)-L2);
f6v=1/3*D*exp(2*b*(z-x))*cos(z)*cos(z);
f7v=1/2*H^2*sin(beta-beta_f)/sin(beta)/sin(beta_f)*(cos(x)-L1*cos(alpha)-1/3*H*(1/tan(beta_f)+1/tan(beta)));

if Kh==0
    fh=0;
else
    f1h=(exp(3*b*(y-x))*(-cos(y)+3*b*sin(y))-3*b*sin(x)+cos(x))/(3*(1+9*b^2));
    f2h=1/6*L1*(2*sin(x)+L1*sin(alpha))*sin(x+alpha);
    f3h=1/6*exp(b*(y-x))*(sin(y-x)-L1*sin(y+alpha))*(sin(x)+exp(b*(y-x))*sin(y));
    f4h=(exp(3*b*(z-x))*(-cos(z)+3*b*sin(z))-3*b*sin(x)+cos(x))/(3*(1+9*b^2));
    f5h=1/3*L2*sin(x+alpha)*sin(x+alpha);
    f6h=1/6*D*exp(b*(z-x))*cos(z)*(2*exp(b*(z-x))*sin(z)-D);
    fh=Kh*(f1h-f2h-f3h-f4h+f5h+f6h);
end

flag=1;
options = optimset('TolX',1e-3);
[theta,fval,exitflag,output] = fzero(@(theta)cos(theta)*exp(b*(theta-x))-p*L-sin(beta-beta_f)/sin(beta)/sin(beta_f)*H-ry*cos(y),(x+y)/2,options);
if (exitflag~=1) || (theta<x) || (theta>y)
    flag=0;
end

if gamma_ratio==0
    fw1=0;
    fw2=0;
    fw3=0;
else
    options = optimset('TolX',1e-5);
    [thetal,fval,exitflag,output] = fzero(@(thetal)cos(thetal)*exp(b*(thetal-x))-cos(x)+L1*cos(alpha),(z+y)/2,options);
    if (exitflag==1) && (thetal>z) && (thetal<y)
        fw1=integral(@(angle)funw1(angle,x,b),z,thetal);
        fw2=integral(@(angle)funw2(angle,x,y,b,beta),thetal,y);
        fw3=1/2*Kw*Kw*D*D*(exp(b*(z-x))*sin(z)-1/3*Kw*D);
    else
        flag=0;
    end
end

if flag==1

```

```

h=abs(exp(b*(theta-x))*sin(theta)-ry*sin(y))+p*L*tan(beta);
% indicate pile diameter and spacing
D1=H;
D2=0.6*H;
Np=tan(pi/4+atan(b)/2)*tan(pi/4+atan(b)/2);
A=D1*(D1/D2)^(b*Np^0.5+Np-1);
C1=A*(1/Np/b*(exp((D1-D2)/D2*Np*b*tan(pi/8+atan(b)/4))-2*b*Np^0.5-
1)+(2*b+2*Np^0.5+Np^(-0.5))/(b*Np^0.5+Np-1))-(D1*(2*b+2*Np^0.5+Np^(-0.5))/(b*Np^0.5+Np-
1)-2*D2*Np^(-0.5));
C2=(A*exp((D1-D2)/D2*Np*b*tan(pi/8+atan(b)/4))-D2)/Np;
C3=sin(theta)*exp(b*(theta-x))-m*h;
C1=C1/D1;
C2=C2/D1;

N=H*(g+C1*C3*h)/((1+Kv)*(f1v-f2v-f3v-f4v+f5v+f6v-f7v)-
0.5*C2*C3*h^2+(fw1+fw2+fw3)*gamma_ratio+fh);

if N<1 || N>400
    N=NaN;
end
else
    N=NaN;
end

% Main program: Performance-based optimal design
% -----
clear;

% slope inclination [deg]
beta_grad=60;
% friction angle [deg]
phi_grad=20;
% initial slope inclination [deg]
alpha_grad=0;

% derived variables in radian
% -----
beta=beta_grad/180*pi;
alpha=alpha_grad/180*pi;
phi=phi_grad/180*pi;
b=tan(phi);

m=1/3;
Kw=1;
gamma_ratio=0;
N=1/5.5;

x_guess_grad=50;
y_guess_grad=88;
z_guess_grad=50;
x_delta_grad=24;
y_delta_grad=20;
z_delta_grad=24;
beta_delta_grad=10;
x_pass_grad=1;
y_pass_grad=1;
z_pass_grad=1;
beta_pass_grad=1;

x_range_grad=(-x_delta_grad+x_guess_grad):x_pass_grad:(x_delta_grad+x_guess_grad);
y_range_grad=(-y_delta_grad+y_guess_grad):y_pass_grad:(y_delta_grad+y_guess_grad);
z_range_grad=(-z_delta_grad+z_guess_grad):z_pass_grad:(z_delta_grad+z_guess_grad);
beta_range_grad=(beta_grad-beta_delta_grad):beta_pass_grad:beta_grad;

x_range=x_range_grad/180*pi;
y_range=y_range_grad/180*pi;
z_range=z_range_grad/180*pi;
beta_range=beta_range_grad/180*pi;

position_left=0.04;
position_right=0.96;
position_step=0.02;

Position=position_left:position_step:position_right;

temp=size(Position);
n=temp(2);

X=zeros(n,4);
Kw=zeros(1,n);
C=zeros(1,n);
DISP=zeros(1,n);

for i=1:n

```

```

[X(i,:), Kw(i),
CC(i)]=Grid_Fun_Pile_Displacement(alpha,beta,b,x_range,y_range,z_range,beta_range,m,Position(i)
,Kw,gamma_ratio,N);
DISP(i)=CC(i)*9.81*Displacement(Kw(i));
end

function [X, K_,
C_]=Grid_Fun_Pile_Displacement(alpha,beta,b,x_range,y_range,z_range,beta_range,m,p,Kw,gamma_ratio,N)

temp=size(x_range);
n1=temp(2);
temp=size(y_range);
n2=temp(2);
temp=size(z_range);
n3=temp(2);
temp=size(beta_range);
n4=temp(2);
MatrixN=zeros(n1,n2,n3,n4);

for i=1:n1
    for j=1:n2
        for k=1:n3
            for l=1:n4
                x=x_range(i);
                y=y_range(j);
                z=z_range(k);
                beta_f=beta_range(l);
                if (x>y-10e-6) || (x>z-10e-6) || (z>y-10e-6)
                    MatrixN(i,j,k,l)=NaN;
                else
                    MatrixN(i,j,k,l)=funXYZ_Pile_Displacement(alpha,beta,b,x,y,z,beta_f,m,p,Kw,gamma_ratio,N);
                end
            end
        end
    end
end

[K_,BiI]=min(MatrixN(:));
[x_f,y_f,z_f,b_f]=ind2sub(size(MatrixN),BiI);
X(1)=x_range(x_f);
X(2)=y_range(y_f);
X(3)=z_range(z_f);
X(4)=beta_range(b_f);

H=sin(X(4))/sin(X(4)-alpha)*(exp(b*(X(2)-X(1)))*sin(X(2)+alpha)-sin(X(1)+alpha));
L1=sin(X(2)-X(1))/sin(X(2)+alpha)-sin(X(2)+X(4))/(sin(X(2)+alpha)*sin(X(4)-alpha));
L2=sin(X(3)-X(1))/sin(X(3)+alpha)-cos(X(3))/sin(X(3)+alpha)/cos(alpha)*(exp(b*(X(3)-X(1)))*sin(X(3)+alpha)-sin(X(1)+alpha));
D=1/cos(alpha)*(exp(b*(X(3)-X(1)))*sin(X(3)+alpha)-sin(X(1)+alpha));

a1=(exp(2*b*(X(2)-X(1)))-1)/2/b;
a2=L1*sin(X(1)+alpha);
a3=H*(cos(X(1))-L1*cos(alpha)+(sin(X(1))+L1*sin(alpha))/tan(X(4)));
a4=(exp(2*b*(X(3)-X(1)))-1)/2/b;
a5=L2*sin(X(1)+alpha);
a6=D*exp(b*(X(3)-X(1)))*cos(X(3));

f1v=(exp(3*b*(X(2)-X(1)))*(sin(X(2))+3*b*cos(X(2)))-3*b*cos(X(1))-sin(X(1)))/(3*(1+9*b^2));
f2v=1/6*L1*sin(X(1)+alpha)*(2*cos(X(1))-L1*cos(alpha));
f3v=1/6*exp(b*(X(2)-X(1)))*(sin(X(2)-X(1))-L1*sin(X(2)+alpha))*(cos(X(1))-L1*cos(alpha)+exp(b*(X(2)-X(1)))*cos(X(2)));
f4v=(exp(3*b*(X(3)-X(1)))*(sin(X(3))+3*b*cos(X(3)))-3*b*cos(X(1))-sin(X(1)))/(3*(1+9*b^2));
f5v=1/6*L2*sin(X(1)+alpha)*(2*cos(X(1)+alpha)-L2);
f6v=1/3*D*exp(2*b*(X(3)-X(1)))*cos(X(3))*cos(X(3));

f1h=(exp(3*b*(X(2)-X(1)))*(-cos(X(2))+3*b*sin(X(2)))-3*b*sin(X(1))+cos(X(1)))/(3*(1+9*b^2));
f2h=1/6*L1*(2*sin(X(1))+L1*sin(alpha))*sin(X(1)+alpha);
f3h=1/6*exp(b*(X(2)-X(1)))*(sin(X(2)-X(1))-L1*sin(X(2)+alpha))*(sin(X(1))+exp(b*(X(2)-X(1)))*sin(X(2)));
f4h=(exp(3*b*(X(3)-X(1)))*(-cos(X(3))+3*b*sin(X(3)))-3*b*sin(X(1))+cos(X(1)))/(3*(1+9*b^2));
f5h=1/3*L2*sin(X(1)+alpha)*sin(X(1)+alpha);
f6h=1/6*D*exp(b*(X(3)-X(1)))*cos(X(3))*(2*exp(b*(X(3)-X(1)))*sin(X(3))-D);

G=1/2*(a1-a2-a3-a4+a5+a6-a7);
l=1/G*sqrt((f1h-f2h-f3h-f4h+f5h+f6h-f7h)^2+(f1v-f2v-f3v-f4v+f5v+f6v-f7v)^2);
C_=sin(X(2))*exp(b*(X(2)-X(1)))/(G*l)*((f1h-f2h-f3h-f4h+f5h+f6h-f7h);

X=X/pi*180;

```

```

function N=funXYZ_Pile_Displacement(alpha,beta,b,x,y,z,beta_f,m,p,Kw,gamma_ratio,N)

H=sin(beta_f)/sin(beta_f-alpha)*(exp(b*(y-x))*sin(y+alpha)-sin(x+alpha));
L=H/tan(beta);
ry=exp(b*(y-x));
L1=sin(y-x)/sin(y+alpha)-sin(y+beta_f)/(sin(y+alpha)*sin(beta_f-alpha))*(exp(b*(y-x))*sin(y+alpha)-sin(x+alpha));
L2=sin(z-x)/sin(z+alpha)-cos(z)/sin(z+alpha)/cos(alpha)*(exp(b*(z-x))*sin(z+alpha)-sin(x+alpha));
D=1/cos(alpha)*(exp(b*(z-x))*sin(z+alpha)-sin(x+alpha));
g=exp(2*b*(z-x))*(exp(2*b*(y-z))-1)/(2*b);
f1v=(exp(3*b*(y-x))*(sin(y)+3*b*cos(y))-3*b*cos(x)-sin(x))/(3*(1+9*b^2));
f2v=1/6*L1*sin(x+alpha)*(2*cos(x)-L1*cos(alpha));
f3v=1/6*exp(b*(y-x))*(sin(y-x)-L1*sin(y+alpha))*(cos(x)-L1*cos(alpha)+exp(b*(y-x))*cos(y));
f4v=(exp(3*b*(z-x))*(sin(z)+3*b*cos(z))-3*b*cos(x)-sin(x))/(3*(1+9*b^2));
f5v=1/6*L2*sin(x+alpha)*(2*cos(x+alpha)-L2);
f6v=1/3*D*exp(2*b*(z-x))*cos(z)*cos(z);
f7v=1/2*H^2*sin(beta-beta_f)/sin(beta)/sin(beta_f)*(cos(x)-L1*cos(alpha)-1/3*H*(1/tan(beta_f)+1/tan(beta)));

f1h=(exp(3*b*(y-x))*(-cos(y)+3*b*sin(y))-3*b*sin(x)+cos(x))/(3*(1+9*b^2));
f2h=1/6*L1*(2*sin(x)+L1*sin(alpha))*sin(x+alpha);
f3h=1/6*exp(b*(y-x))*(sin(y-x)-L1*sin(y+alpha))*(sin(x)+exp(b*(y-x))*sin(y));
f4h=(exp(3*b*(z-x))*(-cos(z)+3*b*sin(z))-3*b*sin(x)+cos(x))/(3*(1+9*b^2));
f5h=1/3*L2*sin(x+alpha)*sin(x+alpha);
f6h=1/6*D*exp(b*(z-x))*cos(z)*(2*exp(b*(z-x))*sin(z)-D);

flag=1;
options = optimset('TolX',1e-3);
[theta,fval,exitflag,output] = fzero(@(theta)cos(theta)*exp(b*(theta-x))-p*L-sin(beta-beta_f)/sin(beta)/sin(beta_f)*H-ry*cos(y),(x+y)/2,options);
if (exitflag~=1) || (theta<x) || (theta>y)
    flag=0;
end

if gamma_ratio==0
    fw1=0;
    fw2=0;
    fw3=0;
else
    options = optimset('TolX',1e-5);
    [thetal,fval,exitflag,output] = fzero(@(thetal)cos(thetal)*exp(b*(thetal-x))-cos(x)+L1*cos(alpha),(z+y)/2,options);
    if (exitflag==1) && (thetal>z) && (thetal<y)
        fw1=integral(@(angle)funw1(angle,x,b),z,thetal);
        fw2=integral(@(angle)funw2(angle,x,y,b,beta),thetal,y);
        fw3=1/2*Kw*Kw*D*D*(exp(b*(z-x))*sin(z)-1/3*Kw*D);
    else
        flag=0;
    end
end

if flag==1
    h=abs(exp(b*(theta-x))*sin(theta)-ry*sin(y))+p*L*tan(beta);
    D1=0.15*H;
    D2=0.09*H;
    Np=tan(pi/4+atan(b)/2)*tan(pi/4+atan(b)/2);
    A=D1*(D1/D2)^(b*Np^0.5+Np-1);
    C1=A*(1/Np/b*(exp((D1-D2)/D2*Np*b*tan(pi/8+atan(b)/4))-2*b*Np^0.5-1)+(2*b+2*Np^0.5+Np^(-0.5))/(b*Np^0.5+Np-1)-(D1*(2*b+2*Np^0.5+Np^(-0.5))/(b*Np^0.5+Np-1)-2*D2*Np^(-0.5)));
    C2=(A*exp((D1-D2)/D2*Np*b*tan(pi/8+atan(b)/4))-D2)/Np;
    C3=sin(theta)*exp(b*(theta-x))-m*h;

    N=(N*H*(g+C1*C3*h)-(f1v-f2v-f3v-f4v+f5v+f6v-f7v-0.5*C2*C3*h^2+(fw1+fw2+fw3)*gamma_ratio))/(f1h-f2h-f3h-f4h+f5h+f6h-f7h);

    if N<0 || N>1
        N=NaN;
    end
else
    N=NaN;
end

function TotalD=Displacement(Kc)

Rec_N=1000;
acc=load('Northridge Moorpark.txt'); % importing earthquake acceleration data.
acc_t=acc';
acc_r=(acc_t(:))';
Ka=acc_r(1:Rec_N);
t_interval= 0.02; % the time interval (sec)
t_step=0:t_interval:(Rec_N-1)*(t_interval);

```

```

K=Ka-Kc;
A_add=zeros(1,Rec_N);

for i=1:(Rec_N-1)
    A_add(i+1)=(K(i)+K(i+1))*t_interval/2;
end
Velo=zeros(1,Rec_N);
for i=1:(Rec_N-1)
    Velo(i+1)=Velo(i)+A_add(i+1);

    if Velo(i+1)<0
        Velo(i+1)=0;
    end
end
V_add=zeros(1,Rec_N);

for i=1:(Rec_N-1)
    V_add(i+1)=(Velo(i)+Velo(i+1))*t_interval/2;
end
Disp=zeros(1,Rec_N);
for i=1:(Rec_N-1)
    Disp(i+1)=Disp(i)+V_add(i+1);
end
TotalD=Disp(Rec_N);

```

## v. Chapter 7

```

% Main program: Unitary Formulation
% -----
clear

% height [m]
Height=20;
% slope inclination [deg]
beta_grad=45;
% upper slope inclination [deg]
alpha_grad=0;
% position of phreatic line
water_pos=0.01;
% unit weights [kN/m^3]
gamma_w=9.81;
% seismic coefficients
Kh=0;
Kv=0;
% crack
crack_type=1; % 1)known depth 2)known location 3) free
crack_x=0; % departs from slope crest
crack_depth=0;
% slope profile
shape=1; % 1)planar 2)circular
Radius=Height; % circular radius

% determination of angles in radians
beta=beta_grad/180*pi;
alpha=alpha_grad/180*pi;

% x,y,z represent different failure mechanisms
x_guess_grad=50;
y_guess_grad=88;
z_guess_grad=50;
x_delta_grad=24;
y_delta_grad=20;
z_delta_grad=24;
x_pass_grad=1;
y_pass_grad=1;
z_pass_grad=1;

x_range_grad=(-x_delta_grad+x_guess_grad):x_pass_grad:(x_delta_grad+x_guess_grad);
y_range_grad=(-y_delta_grad+y_guess_grad):y_pass_grad:(y_delta_grad+y_guess_grad);
z_range_grad=(-z_delta_grad+z_guess_grad):z_pass_grad:(z_delta_grad+z_guess_grad);

x_range=x_range_grad/180*pi;
y_range=y_range_grad/180*pi;
z_range=z_range_grad/180*pi;

% number of points used to discretize slope profile
n_points=19;

% number of points used to discretize crack depth
n_depth=10;

% to indicate a Mohr-Coulomb or Hoek-Brown failure criterion 1)M-C 2)H-B

```

```

failure_criterion=1;

if failure_criterion==1
    % friction angle [deg]
    phi_grad=20;
    phi=phi_grad/180*pi;
    % cohesion [kPa]
    c=20;
    % unit weights [kN/m^3]
    gamma_s=19;
    % strength reduction
    SR_ratio=1; % Fc/Ff 0 if reduce cohesion only

[FS,X_ini,N_ini]=Fryctoria_MohrCoulomb(x_range,y_range,z_range,n_depth,n_points,beta,alpha,phi,c,Height,water_pos,gamma_s,gamma_w,Kh,Kv,crack_type,crack_x,crack_depth,shape,Radius,SR_ratio);

elseif failure_criterion==2
    % rock parameters
    mi=7.3;
    GSI=100;
    D=0;
    m=mi*exp((GSI-100)/(28-14*D));
    s=exp((GSI-100)/(9-3*D));
    n=1/2+1/6*(exp(-GSI/15)-exp(-20/3));
    sigma_c=20;
    % unit weights [kN/m^3]
    gamma_r=20;
    % tangential technique
    phi_guess_grad=20;
    phi_delta_grad=10;
    phi_pass_grad=1;
    phi_range_grad=(-
phi_delta_grad+phi_guess_grad):phi_pass_grad:(phi_delta_grad+phi_guess_grad);
    phi_range=phi_range_grad/180*pi;

[FS,X_ini,N_ini]=Fryctoria_HoekBrown(x_range,y_range,z_range,phi_range,n_depth,n_points,beta,alpha,m,s,n,sigma_c,Height,water_pos,gamma_r,gamma_w,Kh,Kv,crack_type,crack_x,crack_depth,shape,Radius);
end

function [FS,X,N_ini] =
Fryctoria_MohrCoulomb(x_range,y_range,z_range,n_depth,n_points,beta,alpha,phi,c,Height,Ru,gamma_s,gamma_w,Kh,Kv,crack_type,crack_x,crack_depth,shape,Radius,SR_ratio)

% normalized crack depth
d_norm=crack_depth/Height;

% normalized crack position
hx_norm=crack_x/Height;

temp=size(x_range);
n1=temp(2);
temp=size(y_range);
n2=temp(2);
temp=size(z_range);
n3=temp(2);

beta_new=beta;
if shape==1 % planar profile, similarity exists
    n_points=0;
    R_new=NaN;
else
    R_new=Fryctoria_Circular_Coordinates(Radius,Height,beta,n_points); % profile
nodes coordinates for a circular profile
end

N_all=zeros(1,n_points+1);
X_all=zeros(3,n_points+1);

H_R=zeros(1,n_points+1);
for l=1:(n_points+1)
    H_R(l)=(n_points+1)/(n_points+2-l);
end

gamma_ratio=gamma_w/gamma_s;

F=1;
SR_Flag=1;
SR_Count=1;

%Crack Free
if crack_type==3
    while SR_Flag
        b=tan(phi)/F*SR_ratio;
        MatrixN=zeros(n1,n2,n3);

```

```

        for loop=1:(n_points+1)
            for i=1:n1
                for j=1:n2
                    for k=1:n3
                        x=x_range(i);
                        y=y_range(j);
                        z=z_range(k);
                        if (x>y-10e-6) || (x>z-10e-6) || (z>y-10e-6)
                            MatrixN(i,j,k)=NaN;
                        else
MatrixN(i,j,k)=Fryctoria_MatrixN(x,y,z,alpha,beta_new,b,Kh,Kv,Ru,gamma_ratio,(n_points+
1-loop),R_new);
                        end
                    end
                end
            end
            [N_all(loop),BiI]=min(MatrixN(:));
            [x_f,y_f,z_f]=ind2sub(size(MatrixN),BiI);
            X_all(1,loop)=x_range(x_f);
            X_all(2,loop)=y_range(y_f);
            X_all(3,loop)=z_range(z_f);
            if shape~=1
                R_temp=R_new;
                if (n_points+1-loop)==0
                    R_new=NaN;
                    beta_new=NaN;
                else
                    if (n_points-loop)==0
                        R_new=NaN;
                    else
                        R_new=zeros(1,n_points-loop);
                        for k=1:(n_points-loop)
                            R_new(k)=R_temp(k)/R_temp(n_points+1-loop);
                        end
                    end
                    beta_new=atan(tan(beta_new)*(n_points+1-loop)/(n_points+2-
loop)/R_temp(n_points+1-loop));
                end
            end
            N_all=H_R.*N_all;
            [N, toe]=min(N_all);
            X(1)=X_all(1,toe);
            X(2)=X_all(2,toe);
            X(3)=X_all(3,toe);
            if (SR_Count==1)
                N_ini=N;
            end
            if SR_ratio==0
                FS=N_ini*c/gamma_s/Height;
                SR_Flag=0;
            else
                SR_Count=SR_Count+1;
                N_Actual=gamma_s*Height/c*F;
                if ((gamma_s*Height/c-N_ini)*(N_Actual-N))<=0
                    SR_Flag=0;
                    FS=(1+SR_ratio)*F/2;
                end
                if(N_Actual<N)
                    F=F+0.01
                else
                    F=F-0.01
                end
                if isnan(N)
                    disp('Error');
                    FS=NaN;
                    X=NaN;
                    N_ini=NaN;
                    break
                end
            end
        end
    end
end

%Crack Depth
if crack_type==1
    if d_norm==0
        n_depth=1;
    end
    while SR_Flag
        b=tan(phi)/F*SR_ratio;
        MatrixN=zeros(n1,n2,n_depth);
        z_depth=zeros(n1,n2,n_depth);
        for loop=1:(n_points+1)
            for i=1:n1
                for j=1:n2

```



```

        for l=1:n_depth
            x=x_range(i);
            y=y_range(j);
            if (x>y-10e-6)
                MatrixN(i,j,l)=NaN;
            else
                const=(1-d_norm/n_depth*1*sin(beta)/sin(beta-
alpha))*exp(b*x)*sin(x+alpha)+d_norm/n_depth*1*sin(beta)/sin(beta-
alpha)*exp(b*y)*sin(y+alpha);
                options = optimset('TolX',1e-3);
                [z,fval,exitflag,output] = fzero(@(z)exp(b*z)*sin(z+alpha)-
const,(x+y)/2,options);
                if (exitflag~=1) || (z>y) || (z<x)
                    MatrixN(i,j,l)=NaN;
                else
                    z_depth(i,j,l)=z;
                end
            end
        end
        MatrixN(i,j,l)=Fryctoria_MatrixN(x,y,z,alpha,beta_new,b,Kh,Kv,Ru,gamma_ratio,(n_points+
1-loop),R_new);
    end
end
end
end
end
[N_all(loop),BiI]=min(MatrixN(:));
[x_f,y_f,d_f]=ind2sub(size(MatrixN),BiI);
X_all(1,loop)=x_range(x_f);
X_all(2,loop)=y_range(y_f);
X_all(3,loop)=z_depth(x_f,y_f,d_f);
if shape~=1
    R_temp=R_new;
    if (n_points+1-loop)==0
        R_new=NaN;
        beta_new=NaN;
    else
        if (n_points-loop)==0
            R_new=NaN;
        else
            R_new=zeros(1,n_points-loop);
            for k=1:(n_points-loop)
                R_new(k)=R_temp(k)/R_temp(n_points+1-loop);
            end
        end
        beta_new=atan(tan(beta_new)*(n_points+1-loop)/(n_points+2-
loop)/R_temp(n_points+1-loop));
    end
end
end
N_all=H_R.*N_all;
[N, toe]=min(N_all);
X(1)=X_all(1,toe);
X(2)=X_all(2,toe);
X(3)=X_all(3,toe);
if (SR_Count==1)
    N_ini=N;
end
if SR_ratio==0
    FS=N_ini*c/gamma_s/Height;
    SR_Flag=0;
else
    SR_Count=SR_Count+1;
    N_Actual=gamma_s*Height/c*F;
    if ((gamma_s*Height/c-N_ini)*(N_Actual-N))<=0
        SR_Flag=0;
        FS=(1+SR_ratio)*F/2;
    end
    if(N_Actual<N)
        F=F+0.01
    else
        F=F-0.01
    end
    if isnan(N)
        disp('Error');
        FS=NaN;
        X=NaN;
        N_ini=NaN;
        break
    end
end
end
end
end
end
%Crack H-distance
if crack_type==2
    while SR_Flag
        b=tan(phi)/F*SR_ratio;
        MatrixN=zeros(n2,n3);
    end
end

```

```

x_pos=zeros(n2,n3);
for loop=1:(n_points+1)
    for j=1:n2
        for k=1:n3
            y=y_range(j);
            z=z_range(k);
            if (z>y-10e-6)
                MatrixN(j,k)=NaN;
            else
                const=(exp(b*y)*cos(y)-
exp(b*z)*cos(z))/(hx_norm+cot(beta))+exp(b*y)*sin(y);
                options = optimset('TolX',1e-3);
                [x,fval,exitflag,output] = fzero(@(x)exp(b*x)*sin(x)-
const,[xlim_inf xlim_sup],options);
                if (exitflag~=1) || (x>z)
                    MatrixN(j,k)=NaN;
                else
                    x_pos(j,k)=x;

MatrixN(j,k)=min(Fryctoria_MatrixN(x,y,x,alpha,beta_new,b,Kh,Kv,Ru,gamma_ratio,(n_point
s+1-
loop),R_new),Fryctoria_MatrixN(x,y,z,alpha,beta_new,b,Kh,Kv,Ru,gamma_ratio,(n_points+1-
loop),R_new));
            end
        end
    end
end

[N_all(loop),BiI]=min(MatrixN(:));
[y_f,z_f]=ind2sub(size(MatrixN),BiI);
X_all(1,loop)=x_pos(y_f,z_f);
X_all(2,loop)=y_range(y_f);
X_all(3,loop)=z_range(z_f);
if shape~=1
    R_temp=R_new;
    if (n_points+1-loop)==0
        R_new=NaN;
        beta_new=NaN;
    else
        if (n_points-loop)==0
            R_new=NaN;
        else
            R_new=zeros(1,n_points-loop);
            for k=1:(n_points-loop)
                R_new(k)=R_temp(k)/R_temp(n_points+1-loop);
            end
            beta_new=atan(tan(beta_new)*(n_points+1-loop)/(n_points+2-
loop)/R_temp(n_points+1-loop));
        end
    end
end
end
N_all=H_R.*N_all;
[N, toe]=min(N_all);
X(1)=X_all(1,toe);
X(2)=X_all(2,toe);
X(3)=X_all(3,toe);
if (SR_Count==1)
    N_ini=N;
end
if SR_ratio==0
    FS=N_ini*c/gamma_s/Height;
    SR_Flag=0;
else
    SR_Count=SR_Count+1;
    N_Actual=gamma_s*Height/c*F;
    if ((gamma_s*Height/c-N_ini)*(N_Actual-N))<=0
        SR_Flag=0;
        FS=(1+SR_ratio)*F/2;
    end
    if(N_Actual<N)
        F=F+0.01
    else
        F=F-0.01
    end
    if isnan(N)
        disp('Error');
        FS=NaN;
        X=NaN;
        N_ini=NaN;
        break
    end
end
end
end
end

```

```

function [FS,X,N_ini] =
Fryctoria_HoekBrown(x_range,y_range,z_range,phi_range,n_depth,n_points,beta,alpha,m,s,n
,sigma_c,Height,Ru,gamma_r,gamma_w,Kh,Kv,crack_type,crack_x,crack_depth,shape,Radius)

% normalized crack depth
d_norm=crack_depth/Height;

% normalized crack position
hx_norm=crack_x/Height;

temp=size(x_range);
n1=temp(2);
temp=size(y_range);
n2=temp(2);
temp=size(z_range);
n3=temp(2);
temp=size(phi_range);
n4=temp(2);

beta_new=beta;
if shape==1 % planar profile, similarity exists
    n_points=0;
    R_new=NaN;
else
    R_new=Fryctoria_Circular_Coordinates(Radius,Height,beta,n_points); % profile
nodes coordinates for a circular profile
end

N_all=zeros(1,n_points+1);
X_all=zeros(4,n_points+1);

H_R=zeros(1,n_points+1);
for l=1:(n_points+1)
    H_R(l)=(n_points+1)/(n_points+2-l);
end

gamma_ratio=gamma_w/gamma_r;

%Crack Free
if crack_type==3
    MatrixN=zeros(n1,n2,n3,n4);
    for loop=1:(n_points+1)
        for i=1:n1
            for j=1:n2
                for k=1:n3
                    for q=1:n4
                        x=x_range(i);
                        y=y_range(j);
                        z=z_range(k);
                        phi=phi_range(q);
                        b=tan(phi);
                        strength_ratio=(cos(phi)/2*(m*n*(1-sin(phi))/2/sin(phi))^(n/(1-
n)))-b/m*(1+sin(phi)/n)*(m*n*(1-sin(phi))/2/sin(phi))^(1/(1-n))+s/m*b)/(s^n);
                        if (x>y-10e-6) || (x>z-10e-6) || (z>y-10e-6)
                            MatrixN(i,j,k,q)=NaN;
                        else
                            MatrixN(i,j,k,q)=strength_ratio*Fryctoria_MatrixN(x,y,z,alpha,beta_new,b,Kh,Kv,Ru,gamma
_ratio,(n_points+1-loop),R_new);
                        end
                    end
                end
            end
        end
        [N_all(loop),BiI]=min(MatrixN(:));
        [x_f,y_f,z_f,p_f]=ind2sub(size(MatrixN),BiI);
        X_all(1,loop)=x_range(x_f);
        X_all(2,loop)=y_range(y_f);
        X_all(3,loop)=z_range(z_f);
        X_all(4,loop)=phi_range(p_f);
        if shape~=1
            R_temp=R_new;
            if (n_points+1-loop)==0
                R_new=NaN;
                beta_new=NaN;
            else
                if (n_points-loop)==0
                    R_new=NaN;
                else
                    R_new=zeros(1,n_points-loop);
                    for k=1:(n_points-loop)
                        R_new(k)=R_temp(k)/R_temp(n_points+1-loop);
                    end
                    beta_new=atan(tan(beta_new)*(n_points+1-loop)/(n_points+2-
loop)/R_temp(n_points+1-loop));
                end
            end
        end
    end
end

```

```

end
N_all=H_R.*N_all;
[N_ini, toe]=min(N_all);
X(1)=X_all(1,toe);
X(2)=X_all(2,toe);
X(3)=X_all(3,toe);
X(4)=X_all(4,toe);
FS=N_ini*(s^n)*sigma_c/gamma_r/Height;
end

%Crack Depth
if crack_type==1
    if d_norm==0
        n_depth=1;
    end
    MatrixN=zeros(n1,n2,n4,n_depth);
    z_depth=zeros(n1,n2,n4,n_depth);
    for loop=1:(n_points+1)
        for i=1:n1
            for j=1:n2
                for q=1:n4
                    for l=1:n_depth
                        x=x_range(i);
                        y=y_range(j);
                        phi=phi_range(q);
                        b=tan(phi);
                        strength_ratio=(cos(phi)/2*(m*n*(1-sin(phi))/2/sin(phi)))^(n/(1-
n))-b/m*(1+sin(phi)/n)*(m*n*(1-sin(phi))/2/sin(phi))^(1/(1-n))+s/m*b)/(s^n);
                        if (x>y-10e-6)
                            MatrixN(i,j,q,l)=NaN;
                        else
                            const=(1-d_norm/n_depth*l*sin(beta)/sin(beta-
alpha))*exp(b*x)*sin(x+alpha)+d_norm/n_depth*l*sin(beta)/sin(beta-
alpha)*exp(b*y)*sin(y+alpha);
                            options = optimset('TolX',1e-3);
                            [z,fval,exitflag,output] = fzero(@(z)exp(b*z)*sin(z+alpha)-
const,(x+y)/2,options);
                            if (exitflag~=1) || (z>y) || (z<x)
                                MatrixN(i,j,q,l)=NaN;
                            else
                                z_depth(i,j,q,l)=z;
                            end
                        end
                    end
                end
            end
        end
        MatrixN(i,j,q,l)=strength_ratio*Fryctoria_MatrixN(x,y,z,alpha,beta_new,b,Kh,Kv,Ru,gamma
_ratio,(n_points+1-loop),R_new);
    end
end
end
end
end
[N_all(loop),BiI]=min(MatrixN(:));
[x_f,y_f,p_f,d_f]=ind2sub(size(MatrixN),BiI);
X_all(1,loop)=x_range(x_f);
X_all(2,loop)=y_range(y_f);
X_all(3,loop)=z_depth(x_f,y_f,p_f,d_f);
X_all(4,loop)=phi_range(p_f);
if shape~=1
    R_temp=R_new;
    if (n_points+1-loop)==0
        R_new=NaN;
        beta_new=NaN;
    else
        if (n_points-loop)==0
            R_new=NaN;
        else
            R_new=zeros(1,n_points-loop);
            for k=1:(n_points-loop)
                R_new(k)=R_temp(k)/R_temp(n_points+1-loop);
            end
            beta_new=atan(tan(beta_new)*(n_points+1-loop)/(n_points+2-
loop)/R_temp(n_points+1-loop));
        end
    end
end
end
N_all=H_R.*N_all;
[N_ini, toe]=min(N_all);
X(1)=X_all(1,toe);
X(2)=X_all(2,toe);
X(3)=X_all(3,toe);
X(4)=X_all(4,toe);
FS=N_ini*(s^n)*sigma_c/gamma_r/Height;
end

%Crack H-distance
if crack_type==2
    MatrixN=zeros(n2,n3,n4);

```

```

x_pos=zeros(n2,n3,n4);
for loop=1:(n_points+1)
    for j=1:n2
        for k=1:n3
            for q=1:n4
                y=y_range(j);
                z=z_range(k);
                phi=phi_range(q);
                b=tan(phi);
                strength_ratio=(cos(phi)/2*(m*n*(1-sin(phi))/2/sin(phi))^(n/(1-n))-
b/m*(1+sin(phi)/n)*(m*n*(1-sin(phi))/2/sin(phi))^(1/(1-n))+s/m*b)/(s^n);
                if (z>y-10e-6)
                    MatrixN(j,k)=NaN;
                else
                    const=(exp(b*y)*cos(y)-
exp(b*z)*cos(z))/(hx_norm+cot(beta))+exp(b*y)*sin(y);
                    options = optimset('TolX',1e-3);
                    [x,fval,exitflag,output] = fzero(@(x)exp(b*x)*sin(x)-
const,z/2,options);
                    if (exitflag~=1) || (x>z)
                        MatrixN(j,k,q)=NaN;
                    else
                        x_pos(j,k,q)=x;
                    end
                end
            end
        end
    end
    MatrixN(j,k,q)=strength_ratio*min(Fryctoria_MatrixN(x,y,x,alpha,beta_new,b,Kh,Kv,Ru,gam
ma_ratio,(n_points+1-
loop),R_new),Fryctoria_MatrixN(x,y,z,alpha,beta_new,b,Kh,Kv,Ru,gamma_ratio,(n_points+1-
loop),R_new));
end
end
end
end
[N_all(loop),BiI]=min(MatrixN(:));
[y_f,z_f,p_f]=ind2sub(size(MatrixN),BiI);
X_all(1,loop)=x_pos(y_f,z_f,p_f);
X_all(2,loop)=y_range(y_f);
X_all(3,loop)=z_range(z_f);
X_all(4,loop)=phi_range(p_f);
if shape~=1
    R_temp=R_new;
    if (n_points+1-loop)==0
        R_new=NaN;
        beta_new=NaN;
    else
        if (n_points-loop)==0
            R_new=NaN;
        else
            R_new=zeros(1,n_points-loop);
            for k=1:(n_points-loop)
                R_new(k)=R_temp(k)/R_temp(n_points+1-loop);
            end
            beta_new=atan(tan(beta_new)*(n_points+1-loop)/(n_points+2-
loop)/R_temp(n_points+1-loop));
        end
    end
end
N_all=H_R.*N_all;
[N_ini, toe]=min(N_all);
X(1)=X_all(1,toe);
X(2)=X_all(2,toe);
X(3)=X_all(3,toe);
X(4)=X_all(4,toe);
FS=N_ini*(s^n)*sigma_c/gamma_r/Height;
end

function N=Fryctoria_MatrixN(x,y,z,alpha,beta,b,Kh,Kv,Ru,gamma_ratio,n_points,R)

H=sin(beta)/sin(beta-alpha)*(exp(b*(y-x))*sin(y+alpha)-sin(x+alpha));
L=H/tan(beta);
L1=sin(y-x)/sin(y+alpha)-sin(y+beta)/(sin(y+alpha)*sin(beta-alpha))*(exp(b*(y-
x))*sin(y+alpha)-sin(x+alpha));
L2=sin(z-x)/sin(z+alpha)-cos(z)/sin(z+alpha)/cos(alpha)*(exp(b*(z-x))*sin(z+alpha)-
sin(x+alpha));
D=1/cos(alpha)*(exp(b*(z-x))*sin(z+alpha)-sin(x+alpha));
g=exp(2*b*(z-x))*(exp(2*b*(y-z))-1)*(exp(b*(y-x))*sin(y)-sin(x))/(2*b);
f1v=(exp(3*b*(y-x))*(sin(y)+3*b*cos(y))-3*b*cos(x)-sin(x))/(3*(1+9*b^2));
f1h=(exp(3*b*(y-x))*(-cos(y)+3*b*sin(y))-3*b*sin(x)+cos(x))/(3*(1+9*b^2));
f2v=1/6*L1*sin(x+alpha)*(2*cos(x)-L1*cos(alpha));
f2h=1/6*L1*(2*sin(x)+L1*sin(alpha))*sin(x+alpha);
f4v=(exp(3*b*(z-x))*(sin(z)+3*b*cos(z))-3*b*cos(x)-sin(x))/(3*(1+9*b^2));
f4h=(exp(3*b*(z-x))*(-cos(z)+3*b*sin(z))-3*b*sin(x)+cos(x))/(3*(1+9*b^2));
f5v=1/6*L2*sin(x+alpha)*(2*cos(x+alpha)-L2);
f5h=1/3*L2*sin(x+alpha)*sin(x+alpha);
f6v=1/3*D*exp(2*b*(z-x))*cos(z)*cos(z);

```

```

f6h=1/6*D*exp(b*(z-x))*cos(z)*(2*exp(b*(z-x))*sin(z)-D);

flag=1;

if Ru>0
    options = optimset('TolX',1e-3);
    [thetal,fval,exitflag,output] = fzero(@(thetal)cos(thetal)*exp(b*(thetal-x))-
cos(x)+L1*cos(alpha),(z+y)/2,options);
    if (exitflag==1) && (thetal>z) && (thetal<y)
        fw1=integral(@(angle)funw1(angle,x,y,b,alpha,beta,water_pos),z,thetal);
    else
        fw1=NaN;
        flag=0;
    end
end

t=atan(sin(x+alpha)/(cos(x+alpha)-L1))-alpha;
if t<0
    t=pi+atan(sin(x+alpha)/(cos(x+alpha)-L1))-alpha;
end

rt=sqrt(sin(x+alpha)*sin(x+alpha)+(cos(x+alpha)-L1)^2);
ry=exp(b*(y-x));

H_points=zeros(1,n_points);
L_points=zeros(1,n_points);
ss=zeros(1,n_points);
rr=zeros(1,n_points);

for i=1:n_points
    H_points(i)=sin(x)+L1*sin(alpha)+H*i/(n_points+1);
    L_points(i)=cos(x)-L1*cos(alpha)-R(i)*L;
    rr(i)=sqrt(H_points(i)*H_points(i)+L_points(i)*L_points(i));
    ss(i)=acos(L_points(i)/rr(i));
    if rr(i)>exp(b*(ss(i)-x))
        flag=0;
    end
    if ss(i)>y
        flag=0;
    end
end

if (flag==1) && (water_pos>=0)
    f3v=0;
    f3h=0;
    fw2=0;
    if n_points==0
        f3v=fun3v(rt,t,ry,y);
        f3h=fun3h(rt,t,ry,y);
        fw2=integral(@(angle)funw3(angle,x,y,b,alpha,beta,water_pos),thetal,y);
    end
    if n_points==1
        f3v=fun3v(rt,t,rr(1),ss(1))+fun3v(rr(1),ss(1),ry,y);
        f3h=fun3h(rt,t,rr(1),ss(1))+fun3h(rr(1),ss(1),ry,y);
    end
    fw2=fw2sum(x,y,thetal,b,alpha,beta,water_pos,sin(x)+L1*cos(alpha),H_points(1),0,L_point
s(1))+fw2sum(x,y,thetal,b,alpha,beta,water_pos,H_points(1),ry*sin(y),L_points(1),L);
    if n_points>1
        f3v=fun3v(rt,t,rr(1),ss(1));
        f3h=fun3h(rt,t,rr(1),ss(1));
    end
    fw2=fw2sum(x,y,thetal,b,alpha,beta,water_pos,sin(x)+L1*cos(alpha),H_points(1),0,L_point
s(1));

    for i=1:(n_points-1)
        f3v=f3v+fun3v(rr(i),ss(i),rr(i+1),ss(i+1));
        f3h=f3h+fun3h(rr(i),ss(i),rr(i+1),ss(i+1));
    end
    fw2=fw2+fw2sum(x,y,thetal,b,alpha,beta,water_pos,H_points(i),H_points(i+1),L_points(i),
L_points(i+1));
    if n_points==n_points
        f3v=f3v+fun3v(rr(n_points),ss(n_points),ry,y);
        f3h=f3h+fun3h(rr(n_points),ss(n_points),ry,y);
    end
    fw2=fw2+fw2sum(x,y,thetal,b,alpha,beta,water_pos,H_points(n_points),ry*sin(y),L_points(
n_points),L);
    N=g*sin(beta)/sin(beta-alpha)/((1+Kv)*(f1v-f2v-f3v-f4v+f5v+f6v)+Kh*(f1h-f2h-f3h-
f4h+f5h+f6h)+(fw1+fw2)*gamma_ratio*b);
    if N<1 || N>500
        N=NaN;
    end
elseif (flag==1) && (water_pos<0)
    f3v=0;
    f3h=0;
    if n_points==0
        f3v=fun3v(rt,t,ry,y);

```

```

        f3h=fun3h(rt,t,ry,y);
    end
    if n_points==1
        f3v=fun3v(rt,t,rr(1),ss(1))+fun3v(rr(1),ss(1),ry,y);
        f3h=fun3h(rt,t,rr(1),ss(1))+fun3h(rr(1),ss(1),ry,y);
    end
    if n_points>1
        f3v=fun3v(rt,t,rr(1),ss(1));
        f3h=fun3h(rt,t,rr(1),ss(1));
        for i=1:(n_points-1)
            f3v=f3v+fun3v(rr(i),ss(i),rr(i+1),ss(i+1));
            f3h=f3h+fun3h(rr(i),ss(i),rr(i+1),ss(i+1));
        end
        f3v=f3v+fun3v(rr(n_points),ss(n_points),ry,y);
        f3h=f3h+fun3h(rr(n_points),ss(n_points),ry,y);
    end
    N=g*sin(beta)/sin(beta-alpha)/((1+Kv)*(f1v-f2v-f3v-f4v+f5v+f6v)+Kh*(f1h-f2h-f3h-
f4h+f5h+f6h));
    if N<1 || N>500
        N=NaN;
    end
else
    N=NaN;
end
end

% Main program: Sensitivity Analysis
% -----

clear
% Input data (non-variables)
% -----
% height [m]
Height=20;
% slope inclination
beta_grad=45;
beta=beta_grad/180*pi;
% upper slope inclination [deg]
alpha_grad=0;
alpha=alpha_grad/180*pi;
% position of phreatic line
water_pos=-1;
% unit weights [kN/m^3]
gamma_w=10;
gamma_s=20;
% crack
crack_type=1; % 1)known depth 2)known location 3) free
crack_depth=0; % crack depth
crack_x=0; % departs from slope crest
% slope profile
shape=1; % 1)planar 2)circular
Radius=Height; % circular radius
% x,y,z represent different failure mechanisms
x_guess_grad=50;
y_guess_grad=88;
z_guess_grad=50;
x_delta_grad=24;
y_delta_grad=20;
z_delta_grad=24;
x_pass_grad=1;
y_pass_grad=1;
z_pass_grad=1;
x_range_grad=(-x_delta_grad+x_guess_grad):x_pass_grad:(x_delta_grad+x_guess_grad);
y_range_grad=(-y_delta_grad+y_guess_grad):y_pass_grad:(y_delta_grad+y_guess_grad);
z_range_grad=(-z_delta_grad+z_guess_grad):z_pass_grad:(z_delta_grad+z_guess_grad);
x_range=x_range_grad/180*pi;
y_range=y_range_grad/180*pi;
z_range=z_range_grad/180*pi;

% number of points used to discretize slope profile
n_points=19;
% number of points used to discretize crack depth
n_depth=10;
% strength reduction
SR_ratio=1; % Fc/Ff 0 if reduce cohesion only

% to indicate a Mohr-Coulomb or Hoek-Brown failure criterion 1)M-C 2)H-B
failure_criterion=1;
% create a new sensitivity analysis project
pro = pro_Create();
% parameters and their distribution
pro = pro_AddInput(pro, @()pdf_Sobol([15/180*pi 25/180*pi]), 'Friction');
% pro = pro_AddInput(pro, @()pdf_Sobol([15 25]), 'Cohesion');
pro = pro_AddInput(pro, @()pdf_Sobol([0.1 0.3]), 'Kh');
pro = pro_AddInput(pro, @()pdf_Sobol([0.0 0.5]), 'Water');
pro = pro_AddInput(pro, @()pdf_Sobol([0.1 0.2]), 'Crack');
% Set the model

```

```

pro = pro_SetModel(pro, @(ParaArray)
Fryctoria_Sensitivity_Fcn(ParaArray,x_range,y_range,z_range,n_depth,n_points,beta,alpha
,Height,gamma_s,gamma_w,crack_type,crack_x,shape,Radius,SR_ratio), 'Fryctoria');
% Set the number of samples for the quasi-random Monte Carlo sampling
pro.N = 10;
% Initialize the project by calculating the model at the sample points
pro = GSA_Init(pro);
[Sen Err pro] = GSA_GetSy(pro, {'Friction','Kh','Water','Crack'});
Sfast = GSA_FAST_GetSi(pro);

function Fryctoria_Plot_FailureMechanism(handle,X,alpha,beta,b,Height,shape,n_points,R)

x=X(1);
y=X(2);
z=X(3);

rx=Height/(sin(beta)/sin(beta-alpha)*(exp(b*(y-x))*sin(y+alpha)-sin(x+alpha)));
L=Height/tan(beta);
L1=rx*(sin(y-x)/sin(y+alpha)-sin(y+beta)/(sin(y+alpha)*sin(beta-alpha))*(exp(b*(y-
x))*sin(y+alpha)-sin(x+alpha)));
L2=rx*(sin(z-x)/sin(z+alpha)-cos(z)/sin(z+alpha)/cos(alpha)*(exp(b*(z-x))*sin(z+alpha)-
sin(x+alpha)));
D=rx/cos(alpha)*(exp(b*(z-x))*sin(z+alpha)-sin(x+alpha));
xf=rx*cos(x);
yf=rx*sin(x);
xb=xf-L2*cos(alpha);
yb=yf+L2*sin(alpha);
xc=xb;
yc=yb+D;
xe=xf-L1*cos(alpha);
ye=yf+L1*sin(alpha);
xd=xe-L;
yd=ye+Height;
xrb=xf+Height/4*cos(alpha);
yrb=yf-Height/4*sin(alpha);
xlb=xd-Height/2;
ylb=yd;
Angle=z*(y-z)/100*y;
xLogS=rx*exp(b*(Angle-x)).*cos(Angle);
yLogS=rx*exp(b*(Angle-x)).*sin(Angle);

if shape==1
    line([xrb xe],[-yrb -ye],'Color','k','LineWidth',2.0);
    hold on
    line([xb xc],[-yb -yc],'Color','b','LineStyle',':');
    hold on
    line([xe xd],[-ye -yd],'Color','k','LineWidth',2.0);
    hold on
    line([xd xlb],[-yd -ylb],'Color','k','LineWidth',2.0);
    hold on
    plot(xLogS,-yLogS,'Color','r')
    axis equal
    set(gca,'xtick',[])
    set(gca,'ytick',[])
elseif shape==2
    R=[0 R 1];
    xProfile=zeros(1,n_points+2);
    yProfile=zeros(1,n_points+2);
    for i=1:(n_points+2)
        xProfile(i)=xe-L*R(i);
        yProfile(i)=ye+(i-1)/(n_points+1)*Height;
    end
    line([xrb xe],[-yrb -ye],'Color','k','LineWidth',2.0);
    hold on
    line([xb xc],[-yb -yc],'Color','b','LineStyle',':');
    hold on
    plot(xProfile,-yProfile,'Color','k','LineWidth',2.0);
    hold on
    line([xd xlb],[-yd -ylb],'Color','k','LineWidth',2.0);
    hold on
    plot(xLogS,-yLogS,'Color','r')
    axis equal
    set(gca,'xtick',[])
    set(gca,'ytick',[])
end

```



## Bibliography

- Abdoun, T., Dobry, R., O'rourke, T. D. & Goh, S. (2003) Pile response to lateral spreads: centrifuge modeling. *Journal of Geotechnical and Geoenvironmental Engineering* **129**(10):869-878.
- Abramson, L. W. (2002) *Slope stability and stabilization methods*. John Wiley & Sons.
- Agar, J. G., Morgenstern, N. R. & Scott, J. D. (1987) Shear-strength and stress-strain behavior of Athabasca oil sand at elevated-temperatures and pressures. *Canadian Geotechnical Journal* **24**(1):1-10.
- Al-Karni, A. A. & Al-Shamrani, M. A. (2000) Study of the effect of soil anisotropy on slope stability using method of slices. *Computers and Geotechnics* **26**(2):83-103.
- Andrianopoulos, K. I., Papadimitriou, A. G., Bouckovalas, G. D. & Karamitros, D. K. (2014) Insight into the seismic response of earth dams with an emphasis on seismic coefficient estimation. *Computers and Geotechnics* **55**:195-210.
- Ausilio, E., Conte, E. & Dente, G. (2000) Seismic stability analysis of reinforced slopes. *Soil Dynamics and Earthquake Engineering* **19**(3):159-172.
- Ausilio, E., Conte, E. & Dente, G. (2001) Stability analysis of slopes reinforced with piles. *Computers and Geotechnics* **28**(8):591-611.
- Baker, R. (1981) Tensile strength, tension cracks, and stability of slopes. *Soils and Foundation* **21**(2):1-17.
- Baker, R. (2003) Sufficient conditions for existence of physically significant solutions in limiting equilibrium slope stability analysis. *International Journal of Solids and Structures* **40**(13):3717-3735.
- Baker, R. (2004) Nonlinear Mohr envelopes based on triaxial data. *Journal of Geotechnical and Geoenvironmental Engineering* **130**(5):498-506.
- Baker, R. & Frydman, S. (1983) Upper bound limit analysis of soil with non-linear failure criterion. *Soils and Foundation* **23**(4):34-42.
- Baker, R. & Garber, M. (1978) Theoretical analysis of stability of slopes. *Geotechnique* **28**(4):395-411.
- Barnes, G. (1999) A commentary on the use of the pore pressure ratio  $ru$  in slope stability analysis. *Ground engineering* **32**(8).
- Bell, J. M. (1966) Dimensionless parameters for homogeneous earth slopes. *Journal of the Soil Mechanics and Foundations Division* **92**(5):51-66.
- Bishop, A. & Morgenstern, N. (1960) Stability coefficients for earth slopes. *Geotechnique* **10**(4):129-153.
- Bishop, A. W. (1955) The use of the slip circle in the stability analysis of slopes. *Geotechnique* **5**:7-17.
- Brandenberg, S. J., Boulanger, R. W., Kutter, B. L. & Chang, D. (2005) Behavior of pile foundations in laterally spreading ground during centrifuge tests. *Journal of Geotechnical and Geoenvironmental Engineering* **131**(11):1378-1391.
- Cai, F. E. I. & Ugai, K. (2000) Numerical analysis of the stability of a slope reinforced with piles. *Soils and Foundation* **40**(1):73-84.
- Cała, M. (2007) Convex and concave slope stability analyses with numerical methods. *Archives of Mining Sciences* **52**(1):75-89.
- Cannavó, F. (2012) Sensitivity analysis for volcanic source modeling quality assessment and model selection. *Computers & Geosciences* **44**:52-59.

- Castillo, E. & Luceno, A. (1982) A critical analysis of some variational methods in slope stability analysis. *International Journal for Numerical and Analytical Methods in Geomechanics* **6(2)**:195-209.
- Cetin, K. O., Isik, N. & Unutmaz, B. (2004) Seismically induced landslide at Degirmendere Nose, Izmit Bay during Kocaeli (Izmit)-Turkey earthquake. *Soil Dynamics and Earthquake Engineering* **24(3)**:189-197.
- Chang, C.-J., Chen, W. F. & Yao, J. T. (1984) Seismic displacements in slopes by limit analysis. *Journal of Geotechnical engineering* **110(7)**:860-874.
- Chen, L. & Poulos, H. (1993) Analysis of pile-soil interaction under lateral loading using infinite and finite elements. *Computers and Geotechnics* **15(4)**:189-220.
- Chen, W.-F. (1975) *Limit analysis and soil plasticity*. Amsterdam ; Oxford, Elsevier.
- Chen, W.-F. & Drucker, D. (1969) Bearing capacity of concrete blocks or rock. *Journal of Engineering Mechanics*.
- Chen, W.-F. & Giger, M. (1971) Limit analysis of stability of slopes. *Journal of Soil Mechanics & Foundations Div.*
- Chen, W. F. (1969) Soil mechanics and theorems of limit analysis. *Journal of the Soil Mechanics and Foundations Division* **95(2)**:493-518.
- Chen, W. F. & Liu, X. (1990) *Limit analysis in soil mechanics*. Amsterdam, Elsevier.
- Chen, Z.-Y. & Shao, C.-M. (1988) Evaluation of minimum factor of safety in slope stability analysis. *Canadian Geotechnical Journal* **25(4)**:735-748.
- Cheng, Y. (2003) Location of critical failure surface and some further studies on slope stability analysis. *Computers and Geotechnics* **30(3)**:255-267.
- Cheng, Y. (2007) Global optimization analysis of slope stability by simulated annealing with dynamic bounds and Dirac function. *Engineering Optimization* **39(1)**:17-32.
- Cheng, Y., Lansivaara, T. & Wei, W. (2007a) Two-dimensional slope stability analysis by limit equilibrium and strength reduction methods. *Computers and Geotechnics* **34(3)**:137-150.
- Cheng, Y., Li, L., Chi, S.-C. & Wei, W. (2007b) Particle swarm optimization algorithm for the location of the critical non-circular failure surface in two-dimensional slope stability analysis. *Computers and Geotechnics* **34(2)**:92-103.
- Cheng, Y., Li, L. & Chi, S. (2007c) Performance studies on six heuristic global optimization methods in the location of critical slip surface. *Computers and Geotechnics* **34(6)**:462-484.
- Cheng, Y., Li, L., Lansivaara, T., Chi, S. & Sun, Y. (2008) Minimization of factor of safety using different slip surface generation methods and an improved harmony search minimization algorithm. *Engineering Optimization* **40(2)**:95-115.
- Cheng, Y. M. & Lau, C. (2014) *Slope stability analysis and stabilization: new methods and insight*. CRC Press.
- Ching, R. & Fredlund, D. (1983) Some difficulties associated with the limit equilibrium method of slices. *Canadian Geotechnical Journal* **20(4)**:661-672.
- Chowdhury, R. N. & Zhang, S. (1991) Tension cracks and slope failure. In *Slope Stability Engineering: Developments and Applications* ,pp. 27-32.
- Christian, J. T., Ladd, C. C. & Baecher, G. B. (1994) Reliability applied to slope stability analysis. *Journal of Geotechnical engineering*.
- Clough, G. W. & Duncan, J. M. (1971) Finite element analyses of retaining wall behavior. *Journal of the Soil Mechanics and Foundations Division* **97(12)**:1657-1673.
- Clough, R. W. & Chopra, A. K. (1966) Earthquake stress analysis in earth dams. *Journal of the Engineering Mechanics Division* **92(2)**:197-212.

- Collins, I. F., Gunn, C. I. M., Pender, M. J. & Yan, W. (1988) Slope stability analyses for materials with a non-linear failure envelope. *International Journal for Numerical and Analytical Methods in Geomechanics* **12(5)**:533-550.
- Cundall, P. A. & Strack, O. D. (1979) A discrete numerical model for granular assemblies. *Geotechnique* **29(1)**:47-65.
- De Josselin De Jong, G. (1981) Variational fallacy. *Geotechnique* **31(4)**:289-290.
- Deng, D.-P., Zhao, L.-H. & Li, L. (2014) Limit equilibrium slope stability analysis using the nonlinear strength failure criterion. *Canadian Geotechnical Journal* **52(5)**:563-576.
- Descamps, F., Da Silva, M. R., Schroeder, C., Verbrugge, J. C. & Tshibangu, J. P. (2012) Limiting envelopes of a dry porous limestone under true triaxial stress states. *International Journal of Rock Mechanics and Mining Sciences* **56**:88-99.
- De Sousa Coutinho, A. G. (2006) Data reduction of horizontal load full-scale tests on bored concrete piles and pile groups. *Journal of Geotechnical and Geoenvironmental Engineering* **132(6)**:752-769.
- Donald, I. B. & Chen, Z. Y. (1997) Slope stability analysis by the upper bound approach: fundamentals and methods. *Canadian Geotechnical Journal* **34(6)**:853-862.
- Drescher, A. & Christopoulos, C. (1988) Limit analysis slope stability with nonlinear yield condition. *International Journal for Numerical and Analytical Methods in Geomechanics* **12(3)**:341-345.
- Drucker, D., Prager, W. & Greenberg, H. (1952) Extended limit design theorems for continuous media.
- Drucker, D. C., Greenberg, H. & Prager, W. (1950) *The safety factor of an elastic-plastic body in plane strain*. Division of Applied Mathematics, Brown University.
- Duncan, J. M. (1996) State of the art: limit equilibrium and finite-element analysis of slopes. *Journal of Geotechnical engineering* **122(7)**:577-596.
- Duncan, J. M. & Seed, H. B. (1966) Anisotropy and stress reorientation in clay. *Journal of the Soil Mechanics and Foundations Division* **92(5)**:21-50.
- Dym, C. L. & Shames, I. H. (1973) *Solid mechanics*. Springer.
- El-Ramly, H., Morgenstern, N. & Cruden, D. (2002) Probabilistic slope stability analysis for practice. *Canadian Geotechnical Journal* **39(3)**:665-683.
- Elia, G., Amorosi, A., Chan, A. & Kavvas, M. (2010) Fully coupled dynamic analysis of an earth dam. *Geotechnique* **61(7)**:549-563.
- Espinoza, R. D., Bourdeau, P. L. & Muhunthan, B. (1994) Unified formulation for analysis of slopes with general slip surface. *Journal of Geotechnical Engineering-Asce* **120(7)**:1185-1204.
- Fellenius, W. (1936) Calculations of the stability of earth dams. In *Transactions of the 2nd Congress on Large Dams.*, Washington, D.C., vol. 4, pp. 445-463.
- Firat, S. (2009) Stability analysis of pile-slope system. *Scientific Research and Essays* **4(9)**:842-852.
- Fraldi, M. & Guarracino, F. (2009) Limit analysis of collapse mechanisms in cavities and tunnels according to the Hoek–Brown failure criterion. *International Journal of Rock Mechanics and Mining Sciences* **46(4)**:665-673.
- Frank, R. & Pouget, P. (2008) Experimental pile subjected to long duration thrusts owing to a moving slope. *Geotechnique* **58(8)**:645-658.
- Fredlund, D. (1984) Analytical methods for slope stability analysis. In *Proceedings of the 4th International Symposium on Landslides.* s. l.: [sn], pp. 229-250.
- Fredlund, D. & Krahn, J. (1977) Comparison of slope stability methods of analysis. *Canadian Geotechnical Journal* **14(3)**:429-439.

- Fu, W. X. & Liao, Y. (2010) Non-linear shear strength reduction technique in slope stability calculation. *Computers and Geotechnics* **37(3)**:288-298.
- Gao, W. (2014) Forecasting of landslide disasters based on bionics algorithm (Part 1: Critical slip surface searching). *Computers and Geotechnics* **61**:370-377.
- Gao, Y., Zhang, F., Lei, G., Li, D., Wu, Y. & Zhang, N. (2012) Stability charts for 3D failures of homogeneous slopes. *Journal of Geotechnical and Geoenvironmental Engineering* **139(9)**:1528-1538.
- Gao, Y. F., Zhu, D. S., Zhang, F., Lei, G. H. & Qin, H. Y. (2014) Stability analysis of three-dimensional slopes under water drawdown conditions. *Canadian Geotechnical Journal* **51(11)**:1355-1364.
- Gazetas, G. (1987) Seismic response of earth dams: some recent developments. *Soil Dynamics and Earthquake Engineering* **6(1)**:2-47.
- Geosure (2011) *Landslides (slope instability)*. British Geological Survey, See <http://www.bgs.ac.uk/products/geosure/landslides.html> (accessed 25/10/2015).
- Griffiths, D. & Lane, P. (1999) Slope stability analysis by finite elements. *Geotechnique* **49(3)**:387-403.
- Griffiths, D. & Marquez, R. (2007) Three-dimensional slope stability analysis by elasto-plastic finite elements. *Geotechnique* **57(6)**:537-546.
- Griffiths, D. V. & Fenton, G. A. (2004) Probabilistic slope stability analysis by finite elements. *Journal of Geotechnical and Geoenvironmental Engineering* **130(5)**:507-518.
- Guo, W. D. & Qin, H. (2010) Thrust and bending moment of rigid piles subjected to moving soil. *Canadian Geotechnical Journal* **47(2)**:180-196.
- Hammah, R. (2005) A comparison of finite element slope stability analysis with conventional limit-equilibrium investigation. In *Proceedings of the 58th Canadian Geotechnical and 6th Joint IAH-CNC and CGS Groundwater Specialty Conferences—GeoSask 2005*. Citeseer.
- Hassiotis, S., Chameau, J. & Gunaratne, M. (1997) Design method for stabilization of slopes with piles. *Journal of Geotechnical and Geoenvironmental Engineering* **123(4)**:314-323.
- Hayward, T., Lees, A., Powrie, W., Richards, D. & Smethurst, J. (2000) *Centrifuge modelling of a cutting slope stabilised by discrete piles*. Transport Research Laboratory.
- Hestenes, M. R. & Stiefel, E. (1952) Methods of conjugate gradients for solving linear systems.
- Hoek, E. (1983) Strength of jointed rock masses. *Geotechnique* **33(3)**:187-223.
- Hoek, E. & Bray, J. D. (1981) *Rock slope engineering*. CRC Press.
- Hoek, E. & Brown, E. (1997) Practical estimates of rock mass strength. *International Journal of Rock Mechanics and Mining Sciences* **34(8)**:1165-1186.
- Hoek, E. & Brown, E. T. (1980) Empirical strength criterion for rock masses. *Journal of Geotechnical and Geoenvironmental Engineering* **106(ASCE 15715)**.
- Hoek, E., Carranza-Torres, C. & Corkum, B. (2002) Hoek-Brown failure criterion-2002 edition. *Proceedings of NARMS-Tac* **1**:267-273.
- Hoek, E., Kaiser, P. K. & Bawden, W. F. (1995) *Support of underground excavations in hard rock*. Rotterdam, Balkema.
- Hu, J., Zhong, L. & Yang, X. G. (2013) Upper bound approach for slope stability analysis based on arbitrary sliding surface and horizontal slices (in Chinese). *China Civil Engineering Journal* **46(6)**:117-121.

- Huang, F. & Yang, X. (2011) Upper bound limit analysis of collapse shape for circular tunnel subjected to pore pressure based on the Hoek–Brown failure criterion. *Tunnelling and Underground Space Technology* **26**(5):614-618.
- Huang, R., Pei, X., Fan, X., Zhang, W., Li, S. & Li, B. (2012) The characteristics and failure mechanism of the largest landslide triggered by the Wenchuan earthquake, May 12, 2008, China. *Landslides* **9**(1):131-142.
- Hudson, J. A. & Harrison, J. P. (2000) *Engineering rock mechanics- an introduction to the principles*. Elsevier Science.
- Hunter, J. H. & Schuster, R. (1968) Stability of simple cuttings in normally consolidated clays. *Geotechnique* **18**(3):372-378.
- Isakov, A. & Moryachkov, Y. (2014) Estimation of Slope Stability Using Two-Parameter Criterion of Stability. *International Journal of Geomechanics* **14**(3):3.
- Ito, T. & Matsui, T. (1975) Methods to estimate lateral force acting on stabilizing piles. *Soils and Foundation* **15**(4):43-59.
- Ito, T., Matsui, T. & Hong, W. P. (1979) Design method for the stability analysis of the slope with landing pier. *Soils and Foundation* **19**(4):43-57.
- Ito, T., Matsui, T. & Hong, W. P. (1981) Design method for stabilizing piles against landslide: one row of piles. *Soils and Foundation* **21**(1):21-37.
- Ito, T., Matsui, T. & Hong, W. P. (1982) Extended design method for multi-row stabilizing piles against landslide. *Soils and Foundation* **22**(1):1-13.
- Janbu, N. (1954) Application of composite slip surfaces for stability analysis. In *Proc. European Conf. on Stability of Earth Slopes, Stockholm, 1954.*, vol. 3, pp. 43-49.
- Janbu, N. (1972) Earth pressure computations in theory and practice. In *Fifth Eur Conf On Soil Proc/Sp/.*
- Jeldes, I. A., Drumm, E. C. & Yoder, D. C. (2014) Design of Stable Concave Slopes for Reduced Sediment Delivery. *Journal of Geotechnical and Geoenvironmental Engineering* **141**(2):04014093.
- Jeldes, I. A., Vence, N. E. & Drumm, E. C. (2013) Approximate solution to the Sokolovskii concave slope at limiting equilibrium. *International Journal of Geomechanics*.
- Jenike, A. W. & Yen, B. C. (1962) *Slope Stability in Axial Symmetry*.
- Jeong, S., Kim, B., Won, J. & Lee, J. (2003) Uncoupled analysis of stabilizing piles in weathered slopes. *Computers and Geotechnics* **30**(8):671-682.
- Jiang, J.-C. & Yamagami, T. (2006) Charts for estimating strength parameters from slips in homogeneous slopes. *Computers and Geotechnics* **33**(6):294-304.
- Jiang, S.-H., Li, D.-Q., Zhang, L.-M. & Zhou, C.-B. (2014) Slope reliability analysis considering spatially variable shear strength parameters using a non-intrusive stochastic finite element method. *Engineering geology* **168**:120-128.
- Jibson, R. W. (2011) Methods for assessing the stability of slopes during earthquakes—a retrospective. *Engineering geology* **122**(1):43-50.
- Jurado-Piña, R. & Jimenez, R. (2015) A genetic algorithm for slope stability analyses with concave slip surfaces using custom operators. *Engineering Optimization* **47**(4):453-472.
- Kahatadeniya, K. S., Nanakorn, P. & Neaupane, K. M. (2009) Determination of the critical failure surface for slope stability analysis using ant colony optimization. *Engineering geology* **108**(1):133-141.
- Kaniraj, S. R. & Abdullah, H. (1994) The effect of berms and tension cracks on the maximum reinforcement force in embankments on soft soils. *Geotextiles and Geomembranes* **13**(2):101-117.

- Knappett, J. & Madabhushi, S. (2011) Effects of axial load and slope arrangement on pile group response in laterally spreading soils. *Journal of Geotechnical and Geoenvironmental Engineering* **138(7)**:799-809.
- Koppula, S. (1984) Pseudo-static analysis of clay slopes subjected to earthquakes. *Geotechnique* **34(1)**:71-79.
- Kourkoulis, R., Gelagoti, F., Anastasopoulos, I. & Gazetas, G. (2010) Slope stabilizing piles and pile-groups: parametric study and design insights. *Journal of Geotechnical and Geoenvironmental Engineering* **137(7)**:663-677.
- Kourkoulis, R., Gelagoti, F., Anastasopoulos, I. & Gazetas, G. (2011) Hybrid method for analysis and design of slope stabilizing piles. *Journal of Geotechnical and Geoenvironmental Engineering*.
- Krabbenhoft, K., Lyamin, A. V., Hjaaj, M. & Sloan, S. W. (2005) A new discontinuous upper bound limit analysis formulation. *International Journal for Numerical Methods in Engineering* **63(7)**:1069-1088.
- Krahn, J. (2003) The 2001 RM Hardy Lecture: The limits of limit equilibrium analyses. *Canadian Geotechnical Journal* **40(3)**:643-660.
- Lam, L. & Fredlund, D. (1993) A general limit equilibrium model for three-dimensional slope stability analysis. *Canadian Geotechnical Journal* **30(6)**:905-919.
- Leca, E. & Dormieux, L. (1990) Upper and lower bound solutions for the face stability of shallow circular tunnels in frictional material. *Geotechnique* **40(4)**:581-606.
- Lee, C., Hull, T. & Poulos, H. (1995) Simplified pile-slope stability analysis. *Computers and Geotechnics* **17(1)**:1-16.
- Lee, I.-M. & Nam, S.-W. (2001) The study of seepage forces acting on the tunnel lining and tunnel face in shallow tunnels. *Tunnelling and Underground Space Technology* **16(1)**:31-40.
- Leshchinsky, D. & Huang, C.-C. (1992) Generalized three-dimensional slope-stability analysis. *Journal of Geotechnical engineering* **118(11)**:1748-1764.
- Leung, C., Chow, Y. & Shen, R. (2000) Behavior of pile subject to excavation-induced soil movement. *Journal of Geotechnical and Geoenvironmental Engineering* **126(11)**:947-954.
- Li, A., Lyamin, A. & Merifield, R. (2009a) Seismic rock slope stability charts based on limit analysis methods. *Computers and Geotechnics* **36(1)**:135-148.
- Li, A., Merifield, R. & Lyamin, A. (2011) Effect of rock mass disturbance on the stability of rock slopes using the Hoek–Brown failure criterion. *Computers and Geotechnics* **38(4)**:546-558.
- Li, A. J., Merifield, R. S. & Lyamin, A. V. (2008) Stability charts for rock slopes based on the Hoek-Brown failure criterion. *International Journal of Rock Mechanics and Mining Sciences* **45(5)**:689-700.
- Li, L., Tang, C., Zhu, W. & Liang, Z. (2009b) Numerical analysis of slope stability based on the gravity increase method. *Computers and Geotechnics* **36(7)**:1246-1258.
- Li, X., He, S. & Wu, Y. (2009c) Seismic displacement of slopes reinforced with piles. *Journal of Geotechnical and Geoenvironmental Engineering* **136(6)**:880-884.
- Li, X., Pei, X., Gutierrez, M. & He, S. (2012) Optimal location of piles in slope stabilization by limit analysis. *Acta Geotechnica* **7(3)**:253-259.
- Li, Y.-C., Chen, Y.-M., Zhan, T. L., Ling, D.-S. & Cleall, P. J. (2010) An efficient approach for locating the critical slip surface in slope stability analyses using a real-coded genetic algorithm. *Canadian Geotechnical Journal* **47(7)**:806-820.

- Lo, K. Y. (1965) Stability of slopes in anisotropic soils. *Journal of the Soil Mechanics and Foundations Division* **91(4)**:85-106.
- Lorig, L. & Varona, P. (2001) Practical slope-stability analysis using finite-difference codes. *Slope stability in surface mining*:115-124.
- Low, B., Gilbert, R. & Wright, S. (1998) Slope reliability analysis using generalized method of slices. *Journal of Geotechnical and Geoenvironmental Engineering* **124(4)**:350-362.
- Luan, M. T., Wu, Y. J. & Nian, T. K. (2003) A criterion for evaluating slope stability based on development of plastic zone by shear strength reduction FEM (in Chinese). *Journal of Disaster Prevention and Mitigation Engineering* **23(3)**:1-8.
- Lyamin, A. & Sloan, S. (2002a) Lower bound limit analysis using non - linear programming. *International Journal for Numerical Methods in Engineering* **55(5)**:573-611.
- Lyamin, A. V. & Sloan, S. (2002b) Upper bound limit analysis using linear finite elements and non - linear programming. *International Journal for Numerical and Analytical Methods in Geomechanics* **26(2)**:181-216.
- Lysmer, J. (1970) Limit analysis of plane problems in soil mechanics. *Journal of Soil Mechanics & Foundations Div.*
- Makdisi, F. I. & Seed, H. B. (1977) Simplified procedure for estimating dam and embankment earthquake-induced deformations. In *ASAE Publication No. 4-77. Proceedings of the National Symposium on Soil Erosion and Sediment by Water, Chicago, Illinois, December 12-13, 1977.*
- Makrodimopoulos, A. & Martin, C. (2006) Lower bound limit analysis of cohesive - frictional materials using second - order cone programming. *International Journal for Numerical Methods in Engineering* **66(4)**:604-634.
- Makrodimopoulos, A. & Martin, C. (2007) Upper bound limit analysis using simplex strain elements and second - order cone programming. *International Journal for Numerical and Analytical Methods in Geomechanics* **31(6)**:835-865.
- Marinos, V., Marinos, P. & Hoek, E. (2005) The geological strength index: applications and limitations. *Bulletin of Engineering Geology and the Environment* **64(1)**:55-65.
- Martin, C., Kaiser, P. & McCreath, D. (1999) Hoek-Brown parameters for predicting the depth of brittle failure around tunnels. *Canadian Geotechnical Journal* **36(1)**:136-151.
- Mathworks (2014) MATLAB 2014b. Mathworks, Natick, United States.
- Matsui, T., Hong, W. P. & Ito, T. (1982) Earth pressures on piles in a row due to lateral soil movements. *Soils and Foundation* **22(2)**:71-81.
- Matsui, T. & San, K.-C. (1992) Finite element slope stability analysis by shear strength reduction technique. *Soils and Foundation* **32(1)**:59-70.
- Mayne, P. W. (1985) Stress anisotropy effects on clay strength. *Journal of Geotechnical engineering* **111(3)**:356-366.
- Mccombie, P. & Wilkinson, P. (2002) The use of the simple genetic algorithm in finding the critical factor of safety in slope stability analysis. *Computers and Geotechnics* **29(8)**:699-714.
- Meng, F. Z., Zhou, H., Zhang, C. Q., Xu, R. C. & Lu, J. J. (2015) Evaluation Methodology of Brittleness of Rock Based on Post-Peak Stress-Strain Curves. *Rock Mechanics and Rock Engineering* **48(5)**:1787-1805.
- Merifield, R. S., Lyamin, A. V. & Sloan, S. (2006) Limit analysis solutions for the bearing capacity of rock masses using the generalised Hoek–Brown criterion. *International Journal of Rock Mechanics and Mining Sciences* **43(6)**:920-937.

- Mezazigh, S. & Levacher, D. (1998) Laterally loaded piles in sand: slope effect on PY reaction curves. *Canadian Geotechnical Journal* **35(3)**:433-441.
- Michalowski, R. (1997a) An estimate of the influence of soil weight on bearing capacity using limit analysis. *Soils and Foundation* **37(4)**:57-64.
- Michalowski, R. (2008) Limit analysis with anisotropic fibre-reinforced soil. *Geotechnique* **58(6)**:489-501.
- Michalowski, R. L. (1995) Slope stability analysis: A kinematical approach. *Geotechnique* **45(2)**:283-293.
- Michalowski, R. L. (1997b) Stability of uniformly reinforced slopes. *Journal of Geotechnical and Geoenvironmental Engineering* **123(6)**:546-556.
- Michalowski, R. L. (1998) Limit analysis in stability calculations of reinforced soil structures. *Geotextiles and Geomembranes* **16(6)**:311-331.
- Michalowski, R. L. (2002) Stability charts for uniform slopes. *Journal of Geotechnical and Geoenvironmental Engineering* **128(4)**:351-355.
- Michalowski, R. L. (2013) Stability assessment of slopes with cracks using limit analysis. *Canadian Geotechnical Journal* **50(10)**:1011-1021.
- Mo, H., Tang, C. & Liu, S. (1999) Determination of the most dangerous slip surface with pattern search method. *CHINESE JOURNAL OF GEOTECHNICAL ENGINEERING-CHINESE EDITION* **21(6)**:696-699.
- Morgenstern, N. & Price, V. E. (1965) The analysis of the stability of general slip surfaces. *Geotechnique* **15(1)**:79-93.
- Navarro, V., Yustres, A., Candel, M., López, J. & Castillo, E. (2010) Sensitivity analysis applied to slope stabilization at failure. *Computers and Geotechnics* **37(7)**:837-845.
- Newmark, N. M. (1965) Effects of Earthquakes on Dams and Embankments. *Geotechnique* **15(2)**:139-160.
- Nian, T.-K., Huang, R.-Q., Wan, S.-S. & Chen, G.-Q. (2012) Three-dimensional strength-reduction finite element analysis of slopes: geometric effects. *Canadian Geotechnical Journal* **49(5)**:574-588.
- Nian, T., Chen, G., Luan, M., Yang, Q. & Zheng, D. (2008) Limit analysis of the stability of slopes reinforced with piles against landslide in nonhomogeneous and anisotropic soils. *Canadian Geotechnical Journal* **45(8)**:1092-1103.
- Ning, Y., An, X. & Ma, G. (2011) Footwall slope stability analysis with the numerical manifold method. *International Journal of Rock Mechanics and Mining Sciences* **48(6)**:964-975.
- Optumce (2013) Optum G2. Optum Computational Engineering, Newcastle, Australia.
- Pan, J., Goh, A., Wong, K. & Teh, C. (2002) Ultimate soil pressures for piles subjected to lateral soil movements. *Journal of Geotechnical and Geoenvironmental Engineering* **128(6)**:530-535.
- Poulos, H. G. (1995) Design of reinforcing piles to increase slope stability. *Canadian Geotechnical Journal* **32(5)**:808-818.
- Prévost, J.-H., Abdel-Ghaffar, A. M. & Elgamal, A.-W. M. (1985) Nonlinear hysteretic dynamic response of soil systems. *Journal of Engineering Mechanics* **111(5)**:696-713.
- Rassam, D. W. & Williams, D. J. (1999) 3-Dimensional effects on slope stability of high waste rock dumps. *International Journal of Surface Mining, Reclamation and Environment* **13(1)**:19-24.
- Rathje, E. M. & Bray, J. D. (1999) An examination of simplified earthquake-induced displacement procedures for earth structures. *Canadian Geotechnical Journal* **36(1)**:72-87.



- Rathnaweera, T. D., Ranjith, P. G., Perera, M. S. A., Lashin, A. & Al Arifi, N. (2015) Non-linear stress-strain behaviour of reservoir rock under brine saturation: An experimental study. *Measurement* **71**:56-72.
- Rieke-Zapp, D. & Nearing, M. (2005) Slope shape effects on erosion. *Soil Science Society of America Journal* **69**(5):1463-1471.
- Rocscience (2006) Slide 5.0. Rocscience Inc., Toronto, Canada.
- Rocscience (2015) Phase2 9.0. Rocscience Inc., Toronto, Canada.
- Rojat, F., Labiouse, V. & Mestat, P. (2015) Improved analytical solutions for the response of underground excavations in rock masses satisfying the generalized Hoek–Brown failure criterion. *International Journal of Rock Mechanics and Mining Sciences* **79**:193-204.
- Saltelli, A., Chan, K. & Scott, E. M. (2009) *Sensitivity Analysis*. Wiley.
- San, K.-C. & Leshchinsky, D. O. V. (1994) Seismic slope stability analysis: pseudo-static generalized method. *Soils and Foundation* **34**(2):73-77.
- Sarma, S. K. (1979) Stability analysis of embankments and slopes. *Journal of the Geotechnical Engineering Division* **105**(12):1511-1524.
- Scavia, C. (1990) Fracture mechanics approach to stability analysis of rock slopes. *Engineering Fracture Mechanics* **35**(4):899-910.
- Seed, H. B., Idriss, I., Lee, K. L. & Makdisi, F. (1975) Dynamic analysis of the slide in the Lower San Fernando Dam during the earthquake of February 9, 1971. *Journal of Geotechnical and Geoenvironmental Engineering* **101**(ASCE# 11541 Proceeding).
- Seed, H. B. & Idriss, I. M. (1969) Influence of soil conditions on ground motions during earthquakes. *Journal of the Soil Mechanics and Foundations Division* **95**(1):99-138.
- Shen, J. & Karakus, M. (2013) Three-dimensional numerical analysis for rock slope stability using shear strength reduction method. *Canadian Geotechnical Journal* **51**(2):164-172.
- Shen, J., Karakus, M. & Xu, C. (2013) Chart-based slope stability assessment using the Generalized Hoek–Brown criterion. *International Journal of Rock Mechanics and Mining Sciences* **64**:210-219.
- Siad, L. (2003) Seismic stability analysis of fractured rock slopes by yield design theory. *Soil Dynamics and Earthquake Engineering* **23**(3):21-30.
- Sloan, S. (1988) Lower bound limit analysis using finite elements and linear programming. *International Journal for Numerical and Analytical Methods in Geomechanics* **12**(1):61-77.
- Sloan, S. (1989) Upper bound limit analysis using finite elements and linear programming. *International Journal for Numerical and Analytical Methods in Geomechanics* **13**(3):263-282.
- Sloan, S. (2013) Geotechnical stability analysis. *Geotechnique* **63**(7):531-571.
- Smethurst, J. & Powrie, W. (2007) Monitoring and analysis of the bending behaviour of discrete piles used to stabilise a railway embankment. *Geotechnique* **57**(8):663-677.
- Sokolovskii, V. V. (1965) *Statics of Granular Media*. Oxford, U.K., Pergamon Press.
- Sokolovskii, V. V. (1960) *Statics of soil media*. London, Butterworths Scientific Publications.
- Soubra, A.-H. (1999) Upper-bound solutions for bearing capacity of foundations. *Journal of Geotechnical and Geoenvironmental Engineering* **125**(1):59-68.
- Soubra, A.-H. (2000) Static and seismic passive earth pressure coefficients on rigid retaining structures. *Canadian Geotechnical Journal* **37**(2):463-478.

- Spencer, E. (1967) A method of analysis of the stability of embankments assuming parallel inter-slice forces. *Geotechnique* **17**(1):11-26.
- Spencer, E. (1968) Effect of tension on stability of embankments. *Journal of the Soil Mechanics and Foundations Division* **94**(5):1159-1176.
- Spencer, E. (1973) Thrust line criterion in embankment stability analysis. *Geotechnique* **23**(1).
- Stefano, C. D., Ferro, V., Porto, P. & Tusa, G. (2000) Slope curvature influence on soil erosion and deposition processes. *Water resources research* **36**(2):607-617.
- Sun, J., Li, J. & Liu, Q. (2008) Search for critical slip surface in slope stability analysis by spline-based GA method. *Journal of Geotechnical and Geoenvironmental Engineering*.
- Tang, G.-P., Zhao, L.-H., Li, L. & Yang, F. (2015) Stability charts of slopes under typical conditions developed by upper bound limit analysis. *Computers and Geotechnics* **65**:233-240.
- Taylor, D. W. (1948) Fundamentals of soil mechanics. *Soil Science* **66**(2):161.
- Terzaghi, K. (1943) *Theoretical soil mechanics*. Wiley.
- Terzaghi, K. (1950) *Mechanism of Landslides*. New York, Geological Society of America.
- Tika, T. E., Vaughan, P. & Lemos, L. (1996) Fast shearing of pre-existing shear zones in soil. *Geotechnique* **46**(2):197-233.
- Tschuchnigg, F., Schweiger, H. & Sloan, S. (2015) Slope stability analysis by means of finite element limit analysis and finite element strength reduction techniques. Part I: Numerical studies considering non-associated plasticity. *Computers and Geotechnics* **70**:169-177.
- Ugai, K. (1989) A Method of Calculation of Total Safety Factor of Slope by Elasto-Plastic FEM. *Soils and Foundation* **29**(2):190-195.
- Ugai, K. & Leshchinsky, D. O. V. (1995) Three-dimensional limit equilibrium and finite element analyses: a comparison of results. *Soils and Foundation* **35**(4):1-7.
- Usgs (2015) *Catastrophic Landslides of the 20th Century - Worldwide*. United States Geological Survey, See <http://landslides.usgs.gov/learn/majorls.php> (accessed 25/10 /2015).
- Utili, S. (2013) Investigation by limit analysis on the stability of slopes with cracks. *Geotechnique* **63**(2):140-154.
- Utili, S. (2015) Slopes of optimal shape.) Invited presentation at Newcastle University (U.K.) edn., Newcastle University (U.K.).
- Utili, S. & Abd, A. (2016) On the stability of fissured slopes subject to seismic action. *International Journal for Numerical and Analytical Methods in Geomechanics*.
- Utili, S. & Nova, R. (2007) On the optimal profile of a slope. *Soils and Foundations* **47**(4):717-729.
- Viratjandr, C. & Michalowski, R. L. (2006) Limit analysis of submerged slopes subjected to water drawdown. *Canadian Geotechnical Journal* **43**(8):802-814.
- Wang, L. P. & Zhang, G. (2014) Progressive failure behavior of pile-reinforced clay slopes under surface load conditions. *Environmental earth sciences* **71**(12):5007-5016.
- Wei, W. & Cheng, Y. (2009) Strength reduction analysis for slope reinforced with one row of piles. *Computers and Geotechnics* **36**(7):1176-1185.
- Won, J., You, K., Jeong, S. & Kim, S. (2005) Coupled effects in stability analysis of pile-slope systems. *Computers and Geotechnics* **32**(4):304-315.

- Wright, S. G., Kulhawy, F. H. & Duncan, J. M. (1973) Accuracy of equilibrium slope stability analysis. *Journal of the Soil Mechanics and Foundations Division* **99(10)**:783-791.
- Wyllie, D. C., Mah, C. W. & Hoek, E. R. S. E. (2004) *Rock slope engineering : civil and mining*. 4th ed. / Duncan C. Wyllie and Christopher W. Mah. edn. London, Spon.
- Xie, M., Esaki, T. & Cai, M. (2004) A GIS-based method for locating the critical 3D slip surface in a slope. *Computers and Geotechnics* **31(4)**:267-277.
- Xing, Z. (1988) Three-dimensional stability analysis of concave slopes in plan view. *Journal of Geotechnical engineering* **114(6)**:658-671.
- Yang, X.-L. (2007) Upper bound limit analysis of active earth pressure with different fracture surface and nonlinear yield criterion. *Theoretical and Applied Fracture Mechanics* **47(1)**:46-56.
- Yang, X. L., Li, L. & Yin, J. H. (2004) Stability analysis of rock slopes with a modified Hoek-Brown failure criterion. *International Journal for Numerical and Analytical Methods in Geomechanics* **28(2)**:181-190.
- Yang, X. L. & Zou, J. F. (2006) Stability factors for rock slopes subjected to pore water pressure based on the Hoek-Brown failure criterion. *International Journal of Rock Mechanics and Mining Sciences* **43(7)**:1146-1152.
- Yegian, M., Gazetas, G., Dakoulas, P. & Makris, N. (1995) The Northridge earthquake of 1994: Ground motions and geotechnical aspects. In *Third International Conference on Recent Advances in Geotechnical Earthquake Engineering and Soil Dynamics (1981: April 2-7; St. Louis, Missouri)*.) Missouri S&T (formerly the University of Missouri--Rolla).
- Yiagos, A. & Prevost, J. (1991) Two-phase elasto-plastic seismic response of earth dams: theory. *Soil Dynamics and Earthquake Engineering* **10(7)**:357-370.
- You, L. & Michalowski, R. L. (1999) Displacement charts for slopes subjected to seismic loads. *Computers and Geotechnics* **25(1)**:45-55.
- Yu, H., Salgado, R., Sloan, S. & Kim, J. (1998) Limit analysis versus limit equilibrium for slope stability. *Journal of Geotechnical and Geoenvironmental Engineering* **124(1)**:1-11.
- Zeng, S. & Liang, R. (2002) Stability analysis of drilled shafts reinforced slope. *Soils and Foundation* **42(2)**:93-102.
- Zhang, L., Fredlund, M. D., Fredlund, D. G., Lu, H. & Wilson, G. (2015) The influence of the unsaturated soil zone on 2-D and 3-D slope stability analyses. *Engineering geology*.
- Zhang, X. J. & Chen, W. F. (1987) Stability analysis of slopes with general nonlinear failure criterion. *International Journal for Numerical and Analytical Methods in Geomechanics* **11(1)**:33-50.
- Zhang, Y., Chen, G., Zheng, L., Li, Y. & Zhuang, X. (2013) Effects of geometries on three-dimensional slope stability. *Canadian Geotechnical Journal* **50(3)**:233-249.
- Zhou, X. & Cheng, H. (2014) Stability analysis of three-dimensional seismic landslides using the rigorous limit equilibrium method. *Engineering geology* **174**:87-102.
- Zhu, D., Lee, C. & Jiang, H. (2003) Generalised framework of limit equilibrium methods for slope stability analysis. *Geotechnique* **53(4)**:377-395.
- Zienkiewicz, O., Chang, C. & Bettess, P. (1980) Drained, undrained, consolidating and dynamic behaviour assumptions in soils. *Geotechnique* **30(4)**:385-395.

- Zienkiewicz, O. C., Humpheson, C. & Lewis, R. W. (1975) Associated and non-associated visco-plasticity and plasticity in soil mechanics. *Geotechnique* **25(4)**:671-689.
- Zolfaghari, A. R., Heath, A. C. & McCombie, P. F. (2005) Simple genetic algorithm search for critical non-circular failure surface in slope stability analysis. *Computers and Geotechnics* **32(3)**:139-152.